

University of Alberta

Reformer Gas Application in HCCI Combustion Engine

by

Vahid Hosseini



A thesis submitted to the Faculty of Graduate Studies and Research in partial fulfillment of the requirements for the degree of **Doctor of Philosophy**.

Department of Mechanical Engineering

Edmonton, Alberta
Spring 2008



Library and
Archives Canada

Bibliothèque et
Archives Canada

Published Heritage
Branch

Direction du
Patrimoine de l'édition

395 Wellington Street
Ottawa ON K1A 0N4
Canada

395, rue Wellington
Ottawa ON K1A 0N4
Canada

Your file *Votre référence*
ISBN: 978-0-494-45447-3
Our file *Notre référence*
ISBN: 978-0-494-45447-3

NOTICE:

The author has granted a non-exclusive license allowing Library and Archives Canada to reproduce, publish, archive, preserve, conserve, communicate to the public by telecommunication or on the Internet, loan, distribute and sell theses worldwide, for commercial or non-commercial purposes, in microform, paper, electronic and/or any other formats.

The author retains copyright ownership and moral rights in this thesis. Neither the thesis nor substantial extracts from it may be printed or otherwise reproduced without the author's permission.

AVIS:

L'auteur a accordé une licence non exclusive permettant à la Bibliothèque et Archives Canada de reproduire, publier, archiver, sauvegarder, conserver, transmettre au public par télécommunication ou par l'Internet, prêter, distribuer et vendre des thèses partout dans le monde, à des fins commerciales ou autres, sur support microforme, papier, électronique et/ou autres formats.

L'auteur conserve la propriété du droit d'auteur et des droits moraux qui protègent cette thèse. Ni la thèse ni des extraits substantiels de celle-ci ne doivent être imprimés ou autrement reproduits sans son autorisation.

In compliance with the Canadian Privacy Act some supporting forms may have been removed from this thesis.

Conformément à la loi canadienne sur la protection de la vie privée, quelques formulaires secondaires ont été enlevés de cette thèse.

While these forms may be included in the document page count, their removal does not represent any loss of content from the thesis.

Bien que ces formulaires aient inclus dans la pagination, il n'y aura aucun contenu manquant.

■*■
Canada

Abstract

A series of experiments was conducted on a Cooperative Fuel Research (CFR) engine operated in the homogenous charge compression ignition (HCCI) mode to study the effect of reformer gas (H_2 and CO mixture) on combustion timing. Base fuels of natural gas, iso-Octane, n-Heptane and primary reference fuels were used for experiments. The engine was tested at steady state conditions. Reformer gas blending expanded the operating region of natural gas HCCI combustion toward the lean side. Keeping all other influential parameters constant, increasing reformer gas fraction in the fuel mixture advanced combustion timing and increased combustion severity. Alternatively, reformer gas addition decreased the intake heating requirement of natural gas HCCI combustion. Combustion timing alteration was attributed to changed mixture thermodynamic properties.

For low octane fuels with dual-stage ignition, reformer gas suppressed the first stage of combustion by reducing intermediate radical concentration, thus retarding the main stage of combustion. Keeping all influential parameters constant, the delayed combustion timing reduced combustion intensity and improved efficiency.

Reformer gas blending had negligible effects on engine operating parameters

and HCCI combustion characteristics of high octane liquid fuels in the in the normally aspirated mode.

Changing reformer gas composition did not have strong effects on engine and combustion parameters. A mixture of 75% H_2 /25% CO had slightly stronger effect on combustion timing variation than that of 50% H_2 /50%CO.

It was found that reformer gas can be used to effectively control combustion timing of both natural gas and low octane fuels, although with different effective mechanisms in each case.

To Shekoufeh and Zahra

Acknowledgements

The wise, mature, knowledgeable, and humorous supervision of Professor M David Checkel is gratefully acknowledged. He contributed actively in all steps of this research from experimental setup to analyzing data, writing paper, and finally preparing this thesis. Without his guidance, it was impossible for me to get this far.

Dr. Bob Kock guidance is also greatly appreciated. Technical support in design, fabrication, and troubleshooting of experimental setup was provided by Mr. Bernie Faulkner and Mr. Terry Nord that is gratefully acknowledged. The financial supports of Auto21 National Center of Excellence, University of Alberta FS Chia PhD Scholarship Program, Queen Elizabeth II Doctoral Scholarship Program, Lehigh Inland Cement Graduate Scholarship in Environmental Studies, Sadler Graduate Scholarship of Faculty of Engineering at University of Alberta are acknowledged. I would like to thank National Research Council Canada, Institute for Chemical Process and Environmental Technology for financial support for final phase of completion of this study.

I also thank my friends for their contribution. Mr. Mathew Atkins and Dr. David Arthur contributed to the engine laboratory development before this study and their valuable technical advices are gratefully acknowledged. I also thank Dr. Paitoon Kongsereparp for technical and general discussions and development of chemical kinetic model that was used in this study. Technical contributions of Mr. Rob Lupul and Mr. Dan Hanford are also recognized.

I would like to thank my friends in Iranian community for their supports. Among several of them, I had supports of Dr. Iman Izadi in data acquisition system troubleshooting, Dr. Alireza Simchi in statistical analysis of experimental results, and Mr. Mahdi Shahbakhti in several useful scientific discussions.

I also thank my family, my mom, my brothers Majid and Mahdi, and my sister Reihaneh. I am also grateful to my wife Shekoufeh and my daughter Zahra. Their supports had a direct impact on completion of this work.

Contents

1	Introduction	1
1.1	HCCI Combustion Engine	2
1.1.1	Definition	2
1.1.2	History	4
1.1.3	HCCI Combustion Characteristics	5
1.1.4	HCCI Combustion Emissions Characteristics	10
1.1.5	Summary of HCCI Combustion Advantages and Disadvantages	13
1.2	Solutions to HCCI Combustion Problems	14
1.2.1	Conventional Solutions	14
1.2.2	Dual Fuel HCCI Combustion Engine	16
1.2.3	Fuel Reforming, a Bridge to Practical Dual Fuel HCCI Engine	17
1.2.4	Variable Valve Timing (VVT)	18
1.3	Reformer Gas (RG) and Reforming Techniques	19
1.3.1	Reformer Gas Properties	19
1.3.2	Reforming Methods	20
1.3.3	Related Reforming Studies	22
1.3.4	Reformer Gas Application in Conventional Combustion IC Engines	24

1.4	HCCI Autoignition Chemistry of Hydrocarbons	26
1.4.1	Multi-stage Autoignition of Hydrocarbons	27
1.4.2	Octane Number	32
1.5	Previous Use of Reformer Gas for HCCI Ignition Control	32
1.6	Motivation and Objectives	34
1.7	Organization of Thesis	36
2	Experimental Setup and Definitions of Parameters	37
2.1	Main Experimental Hardware	38
2.1.1	Engine and Dynamometer	38
2.1.2	Gaseous Fueling System	43
2.1.3	Liquid Fueling System	46
2.1.4	Intake and Exhaust Gas Recirculation Systems	48
2.2	Measurement and Control Devices	50
2.2.1	Temperature Measurement	50
2.2.2	Flow Measurement	51
2.2.3	Pressure Measurement	54
2.2.4	Exhaust Gas Composition Analysis	57
2.2.5	Cylinder Vibration Measurement	59
2.2.6	Intake Temperature Control	60
2.2.7	Engine Speed Control	60
2.2.8	Fuel Injection Control	61
2.3	Data Acquisition (DAQ) System	62
2.4	Definitions of Parameters	66
2.4.1	Compression Ratio (CR)	66
2.4.2	Relative Air/Fuel Ratio (λ)	68
2.4.3	EGR	69
2.4.4	RG Mass Fraction (RG blend fraction)	69
2.4.5	Indicated Mean Effective Pressure (IMEP)	69
2.4.6	Cyclic Variation (COV_{IMEP})	70

2.4.7	Thermal Efficiency (η_{th})	70
2.4.8	Combustion Efficiency (η_c)	71
2.4.9	Indicated Specific Emissions	71
2.4.10	Cylinder Pressure Trace Characteristics	73
2.4.11	Knock Indicators	73
2.5	Experimental Matrix and Procedures	80
2.6	Uncertainty Analysis	81
2.6.1	Error Estimation of the Primary Parameters	82
2.6.2	Error Estimation of the Secondary Parameters	83
2.6.3	Error Estimation of Cyclic Related Variables	83
2.7	Summary	84
3	Basic Operating Characteristics of HCCI Combustion Engine	85
3.1	Operating Region	85
3.2	Influential Parameters' Effects on the Engine Operating Parameters and Combustion Characteristics	96
3.2.1	λ and EGR	96
3.2.2	Intake and Exhaust Pressure	119
3.3	Factorial Design Tests for Significants of CR, EGR, $T_{intake,mix}$, and Speed	131
3.4	Summary	138
4	Reformer Gas Application in n-Heptane HCCI Combustion	
	Timing Control	140
4.1	Effect of RG on Low Octane PRF HCCI Combustion in the Naturally Aspirated Mode	143
4.1.1	Operating Region	143
4.1.2	Combustion Timing, and Combustion Duration	145
4.1.3	Pressure Trace Characteristics	147
4.1.4	Engine Operating Parameters	148
4.2	Effect of RG on Supercharged n-Heptane HCCI Combustion	150

4.2.1	Operating Region	150
4.2.2	Combustion Timing, Combustion Duration, and other Heat Release Characteristics	152
4.2.3	Pressure Trace Characteristics	158
4.2.4	Engine Operating Parameters	160
4.3	RG Composition Effects	163
4.4	Modeling Analysis	169
4.4.1	Description of Chemical Kinetic Model	169
4.4.2	Effect of RG on n-Heptane HCCI Combustion Timing .	170
4.4.3	Comparison of Simulation and Experiments	171
4.4.4	Detailed Analysis using ChemComb-SZM	171
4.4.5	Detailed Analysis of Effect of RG Composition on HCCI Combustion Timing	179
4.5	Summary	181
5	Reformer Gas Application in Combustion Timing Control of iso-Octane	185
5.1	Effect of RG on High Octane PRF HCCI Combustion in the Naturally Aspirated Mode	186
5.1.1	Operating Region	186
5.1.2	Comparison of RG Effect on PRF100 and PRF80	189
5.2	Effect of RG on Supercharged iso-Octane HCCI Combustion .	193
5.2.1	Operating Region	194
5.2.2	Combustion Timing, Combustion Duration, and Pres- sure Characteristics	196
5.2.3	Power, Efficiency and Emissions	199
5.3	RG Composition Effects	201
5.4	Summary	204
6	Improvement of Natural Gas HCCI Combustion using Re- former Gas	206

6.1	Effects of RG on Naturally Aspirated Natural Gas HCCI Combustion	208
6.1.1	Operating Region	208
6.1.2	Combustion Timing and Duration	210
6.1.3	Pressure Trace Characteristics	211
6.1.4	Engine Operating Parameters	213
6.2	Effects of RG on Supercharged Natural Gas HCCI	218
6.2.1	Operating Region	219
6.2.2	Combustion Timing, Combustion Duration, and Pressure Characteristics	220
6.2.3	Power, Efficiency, and Emissions	224
6.3	RG Composition Effects	227
6.4	Modeling Analysis	232
6.4.1	Effect of RG on Natural Gas HCCI Combustion Timing	232
6.4.2	Comparison of Simulation and Experiment	233
6.4.3	Detailed Analysis using ChemComb-SZM	234
6.4.4	Effect of RG Composition on HCCI Combustion Timing	236
6.5	Summary	238
7	Conclusion	241
7.1	HCCI Engine Laboratory Development	241
7.2	HCCI Combustion Timing	242
7.3	Basic HCCI Combustion Operation	243
7.4	Effect of RG on Low Octane Fuels HCCI Combustion	244
7.5	Effect of RG on High Octane Fuels HCCI Combustion	246
7.6	Effect of RG on Natural Gas HCCI Combustion	247
7.7	General Conclusions	248
7.8	Contributions	249
7.9	Future Work	249

A	Chemical and Physical Properties	264
A.1	Natural Gas	264
A.2	n-Heptane	265
A.3	iso-Octane	265
A.4	PRFs	266
A.5	RG	266
B	Measurement and Control Devices Specifications	267
B.1	Air mass flow meter	267
B.2	Gaseous fuel mass flow meter	268
B.3	Liquid fuel volume flow meter	268
B.4	Cylinder pressure	269
C	Calibration Curves	270
C.1	Cylinder pressure sensor calibration	270
C.2	Liquid fuel flow meter calibration	271
C.3	Gaseous fuel flow meter calibration	273
C.3.1	Natural gas flow meter	273
C.3.2	RG low mass flow	274
C.3.3	RG high mass flow	274
D	Pressure Trace Signal Analysis	276
D.1	Matlab Program for low pass and band pass filter	279
D.1.1	Main Program	279
D.1.2	Low pass filter Matlab function	283
D.1.3	Band pass filter Matlab function	284
E	Motoring Curves and CR Estimation	285
F	Knock Characterization Parameters	288
F.1	Filtered and Un-filtered Pressure Signal Difference (ΔP_P) . . .	289
F.2	Root Mean Square of Band Pass Filtered Pressure Trace (RMS_P)	290

F.3	Vibration Analysis of Cylinder Structure	291
F.4	Evaluation of Knock Indicators	292
G	Error and Uncertainty Analysis	295
G.1	Primary variables error analysis	295
G.2	Secondary variables error analysis	297
G.3	Cyclic variation related variables error analysis	298
H	Additional Experimental Results	299
H.1	Baseline Experiments- Emission Results	299
H.2	Baseline Experiments- Effect of λ and EGR on Knock	306

List of Tables

1.1	HCCI combustion advantages and disadvantages summary . . .	14
1.2	Engine parameters affecting HCCI combustion timing	15
2.1	CFR engine specification	39
2.2	CFR engine variable compression ratio assembly in Figure 2.2	41
2.3	List of the main components of the engine hardware in Figure 2.3	41
2.4	List of the components of the gaseous fueling system in Figure 2.4	44
2.5	List of the components of the liquid fueling system in Figure 2.5	46
2.6	List of the components of the intake system in Figure 2.6 . . .	49
2.7	List of the sensors and controllers in Figure 2.7	51
2.8	List of the components of the exhaust gas supply system for gas analyzer in Figure 2.8	57
2.9	E series NI DAQ card specifications	62
2.10	Description of the signal connections to the NI E series DAQ cards device 1 to 3 using SCB-68 terminal boxes	63
3.1	PRF fuel experimental matrix	94
3.2	Supercharged HCCI combustion engine experimental matrix .	96
3.3	Operating conditions for supercharged natural gas HCCI com- bustion and n-Heptane to investigate intake boost pressure effects	120
3.4	Main variables and their levels for full factorial design tests . .	132

3.5	Analysis of variance (ANOVA) for testing the significance of model for SOC	134
3.6	Absolute Normalized coefficients for coded value models of two-level factorial design indicated in Table 3.4	137
4.1	Operating conditions of n-Heptane and PRF20 naturally aspirated HCCI combustion	143
4.2	Selected constant λ cases from Table 4.1	145
4.3	Selected λ -EGR constant data groups, supercharged n-Heptane HCCI combustion at N=800 RPM, CR=11.8, $T_{\text{intake,mix}}=110$ °C	151
4.4	A comparison of selected RG composition properties	163
4.5	Initial conditions for two cases of RG 75/25 and RG 50/50, n-Heptane HCCI combustion	164
5.1	Operating conditions of naturally aspirated iso-Octane and PRF80 HCCI combustion	186
5.2	Selected constant λ -EGR cases from Table 5.1	189
5.3	Selected λ -EGR constant groups of data, supercharged HCCI combustion of iso-Octane at N=800 RPM, CR=14.4, $T_{\text{intake,mix}}=100$ °C	195
6.1	Initial conditions for natural gas fueled HCCI combustion operated in the naturally aspirated mode	208
6.2	Selected groups of constant λ /constant EGR operating points from supercharged natural gas HCCI combustion with RG, N=800 RPM, $T_{\text{intake,mix}}=140$ °C, CR=19.5, labeled in Figure 6.13	221
6.3	Initial conditions for two cases of RG 75/25 and RG 50/50, natural gas HCCI combustion	228
A.1	Domestic natural gas properties	264
A.2	n-Heptane properties	265
A.3	iso-Octane properties	266

A.4	H ₂ and CO properties from [1]	266
B.1	Hot wire TSI air mass flow meter specifications	268
B.2	Omega gaseous flammable mass flow meter specifications	268
B.3	General specifications of Max Machinery volume flow meters	269
B.4	Specifications of Kistler pressure transducer	269
E.1	Geometrical and effective compression ratio with indication of motoring P _{max}	286
E.2	A comparison of experimental P _{max} for CFR engine motoring under identical initial conditions at University of Alberta (UofA- current study) and Alberta Research Council (ARC- standard CFR) research facilities	287

List of Figures

1.1	A comparison of the Pressure-Volume diagrams of an HCCI engine and a SI engine: CFR Engine, CR=11.5, Speed=800 RPM, HCCI fueled with n-Heptane, SI fueled with CNG . . .	7
1.2	A comparison of 90 consecutive cycles of HCCI and SI pressure traces, (a) n-Heptane HCCI, IMEP=4.91 bar, $COV_{IMEP} = 1.04\%$, (b) natural gas SI, IMEP=5.3 bar, $COV_{IMEP} = 3.06\%$. Both in CFR engine, CR=11.5, N=800 RPM	8
1.3	A comparison of SI (natural gas, CR=11.5, throttled) with HCCI (natural gas, CR=19.5, supercharged) pressure traces with the same indicated power (IMEP=2.71 bar) (a) P-CAD digram, (b) P-V diagram	9
1.4	Decision making flowchart for the selection of partial reforming concept to control HCCI combustion timing	35
2.1	Valve timing diagram of the CFR engine, IVC: Intake Valve Close, IVO: Intake Valve Open, EVC: Exhaust Valve Close, EVO: Exhaust Valve Open, TDC: Top Dead Center	40
2.2	CFR variable compression ratio mechanism	40
2.3	A schematic of the CFR engine and main experimental components described in Table 2.3	42
2.4	A schematic of the components of the gaseous fueling system described in Table 2.4	45

2.5	A schematic of the components of the liquid fueling system described in Table 2.5	47
2.6	A schematic of the main components of the intake supercharging system	49
2.7	A schematic of the sensors and control instruments described in Table 2.7	52
2.8	A schematic of the exhaust sample gas supply to the emission measurement bench described in Table 2.8	57
2.9	Samples of accelerometer analog output for (a) non-knocking cycle and (b) knocking cycle. Note the difference in Y-axes scales	59
2.10	Low speed engine mean value parameters data acquisition program flowchart	64
2.11	A snapshot of the Labview TM based mean value data acquisition program	65
2.12	A comparison of pressure trace (P), net rate of heat release (NRHR), and gross accumulative heat release (GHR) for HCCI combustion of n-Heptane at $\lambda=1.98$, EGR=10%, CR=9.5, N=700 RPM	78
2.13	Combustion characteristics definition using NRHR and GHR plots, HCCI combustion of n-Heptane	79
3.1	A typical λ -EGR operating region for HCCI combustion with various definitions of operating boundaries	86
3.2	λ -EGR operating region of n-Heptane, supercharged HCCI combustion, initial conditions indicated in Table 3.2	88
3.3	A comparison of pressure traces for operating points at boundaries, P ₁ a knocking cycle , P ₂ a misfiring cycle, and P ₃ a motoring cycle, supercharged natural gas HCCI combustion, initial conditions indicated in Table 3.2	91

3.4	λ -EGR operating region with PRFs in the naturally aspirated mode, initial conditions indicated in Table 3.1	95
3.5	λ -EGR operating region with natural gas, n-Heptane and iso-Octane supercharged HCCI engine with and without partial reforming, initial conditions indicated in Table 3.2	97
3.6	Effect of λ and EGR on combustion timing (SOC), HCCI combustion of PRFs in CFR engine, Experimental matrix indicated in Table 3.1, error bars indicate $\pm 2\sigma_{n-1}$	102
3.7	Effect of λ and EGR on start of combustion (SOC), Supercharged n-Heptane, iso-Octane, and natural gas HCCI combustion, initial conditions indicated in Table 3.2, error bars indicate $\pm 2\sigma_{n-1}$	103
3.8	Effect of λ and EGR on combustion duration (CD), initial conditions indicated in Table 3.1, error bars indicate $\pm 2\sigma_{n-1}$	104
3.9	Effect of λ and EGR on combustion duration (CD), Supercharged HCCI combustion of natural gas, n-Heptane and iso-Octane, initial conditions indicated in Table 3.2, error bars indicate $\pm 2\sigma_{n-1}$	105
3.10	Effect of λ and EGR on low negative temperature coefficient (NTC), low-temperature reaction timing (LTR_{max}) and the ratio of low-temperature to high-temperature reaction that were defined in Figure 2.13, Supercharged n-Heptane HCCI combustion, initial conditions indicated in Table 3.2, error bars indicate $\pm 2\sigma_{n-1}$	106
3.11	Effect of λ and EGR on cylinder maximum pressure P_{max} , initial conditions indicated in Table 3.1, error bars indicate $\pm 2\sigma_{n-1}$	107
3.12	Effect of λ and EGR on maximum cylinder pressure - P_{max} - Supercharged HCCI combustion of natural gas, n-Heptane and iso-Octane, initial conditions indicated in Table 3.2, error bars indicate $\pm 2\sigma_{n-1}$	108

3.13	Effect of λ and EGR on cylinder maximum pressure rate $(dP/d\theta)_{\max}$, initial conditions indicated in Table 3.1, error bars indicate $\pm 2\sigma_{n-1}$	109
3.14	Effect of λ and EGR on cylinder maximum pressure rate $(dP/d\theta)_{\max}$, Supercharged HCCI combustion of natural gas, n-Heptane and iso-Octane, initial conditions indicated in Table 3.2, error bars indicate $\pm 2\sigma_{n-1}$	110
3.15	Effect of λ and EGR on indicated power, initial conditions in- dicated in Table 3.1, error bars indicate $\pm 2\sigma_{n-1}$	112
3.16	Effect of λ and EGR on indicated power, Supercharged natu- ral gas, n-Heptane, and iso-Octane HCCI combustion, initial conditions indicated in Table 3.2, error bars indicate $\pm 2\sigma_{n-1}$.	113
3.17	Effect of λ and EGR on indicated thermal efficiency, initial con- ditions indicated in Table 3.1, error bars indicate $\pm 2\sigma_{n-1}$. . .	114
3.18	Effect of λ and EGR on indicated power, Supercharged HCCI combustion of natural gas, n-Heptane and iso-Octane, initial conditions indicated in Table 3.2, error bars indicate $\pm 2\sigma_{n-1}$.	115
3.19	Supercharged HCCI combustion operating region with selected λ constant cases	121
3.20	variation of air mass flow rate and natural gas flow rate with intake pressure keeping λ constant at 3.62, supercharged natural gas HCCI combustion, operating condition in Table 3.3	121
3.21	Effect of intake pressure on (a) pressure trace and, (b) P_{\max} and $(dP/d\theta)_{\max}$, HCCI combustion of natural gas, initial conditions indicated in Table 3.3, error bars indicate $\pm 2\sigma_{n-1}$	122
3.22	Effect of intake pressure on indicated power (IMEP) and cyclic variation (COV_{IMEP}), supercharged HCCI combustion of natu- ral gas, initial conditions indicated in Table 3.3, error bars indicate $\pm 2\sigma_{n-1}$	123

3.23	Effect of intake pressure on thermal (η_{th}) and combustion (η_c) efficiencies, supercharged HCCI combustion of natural gas, initial conditions indicated in Table 3.3, error bars indicate $\pm 2\sigma_{n-1}$	123
3.24	Effect of intake pressure on rate of heat release (RHR) top plot and start of combustion (SOC) and combustion duration (CD), supercharged natural gas HCCI combustion indicated in Table 3.3, error bars indicate $\pm 2\sigma_{n-1}$	124
3.25	Supercharged HCCI combustion with n-Heptane, test points indicated in Table 3.3	125
3.26	Effect of intake pressure on indicated power (IMEP) and cyclic variation (COV_{IMEP}), supercharged n-Heptane HCCI combustion indicated in Table 3.3, error bars indicate $\pm 2\sigma_{n-1}$	126
3.27	Effect of intake pressure on (a) pressure trace and (b) P_{max} and $(dP/d\theta)_{max}$, supercharged n-Heptane HCCI combustion, initial conditions indicated in Table 3.3, error bars indicate $\pm 2\sigma_{n-1}$	127
3.28	Effect of intake pressure on the (a) net rate of heat release (NRHR), (b) combustion timing (SOC) and duration (CD), and (c) negative temperature coefficient length (NTC) and (LTR/HTR-Ratio), supercharged n-Heptane HCCI combustion, initial conditions indicated in Table 3.3, error bars indicate $\pm 2\sigma_{n-1}$	128
3.29	Effect of exhaust pressure on supercharged iso-Octane HCCI combustion, initial conditions indicated in Table 3.2, $P_{intake} = 142.80 \pm 1.1 kPa$, error bars indicate $\pm 2\sigma_{n-1}$	130
3.30	Half-normal probability of main effects and interaction for SOC (response Y_1), two-level factorial design tests, n-Heptane HCCI combustion indicated in Table 3.4	133
3.31	normal probability plot of the residual of predicted values by coded model and actual values of SOC (response Y_1), n-Heptane HCCI combustion indicated in Table 3.4	135

3.32	Interaction plot for combined effect of CR and EGR on SOC for coded values, n-Heptane HCCI combustion indicated in Table 3.4, ▲ is high EGR (coded value =+1, EGR =30%) and ■ is low EGR (coded value =+1, EGR =20%)	136
4.1	EGR- λ operating region for (a) data Set I and (b) data Set II indicated in Table 4.1, n-Heptane HCCI combustion in the naturally aspirated mode	144
4.2	EGR- λ operating region for (a) Set II and (b) Set III of data indicated in Table 4.1, n-Heptane and PRF20 HCCI combustion in the naturally aspirated mode	144
4.3	Effect of RG blend fraction on (a) start of combustion and (b) combustion duration, initial conditions indicated in Table 4.2 .	146
4.4	Effect of RG blend fraction on (a) P_{\max} and (b) $(dP/d\theta)_{\max}$ emissions of cases in Table 4.2	147
4.5	Effect of RG blend fraction on (a) IMEP and (b) COV_{IMEP} , initial conditions indicated in Table 4.2, error bars indicate $\pm 2\sigma_{n-1}$	148
4.6	Effect of RG blend fraction on (a) η_{th} and (b) η_c , initial conditions indicated in Table 4.2	149
4.7	Effect of RG blend fraction on (a) HC and (b) CO emissions, initial conditions indicated in Table 4.2	149
4.8	λ -EGR operating region for n-Heptane HCCI combustion at elevated intake pressure (a) without RG blending and (b) with RG blending, N=800 RPM, $T_{intake,mix} = 110$ °C, CR=11.8 . . .	150
4.9	(a) RG- λ and (b) RG-EGR operating regions with indication of constant λ groups of data indicated in Table 4.3, N=800 RPM, $T_{intake,mix} = 110$ °C, CR=11.8	151
4.10	Effect of RG blend fraction on (a) start of combustion and (b) combustion duration at constant λ and EGR for data indicated in Table 4.3, error bars indicate $\pm 2\sigma_{n-1}$	153

4.11	Effect of RG blend fraction on (a) maximum low-temperature heat release , LTR_{max} , and (b) maximum low-temperature heat release timing, $LTR_{max,time}$ at constant λ and EGR for data indicated in Table 4.3, error bars indicate $\pm 2\sigma_{n-1}$	154
4.12	Effect of RG blend fraction on (a) maximum high temperature heat release , HTR_{max} and (b) maximum high temperature heat release timing, $HTR_{max,time}$ at constant λ and EGR for data indicated in Table 4.3, error bars indicate $\pm 2\sigma_{n-1}$	155
4.13	Effect of RG blend fraction on (a) negative temperature coefficient and (b) ratio of the first to second stage maximum heat release at constant λ and EGR for data indicated in Table 4.3, error bars indicate $\pm 2\sigma_{n-1}$	156
4.14	Effect of RG blend fraction on pressure traces of data group B in Table 4.3, error bars indicate $\pm 2\sigma_{n-1}$	157
4.15	Effect of RG blend fraction on (a) net rate of heat release and (b) gross accumulative heat release of data group B in Table 4.3, error bars indicate $\pm 2\sigma_{n-1}$	158
4.16	Effect of RG blend fraction on (a) cylinder maximum pressure and (b) cylinder maximum pressure rise rate at constant λ and EGR for data indicated in Table 4.3, error bars indicate $\pm 2\sigma_{n-1}$	159
4.17	Effect of RG blend fraction on knock intensity parameters of (a) average maximum peak-to-peak accelerometer voltage and (b) average root mean square of accelerometer voltage at constant λ and EGR for data indicated in Table 4.3, error bars indicate $\pm 2\sigma_{n-1}$	160
4.18	Effect of RG blend fraction on (a) IMEP and (b) COV_{IMEP} at constant λ and EGR for data indicated in Table 4.3, error bars indicate $\pm 2\sigma_{n-1}$	161

4.19	Effect of RG blend fraction on (a) η_{th} and (b) η_c at constant λ and EGR for data indicated in Table 4.3, error bars indicate $\pm 2\sigma_{n-1}$	161
4.20	Effect of RG blend fraction on (a) indicated specific HC and (b) indicated specific CO at constant λ and EGR for data indicated in Table 4.3, error bars indicate $\pm 2\sigma_{n-1}$	162
4.21	n-Heptane fueled supercharged HCCI combustion enriched with RG (a) λ -RG and (b) IMEP-RG operating windows, initial conditions indicated in Table 4.5	165
4.22	IMEP variation for the cases of λ -RG constant, initial conditions indicated in Table 4.5, error bars indicate $\pm 2\sigma_{n-1}$	165
4.23	Effect of RG composition on indicated thermal efficiency of n-Heptane HCCI combustion, initial conditions indicated in Table 4.5, error bars indicate $\pm 2\sigma_{n-1}$	166
4.24	Effect of RG composition on (a) start of combustion and (b) combustion duration of n-Heptane HCCI combustion, initial conditions indicated in Table 4.5, error bars indicate $\pm 2\sigma_{n-1}$	167
4.25	Effect of RG composition on net rate of heat release for (a) RG 75/25 and (b) RG 50/50 for n-Heptane HCCI combustion, initial conditions indicated in Table 4.5, error bars indicate $\pm 2\sigma_{n-1}$	168
4.26	Effect of RG composition on (a) HC and (b) CO emissions of HCCI n-Heptane combustion, initial conditions indicated in Table 4.5, error bars indicate $\pm 2\sigma_{n-1}$	169
4.27	Comparison of experimental pressure traces of point 1, data set F with ChemComb-SZM, Experiment: supercharged n-Heptane HCCI combustion, N=800 RPM, CR=11.8, $T_{intake,mix} = 100$ °C, Intake pressure =143 kPa, $\lambda=2.94$, EGR=19.9%, RG blend fraction =0.0%	172

4.28	Comparison of experimental pressure traces of point 2, data set F with ChemComb-SZM, Experiment: supercharged n-Heptane HCCI combustion, N=800 RPM, CR=11.8, $T_{\text{intake,mix}}=100$ °C, Intake pressure =143 kPa, $\lambda=2.98$, EGR=21.9%, RG blend fraction =10.5%	172
4.29	Comparison of experimental pressure traces of point 3, data set F with ChemComb-SZM, Experiment: supercharged n-Heptane HCCI combustion, N=800 RPM, CR=11.8, $T_{\text{intake,mix}}=100$ °C, Intake pressure =143 kPa, $\lambda=2.98$, EGR=20.9%, RG blend fraction =25.4%	173
4.30	Comparison of experimental pressure traces of point 4, data set F with ChemComb-SZM, Experiment: supercharged n-Heptane HCCI combustion, N=800 RPM, CR=11.8, $T_{\text{intake,mix}}=100$ °C, Intake pressure =143 kPa, $\lambda=3.00$, EGR=21.7%, RG blend fraction =30.4%	173
4.31	A comparison of combustion timing (SOC) prediction by ChemComb-SZM with actual experimental combustion timing for data set F in Table 4.3, error bars indicate $\pm 2\sigma_{n-1}$	174
4.32	ChemComb-SZM simulation results for (a) in-cylinder temperature during and after compression, and (b) predicted pressure for data set F in Table 4.3	174
4.33	Typical mole fraction traces of key species of OH, H_2O_2 , and CH_2O compared with net rate of heat release in n-Heptane HCCI combustion	175
4.34	Effect of RG on mole fraction of (a) Formaldehyde (CH_2O), and (b) hydrogen peroxide (H_2O_2), n-Heptane HCCI combustion simulated by ChemComb-SZM for data set F in Table 4.3	175
4.35	Effect of RG on mole fraction of OH during (a) low-temperature heat release, and (b) early stage of high temperature heat release, n-Heptane HCCI combustion simulated by ChemComb-SZM for data set F in Table 4.3	176

4.36	Effect of RG on the reaction rates of H_2O_2 , (a) production rate for reaction 122 (Equation 4.1, (b) production rate for reaction 123 (Equation 4.2, and (c) total production rate (from all 19 reactions), n-Heptane HCCI combustion simulated by ChemComb-SZM for data set F in Table 4.3	177
4.37	Effect of RG on the ratio of maximum mole fraction during LTR for OH over H_2O_2	178
4.38	A comparison of SOC prediction by ChemComb-SZM and experimental results for two cases of RG 75/25 (left Y-axis) and RG 50/50 (right Y-axis), error bars indicate $\pm 2\sigma_{n-1}$	179
4.39	Effect of RG composition on H_2O_2 mole fraction for (a) RG 75/25 and (b) RG 50/50 cases	180
5.1	EGR- λ operating region for (a) Set I and (b) Set II of data indicated in Table 5.1, iso-Octane HCCI combustion, naturally aspirated mode	187
5.2	EGR- λ operating region for (a) Set II and (b) Set III of data indicated in Table 5.1, PRF100 and PRF80 HCCI combustion, naturally aspirated mode	188
5.3	A comparison of effect of RG blend fraction on (a) start of combustion SOC and (b) combustion duration CD, PRF100 and PRF80 HCCI combustion for constant λ -EGR cases indicated in Table 5.2, error bars indicate $\pm 2\sigma_{n-1}$	189
5.4	A comparison of effect of RG blend fraction on (a) P_{max} and (b) $(dP/d\theta)_{max}$, PRF100 and PRF80 HCCI combustion for constant λ -EGR cases indicated in Table 5.2, error bars indicate $\pm 2\sigma_{n-1}$	190

5.5	A comparison of effect of RG blend fraction on (a) indicated power and (b) cyclic variation of PRF100 and PRF80 HCCI combustion for constant λ -EGR cases indicated in Table 5.2, error bars indicate $\pm 2\sigma_{n-1}$	191
5.6	A comparison of effect of RG blend fraction on (a) indicated thermal efficiency η_{th} and (b) combustion efficiency η_c , HCCI combustion of PRF100 and PRF80 for constant λ -EGR cases indicated in Table 5.2, error bars indicate $\pm 2\sigma_{n-1}$	192
5.7	A comparison of effect of RG blend fraction on (a) indicated specific HC and (b) indicated specific CO, HCCI combustion of PRF100 and PRF80 for constant λ -EGR cases indicated in Table 5.2, error bars indicate $\pm 2\sigma_{n-1}$	193
5.8	λ -EGR operating region for iso-Octane HCCI combustion in the supercharged mode with and without RG blending, N=800 RPM, $T_{intake,mix}=100$ °C, CR=14.4	194
5.9	(a) RG-EGR and (b) RG- λ operating regions with indication of constant λ -EGR groups of data indicated in Table 5.3	195
5.10	Effect of RG blend fraction on (a) start of combustion and (b) combustion duration for constant λ -EGR groups of data indicated in Table 5.3, error bars indicate $\pm 2\sigma_{n-1}$	196
5.11	Effect of RG blend fraction on pressure traces of data group C in Table 5.3	197
5.12	Effect of RG blend fraction on (a) net rate of heat release (NRHR) and (b) gross accumulative heat release (GHR) of data group C in Table 5.3	198
5.13	Effect of RG blend fraction on (a) P_{max} and (b) $(dP/d\theta)_{max}$ for constant λ -EGR groups of data indicated in Table 5.3, error bars indicate $\pm 2\sigma_{n-1}$	198

5.14	Effect of RG blend fraction on knocking intensity indicators of (a) $P_{k,Acc}$ and (b) RMS_{Acc} for constant λ -EGR groups of data indicated in Table 5.3, error bars indicate $\pm 2\sigma_{n-1}$	199
5.15	Effect of RG blend fraction on (a) indicated power and (b) cyclic variation for constant λ -EGR groups of data indicated in Table 5.3, error bars indicate $\pm 2\sigma_{n-1}$	200
5.16	Effect of RG blend fraction on (a) indicated thermal efficiency η_{th} and (b) combustion efficiency η_c for constant λ -EGR groups of data indicated in Table 5.3, error bars indicate $\pm 2\sigma_{n-1}$	200
5.17	Effect of RG blend fraction on (a) indicated specific HC and (b) indicated specific CO emissions for constant λ -EGR groups of data indicated in Table 5.3, error bars indicate $\pm 2\sigma_{n-1}$	201
5.18	Supercharged iso-Octane HCCI combustion blended with RG 75/25 and RG 50/50 (a) λ -RG and (b) IMEP-RG operating windows	202
5.19	Demonstration of λ difference for selected pairs of constant IMEP in Figure 5.18, constant RG blend fraction points, supercharged iso-Octane HCCI combustion, error bars indicate $\pm 2\sigma_{n-1}$	202
5.20	Effect of RG composition on indicated thermal efficiency of iso-Octane HCCI combustion, error bars indicate $\pm 2\sigma_{n-1}$	203
5.21	Effect of RG composition on change of start of combustion (SOC) of iso-Octane HCCI combustion, error bars indicate $\pm 2\sigma_{n-1}$	203
6.1	IMEP- λ operating region with indication of cyclic variation comparing (a) pure natural gas (b) natural gas blended with RG both at three sets of experiments indicated in Table 6.1, natural gas HCCI combustion in the naturally aspirated mode with wide open throttle	209

6.2	Effect of RG blend fraction increase on operating region of HCCI combustion of natural gas for Set II indicated in Table 6.1, EGR=5.5%	210
6.3	Effect of RG blend fraction on (a) combustion timing (SOC) and (b) combustion duration (CD) at constant λ lines, EGR=5.5%, Set II in Table 6.1	211
6.4	Effect of RG blend fraction on (a) P_{\max} and (b) $(dP/d\theta)_{\max}$ at constant λ lines, EGR=5.5%, Set II in Table 6.1	212
6.5	Effect of RG blend fraction on (a) P_{\max} timing and (b) $(dP/d\theta)_{\max}$ timing at constant λ lines, EGR=5.5%, Set II in Table 6.1	213
6.6	Effect of RG blend fraction on (a) T_{exhaust} at constant λ lines and (b) T_{exhaust} at constant RG blend fraction lines, EGR=5.5%, Set II in Table 6.1	214
6.7	Effect of RG blend fraction on (a) indicated power (IMEP) and (b) cyclic variation COV_{IMEP} at constant λ lines, EGR=5.5%, Set II in Table 6.1	215
6.8	Effect of RG blend fraction on (a) indicated thermal efficiency (η_{th}) and (b) combustion efficiency (η_c) at constant λ lines, EGR=5.5%, Set II in Table 6.1	215
6.9	Effect of RG blend fraction on (a) indicated specific HC (isHC) and (b) indicated specific CO (isCO) at constant λ lines, EGR=5.5%, Set II in Table 6.1	216
6.10	Effect of RG blend fraction on indicated specific NO_x (is NO_x) at constant λ lines, HCCI combustion of natural gas in naturally aspirated mode with wide open throttle, EGR=5.5%, Set II in Table 6.1	217
6.11	Effect of λ and RG blend fraction on indicated specific NO_x (is NO_x) at constant RG blend fraction lines, HCCI combustion of natural gas in naturally aspirated mode with wide open throttle, EGR=5.5%, Set II in Table 6.1	218

6.12	The operating region of supercharged natural gas HCCI combustion (●) and natural gas HCCI combustion blended with RG (○)	219
6.13	The operating window of RG-blended supercharged natural gas HCCI combustion in (a) RG- λ and (b) RG-EGR spaces with indication of constant λ -EGR groups of Table 6.2	220
6.14	Effect of RG blend fraction on (a) SOC and (b) CD, HCCI combustion of cases A to E in Table 6.2, error bars indicate $\pm 2\sigma_{n-1}$	221
6.15	Effect of RG blend fraction on (a) P_{\max} and (b) $(dP/d\theta)_{\max}$, HCCI combustion of cases A to E in Table 6.2, error bars indicate $\pm 2\sigma_{n-1}$	222
6.16	Effect of RG blend fraction on knock intensity parameters of (a) $\text{RMS}_{\text{Acc.}}$ and (b) $\text{Pk}_{\text{Acc.}}$, HCCI combustion of cases A to E in Table 6.2, error bars indicate $\pm 2\sigma_{n-1}$	223
6.17	Effect of RG blend fraction increase on pressure traces of constant λ cases of Table 6.2, data group B, Supercharged natural gas HCCI combustion	223
6.18	Effect of RG blend fraction increase on (a) net rate of heat release (NRHR) and (b) gross accumulative heat release (GHR) of constant λ cases of Table 6.2, data group B, Supercharged natural gas HCCI combustion	224
6.19	Effect of RG blend fraction on (a) IMEP and (b) COV_{IMEP} for HCCI combustion of cases A to E in Table 6.2, error bars indicate $\pm 2\sigma_{n-1}$	225
6.20	Effect of RG blend fraction on (a) indicated thermal efficiency (η_{th}) and (b) combustion efficiency (η_c), HCCI combustion of cases A to E in Table 6.2, error bars indicate $\pm 2\sigma_{n-1}$	226

6.21	isHC (left) and isCO (right) for HCCI combustion of cases A to E in Table 6.2 as functions of RG blend fraction , error bars indicate $\pm 2\sigma_{n-1}$	227
6.22	Natural gas fueled supercharged HCCI combustion with RG blending: (a) λ -RG and (b) IMEP-RG operating windows . .	229
6.23	Demonstration of λ difference for selected pairs of constant IMEP, constant RG blend fraction points in Figure 6.22, error bars indicate $\pm 2\sigma_{n-1}$	229
6.24	Effect of RG composition on indicated thermal efficiency for constant RG blend fraction points in Figure 6.22, error bars indicate $\pm 2\sigma_{n-1}$	231
6.25	Effect of RG composition on (a) indicated specific HC and (b) indicated specific CO for constant RG blend fraction points in Figure 6.22, error bars indicate $\pm 2\sigma_{n-1}$	231
6.26	Effect of RG composition on (change of start of combustion (SOC) for constant RG blend fraction points in Figure 6.22, error bars indicate $\pm 2\sigma_{n-1}$	232
6.27	Comparison of experimental pressure traces of point 1, data set B with ChemComb-SZM, Experiment: supercharged natural gas HCCI combustion, N=800 RPM, CR=19.5, $T_{\text{intake,mix}} = 140$ °C, Intake pressure =143 kPa, $\lambda=2.11$, EGR=41.8%, RG blend fraction =8.7%	233
6.28	Comparison of experimental pressure traces of point 2, data set B with ChemComb-SZM, Experiment: supercharged natural gas HCCI combustion, N=800 RPM, CR=19.5, $T_{\text{intake,mix}} = 140$ °C, Intake pressure =143 kPa, $\lambda=2.14$, EGR=41.3%, RG blend fraction =15.1%	233

6.29	Comparison of experimental pressure traces of point 3, data set B with ChemComb-SZM, Experiment: supercharged natural gas HCCI combustion, N=800 RPM, CR=19.5, $T_{\text{intake,mix}} = 140$ °C, Intake pressure =143 kPa, $\lambda=2.15$, EGR=43.9%, RG blend fraction =19.7%	234
6.30	Comparison of experimental pressure traces of point 4, data set B with ChemComb-SZM, Experiment: supercharged natural gas HCCI combustion, N=800 RPM, CR=19.5, $T_{\text{intake,mix}} = 140$ °C, Intake pressure =143 kPa, $\lambda=2.14$, EGR=42.8%, RG blend fraction =30.7%	234
6.31	A comparison of combustion timing (SOC) prediction by ChemComb-SZM with actual experimental combustion timing for set B of data in Table 6.2, error bars on experimental SOC show the cyclic variation, error bars indicate $\pm 2\sigma_{n-1}$	235
6.32	Effect of RG blend fraction on (a) temperature trace and (b) heat capacity trace, HCCI combustion of natural gas for case B of Table 6.2 simulated by ChemComb-SZM	236
6.33	Comparison of combustion timing for two cases of RG 50/50 and RG 75/25, experimental results and modeling results for constant IMEP cases indicated in Figure 6.22, error bars indicate $\pm 2\sigma_{n-1}$	237
6.34	Effect of RG blend fraction on ratio of specific heats for two cases of RG 50/50 and RG 75/25, experimental results versus modeling results for constant IMEP cases indicated by circles in Figure 6.22	238
C.1	Kistler 6043A60 pressure transducer calibration (with Kistler 507 charge amplifier, sensitivity= 2.04, range multiplier=200,full scale =3.476 V, date: December 12, 2004	271

C.2	Kistler 6043A60 Pressure transducer calibration (with Kistler 507 charge amplifier) sensitivity= 10.00, range multiplier=200, date: March 29, 2007	271
C.3	Max Machinery flow meter 213-311 and transducer 272-566 (number 14 in Figure 2.5) calibration curve, maximum sensitivity range, Date: January 15, 2007	272
C.4	Omega natural gas flow meter FMA-A2117 flow meter (0-50 SLPM range) calibration, Date: October 6, 2005	273
C.5	Omega RG 25/75 flow meter (0-5 SLPM range) calibration, Date: March 22, 2007	274
C.6	Omega RG 50/50 flow meter (0-5 SLPM range) calibration, Date: May 25, 2007	274
C.7	Omega RG 25/75 flow meter FMA-A2117 flow meter (0-50 SLPM range) calibration, Date: March 22, 2007	275
C.8	Omega RG 50/50 flow meter FMA-A2117 flow meter (0-50 SLPM range) calibration, Date: May 25, 2007	275
D.1	A sample of a raw voltage output of a pressure trace magnified in two locations of around top dead center and late in expansion stroke, note that the cycle exhibited some knocking oscillation	277
D.2	A comparison of noisy signal with filtered signal for (a) a non-knocking cycle and (b) knocking cycle	278
F.1	ΔP_P definition and indication in two various operating points in an HCCI engine at CR=14.4 , N=700 RPM, fueled with PRF80 and EGR=40%. (a) knocking cycle, $\lambda=1.27$, $\Delta P_P = 4.94$ bar (b) non-knocking cycle $\lambda=1.64$, $\Delta P_P =0.27$ bar	290
F.2	RMS definition and indication in two various operating points in an HCCI engine at CR=14.4 , N=700 RPM, fueled with PRF80 and EGR=40%. (a) $\lambda=1.64$, RMS=0.0236 bar (b) $\lambda=1.27$, RMS=1.1979 bar	291

F.3	Maximum cylinder pressure (P_{max}) versus maximum cylinder pressure rate $(dP/d\theta)_{max}$ at CR=9.5, 12.3, and 14.4, also various RON=0, 20, 40, and 80. HCCI combustion in CFR engine, N=700 RPM, various λ and EGR.	292
F.4	A comparison of knock measuring parameters using a nonlinear least square fit and marking $(dP/d\theta)_{max} = 8$ bar/CAD	293
G.1	A Box plot sample for four primary variables of (a) RG mass flow rate, (b) intake air mass flow rate , (c) intake absolute pressure, and (d) HC concentration in the exhaust, HCCI combustion of n-Heptane in the supercharged mode at 800 RPM .	296
H.1	Effect of λ and EGR on indicated specific HC emissions, initial conditions indicated in Table 3.1	300
H.2	Effect of λ and EGR on indicated specific CO emissions, initial conditions indicated in Table 3.1	301
H.3	Effect of λ and EGR on indicated specific HC, Supercharged HCCI combustion of natural gas, n-Heptane and iso-Octane, initial conditions indicated in Table 3.2	302
H.4	Effect of λ and EGR on indicated specific CO, Supercharged HCCI combustion of natural gas, n-Heptane and iso-Octane, initial conditions indicated in Table 3.2	303
H.5	Effect of λ and EGR on combustion efficiency emissions, initial conditions indicated in Table 3.1	304
H.6	Effect of λ and EGR on combustion efficiency, Supercharged HCCI combustion of natural gas, n-Heptane and iso-Octane, initial conditions indicated in Table 3.2	305
H.7	Effect of λ and EGR on knock intensity (ΔP_P), Experimental matrix indicated in Table 3.1	307

H.8 Effect of λ and EGR on knock intensity measured by peak-to-peak voltage output of accelerometer (Pk _{Acc.}), Supercharged HCCI combustion of natural gas, n-Heptane and iso-Octane, initial conditions indicated in Table 3.2	308
---	-----

List of Symbols

ANOVA	Analysis of variance
CD	Combustion duration in CAD
CAD	Crank angle degree
CAD _{aTDC}	CAD after TDC
ChemComb	In-house chemical kinetic combustion model
COV _{IMEP}	Coefficient of variation of IMEP (%)
CR	Compression ratio
$(dP/d\theta)_{\max}$	Maximum rate of pressure rise (bar/CAD)
DME	Dimethyl ether
EGR	Exhaust gas recirculation by volume(%)
FT	Fisher-tropsch
GHR	Gross accumulative heat release (J)
HCCI	Homogeneous Charge Compression Ignition
HTR	High temperature heat release
IEGR	Internal EGR

IMEP	Indicated mean effective pressure (bar)
isCO	Indicated specific carbon monoxide (g/kWh)
isHC	Indicated specific unburned hydrocarbons (g/kWh)
isNO _x	Indicated specific nitrogen oxides (g/kWh)
LTR	Low temperature heat release
MZM	Multi-zone model
N	Engine rotation speed (rev/min)
NRHR	Net rate of heat release (J/CAD)
NTC	Negative temperature coefficient
P _{max}	Maximum cylinder pressure (bar)
PO _x	Partial oxidation
RG 75/25	Reformer gas with 75% H ₂ and 25% CO
RG 50/50	Reformer gas with 50% H ₂ and 50% CO
RG blend fraction	Reformer gas fraction in total fuel by mass (%)
SOC	Start of combustion (CAD,aTDC)
SZM	Single-zone model
TDC	Top dead center
VCR	Variable compression ratio
VVT	Variable valve timing
T _{intake,mix}	Intake mixture (air, fuel, and EGR) temperature (°C)
λ	Air/fuel ratio relative to stoichiometric air/fuel ratio

ϕ	Equivalence ratio
χ	Mole fraction
σ_{n-1}	Standard deviation of measured value or cyclic variation corrected for mean

Introduction

This chapter introduces the history of HCCI combustion, benefits and drawbacks, solutions to HCCI combustion problems, the research motivation, objectives and methods, and summarizes the decision making path to the proposed solution.

Internal combustion engines are important part of the modern life. Over the long history of the modern internal combustion engine, two types of internal combustion engine, i.e. spark ignition (SI, gasoline) and compression ignition (CI, diesel) have dominated. As described by Stone (1999) [2], the basic concept of the SI engine was first stated by Beau de Rochas (1862) and that of the diesel engine by Akroyd Stuart (patented 1890) and Rudolf Diesel (patented 1892). Since then, these two types of combustion have been the basis of the modern engines with many modifications for improving operating range, speed, efficiency, and emissions. The SI engine is limited by knock to relatively lower compression ratio than the CI engine, giving lower initial cost and mass but also lower efficiency. For SI combustion, simultaneous reduction of unburned hydrocarbons (HC), carbon monoxide (CO) and nitrogen oxides (NO_x) is effectively possible using a three-way catalytic converter. For CI engines, it is difficult to reduce NO_x and particulate matter (PM) emissions simultaneously. After-treatment devices are expensive and not easily available in the market. A

combination of in-cylinder combustion control techniques and after-treatment devices are used to minimize the NO_x -PM emissions. A solution that combines low NO_x and PM emission SI engine benefit with high efficiency of CI engine is called **Homogeneous Charge Compression Ignition (HCCI)** combustion engine. While the concept is not original (as discussed in Section 1.4), the idea of using HCCI as a practical engine combustion mode makes it an innovative alternative comparable in some ways with the development of SI and CI combustion engines.

1.1 HCCI Combustion Engine

1.1.1 Definition

HCCI combustion is the autoignition of a premixed air/fuel mixture without any external energy as an ignition source. A mixture of air and fuel that is *nominally* homogeneous is inducted into the engine cylinder, and compression initiates self-ignition of the fuel at a certain pressure and temperature during the compression stroke. This process is an alternative to that of conventional SI and CI engines. HCCI engine incorporates the basic features of SI engines (a premixed charge preparation) with those of CI engines (self-ignition of the fuel at a certain pressure and temperature), and hence, can be called a hybrid of SI and CI engines. Like the charge of the SI engine, the charge is premixed and almost homogeneous, reducing particulate emissions, and like the CI engine, the HCCI engine can tolerate a high compression ratio as well as un-throttled operation at part load, both of which lead to high efficiency. To convert a conventional engine to run in the HCCI mode, the basic engine geometry and fuel properties must be altered. For instance, for a conventional SI engine, increasing compression ratio (CR), heating the mixture, and using a low octane number fuel individually or in combination can be done to run the engine in the HCCI mode. Once the conditions are proper, the spark for combustion initiation is no longer needed, the mixture ignites spontaneously.

As the mixture is homogenous, and the thermal properties are almost uniform, many sites inside the cylinder ignite together. The combustion takes the form of multi-site ignition rather than flame propagation. The multi-site spontaneous combustion of the fuel molecules results in a sudden pressure increase almost instantly, with the maximum pressure higher than usual. Such high pressure rise rate can result in pressure fluctuation, overheating, vibration, knock, and serious damage to the engine structure. To avoid such problems, a highly diluted mixture with excess air and/or EGR should be inducted into the cylinder. Extra lean engine operation and a high tolerance to diluents and inert gas are the HCCI engine's unique characteristics. This creates the possibility of low load operation without the necessity for throttling with an increase in efficiency. As the mixture in an HCCI engine ignites by itself, no direct method can control the start of combustion. Combustion initiation highly depends on the mixture's thermal and chemical properties. The cylinder's pressure and temperature history play a major role in combustion. This leads to the HCCI engine's operating region being limited between knock on the rich side and misfire/low load on the lean side. In addition, the CO and HC emissions from the HCCI engine are higher than those from conventional engines, depending on operating conditions. Thus, the HCCI engine's major drawbacks are the lack of a direct control method, the limited operating region, and the higher HC and CO emissions.

Several acronyms are widely used for HCCI combustion, each of those is based on certain of its characteristic. HCCI was first defined in the late 1980's [3] and is now accepted as a common name, especially in North America. Previously, the first attempt at HCCI combustion in a 4-stroke engine was named Compression Ignited Homogenous Charge (CIHC) combustion [4]. CAI (Controlled Autoignition) is an acronym used mainly by Europeans [5]. Another name for 4-stroke HCCI engines is PCCI (Premixed Charge Compression Ignition)[6]. For HCCI combustion using diesel fuel, UNIBUS (Uniform Bulk Combustion System) [7] and PREDIC (PREmixed lean Diesel Combustion) [8] are also com-

mon terms. Another acronym is OKP(Optimized Kinetic Process) for specially controlled HCCI engines [9]. Toyota-Soken (TS) (Toyota-Soken) combustion, an early version of a 2-stroke engine [10]; the name ATAC (Active Thermo-Atmosphere Combustion) which was used as the most early definition of HCCI combustion [11]; and Activated Radical combustion, which refers to the nature of the combustion [12], are some of the acronyms for this type of combustion in 2-stroke engines.

These definitions all imply slightly different operating conditions. For example, a recent study has identified the different combustion characteristics of ATAC and HCCI [13].

1.1.2 History

The HCCI engine's principle of operation is inherently simple. During the engine's early development, this principle was tried, but technological limitations prevented it from becoming commonly used. The HCCI engine's modern history began with a 2-stroke engine in 1979 known as the ATAC [11]. The first 2-stroke HCCI engine operated with a highly trapped residual or recycling. The early attempts to implement HCCI in a 2-stroke engine resulted in an attempt to develop commercial motorcycle engines [12]. In 1983, 4-stroke HCCI engine was first achieved [4]. Subsequently, mainly in the late 1980's several attempts were made to explore the fundamental principles of HCCI combustion. The first studies focused on the basic understanding of HCCI combustion and combustion mechanisms, chemical reactions, and the effects of the main engine input parameters on HCCI combustion. At this time, researchers found that HCCI combustion is influenced mainly by chemical kinetics due to its type of combustion. It was observed that HCCI combustion produces almost no NO_x while the amount of HC and CO are usually higher than in conventional engines. By that time, some practical endeavors had focused on producing prototype engines and even production versions of HCCI (such as the Nissan MK (Modulated Kinetics) [14] and the Honda AR (Activated Radical) [15]).

The common agreement resulting from the first fundamental studies of HCCI combustion was its domination by chemical kinetics.

After learning the basic characteristics of HCCI combustion, researchers focused mainly on the challenges caused by HCCI's drawbacks, which are mainly the lack of combustion control and the narrow operating range. During the late 1980's, the first suggestion to use conventional SI operation at high loads and HCCI at part loads was published [3]. The idea of a dual mode SI-HCCI and/or CI-HCCI created more challenges for the transient and mode-switch aspects of the engine control system. The ongoing studies of HCCI combustion are concentrating mainly on widening the operating range, controlling the combustion timing, and developing appropriate control strategies and exhaust after-treatment for high HC and CO emissions. The fuel-injection strategies have found that ultra-early injection has NO_x and emission benefits in CI engines [16]. Hence, the partial implementation of HCCI combustion in diesel engines has already started. Diesel engines, with their naturally high compression ratio and strong engine structure, also use more ignitable fuels; hence, they are more likely than other engines be used for HCCI operation. HCCI development for the SI engine is also receiving serious attention. With the help of the new technologies of VVT (Variable Valve Timing) and VCR (Variable Compression Ratio) HCCI combustion can potentially be implemented in the SI engines. Recently, a commercial passenger car was experimentally equipped with a dual-mode SI-HCCI engine and tested by GM (2007) [17].

1.1.3 HCCI Combustion Characteristics

Several experimental and simulation studies have been carried out to learn the basic characteristics of the HCCI combustion. Understanding of HCCI combustion — thanks to global efforts during the last three decades — now appears to be complete, and researchers are now using HCCI's main concepts to overcome difficulties related to its practical implementation.

The fundamental chemistry of HCCI combustion is identical to that of the

knock phenomenon which is unfavorable self-ignition. Because HCCI combustion has the same nature as the knock phenomenon in the end gas of a conventional engine, this type of combustion can be also described by the existing self-ignition studies of conventional engines. The local kinetic reaction rates are commonly understood to dominate the combustion in the HCCI engine. Several experimental studies supported by spectroscopic data have found that the radical formation in HCCI combustion is at the order of the self-ignition rather than the flame propagation [4].

As the HCCI engine's intake mixture is nearly homogeneous, and the start of combustion depends on the local pressure and temperature, several sites inside the cylinder ignite together. Ignition first starts at heterogeneous points that have enough fuel molecules surrounded by oxidizers to be burned and is then distributed by small-scale flame propagations at several points. The temperature and pressure of the air/fuel mixture and unburned gases in-cylinder are increased by the two mechanisms of the piston movement and flame propagation in conventional engines. However, in HCCI engines, no flame propagation occurs but local ignition sites playing approximately the same role create an increase in the rest of the mixture's pressure and temperature. Lack of discernable flame propagation in HCCI combustion also has been observed by optical diagnostics [18, 6]. In conventional SI engines, the radicals have been observed in a spatially distinct region with different phasing during combustion because the front propagation occurs in the combustion chamber while the engine operates in the SI mode. The same observation of an HCCI engine found that the multi-point radicals appeared simultaneously [11]. However, further studies found that the combustion sites in the core region ignited first, resulting in increased pressure and temperature in the boundaries. This sudden and sharp pressure rise and temperature increase causes the remaining unburned mixture to be burned.

The power output in the HCCI engine is lower than that of the SI mode in the same engine despite the higher maximum pressure. One of the greatest advan-

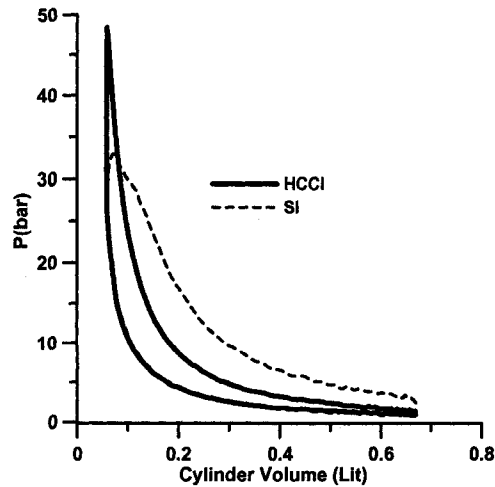


Figure 1.1: A comparison of the Pressure-Volume diagrams of an HCCI engine and a SI engine: CFR Engine, CR=11.5, Speed=800 RPM, HCCI fueled with n-Heptane, SI fueled with CNG

tages of HCCI combustion is its close similarity to the ideal Otto cycle, which is a constant volume combustion. Figure 1.1 shows the similarity between HCCI combustion and constant volume combustion and explicitly indicates the HCCI engine's lower IMEP compared to that of the SI engine. The HCCI combustion's similarity to constant volume combustion has the benefit of high thermodynamic efficiency.

Cyclic variation in a conventional engine, especially a SI engine, is a serious issue. Spark energy variation and the fluid dynamic effects of mixture inhomogeneity are the major causes of cyclic combustion variation. In HCCI combustion, the lack of flame propagation and HCCI's chemically kinetics-controlled combustion result in low cyclic pressure variation [19]. However, the combustion's dependency on the temperature history results in high cylinder-to-cylinder combustion variation in multi-cylinder HCCI engines [20, 21]. Figure 1.2 compares the cyclic variation in the HCCI engine and the SI engine.

The simultaneous ignition of the air/fuel mixture in the HCCI engine creates a high pressure and a fast heat release rate which must be controlled, mainly by

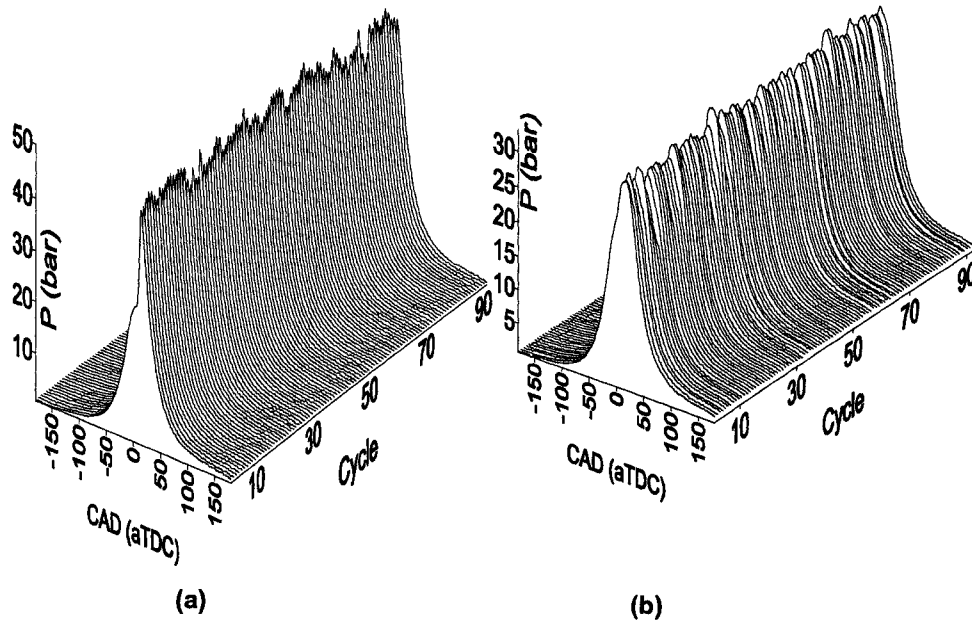


Figure 1.2: A comparison of 90 consecutive cycles of HCCI and SI pressure traces, (a) n-Heptane HCCI, $IMEP=4.91$ bar, $COV_{IMEP} = 1.04\%$, (b) natural gas SI, $IMEP=5.3$ bar, $COV_{IMEP} = 3.06\%$. Both in CFR engine, $CR=11.5$, $N=800$ RPM

mixture dilution. Figure 1.3 shows the difference between pressure characteristics of natural gas SI and HCCI engines at the same power level. Figure 1.3 shows that at the same level of power, HCCI combustion requires much higher compression ratio for the same fuel. Maximum cylinder pressure P_{max} and maximum cylinder pressure rate $(dP/d\theta)_{max}$ are higher for HCCI, thus requiring over-dilution of the air/fuel mixture to avoid engine structural damage. Because combustion starts at locally in-homogenous points in the combustion chamber and then is distributed to the hotter areas, HCCI combustion can be assumed to be a thermal-environment-related autoignition process without a flame front and a localized hot temperature. The approximately homogeneous charge is ignited at specific locations by processes related to its local temperature, pressure and concentration history. Unlike in the CI and SI engines, mixing during the combustion process does not play a major role. However,

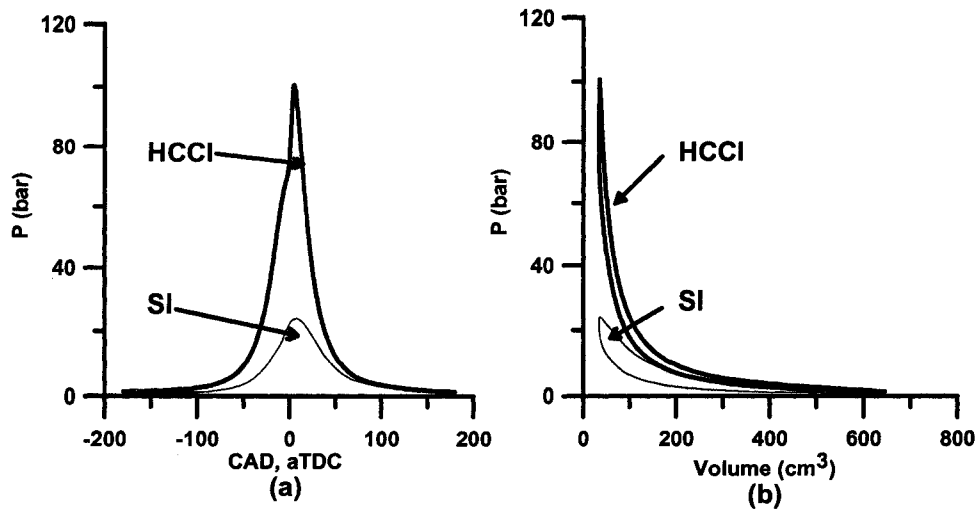


Figure 1.3: A comparison of SI (natural gas, CR=11.5, throttled) with HCCI (natural gas, CR=19.5, supercharged) pressure traces with the same indicated power (IMEP=2.71 bar) (a) P-CAD digram, (b) P-V diagram

the charge stratification, the in-homogenous EGR, and the direct injection patterns, which are discussed later, have serious effects on HCCI combustion. The most attractive features of HCCI combustion, (which dramatically negate its drawbacks), are the low output of NO_x and PM emissions. Like a CI engine, an HCCI engine has a high compression ratio, hence, high efficiency, but unlike a CI engine, it also has ultra low output of NO_x and soot emissions. These advantages are encouraging further development of HCCI despite some major combustion control and operating region concerns. The NO_x -soot trade-off in CI engines is a serious issue, while HCCI provides a natural solution to this problem. In fact, HCCI's advantages are making the partial operation of CI engines in the HCCI mode seem more attractive and have even resulted in the possibility of using a homogenous charge in the fuel injection patterns in the modern diesel engines.

1.1.4 HCCI Combustion Emissions Characteristics

NO_x

Nitrogen oxide's formation mechanisms in SI and CI engines are well understood. High dependency of NO_x concentration on the combustion temperature has been described analytically [1]. Although NO_x has the same kinetics of formation in SI and CI engines, the NO_x formation in them has some major differences mainly due to the differences in the compression ratio, the fuel-preparation method, and the flame characteristics. In SI engines, most NO_x is generated in the zone that was the first to ignite [22]. In CI engines, however, the flame starts with fuel injection and burns at stoichiometric conditions that yield high flame temperature, and as a result, a high NO_x output.

There are three major mechanisms for NO_x formation: thermal (Zeldovich), prompt, and nitrous. The lower combustion temperature of an HCCI engine minimizes the thermal NO_x, but a small amount of NO_x is still produced by the prompt (Fenimore) and, to a lesser extent, by the nitrous mechanism [22]. While most NO_x produced in SI and CI engines is NO rather than NO₂, the N₂O intermediate mechanism has been important in NO_x formation (due to the lean, low-temperature nature of combustion), and the NO₂ fraction in NO_x in some HCCI engines has been high due to the presence of N₂O and HC simultaneously [23]. The benefit of the NO_x reduction in an HCCI engine gives it an advantage over the CI engine because an HCCI engine can eliminate NO_x-soot and NO_x-efficiency trade-offs [24, 25]. The most common method of reducing NO_x in IC engines is to use EGR, but its application in CI engines is less effective because of the trade-off with PM [26]. In addition the HCCI engine's high tolerance of EGR can reduce NO_x emission dramatically.

One of the most common methods of reducing NO_x emissions is using a highly diluted mixture, which is limited by unstable combustion. An HCCI engine has to be operated with highly diluted mixture; hence, a low combustion temperature, and, as a result, a very small amount of NO_x is produced. In addition,

the very fast combustion in the HCCI engine does not allow for enough time for NO_x to be formed [27]. The lack of hot spots in the combustion chamber, also contribute to the low production of NO_x [28]. The amount of NO_x produced by an HCCI engine is typically 98% less than a conventional engine [29], decreasing from a 500-2000 ppm concentration to as little as 1-2 ppm. These results are similar to the output of a very efficient exhaust system using an after-treatment device. The large decrease in NO_x is the most attractive feature of HCCI combustion and can help to eliminate the need for complex after-treatment of NO_x from vehicles.

NO_x in an HCCI engine decreases with an increase in amount of EGR for almost every load and speed of the engine [30]. A numerical study of the different effects of EGR found that dilution effects rather than chemical or thermal effects were mainly responsible for EGR's ability to reduce NO_x [30]. The amount of NO_x emission increases when more load is required and the engine must operate closer to the rich side of the operating region [31, 32]. Very close to the stoichiometric region, the amount of NO_x again decreases due to the lack of enough oxygen [33] but it may be difficult to operate at this point due to knock. The maximum amount of NO_x produced in an HCCI engine is still much less than the typical NO_x production of a conventional engine.

CO

In conventional engines, most of the CO is produced when the mixture is rich and not enough oxygen is present to create CO_2 . CO is believed to be produced in the hot region near the cylinder walls where the temperature is high enough to oxidize the HC, but the wall's cooling prevents the CO from converting to CO_2 . This mechanism has the same effect on bulk quenching during expansion. At a leaner than stoichiometric mixture, only a little CO is produced and its level remains almost constant. Hence, in conventional engines the level of CO increases when the load increases. CO oxidation is highly dependent on intermediate OH radicals. Their presence has a strong

correlation with the in-cylinder gas temperature, which is usually low in HCCI engines. As a result, for gas temperatures less than 1500K, the amount of OH radicals is restricted, and the oxidation mechanism cannot consume much CO [34]. In contrast, with NO_x and particulate emission, HCCI has a higher level of CO, which is one of HCCI's drawbacks. Sometimes, HCCI engines have CO emission up to three times higher than those of SI engines [35]. Usually the amount of CO near to the high load region, which is the operation's knock limit, is slightly less than that in conventional engines and increases at a low load and idle significantly more than it does in a conventional engine [36].

HC

In any internal combustion engine, it is common for 8% or 9% of the hydrocarbons to escape from combustion. However, the fraction of unburned hydrocarbon surviving in the exhaust is usually less than 2%. Post-combustion oxidation, whether in-cylinder or in the exhaust port, is a major mechanism for unburned hydrocarbon reduction. Because HCCI has fairly low temperature combustion and rapid temperature drop with expansion, the lack of enough post-combustion oxidation of fuel molecules is a serious issue [37, 38]. HC formation mechanisms are different in SI and CI engines. However, when HCCI uses premixed compression ignition, the effect of fuel spray, which is important in CI engines, is eliminated in HCCI combustion. Hence, in HCCI combustion without direct injection and charge stratification strategies, the formation of unburned hydrocarbons should be similar to that in SI engines. Hence, an HCCI engine suffers from unburned hydrocarbons in crevices, exhaust leakage, wall quenching, and oil absorption/desorption. Furthermore, HCCI combustion provides additional possible mechanisms for HC formation. Usually, HCCI engines have higher compression ratio than conventional SI engines; and hence, a greater expansion ratio. The cooler combustion temperature along with the higher expansion ratio results in less HC oxidation during the expansion stroke and, hence, higher HC emissions. As well, the

HCCI engine's leaner operating makes the unburned hydrocarbons one of the concerns associated with HCCI engines.

Like CO, HC is another issue of concern for HCCI engines. All of the efforts to reduce the HC level in SI engines can also be applied to HCCI. Because HCCI has an extremely low emission of NO_x , an efficient oxidation catalyst with a low light-off temperature is much simpler and cheaper than a 3-way catalyst and can solve the problem of CO and HC simultaneously. Coating the combustion chamber with a catalytic coating has been suggested as another solution for reducing HC [39]. Different injection patterns [40] and charge stratification [41] also affect HC and CO emission rates.

Soot

Another important advantage of HCCI combustion is its extremely low soot emission. The highly stratified charge of a diesel engine creates extremely lean and extremely rich regions, which are consumed by a diffusion flame, creating considerable amounts of NO_x and soot simultaneously. Any effort toward reducing of NO_x (e.g., a high rate of exhaust recirculation) has the drawback of increasing soot. Particulate matter in CI engines is produced with a high combustion temperature more than 1700K and a rich stoichiometry region of the flame [1]. When an HCCI engine has a premixed homogenous highly diluted charge along with a low combustion temperature, the reduction of NO_x and soot is expected. A recent study examined the concept of PCI (Premixed Compression Ignition), which is similar to HCCI, and reduced NO_x and particulate experimentally [25].

1.1.5 Summary of HCCI Combustion Advantages and Disadvantages

HCCI combustion is highly favorable because of inherently lower NO_x emission while exhibiting high efficiency. The operating range in an HCCI combustion engine is limited to low to medium power ranges. HCCI operating window has

two distinct boundaries of knock at higher load region and misfiring/partial burning at lower load region. More importantly, there is no conventional direct way of controlling combustion timing in an HCCI engine. HCCI combustion also suffers from some minor practical issues such as cold start problem and excessive amount of HC and CO emissions. Table 1.1 summarizes HCCI combustion benefits and drawbacks.

Table 1.1: HCCI combustion advantages and disadvantages summary

Advantages	Disadvantages
Near zero NO _x	Lack of combustion timing control
High thermal efficiency	Limited operating range
Low cyclic variation	High HC and CO emissions
Fuel flexibility	Cold start difficulty

More details on principal operation of HCCI combustion can be found in review papers such as studies done by Stanglmaier and Roberts (1999) [31], Milovanovic and Chen (2001) [42], Coma and Gastaldi (2006), [43], and Johansson (2007) [44].

1.2 Solutions to HCCI Combustion Problems

1.2.1 Conventional Solutions

As indicated in Table 1.1, the most important problem of HCCI combustion is lack of combustion timing control. In fact, proper control of HCCI combustion timing independent of other influential parameters such as air/fuel ratio and/or EGR is a key factor to overcome other HCCI combustion drawbacks while maintaining the benefits. For example, limited operating range at high load of an HCCI engine is caused by too early combustion resulting to further compression of burned and unburned mixture and very fast rate of heat release leading to knock.

HCCI combustion happens as the temperature and pressure of the air/fuel mixture reaches certain autoignition condition depending on the fuel and strongly

dependent to temperature history and chemical compositions. To adjust the autoignition timing indirectly, either of temperature and/or chemical properties can be altered to adjust autoignition timing. Table 1.2 summarizes and classifies the parameters that affect HCCI combustion timing.

Table 1.2: Engine parameters affecting HCCI combustion timing

Temperature	Chemical Composition
Intake Temperature	Fuel autoignition quality
Intake pressure	
Compression ratio	
Air/fuel ratio	
EGR (internal/external)	

Table 1.2 indicates that intake temperature, intake pressure, and compression ratio are affecting combustion timing through alteration of the temperature history of in-cylinder mixture. Intake temperature influences combustion timing and all other engine mean value parameters affected by combustion timing as indicated in several previous studies such as Flowers et al (2001) [45]. They reported that increasing intake temperature advanced combustion timing and shortened combustion duration. Although intake mixture temperature adjustment (using subsystems such as an electrical heater or a heat exchanger that recovers waste heat of exhaust or coolant) seems very effective on HCCI combustion timing control, it is impractically slow for providing the fast cycle-by-cycle control requirement of an engine.

Another method to control combustion timing is using a variable compression ratio (VCR) engine. The method has been demonstrated successfully in previous studies such as Haraldsson et al (200) [46] and Hyvnen et al (2003) [47]. This method suffers from complexity and cost of a VCR engine.

Intake pressure adjustment (throttling or supercharging) is used mostly to control the load output of an HCCI engine or increase the maximum power in the proper operating window. It has limited capability for combustion timing control and is mostly used to widen operating range. An early study by Chris-

tensen et al (1998) [48] showed the application of supercharging in an HCCI engine.

A combination of air/fuel ratio and EGR adjustment as indicated in Table 1.2 is quite effective on combustion timing adjustment. It is quite practical with current level of technology to adjust the air/fuel ratio and EGR level on a cycle-by-cycle basis to achieve controllable combustion timing. Air/fuel ratio and EGR are affecting both temperature and chemistry condition of the in-cylinder mixture. Air/fuel ratio directly affects availability of fuel molecules in vicinity of oxidizer. The effectiveness depends on the base fuel autoignition behavior. It also changes heat capacity of the mixture and alters after-compression temperature.

External EGR has several effects on HCCI combustion characteristics. Five different effects of charge heating, dilution, heat capacity alteration, chemical composition variation, and stratification have been identified and described by Zhao et al (2001) [30]. Internal EGR is even more effective than external EGR because it contributes to high mixture temperature, eliminating the necessity of intake heating for most cases. The problem of using air/fuel ratio and or EGR to control combustion timing is the effect of air/fuel ratio and EGR dilution on the engine load engine load as well as the dilution limits of autoignition (which are wider than normal flame combustion).

1.2.2 Dual Fuel HCCI Combustion Engine

To develop HCCI timing control using adjustable fuel autoignition quality, the dual fuel HCCI engine concept was developed. Blending two fuels with different autoignition qualities at various fractions can potentially control combustion timing. There is not a well defined technique to estimate the octane quality of a fuel blend. HCCI combustion timing is affected by fuel autoignition characteristics and both octane and cetane qualities can be used to qualitatively predict combustion timing. However, HCCI combustion timing is not accurately predicted by octane or cetane quality alone because it effectively

occurs at conditions differing from those of octane and cetane tests. For example, studies such as Koopmans et al (2004) [49] show that octane rating is not a trustable indicator of combustion timing while the engine is operated in HCCI mode with negative valve overlap. Despite that, blending two fuels with different octane quality is a powerful tool to adjust the combustion timing. With current knowledge of the mapping and the calibration of the engine operating parameters, it is possible to adjust combustion timing on a cycle-by-cycle basis using calibration tables.

Several studies have demonstrated multi-fuel capability of the HCCI engine and examined fuel blending as a mean of control combustion timing. For example, in an experimental study performed by Stanglmaier et al (2001) [35], the concept of bifuel (natural gas and FT naphta)/ dual mode (HCCI/SI) engine was demonstrated successfully. The engine was operated at low to medium load in HCCI mode and controlled by fuel blending ratio. It was switched to SI mode at high loads. In another experimental study by Strandh et al (2004) [50], a successful cycle-by-cycle combustion timing control of an HCCI engine using fuel blend of n-Heptane and ethanol on a range of RON from 53 to 106 was performed. Blends of primary reference fuel (PRF is a blend of n-heptane and iso-octane) effectively control combustion timing and have been examined in several studies (e.g. Yao et al (2004) [51]).

1.2.3 Fuel Reforming, a Bridge to Practical Dual Fuel HCCI Engine

Dual fuel HCCI combustion engine is a practical solution for combustion timing control with current technologies, when infrastructure is provided and carrying two fuels onboard is feasible. The other solution is to carry the base fuel onboard and partially convert it to the gaseous secondary fuel with alternated autoignition quality from the base fuel. This process is called fuel reforming and the produced fuel is called reformer gas (RG) or synthesis gas (syngas). Using a single fuel onboard and having two fuels available to be blended and

implemented in an HCCI engine is a practical simple solution that can be applied with current available technologies of fuel reforming and fuel delivery systems.

1.2.4 Variable Valve Timing (VVT)

VVT technology is another break through in internal combustion engine application. There are several useful aspects of availability of a flexible intake/exhaust valve timing system even in conventional SI and CI engines such as reducing throttling loss, internal EGR, variable effective compression ratio, air motion control, faster burn rate at idle. For further details of VVT benefits, see Schechter and Levin (1996) [52]. Recently, several production engines with semi variable valve technology such as cam phaser systems have entered the market. (e.g. Honda VTech or Toyota VVTL-i). A fully flexible valve train using solenoid actuators (such as Chaldny et al (2005) [53]) is an ultimate solution to improve pumping efficiency at part load and to apply hot internal residual through negative valve overlap or exhaust-re-breathing techniques. Several experimental studies demonstrated the capability of VVT to adjust combustion timing in an HCCI engine or to make the practical mode-switch possible in a dual mode HCCI/SI engine. For example, Law et al (2000) [54] used a hydraulic active valve train (AVT) to control HCCI combustion timing with two methods of trapping hot residual and exhaust re-breathing. Both methods were successful on controlling combustion timing. Milovanovic et al (2004) [55] performed experimental and modeling analysis of a fully VVT system and found that HCCI combustion timing can be controlled effectively. The most influential valve event for controlling HCCI combustion characteristics was the Exhaust Valve Closure (EVC) event. Strandh et al (2005) [56] demonstrated a successful control of combustion timing in an HHCI engine using various controllers enabled by VVT.

Although VVT is a key technology for a successful dual mode controllable HCCI engine, it is expensive and complex and requires research to overcome

technical difficulties of a fully VVT system. While VVT is under development, nearer term emission efficiency demands require an alternative solution for a practical HCCI engine. A dual fuel HCCI engine enabled with partial reformer is one of these solutions.

1.3 Reformer Gas (RG) and Reforming Techniques

Reformer gas is a mixture of light gases dominated by H_2 and CO and some inert gases. It can be produced with or without presence of a catalyst using a fuel processor. Development of the onboard fuel processors is mainly driven by fuel cell hydrogen supply requirements. Several research studies have been done to supply H_2 onboard a vehicle using conventional base fuels and fuel processing and purification techniques. Although the high purity of H_2 is not necessary for internal combustion engine applications, reformer gas production for fuel cells had a great influence on technology development.

1.3.1 Reformer Gas Properties

Depending on the reforming technique, base feedstock fuel, reforming temperature, hydrogen to carbon ratio, and presence of a catalyst, RG has a variable composition that is dominated by H_2 and CO. For fuel cell application, further purification is required to produce ultra-pure H_2 . Using a general fuel processor for IC engine application, RG contains mostly H_2 (from 50% to 75% of the H_2 /CO mixture) balanced with CO, N_2 , H_2O , and a small amount of HC. Hence, it is reasonable to approximate RG by H_2 /CO binary mixture.

Free H_2 is available on earth in negligible amounts and the main sources of H_2 are chemical processes involving water, oil ammonia and natural gas. Combustion-wise, H_2 has wide flammability limits in comparison with other conventional fuels. H_2 has an extremely high flame speed that makes it favorable in adverse conditions of combustion such as over-diluted with air and/or

EGR. Despite high flame speed and fast reaction rates, and very low minimum required ignition energy, H_2 has a high resistance to autoignition that categorizes it as a high octane fuel. Although there is no firmly established octane number for H_2 in the literature, Topinka et al (2004) [57] reported an octane number of 140 for it. H_2 has a high energy density on the mass basis and very low energy density on volume basis.

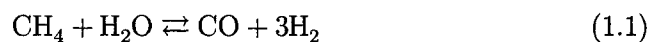
Usually carbon monoxide forms a smaller fraction of RG. CO is an odorless, poisonous gas that is a product of incomplete combustion. CO has lower flammability limits than H_2 . There is no confirmed octane number for CO combustion but it is also considered a high octane fuel, (Topinka et al (2004) [57] reported an octane number of 106 for CO). CO has a higher energy density per volume and lower energy density per mass than H_2 . For a specific RG with an equal fraction of H_2 /CO, most of the mass is occupied with CO and most of the volume with H_2 .

1.3.2 Reforming Methods

Reforming is a controlled incomplete combustion of the feedstock fuel under fuel rich conditions. The reforming can be performed in the presence of a catalyst to operate at lower temperatures. The reforming process can be exothermic or endothermic so it produces heat or needs an external source of energy. There is an energy loss attributed to reforming that can be quantified with reforming efficiency.

Steam Reforming

Steam reforming is a well developed method of H_2 production that is being used in industry. This technique consists of the reaction of the hydrocarbon with steam, usually in the presence of a nickel catalyst. Methane steam reforming is the most-used industrial H_2 production method. The ideal reaction is:



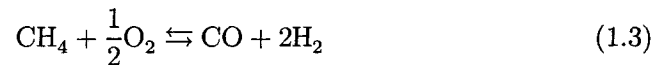
H₂ liberation is maximized under these condition as H₂ comes from feedstock fuel as well as water. As indicated in Reaction (1.1), steam reforming of methane ideally gives 75% H₂ and 25% CO (3/1 H₂/CO ratio) which is the reformer gas composition used in this study for most of the conditions. At these conditions with enough steam available, the water gas shift reaction also occurs converting some of CO to CO₂ and to increase H₂ concentration:



The combination of these two reactions produces H₂/CO ratio more than Reaction (1.1). Reaction (1.1) is endothermic and Reaction (1.2) is exothermic and reaction rates for both reactions are high so they tend to reach equilibrium. For example for reaction (1.1), $\Delta H_r = +205.76$ kJ/mol at 298.15 K, while for reaction (1.2), $\Delta H_r = -41.17$ kJ/mol at 298.15 K ([58]). Hence, excess steam is added to the reactor to move the reactions toward CO₂ and H₂ production. Among available reforming methods, steam reforming operates at higher efficiency and produces more H₂ as it comes from both fuel and steam. Slow response time, possibility of soot production, external heat source requirement, and necessity of carrying water onboard are steam reforming drawbacks for mobile application.

Partial Oxidation(POx)

Partial oxidation is incomplete combustion of a hydrocarbon at low air/fuel ratio. It releases some of the energy content of the fuel. If the released energy is not captured, the system suffers from an efficiency drop. For example, ideal partial oxidation of methane at the presence of O₂ is:



For reaction (1.3), $\Delta H_r = -36.06$ kJ/mol at 298.15 K. POx produces less H₂ than steam reforming and there is an energy loss associated with it. On the other hand, simplicity (cost), compact design and not requiring an external

heat source or water makes it a suitable choice for mobile application. The POx reformer is also more suitable for transient conditions.

Autothermal Reforming

The exhaust of the IC engine is a free source of water vapor and enthalpy which has high availability as the temperature of the exhaust gas is high. If fuel is injected into the EGR line in the presence of a catalyst, it can be reformed to H₂-rich gases by a mechanism that combines steam reforming (Reaction 1.1), water-gas shift reaction (Reaction 1.2), and POx (Reaction 1.3). Autothermal reforming is a thermodynamically balanced reaction that combines endothermic and exothermic reactions. The product of such a reactor -if produced from EGR- is called reformed EGR (REGR). Combining VVT and direct injection technologies, there is also a possibility of in-cylinder autothermal reforming of the fuel.

1.3.3 Related Reforming Studies

There are several detailed studies on reforming techniques, mostly aimed toward high efficiency reforming that leads to pure H₂ production for fuel cell applications. These studies cover a range of base fuels, reforming temperatures, and catalyst materials. Here, the literature is reviewed with relevancy for engine application.

University of Birmingham researchers have focused on various aspects of reforming and its application in IC engine. A comprehensive literature survey was published in 1994 by Jamal and Wyszynski ([59]) covering a range of fuel reforming techniques and H₂ application in IC engines. They presented an idealized approximate reaction for steam reforming of gasoline that leads to a H₂/CO ratio of 65%/35% by just reforming reaction and possibly a ratio of 75%/25% when water-gas shift reaction is added. It was mentioned that the amount of energy required for endothermic steam reforming reaction is in the order of 22% of the lower heating value of the base liquid fuel and reaction

happens at the order of 750°C to 850°C with a nickel catalyst. It also was mentioned that POx reforming of the gasoline releases 17% of the (lower) heat of the combustion of gasoline. The idealized reaction presented for POx reforming of gasoline showed a ratio of 50%/50% for H₂/CO fraction.

Dicks (1996) [60] reviewed reforming technologies for utilization of natural gas in fuel cell applications. It was mentioned that steam reforming of methane in the presence of a nickel catalyst requires temperatures above 500°C. Several fuel processor units for fuel cell application such as regenerative reformer, plate reformer, membrane reformer, intensified combined reactor, and catalytic partial oxidation reactor were discussed.

Docter and Lamm (1999) [61] discussed gasoline fuel cell systems using reformer technologies. They assume that for fuel cell application all of CO is finally reacted to produce pure H₂ and efficiency of reforming for this specific case was defined as:

$$\eta_{\text{ref}} = \frac{(n_{\text{CO}} + n_{\text{H}_2})\text{LHV}_{\text{H}_2}}{n_{\text{fuel}}\text{LHV}_{\text{fuel}}} \quad (1.4)$$

where LHV is lower heating value on a molar basis and n is number of moles. They compare steam reforming with POx and autothermal reforming. It was mentioned that steam reforming for hydrocarbon fuels guarantees the highest efficiency, but POx and autothermal reforming have better dynamics. The efficiency of reforming C₇H₁₂ was estimated at 78% using POx reforming and 78%-84% for autothermal reforming.

Ahmed and Krumpelt (2001) [62] described steam reforming of natural gas as a reversible reaction that should be done under high-temperature, low-pressure and high steam-to-carbon ratio ensuring maximum H₂ production. They categorized POx reforming as catalytic POx, non-catalytic POx, and POx through autothermal reforming. The autothermal reformer was described as a double stage reactor that consists of thermal and catalytic zones. By proper adjustment, reaction in the thermal zone supplies the heat required for steam reforming and water gas shift reaction in the catalytic zone.

More detailed information on available reformer equipment and a list of com-

mercial providers of compact small scale reformers can be found in a report for the *International Energy Agency Agreement on the Production and Utilization of Hydrogen* by Ogden (2001) [63]. A review study by Naidja et al (2003) [64] discussed various aspect of cool flame partial oxidation reforming of natural gas, methanol, gasoline, and diesel fuels.

1.3.4 Reformer Gas Application in Conventional Combustion IC Engines

Application of H_2 or H_2 rich gas in IC engines as the main fuel or as an additive fuel has been studied for several years. In conventional premixed or diffusion flame combustion in an IC engine, the main effect of RG is decreased ignition energy and increased laminar burning velocity, which lead to engine operating parameter changes like expanding flammability limits, increasing dilution and EGR tolerance, cold start emission reduction, and efficiency improvement. Several fundamental studies such as Milton et al (1984) [65], Yu et al (1986) [66], and Rauckis et al (1979) [67] described the effect of H_2 blending on laminar burning velocity of other fuels. They found that the principal effect of added hydrogen was to accelerate the early stage of the combustion process. They indicated that hydrogen addition was more influential at leaner mixture and in the stage of kernel and flame development rather than turbulent flame. Another study by Nagalingam et al (1983) [68] hydrogen-fueled and natural gas-fueled SI engine. Although the study did not focus on effect of increasing hydrogen ratio in hydrogen/CNG mixture, it reported that dedicated hydrogen-fueled engines compared with baseline natural gas-fueled engines had wider operating range (on the lean side), lower indicated power, more retarded combustion timing, higher NO_x and (zero) lower HC and CO emissions. Karim et al (1996) [69] in a study of hydrogen enrichment of a methane-fueled SI engine, described the effects of hydrogen addition as increasing the lean limit of operation and not reducing the anti-knock resistance of methane. This study focused on lean limit expansion at equivalence ratios ranging from 0.6 to 1.4

and pure hydrogen volume fraction from 0% to 100%. The same group (Bade Shrestha et al, 1999 [70]) developed a two-zone SI engine combustion model. They found that hydrogen addition to methane-fueled SI engine, improved the engine performance particularly when operating on relatively lean mixtures, and the optimum concentration of hydrogen in the fuel mixture for producing a power gain and avoiding knock was about 20%-25% by volume. This suggests that only small amount of hydrogen are needed to compensate for flame depletion under adverse combustion conditions (in this case lean mixture) to improve SI engine performance. Hence using an onboard fuel reformer to partially reform the base fuel seems attractive.

Heywood et al (1984) [71] studied flame development of both propane and hydrogen flames in air in a single cylinder engine equipped with a visible combustion chamber. They found that in different cases, hydrogen flame propagated faster and more uniformly than propane.

Allenby et al (2001) [72] investigated the potential of the fuel reforming and EGR limit expansion of a natural gas-fueled SI engine, using reformer gas products (H_2 , CO) of an exhaust catalytic fuel processor. This study found a significant emission improvement and an increase in tolerance of the natural gas engine to EGR because of hydrogen blending.

On-board reforming strategy was used by Quader et al (2004) [73] to extend a SI engine's lean limit. They found that replacement of gasoline with 100% reformate increased the engine's lean limit by 44% (from $\lambda=1.4$ to $\lambda=2.5$) and EGR tolerance by 115%. In this study, the result of a simulated bottled reformate was similar to the result of an actual reformate: lower HC emission (ultimately zero at 100% reformate), higher CO emission, lower NO_x emission, and faster combustion were all achieved by replacing more gasoline with reformate.

Tully et al (2003) [74] used a plasmatron fuel reformer to study the effect of reformer gas blending in a gasoline SI engine. This study found that using plasmatron fuel reformer can improve fuel conversion efficiency by up to

12.3%.

In a recent study by Allgeier et al (2004) [75] the POx technique in an on-board fuel reformer was used to run a SI engine in all modes using gasoline blended with reformer gas. The strategy to run the engine in this study was cold start with reformer gases to achieve HC emission near zero, using reformer gases and excess air to produce a high exothermal reaction and to enhance the catalyst's heat up, and finally using a certain amount of reformer gas at low and medium load to gain efficiency and to reduce NO_x .

The knock improvement capability of H_2 and CO was examined experimentally and numerically in a recent study by Topinka et al [57] using a SI gasoline engine. They found that H_2 and CO have high octane numbers and therefore increase the overall octane number of the fuel mixture when blended with primary reference fuels. It was reported that H_2 and CO inhibited knock by slowing autoignition chemistry and slightly increasing flame speed. It was suggested that in vehicles with onboard reforming the octane number of the fuel mixture that would reach the engine is higher. For example, if 15% of the fuel is reformed to H_2 and CO, the resulting fuel mixture will be approximately 10 octane numbers higher than the original HC fuel.

1.4 HCCI Autoignition Chemistry of Hydrocarbons

HCCI combustion autoignition chemistry is described by chemical kinetic processes comparable with those of knock in conventional combustion engines. Interest in engine knock and octane rating of fuels goes back to the 1920s when the use of n-Heptane and iso-Octane for knock rating was suggested by Edgar [76].

It can be stated that fundamental studies of HCCI combustion which were basically autoignition studies under motored engine condition existed well before HCCI introduction as an alternative for conventional combustion methods.

HCCI became the center of attention years after those fundamental studies because of its desirable feature of low NO_x and soot emissions.

The main feature of hydrocarbon autoignition that initiated several studies was multi-stage autoignition behavior of hydrocarbons. As early as 1948 studies were focused on knock characteristics of hydrocarbons and the fundamental cause behind the different autoignition characteristics of organic compounds [76].

The autoignition of hydrocarbons under high pressure that simulated the engine operating conditions was studied in 1948 by Newitt [77]. It was summarized that under high pressure autoignition conditions similar to engine knock, the chance of molecular collision is increased, certain carriers in chain mechanisms are deactivated and the electrostatic interaction of molecules is increased.

1.4.1 Multi-stage Autoignition of Hydrocarbons

The multi-stage autoignition of hydrocarbons is well understood. In 1951, in a motored CFR engine without spark (It was basically an HCCI engine), distinctive double-stage autoignition was observed for 17 fuels including n-Heptane and iso-Octane by Levedahl et al [78]. It was reported that the low temperature reaction (LTR) was easier to achieve under fuel lean conditions and duration of LTR was a function of mixture composition (the richer the mixture, the longer LTR) and compression pressure. LTR for benzene (an aromatic compound with cyclic molecular shape) was as strong as high temperature reaction (HTR). In 1951, the low temperature reaction zone was referred as "cool flame" and was observed by several researchers such as Thomas et al [79].

An interesting experiment was conducted by Walcutt et al (1954) [80]. Two CFR engines with identical operating conditions and differing compression ratios were connected. The first engine was motored at a particular compression ratio and exhaust product of the motored engine was transferred to the fired

engine to identify the compression ratio onset of knock. It was found that two classes of cool flame existed. The first type is a pre-cool flame reaction that barely releases any heat but provides the radical pool for the main stage of combustion. The second type is the exothermic reaction which contributes to the low temperature heat release. The idea of two classes of cool flame reactions was confirmed later on by Levedhal (1954) [81] confirming that the first cool flame provides radicals and the second cool flame provides heat for the main stage of combustion. Recently Wong and Karim (2000) [82] numerically confirmed the existence of two classes of cool flame in n-Heptane HCCI combustion diluted by EGR.

In 1954, Pahnke et al [83] compared autoignition of n-Heptane, iso-Octane, and benzene. It was found that while n-Heptane formed large amount of intermediate radicals, iso-Octane formed small amount of intermediate radicals, and benzene did not form any intermediate radical after so called preflame oxidation in a motored engine. Walsh (1963) [84] stated that the engine knock is very sensitive to fuel structure, knock resistance of the engine decreases when the molecule length increases, and/or number of methyl group increases. This was preliminary observation of the effect of molecular bonds on different autoignition behavior of hydrocarbons. Ma et al (1966) [85] confirmed that benzene does not create LTR, but adding n-Heptane to benzene increases the LTR characteristics of autoignition. Affleck et al (1967) [86] confirmed that LTR is stronger under fuel rich condition similar to findings of Levedahl et al [78].

The chemistry of autoignition of hydrocarbons is a complex phenomenon with several intermediate chain branching and chain propagation steps. However, it can be summarized as a series of major reactions.

If a hydrocarbon has the general form of RH, the first reaction that occurs at low temperature is attacking fuel molecules by oxygen:



Reaction (1.5) is a chain initiation reaction and it is called H atom abstraction from the fuel molecule. The next step is a crucial reaction for hydrocarbons with multiple reaction stages all in the form of chain propagation:

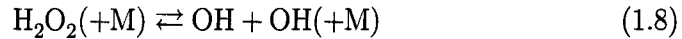


Reaction (1.6) has almost zero activation energy and is highly temperature sensitive. At early stages of autoignition the reaction is in the favor of RO_2 production. The cool flame reaction happens at RO_2 formation. Then, when temperature reaches around 800K, Reaction (1.6) is no longer in forward direction and RO_2 isomerization happens similar to Reaction (1.7).



At this stage of autoignition, further increase in temperature does not accelerate the reactions and heat release by reactions is less than heat transfer. Hence, a reverse temperature profile is observed and reaction rates do not follow the classic Arrhenius form as a function of temperature. This stage is called Negative Temperature Coefficient (NTC) period that is a strong function of RO_2 isomerization. RO_2 isomerization itself is a strong function of C-H bonds in the original fuel structure. A C-H bond that is connected to other H-atoms through C atom is called primary C-H bond. If one of the C atom bonds is C-C, the C-H bond is called a secondary bond. Similarly, if the C atom in C-H bond is connected to two C atoms in form of C-C bonds, the C-H bond is called a tertiary bond. The energy is required for breaking C-H bonds during RO_2 isomerization is strongly depends on the type and position of C-H bonds. The amount of energy to break a C-H bond is maximized from primary C-H bonds, and then secondary C-H bonds. Tertiary C-H is the weakest bond. Now the effect of fuel structure on NTC and knock can be explained. For example n-Heptane has 6 primary C-H and 10 secondary C-H bonds, while iso-Octane (2,2,4-thrymethyl pentane) has 15 primary C-H bonds, and just 2 secondary and one tertiary C-H bonds. Hence, n-Heptane

exhibits much stronger cool flame and NTC and is much more susceptible to knock. During RO_2 isomerization, QOOH radical with HO_2 forms H_2O_2 . H_2O_2 has been indentified as the key intermediate radical for NTC behavior. H_2O_2 decomposition is the key step for the autoignition. The final step before explosive high temperature reaction (HTR) stage is H_2O_2 decomposition to OH radicals:



Hydroxyl radicals produced in Reaction (1.8) attack fuel molecules and form HTR.

The consecutive events of multi-stage autoignition have been confirmed by several studies. These steps were described by Pahnke et al (1954) [83], Levedahl (1955) [81], Affleck et al (1967) [86], Fish et al (1969) [87], Smith et al (1985) [88], and Westbrook (2000)[89] .

Developing understanding of the relation between cool flame and NTC behavior of fuels as well as differences between knock rating of fuels with operating conditions led to studies on inhibition of LTR and prolongation of NTC to suppress engine knock. These fundamental studies of NTC and LTR inhibition and their relation to engine operating parameters are essential for understating HCCI combustion timing and possible methods of combustion timing retardation. In a series of studies by Leppard (1989, 1990, 1992) [90, 91, 92] the origin of octane sensitivity and NTC relation to the knock characteristics were examined. It was found that NTC is more pronounced at higher intake temperature, lower intake pressure and less residence time (higher speed). Karim et al (1970) [93] developed a method to calculate gross heat release from a motored engine experiment. As a result of development of the model and examining effects of methane, propane, and CO_2 on n-Heptane autoignition, it was found that CO_2 dilution or propane or methane enrichment inhibited LTR in n-Heptane autoignition. This concept was the basis of dual fuel natural gas-diesel engine that relied on autoignition of diesel fuel to trigger natural gas combustion (e.g. see Karim et al (1996) [69]). Halstead et al (1973) [94]

described H_2 and CO as the simplest knock inhibitors because they prolong LTR and reduce pressure rise due to LTR. These are major findings that can be implemented in HCCI combustion engine for combustion delay. In a study of H_2 enrichment of SI combustion by Rafael et al (1991) [95], the second stage of autoignition was identified as attacking fuel molecules by OH radicals which was interrupted by H_2 enrichment. Effect of knock inhibitor compounds such as tetraethyl lead also was found to be inhibition of LTR stage by several studies. Not all of fuels under similar operating conditions undergo the multi-stage combustion behavior. For example, dimethyl ether (DME) normally shows a triple stage combustion and methane exhibits single stage combustion in engine operating time scale. In fact, the resistance to autoignition that is an important key fuel characteristic for HCCI combustion and is quantified by RON is related to the intensity of multi-stage combustion in relevant engine operating conditions. While both iso-Octane and n-Heptane have shown double-stage combustion in certain experimental conditions, the high octane number of iso-Octane (RON=100) leads to little indication of double stage combustion in engine operating conditions. For n-Heptane with low octane number (RON=0), the straight chain causes an intensified double stage combustion in engine operating conditions. For example, Minetti et al (1996) [96] identified the cool flame for both n-Heptane and iso-Octane, but cool flame was stronger for n-Heptane and NTC was extended more toward high temperature zones during autoignition. Methane has a simple structure with no indication of double stage combustion and very high octane number (RON=120). Further details of autoignition and chemical kinetic combustion of hydrocarbons can be found in previous literature such as Benson (1981) [97], Westbrook et al (1984, 1987,1991, 2000) [98, 99, 100, 101], Cox et al (1985) [102], Hu et al (1987) [103], and Curran (1998) [104].

1.4.2 Octane Number

American Society of Testing Materials (ASTM) standards D-2699 (ISO 5164) and ASTM D-2700 (ISO 5163) describe the resistance of a fuel to unfavorable autoignition leading to knock in SI engines. Both standards use a specific Waukesha Cooperative Fuel Research (CFR) engine and blends of two base fuels, (n-Heptane C_7H_{16} and iso-Octane C_8H_{16} or 2-2-4 trimethyl pentane) but different operating conditions are used for the two standards. Testing a fuel based on ASTM D-2699 gives research octane number (RON) and that of ASTM D-2700 gives motor octane number (MON). Based on definition, octane number of the base fuels (n-Heptane and iso-Octane) are 0 and 100, respectively. A binary mixture of n-Heptane and iso-Octane is called primary reference fuel (PRF) and the octane number between 0 to 100 indicates the volume fraction of iso-Octane in the blend. For example, PRF80 is a binary blend of 80% iso-Octane and 20% n-Heptane on a volume basis. The arithmetic difference of RON-MON is octane sensitivity. n-Heptane and iso-Octane have 0 octane sensitivity. Sensitive fuels such as mono-olefins, high (RON>100) octane paraffins, or aromatics have RON>MON and they are called derated fuels. Super rated fuels such as most of paraffins have RON<MON and negative octane sensitivity. The origin of octane sensitivity and variation of RON and MON in different fuels comes from a specific autoignition behavior of some fuels (see [91]).

1.5 Previous Use of Reformer Gas for HCCI Ignition Control

Combustion onset control of HCCI using RG blending has been examined previously.

Shudo et al (2002) [105, 106] first examined the effect of variable blend fraction of methanol reformer gas (MRG) and DME. The idea was using the base fuel of methanol and processing it using an onboard fuel processor to convert

to MRG and DME using exhaust or engine coolant heat sources. They found that both H_2 and CO retarded the second stage of combustion of DME considerably, and thus shifted operating range toward richer mixtures. They found that H_2 is more effective at retarding ignition timing than CO, presumably because it consumes more OH radicals before main combustion than does CO. Assuming an ideal fuel reforming and using "free" exhaust heat, they reported an increase in heating value of the reformed fuel to 120% for neat MRG and 104% for neat DME. The same group in [15] (2003) examined the effects of two compositions of RG derived from DME on DME HCCI combustion. The first composition was selected as 44% H_2 , 29% CO, 27% N_2 (POx reforming product), and the second one as 67% H_2 , 33% CO (steam reforming product). They did not find a significant effect of changing RG composition on HCCI combustion timing variation of DME, while steam reforming gave overall higher efficiency. The same group in [107] (2004) examined the effects of four compositions of methanol RG on HCCI combustion of DME and reported that higher H_2 fraction RG was more effective at retarding combustion timing. Summarizing previous studies, Shudo (2006) [108] confirmed that H_2 had far larger effect on combustion timing retardation of DME HCCI combustion than CO. As combining thermal decomposition and water gas shift reaction produces CO_2 , Shudo et al (2006) [109] examined the effect of increased CO_2 fraction in RG composition and reported that the CO_2 thermal effect is more than chemical effect on HCCI combustion timing. Large heat capacity of CO_2 caused a reduction in post-compression temperature and a delay in both first and second stage ignition.

Researchers at University of Birmingham have conducted several studies on combustion timing control of mainly natural gas HCCI combustion engines using catalytic reforming of natural gas with exhaust gas (REGR). Peucheret et al (2004,2005) [110, 58] focused on the exhaust gas reforming technique for application in natural gas HCCI combustion using experimental studies with a mini-reactor monolithic catalytic reformer and thermodynamic equilib-

rium calculations. Yap et al (2004) [111] indicated that H_2 addition to natural gas HCCI combustion reduced intake heating requirement. Intake heating requirement reduction is an indication of advanced combustion timing caused by H_2 fraction increase. Tsolakis et al (2005) [112] examined REGR in a partially premixed compression ignition engine. The reformer gas was mixed with the air in the intake and the diesel engine was fueled with regular diesel and biodiesel. REGR enrichment of the intake mixture improved NO_x and smoke emissions and the effect of REGR varied based on the engine operating mode but basically it retarded combustion timing. Yap et al (2006) [113] found that exhaust gas reforming produced up to maximum 16% H_2 by volumetric concentration and at any given intake temperature REGR advanced combustion timing for natural gas HCCI combustion.

Eng et al (2002) [114] in an experimental and chemical kinetics modeling study examined POx RG effect on HCCI combustion of n-Heptane and iso-Octane with two EGR strategies of internal EGR through exhaust re-breathing and external well mixed EGR. This simulated POx RG had approximately equal quantities of H_2 and CO blended with N_2 based on the ideal rich-oxidation reforming. They found a strong effect of H_2 blending on n-Heptane HCCI combustion when using external EGR, but no or little effect when using internal EGR, possibly because the temperature effect of hot internal EGR dominated the chemical effect of H_2 addition. They operated the engine fueled with iso-Octane in HCCI mode with internal EGR, and found that iso-Octane HCCI combustion timing was advanced by H_2 addition implying that H_2 had a lower octane number than iso-Octane at their particular operating conditions.

1.6 Motivation and Objectives

The HCCI combustion engine is a promising technology for a high efficiency, low NO_x internal combustion engine. It suffers from lack of a direct control over combustion timing to maximize efficiency. Dual fuel HCCI combustion is

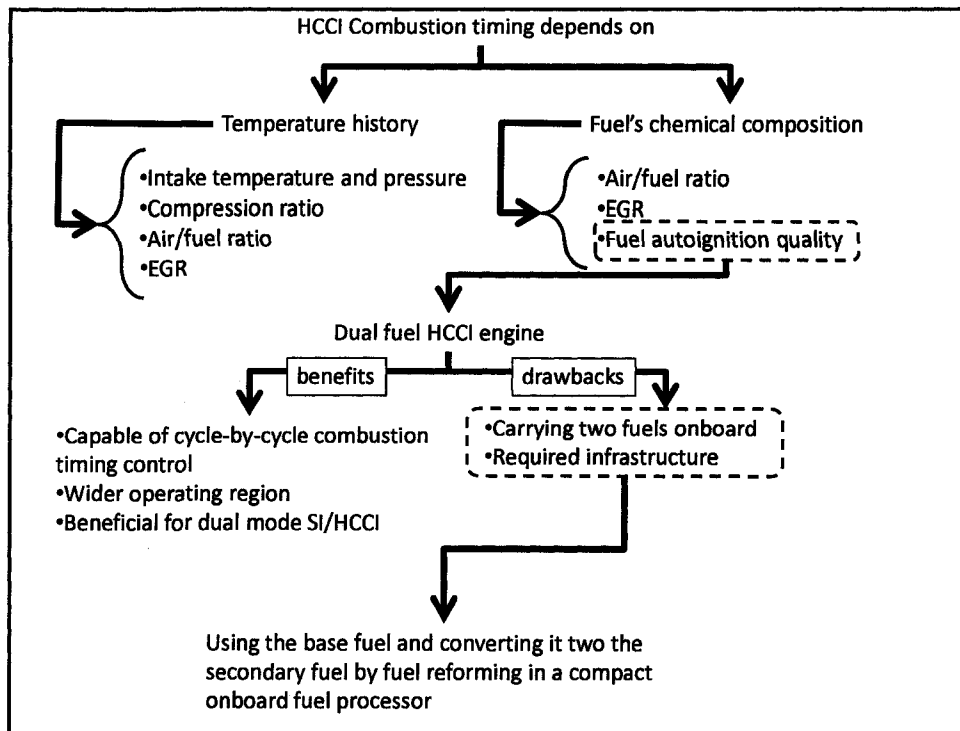


Figure 1.4: Decision making flowchart for the selection of partial reforming concept to control HCCI combustion timing

an effective tool to control combustion timing, but practicality is questionable because of the need to carry two fuels onboard. A compromise to that is to supply one fuel and to partially reform the base fuel to reformer gas (RG). The current study examines the effects of RG on HCCI combustion of a variety of fuels representing gasoline, diesel and alternative fuels. The study focused on basic influential parameters on HCCI combustion, and RG effects on the engine operating parameters and combustion characteristics isolating other influential variables. Figure 1.4 contains a flowchart that summarizes the factors that led to selection of partial fuel reforming as a control method for HCCI combustion timing based on parameters affecting combustion timing as indicated in Table 1.2.

1.7 Organization of Thesis

This thesis is organized in seven chapters and eight appendixes. A review of experimental setup, measurement devices, calibration, experimental matrix, and procedure is presented in Chapter 2. Chapter 3 covers the experimental results from operation of the HCCI combustion engine with the base fuels. Chapters 4, 5, and 6 are presented to discuss details of effect of RG on a diesel-like fuel (n-Heptane and PRF20), a gasoline type fuel (iso-Octane and PRF80), and an alternative fuel (natural gas), respectively. In each chapter, the effects of RG on operating region, engine mean value parameters and combustion characteristics are presented and discussed. In Chapters 4 and 6, modeling analysis is presented and the effect of RG composition on other parameters is discussed. Chapter 7 summarizes the findings in this research. Several technical details of experimental setup, measurement, calculations, and analysis are presented in appendixes.

Experimental Setup and Definitions of Parameters

This chapter describes several aspects of the experimental setup such as instrumentation, calibration, data acquisition, experimental procedures, data analysis, and error estimation.

The internal combustion engine research facility in Mechanical Engineering Department at University of Alberta has been developed since the 1960's and several world class research studies such as laser ignition and knock studies were conducted using a cooperative fuel research (CFR) engine. The same engine was modified to operate in HCCI mode and used for this study. Before the current series of studies on this engine, two other research theses on HCCI combustion of low octane (Primary Reference Fuel) PRF by Atkins (2004) [115], and Exhaust Gas Recirculation (EGR) limit expansion of natural gas SI engines using H_2 by Arthur (2005) [116] were completed. The engine instrumentation was modified considerably after Atkins [115] by Arthur [116]. Further modification of the engine, intake system, liquid fuel system, and data acquisition was performed for the current study. Arthur (2005) [116] developed the intake manifold assembly incorporating three injectors and made an initial development of the gaseous fueling system and data acquisition system.

The current study contributed to:

- Engine modification to achieve higher compression ratios.
- Upgrading the gaseous fuel system for constant-temperature operation and reformer gas low flow / high flow selection.
- Developing a liquid fuelling system including tank, pump, injectors and controls.
- Expanding the data acquisition system to accommodate extra measurements and to reject ambient electrical noise.
- Re-developing the data acquisition program to incorporate multi-fuel HCCI operation with blended fuels.
- Developing an additional, fast data acquisition system to acquire real-time pressure traces.
- Developing an intake supercharging system to operate at elevated manifold absolute pressure.
- Developing an intake CO₂ measurement system to allow continuous EGR monitoring.

2.1 Main Experimental Hardware

2.1.1 Engine and Dynamometer

The co-operative fuel research (CFR) engine was first designed and manufactured under the name of Waukesha engine by Dresser Inc. The first CFR engine was designed, fabricated, functionally tested, and delivered to ASTM in under 45 days in early 1929. Three types of the CFR engine are available. CFR F-1 meets the requirement of ASTM D 2699 for Research octane Number (RON) rating of SI engine fuel. CFR F-2 meets the requirement of ASTM D

Table 2.1: CFR engine specification

Engine model	Waukesha CFR
combustion chamber	pancake with flat-top piston
engine type	water cooled at atmospheric pressure
number of cylinders	1
displacement (cm ³)	612
bore × stroke (mm)	82.6×114.3
compression ratio	4 to 18

2700 for Motor Octane Number (MON) rating of SI engine fuel. A third type called CFR F-1/F-2 can be configured to meet the ASTM requirement for both RON and MON measurement. The cylinder head (that is integral with the cylinder) is called an octane head. Another configuration used for diesel fuel cetane number measurement is called the cetane head and equipped with a prechamber design. The engine used in this study was CFR F-1/F-2 type equipped with octane head. Table 2.1 summarizes the basic specifications of the CFR engine. The engine has an open valve rocker assembly incorporating two rocker arm carriers. The engine has fixed valve timing as indicated in Figure 2.1. The cylinder is made in one piece integrated with cylinder head. The cylinder is equipped with a mechanism enabling variable compression ratio as indicated in Figure 2.2 and Table 2.2. There is a cast iron sleeve fastened rigidly to the crank case which aligns the cylinder with the connecting rod and the piston (2). The cylinder is clamped to the inside diameter of the sleeve by a split flange that is tightened by a clamping bolt. A worm wheel (4) acts between a guide plate on the crank case from the bottom and a shoulder inside the sleeve from the top. This worm wheel is rotated by a hand crank (5) to engage threads on the cylinder sleeve and thus move the cylinder up and down to change the compression ratio. The guide plate (6) provides a bearing surface to protect the top of the crank case. In this study, the guide plate (of 1/8 inch thickness) was removed to achieve higher compression ratio for HCCI combustion. Removing the guide plate caused a decrease in combustion chamber volume (because of lower relative position of the cylinder versus sleeve) and

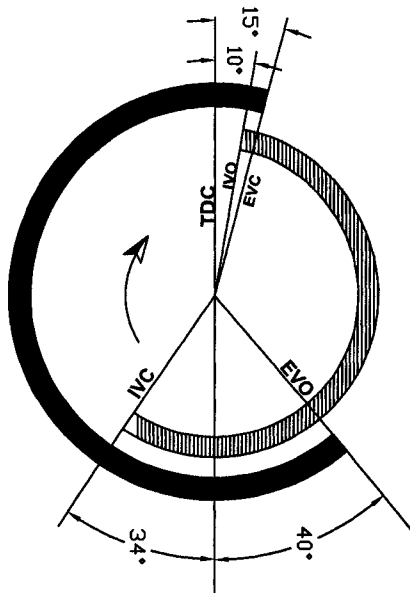


Figure 2.1: Valve timing diagram of the CFR engine, IVC: Intake Valve Close, IVO: Intake Valve Open, EVC: Exhaust Valve Close, EVO: Exhaust Valve Open, TDC: Top Dead Center

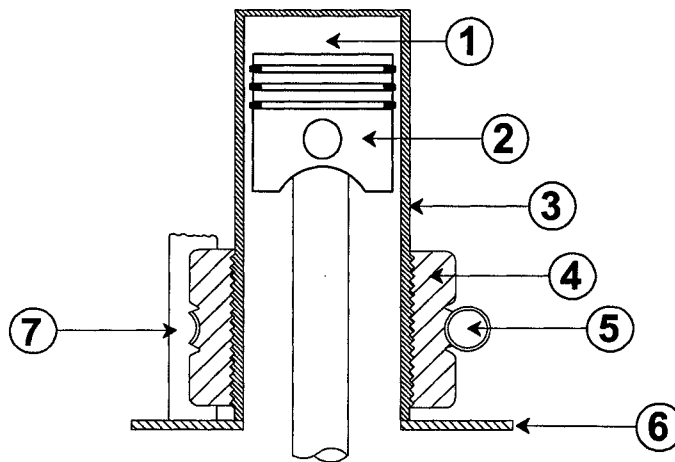


Figure 2.2: CFR variable compression ratio mechanism

Table 2.2: CFR engine variable compression ratio assembly in Figure 2.2

Item #	Description
1	Cylinder Sleeve
2	Piston
3	Cylinder
4	Worm Wheel
5	Hand crank
6	Guide plate

consequently higher compression ratio. A safe distance between the top of the piston and exhaust valve was maintained to avoid any damage to the engine when operated at high compression ratios because of the exhaust valve being overlapped by piston crown. The cylinder head in this specific engine has six access holes to the combustion chamber. Even after inserting steel plugs to make all holes flush with the inner diameter of the combustion chamber, the actual compression ratio of this CFR engine would be slightly lower than that of a standard CFR engine because of the extra volume of the access holes inside combustion chamber.

The engine is coupled with a reluctance type asynchronous electric DC motor

Table 2.3: List of the main components of the engine hardware in Figure 2.3

Item #	Description
1	Intake air mass flow meter
2	Intake air pulsation damping barrel
3	Throttle valve
4	Intake heater
5	Fuel injector
6	Intake plenum
7	Fuel injector
8	CFR engine
9	Intake valve
10	Exhaust valve
11	Exhaust back pressure valve
12	To the building exhaust system
13	EGR pipe, insulated and water cooled
14	EGR valve

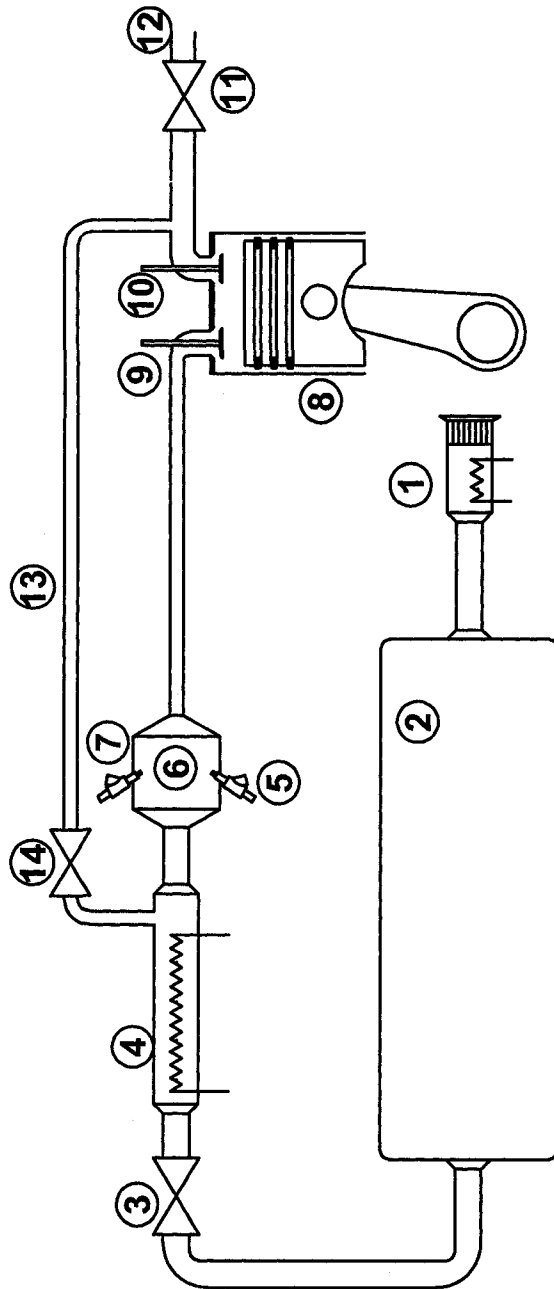


Figure 2.3: A schematic of the CFR engine and main experimental components described in Table 2.3

that is able to start the engine, run the engine at motoring condition, absorb the power and keep the speed/load constant at any required speed using a Digalog™ Testmate™ dynamometer controller module with feed back signal from Encoder 2 (Figure 2.7) and load cell (Figure 2.7). The engine main instrumentation and hardware connections are indicated in Figure 2.3 and Table 2.3. The system includes an intake system that has an air mass flow meter(1), drum(2), intake throttle valve(3), heater(4), and intake plenum(6). There are also three fuel injectors (5,7)in the intake plenum (6), an EGR line (13) with a manual control valve (14) and an exhaust back pressure throttle valve in the exhaust line. Figure 2.3 is a schematic diagram and is not to scale.

The CFR engine designed to operate as a knock rating tool, has a flat combustion chamber with a long flame travel distance and hence, it is a knock prone engine.

The engine is quite durable to operate at various knock level for extended periods. This makes the CFR engine a suitable choice to be operated at HCCI mode that exhibits a high rate of pressure rise. The heavy duty CFR engine has five piston rings, heavy counter balance weights on the crank shaft, cast iron over-sized parts and a heavy flywheel for durability. As a consequence, it suffers from high internal friction which is a drawback for HCCI engine operation.

2.1.2 Gaseous Fueling System

A gaseous fuel system capable of handling two separate pressurized fuels has been developed. The main components of the fueling system are indicated in Figure 2.4 and Table 2.4. The system consisted of two complete sets of equipment to supply both natural gas and RG simultaneously to two gaseous fuel injectors in the intake plenum.

Natural gas was provided from a fiber glass wrapped steel high pressure tank (G_2) typically at 1500 psi. A typical analysis of natural gas composition is in Appendix A. The tank was regularly filled during the experiments using the

Table 2.4: List of the components of the gaseous fueling system in Figure 2.4

Item #	Description
G2	High pressure natural gas tank
G1	High pressure RG tank
R2	AFS Falcon double stage electronic natural gas regulator
R1	Double stage manual pressure regulator
1	Shell and tube heat exchanger
2	Hot water supply from building
3	Drainage
8	Gaseous mass flow meter
4	Floating valver
5	Shut-off normally closed solenoid valve
6	Flow fluctuation damping reservoir
7	Gaseous fuel injector
8	High pressure stainless steel ball valve
HMF	High flow mass flow meter
LMF	Low flow mass floe meter

in-house high pressure natural gas supply system.

An AFS Falcon double stage regulator (R_2) was used to decrease the natural gas pressure of the tank to 550 kPa (80 psi). While there were water jacket plugs provided in the Falcon regulator, no heating was required because of the low natural gas flow of the low speed single cylinder CFR engine. The natural gas regulator included a pressure transducer powered by the AFS Sparrow engine controller unit.

Simulated RG (Reformer Gas consisting of a H_2/CO mixture) was provided from a regular T size steel tank provided by Praxair at any required RG composition. A manual double stage non-heated regulator was used to drop the RG pressure to 655 kPa (100 psi).

A shell and tube heat exchanger (1) was used to keep the gas temperature constant. The heat exchanger is connected to the hot water building supply (2) and to the building drain (3) keeping the level of water constant using a float valve (4).

A solenoid valve (5) operated by the engine control panel acted as a shut-off

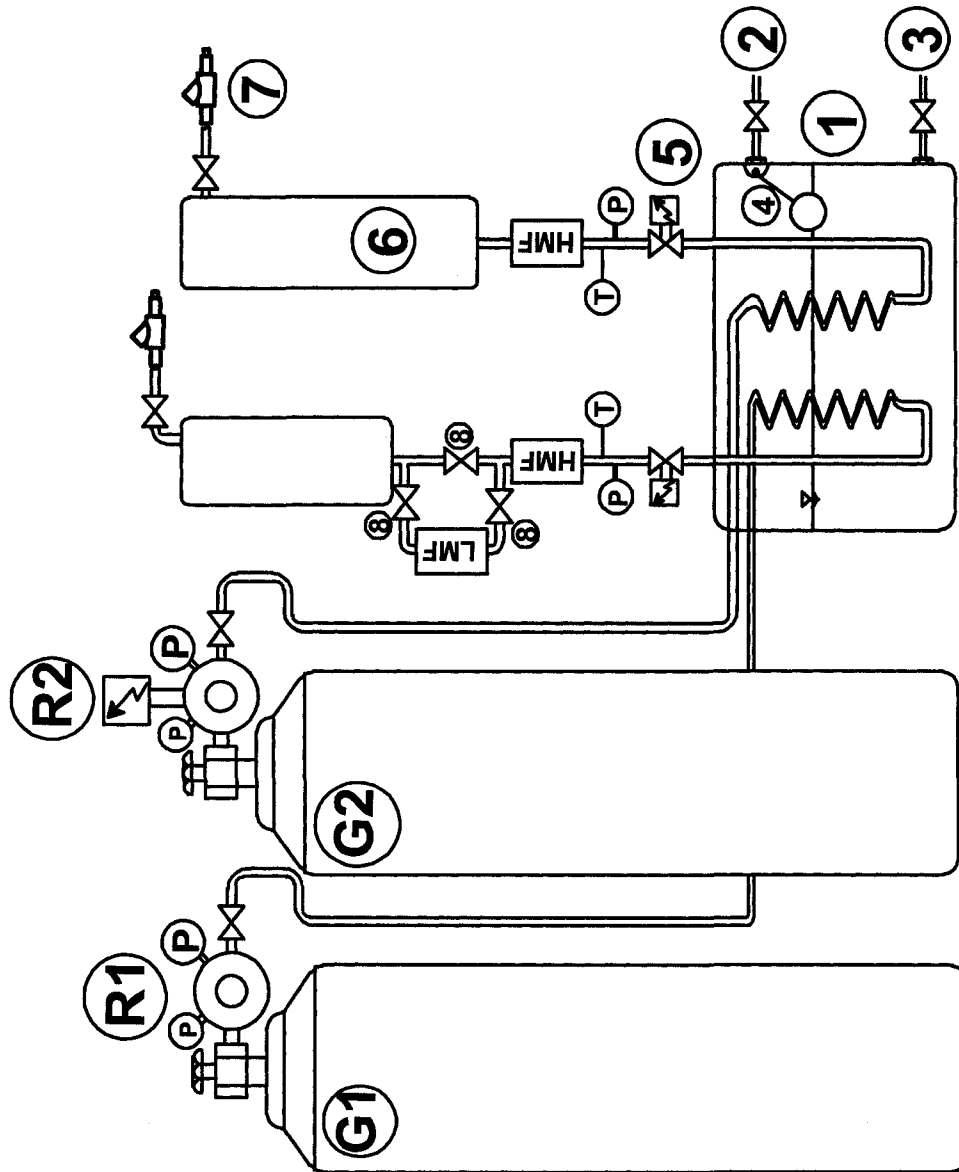


Figure 2.4: A schematic of the components of the gaseous fueling system described in Table 2.4

safety valve and was cooled continuously by cold water copper tubing wrapped around the valve.

An Omega gaseous fuel mass flow meter (HMF) was used to measure the flow of the natural gas before delivery to the fuel injector. The mass flow meter

Table 2.5: List of the components of the liquid fueling system in Figure 2.5

Item #	Description
1	Fuel Tank
2	Sight glass
3	Drain valve
4	Main valve
5	Filter
6	Fuel pump
7	3-way valve
8	Heat exchanger
9	From building hot water
10	Heat exchanger drain
11	4-way valve
12	Microfilter
13	Max Machinery pulse flow meter
14	Max Machinery voltage flow meter
15	Return line to the fuel tank
16	To the injector
17	Fuel pressure regulator

specification can be found in Appendix B and calibration curves in Appendix C. To prevent pressure and flow fluctuations from affecting mass flow meter measurement, a reservoir (6) with approximate volume of 10 liters was installed between the fuel injector and mass flow meter. Using a series of ball valves (8) the mass flow meter for RG was chosen between a high (HMF, 0-50 SLPM) or low (LMF, 0-5 SLPM) flow meter to increase the accuracy of the measurement at any experimental point.

The gaseous fueling systems were capable of operation from 30 °C to 60 °C and 60 psi to 150 psi. Gaseous fuel temperature variation was possible by variation of water supply to the heat exchanger.

2.1.3 Liquid Fueling System

The liquid fueling system was capable of delivering a precisely measured quantity of a liquid fuel at any desirable pressure (between 20 and 80 psi). The components of the liquid fueling system are indicated in Figure 2.5 and Table

2.5. Fuel was provided from the small fuel tank (1) that had a sight glass (2) and a drain valve (3). A regular automotive fuel pump (6) pressurized the fuel to any desired pressure adjusted by a pressure regulator (17). Using the

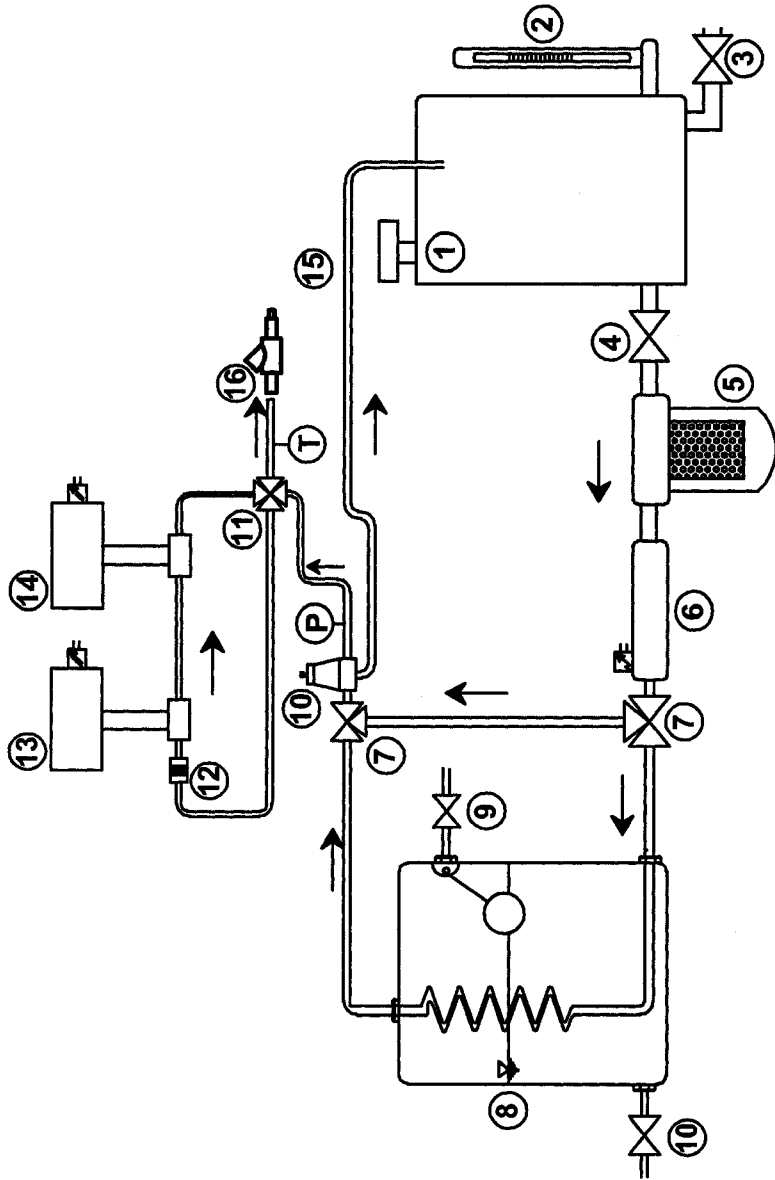


Figure 2.5: A schematic of the components of the liquid fueling system described in Table 2.5

combinations of the 3-way valves (7) it was possible to run the system with or without the heat exchanger (8). A 4-way valve (11) enabled the system to operate with or without volume flow meters in the circuit. Two Max Machinery positive displacement liquid fuel volume flow meters (13) and (14) were used to measure the volume flow rate. One of these mass flow meter was equipped with a transmitter that produced voltage and the other one was equipped with a pulse generator transmitter. The voltage flow meter was used for high flow rates (more than 10 cc/min) while the pulse generator type was more accurate at low flow rates (less than 10 cc/min). Given the situation of the CFR single cylinder engine that operated at relatively low speed, almost all of the fuel was returned through the return line (15) and a small amount of fuel was delivered to the liquid fuel injector (16). Details of the flow meter specifications are in Appendix B and calibration values in Appendix C.

2.1.4 Intake and Exhaust Gas Recirculation Systems

The intake system of the CFR engine was modified to control intake temperature and pressure at any desired set point between 60 °C and 200 °C. A schematic of the intake system components can be found in Figure 2.6 and Table 2.6.

The intake was pressurized by building high pressure supply system using the main control valve (1). A pressure regulator (2) maintained the intake pressure at any desired set point. A pressure relief valve was used to purge the system at 10 psig (A similar barrel to the one in the intake system (6) was tested with pressurized water to establish the failure mode and limits. The barrel caps were considerably deformed at 20 psig (137 kPa) but did not actually fail until 50 psig (344 kPa) at which the press fitted edges of the barrel cracked.). The CFR engine was capable of operating in naturally aspirated mode with air supplied through a low pressure relief valve (4) that was activated when the pressure inside the system was below atmospheric pressure. The low pressure relief valve acted as an air supply to the engine and a safety valve to protect

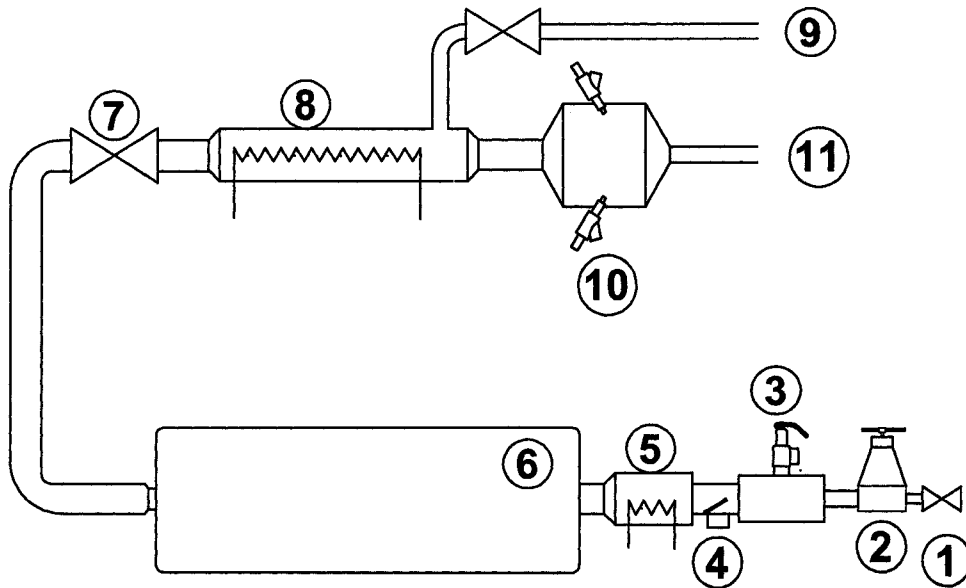


Figure 2.6: A schematic of the main components of the intake supercharging system

the barrel (6) from collapse by low pressure inside the system.

Running in naturally aspirated mode there was a possibility to operate at low intake pressure (gauge vacuum) using throttle valve (7). The intake system was equipped with a 200 L barrel (6) to damp the intake pressure fluctuations.

Table 2.6: List of the components of the intake system in Figure 2.6

Item #	Description
1	Pressurized air main control valve
2	Adjustable air pressure regulator
3	High pressure relief valve
4	Low pressure relief valve
5	Air mass flow meter
6	Intake pulsation damping barrel
7	Throttle
8	Heater
9	From the exhaust (EGR)
10	Intake plenum
11	To the engine

A 2.4 kW heater (8) that operated at 240 V was installed in the intake plenum to heat the intake air. The EGR line was connected to the intake after the heater and before the fuel injectors (10) and was controlled by a manual butterfly valve.

2.2 Measurement and Control Devices

More than 20 variables were measured for each operating point at various sampling rates with a computerized data acquisition (DAQ) system. All sensors were either pre-calibrated by the manufacturer or calibrated using appropriate devices and techniques. Calibration curves of sensors can be found in Appendix C. The main sensors and controllers are indicated in Figure 2.7 and Table 2.7. Liquid and gaseous fueling system sensors are not included here.

2.2.1 Temperature Measurement

All engine operating parameters were measured for several engine cycles and for each cycle the values were averaged for a complete cycle that includes intake, compression, expansion, and exhaust. All temperatures were measured using thermocouples. Shielded wire K type (Chromel Alumel), T type (Copper Constantan), and J type (Iron Constantan) thermocouples were used to measure the temperatures at the following locations:

- Inlet air temperature after the heater (T_1 in Figure 2.7, T type)
- Intake mixture temperature before the intake valve (T_3 in Figure 2.7, K type)
- Exhaust temperature after the exhaust valve (T_4 in Figure 2.7, J type)
- EGR temperature (T_2 in Figure 2.7, T type)
- Gaseous fuel temperature (between (7) and (8) in Figure 2.4, T type)
- Liquid fuel temperature (between (11) and (16) in Figure 2.5, K type)

Table 2.7: List of the sensors and controllers in Figure 2.7

Item #	Description
AMF	Air mass flow meter
T ₁	Air temperature after heater
P ₃	Manifold gauge pressure
T ₂	EGR temperature
CO ₂ analyzer	Five gas portable analyzer
T ₃	Intake mixture (air, fuel, EGR) temperature
P ₃	Cylinder gauge pressure
T ₄	Exhaust temperature
P ₂	Exhaust gauge back pressure
Analyzer	California Analytical Instrument gas analyzer bench
Dyno	Coupling shaft to dynamometer
Encoder1	BEI shaft Encoder
S ₁	Feedback signal to temperature controller
TC	Temperature controller unit for the intake system
S ₂	Command signal to intake heater power supply
HPS	Heater power supply
S ₃	Adjusted power signal to the heater
Digalog controller	Dynamometer speed and load controller
LC	Load cell
Encoder2	Dynamometer encoder
S ₄	RPM feedback signal to dynamometer controller
S ₅	Load cell feedback signal to dynamometer controller
S ₆	Command signal to the dynamometer

2.2.2 Flow Measurement

Air and fuel flow are crucial measurements for a precise determination of air/fuel ratio and engine efficiency. As an oxygenated fuel (RG) was used in several cases in this study, using a conventional air/fuel ratio wide band meter was not practical. Instead, direct measurement of the fuel and the air flow was conducted.

Air Mass Flow Measurement

A TSI model 4235-01-01 air mass flow meter was installed upstream of the engine before the pulsation damping barrel (AMF in Figure 2.7). The flow meter calibration was performed and described by Arthur [116]. The flow

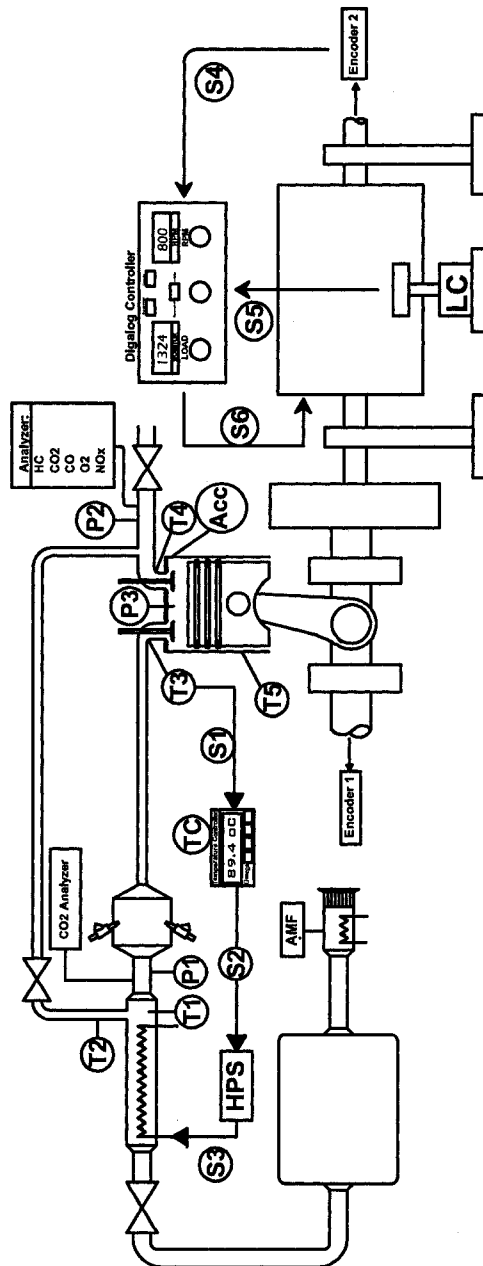


Figure 2.7: A schematic of the sensors and control instruments described in Table 2.7

meter had a range of pressure up to 344 kPa and a flow range of 20 to 1000 L/min as indicated by the manufacturer. Air mass flow meter specification is

in Appendix B and the calibration values were obtained from [116].

Gaseous Fuels Mass Flow Measurement

Omega FMA21 series flow meters were used to measure the gaseous fuel mass flow rate. The flow meters were operated based on heated tube technology enabling them to measure the flow of flammable gases. Two different types with various maximum flow rate were used. For natural gas flow and also RG high flow rate, a 0-50 SLPM model (HMF in Figure 2.4) and for low flow rates of RG a 0-5 SLPM model (LMF in Figure 2.4) were used. Based on operating point and demand of RG, the LMF device was in the line or was bypassed during experiments using a series of ball valves ((8) in Figure 2.7). Calibration values for the natural gas flow meter were obtained from [116]. Mass flow meter specifications are in Appendix B and calibration curves in Appendix C.

Liquid Fuel Volume Flow Measurement

Two Max Machinery positive displacement flow meters were used in the liquid fuel supply line ((13) and (14) in Figure 2.5). The flow meters were capable of measuring a flow of less than 1 cc/min up to 1.8 L/min. The flow meters model 213-311 were connected to transmitters using a coupling vertical shaft. Each crankshaft revolution was equal to 0.887 cc of the liquid.

One flow meter (13) used a 272-565 model transmitter that produced a 0-10 VDC analog output. This transmitter was easier to use as it produces analog voltage similar to other sensors. The problem with 272-565 transmitter was at very low flow rates. Because of the reciprocating nature of the flow meter, the transmitter produced an oscillatory voltage with a low frequency that had a low signal to noise ratio and was difficult to average over a short time. The 213-311 transmitter was equipped with an in-house 15V power supply and analog signal terminal.

The other flow meter (14) was equipped with a pulse generator transmitter

model 284-512 that generated 110.8 pulses per crankshaft revolution. This transmitter was much more accurate at low flow rates but it was difficult to use as it required counting the number of pulses. The 284-512 was equipped with an in-house power supply/signal conditioning unit that supplied 15 VDC to the transmitter and converted the pulse reading to voltage output.

The mass flow meter outputs were automatically chosen during experiments at low and high flow rates to achieve optimum conditions of time versus accuracy of measurement. The specifications of both flow meters can be found in Appendix B and calibration values in Appendix C.

2.2.3 Pressure Measurement

Several pressure gauges were installed on the fuel delivery systems to monitor the fuel pressure during the experiments for the purposes of consistency and safety. The pressures that were measured and saved for data analysis are:

Barometric Pressure

Barometric pressure was measured using a mercury vertical barometer before starting the experiments. The barometer readings were corrected for the temperature and change of gravity due to latitude. The barometric pressure was entered manually to the data acquisition program to adjust the differential pressure readings such as intake and exhaust pressure to an absolute value.

Intake and Exhaust Pressure Measurement

Intake pressure P_1 in Figure 2.7 was measured using a Valydine diaphragm differential pressure sensor and a demodulator. Exhaust pressure P_2 in Figure 2.7 was measured using a Valydine diaphragm differential pressure sensor and a demodulator.

Cylinder Pressure

Lancaster et al (1975) [117] listed the parameters that can be derived from cylinder pressure data as: combustion rate, abnormal combustion behavior, cyclic variation, engine friction, and engine pumping loss.

As cylinder pressure measurement and analysis is one of the key issues in internal combustion engine research, several fundamental studies have discussed it.

Amann (1985) [118] used cylinder pressure data to calculate the burn rate and identify abnormal combustion.

In an early use of the personal computer, Hayes et al (1986) [119] acquired cylinder pressure data of a low speed diesel engine and used it to calculate the heat release rate.

The accuracy of the measurement and analysis depends on referencing of the pressure to a known value, accurate determination of the position of top dead center (TDC) in pressure trace, crank angle resolution of pressure measurement, and number of consecutive engine cycles to be considered for analysis. It is necessary to reference the measured gauge cylinder pressure to a known value to obtain the absolute cylinder pressure. Randolph (1990) [120] summarized and evaluated nine various methods of cylinder pressure referencing techniques.

Cylinder pressure timing is usually indexed with TDC location on the pressure trace signal. Small deviation of TDC location on the pressure trace can cause large errors, especially in calculation of the engine indicated power. Kim et al (1989) [121] determined dynamic TDC location and indicated that experimental measurement of thermodynamic loss angle (TLA) between 0.4 to 1.3 crank angle degree (CAD) resulted to large errors in calculation of indicated power.

Measurement resolution on a crank angle basis is also another important parameter to the engine data analysis. The measurement resolution directly

determines the sampling rate of the pressure trace signal. Burnt et al (1991) [122] indicated that a resolution of 0.5 to 1.0 CAD is enough for diesel engine tests, 1.0 to 2.0 CAD for SI engine while a 10 CAD resolution is enough for an accurate indicated power calculation. Brunt et al (1996) [123] concluded that approximately 3 CAD resolution is enough for any required accuracy for calculation of indicated power, while in view of data storage problems, up to 10 CAD resolution can be enough. They found that the number of engine consecutive cycles to be acquired is much more effective than sampling resolution, and that 150 cycles is required as a minimum for best accuracy although ideally 300 cycles or more should be used. Burnt et al (1997) [124] listed and evaluated the source of errors in cylinder pressure measurement.

In this study, the in-cylinder pressure was measured on several consecutive cycles using a water cooled Kistler 6043A piezoelectric pressure transducer in combination with a Kistler 507 charge amplifier. The combination of the pressure transducer and the charge amplifier was calibrated using a dead weight pressure calibrator. The pressure sensor produced an electric charge of 20 pC/bar which was converted to an analog voltage by a charge amplifier. The pressure measurement was triggered and timed using a BEI shaft encoder that was producing index digital pulses once per crank shaft revolution and once per 0.1 degree of crank shaft revolution. Thus, the pressure was timed using the index signal and was measured 3600 times per revolution of the crank shaft which was necessary to measure the high-frequency (> 5 kHz) pressure oscillation caused by knock in some of the cycles. Top dead center physical location on the crank shaft was determined using a technique that was described in the CFR engine maintenance and operation manuals. Using the spark plug hole, a dial gauge indicator, and rotation of the flywheel, maximum piston height inside the cylinder was determined and marked on the flywheel. Then, the marked location was adjusted with the index pulse of the shaft encoder using an oscilloscope. For most experiments, TDC position happened 104.1 CAD after the index signal of the shaft encoder. Specifications of the pressure

sensor can be found in Appendix B and related calibration curves in Appendix C.

2.2.4 Exhaust Gas Composition Analysis

Exhaust gas analysis was done using a series of California Analytical Instrument measurement devices. A schematic of the sample gas supply to the analyzer bench is indicated in Figure 2.8 and Table 2.8. The gas analyzers

Table 2.8: List of the components of the exhaust gas supply system for gas analyzer in Figure 2.8

Item#	Description
1	Engine
2	Shell and tube heat exchanger
3	Condensed water beaker
4	The beaker drainage
5	Diaphragm pump
6	To the exhaust gas analyzer bench

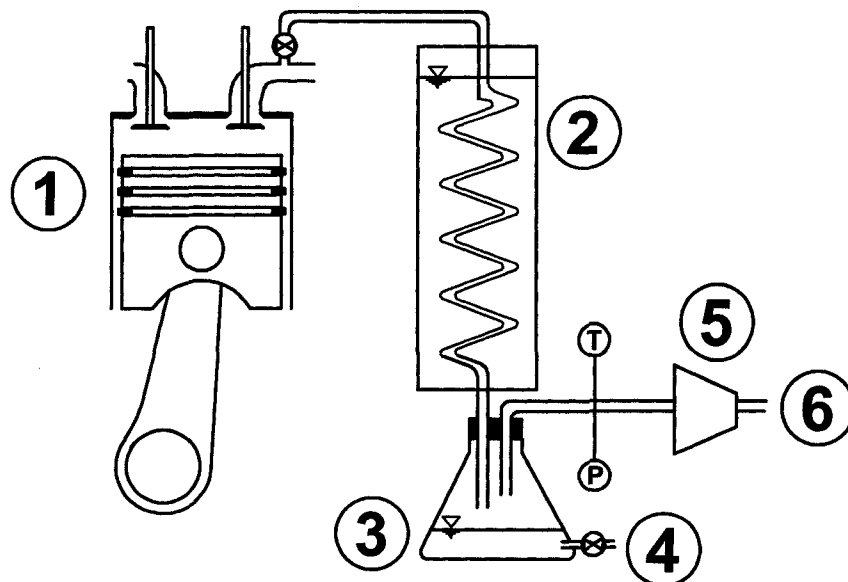


Figure 2.8: A schematic of the exhaust sample gas supply to the emission measurement bench described in Table 2.8

required a cooled, non-condensing sample. The system indicated in Figure 2.8 was designed to condense the water in the exhaust sample without allowing the gas to bubble through water. The sample was taken from the engine (1) exhaust system using a 6mm diameter flexible teflon pipe. The heat exchanger (2) that was filled with cold building water condensed the water included in the exhaust gas to a glass beaker (3) that had a drain valve (4). Gas and condensate flows were arranged so that the gas never bubbled through water. A diaphragm pump (5) increased the sample pressure toward the gas analyzer bench (6). The gas analyzer bench consisted of several devices for exhaust gas concentrations measurement and a Dasibi gas mixer for calibration purposes. The O₂ concentration was measured using a paramagnetic detector and calibrated using a tank of pressurized dry air. The paramagnetic detector had a minimum flow requirement of 1 LPM at any desired positive pressure.

CO and CO₂ were measured using non-dispersive infrared (NDIR) detectors and calibrated using high pressure tanks of the known CO and CO₂ concentrations. The detectors were capable of measuring CO₂ in the range of 0-20%, low CO concentration of 0-200 ppm and high CO concentration of 0-2.5%. The flow requirement for the NDIR detectors was between 0.5 to 2 LPM at any desired pressure.

Hydrocarbons were measured using a flame ionization detector (FID). FID detector was capable of measuring CH₄ or total hydrocarbons THC. In this study, all hydrocarbon measurement were done by THC. FID analyzer operation requires fuel (40% H₂, balance He) that was supplied directly from high pressure tanks.

NO concentration was measured using a chemiluminescence detector (CLD). O₂ supply is required for the operation of the CLD analyzer as it produces Ozone (O₃) to detect the NO and NO₂ in the exhaust gas. The CLD analyzer is capable of measuring NO and NO_x separately. Details of the operation of the emission analyzer bench are described by Arthur [116].

Intake gas was analyzed for the EGR fraction determination. A Vetronix PXA-

1100 portable five gas analyzer was used in the intake system (CO_2 analyzer in Figure 2.7) and EGR connection to the intake plenum to determine the CO_2 concentration in the intake mixture.

2.2.5 Cylinder Vibration Measurement

Cylinder vibration were measured using a Brüel & Kjaer vibration meter model 2511 combined with a Brüel & Kjaer accelerometer model 4370 (Acc in Figure 2.7). The accelerometer produced charge of 100 pC/g and the charge was converted to an analog output of 0-28 V. This voltage was acquired and measured directly without any calibration and used later on to quantify the knock oscillation. The vibration meter was able to identify the oscillation in the range of 0.3 Hz to 15 kHz. The sampling was done using the same Labview program for cylinder pressure. The vibration oscillations were measured in 100 consecutive cycles with 7200 samples per engine cycle. Figure 2.9 shows an example of vibration meter for a whole engine cycle.

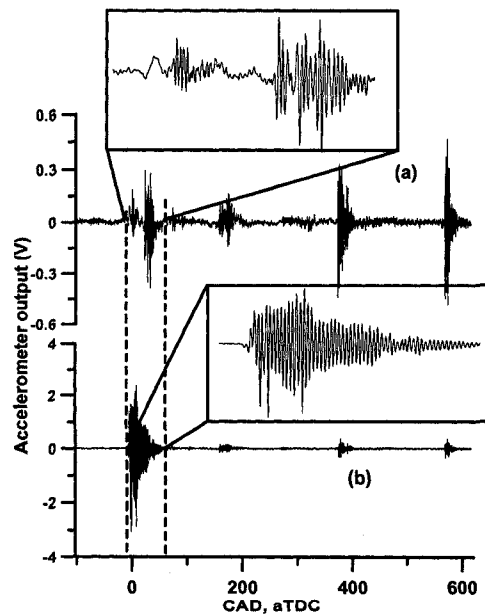


Figure 2.9: Samples of accelerometer analog output for (a) non-knocking cycle and (b) knocking cycle. Note the difference in Y-axes scales

As indicated in Figure 2.9, four different periods of vibration were identified caused by combustion and valve events. As the signal was properly timed, the portion of the signal from -10 CAD,aTDC to 50 CAD,aTDC was considered for calculation knock intensity parameters of $RMS_{Acc.}$ and $Pk_{Acc.}$.

2.2.6 Intake Temperature Control

An Omega temperature PID controller module (TC in Figure 2.7) was used to control the heater. The temperature control used the feedback signal (S_1) from the thermocouple (T_3) installed just before the intake valve to measure the temperature of the intake mixture including air, fuel, and EGR. A command signal (S_2) was provided to a 208 V-25 Amp heater power controller. The power controller conditioned the power signal (S_3) for the heater to satisfy TC demand.

During experiments, the controller adjusted the heater such that the set point temperature was achieved at the intake port. As all the experiments were performed at steady state condition, enough time was given for the intake mixture temperature adjustment system to reach to the set point for each of the operating points.

2.2.7 Engine Speed Control

All experiments were performed at steady state constant speed. the Digalog dynamometer controller unit (Figure 2.7) controlled the engine speed during the experiments. The controller was capable of adjusting the engine speed with an accuracy of ± 1 RPM when enough time was given to reach steady state conditions. The only limitation was during low load operation when the power production by the engine was less than internal friction of the engine and the controller could not keep the engine speed constant because the engine was not motored. Stable operation could only be achieved if the engine produced net power sufficient to exceed engine friction.

The Digalog controller used to feedback control signals from a shaft encoder

(Encoder 2, S_4) and a load cell (LC, S_5). A command signal (S_6) then was provided to the dynamometer to adjust the load such that the engine speed remained constant during experiments.

2.2.8 Fuel Injection Control

The AFS Sparrow II engine electronic controller unit (ECU) was used to adjust both liquid and gaseous fuel rate. The closed loop control option as well as all other feedback and actuation signals were disabled aside from the command signals to the gaseous and liquid injectors. AFS Sparrow controller was able to control two injectors at a time simultaneously; hence, at any given time the system was capable of delivering a binary fuel mixture to the intake plenum. Two gaseous fuel injectors and one liquid fuel injector were installed in the intake plenum.

The AFS Sparrow II ECU was interfaced to the same personal computer as the data acquisition system through a serial port and was controlled using a user interface program.

The user interface program was made specifically by AFS for the current experiments. In the interface program, two parameters were adjustable. The first parameter (which was called displacement with no relation to engine displacement) was total amount of time that the injector was activated. For example, a value of 5.0 for displacement parameter in Sparrow II interface program was equal to 5 ms of injection of fuel into the intake plenum. The second adjustable parameter was named compression ratio (with no relation to the engine compression ratio) and was actually the ratio of opening of the injectors in a binary fuel mixture delivery situation. When compression ratio was assigned a value of 0 or 1, just one injector was operated depending on the wiring connections. The injectors were named after the wire as injector 0 and injector 1 during the experiments. A value between 0 and 1 adjusted the opening time of the injector to the same fraction. For example, a value of 0.325 for compression ratio parameter in Sparrow II program was equal to

32.5% of time of opening assigned to the injector 1 and 67.5% assigned to the injector 0.

The only feedback signal that was required to the AFS Sparrow II was a hall effect sensor signal installed on the camshaft to trigger the injection timing in each engine cycle.

2.3 Data Acquisition (DAQ) System

Computerized data acquisition technique based on National Instrument (NI) hardware and Labview™ programs was used for this study. Three E series National Instrument DAQ cards were used. DAQ card specifications are presented in Table 2.9.

The E series DAQ card is capable of measuring temperature, referencing to a datum temperature. There is a built-in resistive temperature detector (RTD) on the DAQ card that, when activated, occupies one of differential analog input channels of the DAQ card. The NI DAQ cards use the PCI interface inside a personal computer running on Microsoft Windows™. The cards are connected to three SCB-68 shielded I/O connector blocks with 68-Pin connectors through shielded cables.

Two NI Labview programs were developed for data acquisition and real time engine operating parameters display. A low speed data acquisition program

Table 2.9: E series NI DAQ card specifications

Parameter	Description
Model	NI PCI-MIO-16E-1 and ...-4
Sampling resolution and rate	12 bit, 1.25 MS/s
Analog input	16 single ended or 8 differential
Digital I/O	8 channels, 5V TTL
Analog output	two 12 Volt 1MS/s max
Counter/ timer	two 24 bit
Temperature referencing	RTD cold junction compensation

Table 2.10: Description of the signal connections to the NI E series DAQ cards device 1 to 3 using SCB-68 terminal boxes

Device 1		
Ch	Parameter	Channel type
0	RG low flow (LMF)	0-5 V analog input
1	RG high flow (HMF)	0-5 V analog input
2	natural gas flow (HMF)	0-5 V analog input
3	air mass flow (AMF)	0-10 V analog input
4	Torque	0-10 V analog input
5	Liquid fuel mass flow (13) in Figure 2.5	0-5 V analog input
6	Intake pressure P_1 in Figure 2.7	-5 to +5 V analog input
7	Exhaust pressure P_2 in Figure 2.7	-5 to +5 V analog input
PF10	PPR signal of Encoder 1 in Figure 2.7	5V digital TTL
PF18	0.1 CAD signal of Encoder 1 in Figure 2.7	5V digital TTL
Device 2		
0	CJC	Built-in RTD
1	RG temperature, T in Figure 2.4	T type thermocouple
2	natural gas temperature, T in Figure 2.4	T type thermocouple
3	intake air temperature, T_1 in Figure 2.7	T type thermocouple
4	EGR temperature, T_2 in Figure 2.7	T type thermocouple
5	Engine coolant temperature, T_5 in Figure 2.7	T type thermocouple
6	Exhaust temperature, T_4 in Figure 2.7	J type thermocouple
7	Liquid fuel temperature, T in Figure 2.5	K type thermocouple
Device 3		
0	Accelerometer	0-10 V analog input
1	Cylinder pressure, P_3 in Figure 2.7	0-10 V analog input
2	NO_x signal from CLD detector	0-10 V analog input
3	THC signal from FID analyzer	0-10 V analog input
4	CH_4 signal from FID analyzer	0-10 V analog input
5	CO_2 signal from NDIR detector	0-10 V analog input
6	CO signal from NDIR detector	0-10 V analog input
7	CO_2 signal from paramagnetic detector	0-10 V analog input
PF10	PPR signal of Encoder 1 in Figure 2.7	5V digital TTL
PF18	0.1 CAD signal of Encoder 1 in Figure 2.7	5V digital TTL

was developed for each individual fuel, measuring engine mean value operating parameters. The Labview program was developed to measure and acquire engine operating parameters except cylinder pressure. The signals produced by sensors were routed to appropriate channels of a SCB-68 terminal box.

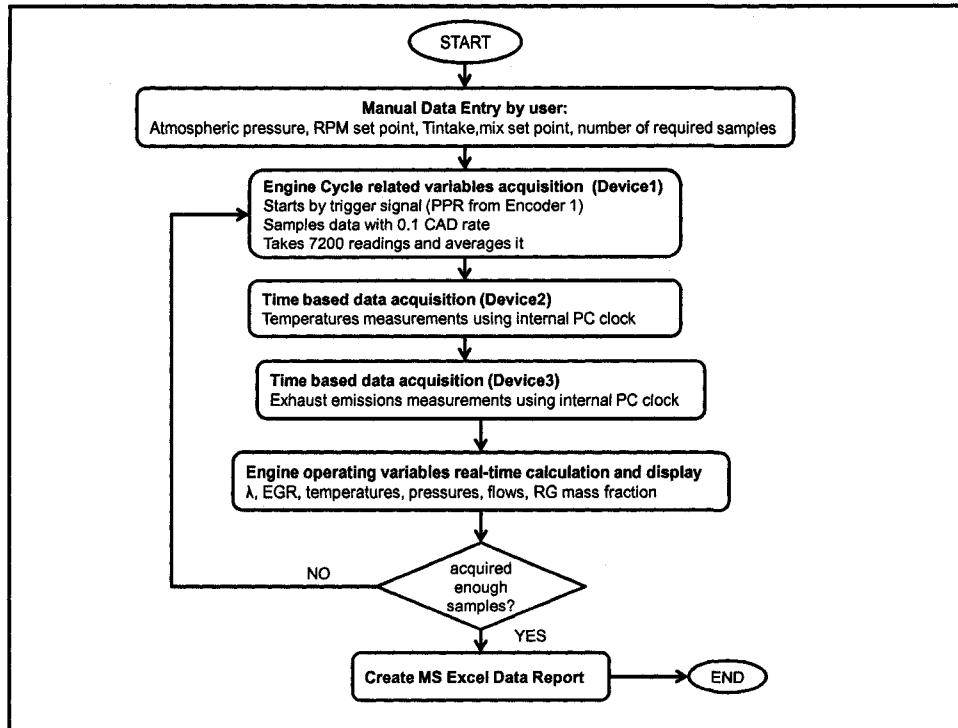


Figure 2.10: Low speed engine mean value parameters data acquisition program flowchart

Using the Labview program, the signals were sampled and digitized. Using the individual calibration values, they were converted to meaningful physical quantities and were saved in a Microsoft Excel file.

The engine mean value parameter data acquisition and saving program used a visual user interface to communicate with the user, manual data entry, real time engine operating parameters, and Excel report generation. The flowchart of the program is indicated in Figure 2.10 and a snapshot from the front panel design of the engine mean value parameter Labview program is indicated in Figure 2.11. A high speed Labview program also was developed to monitor, acquire, and save cylinder pressure data on a cycle-by-cycle basis and with 0.1 CAD resolution. The program data acquisition is started by trigger PPR signal of Encoder 1 and continues until the program reads 7200 sample (two

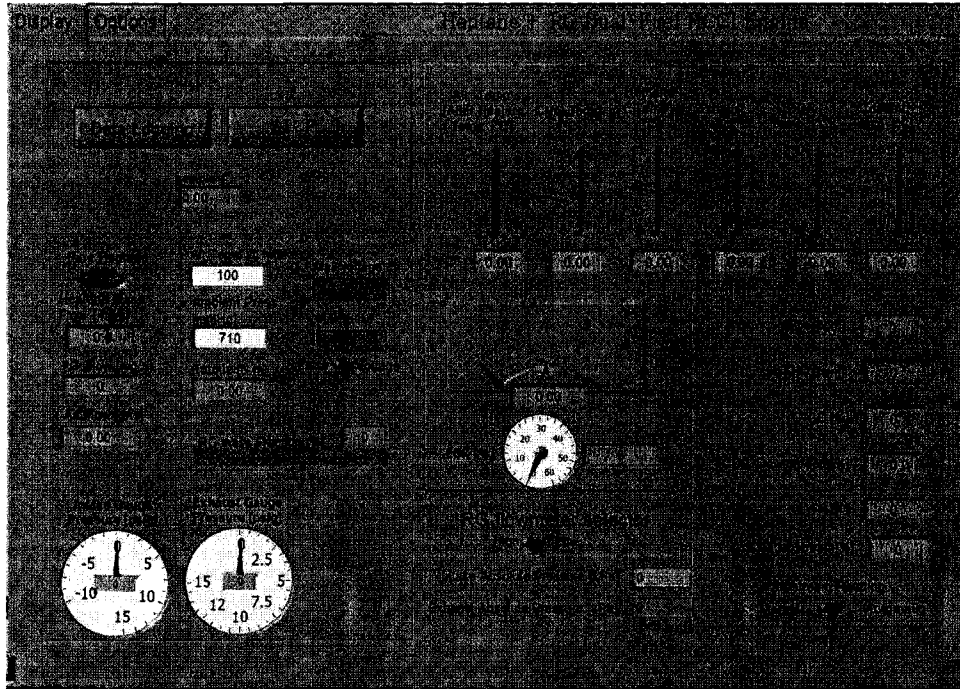


Figure 2.11: A snapshot of the LabviewTM based mean value data acquisition program

crankshaft revolutions, 1 complete engine cycle) and then went to the next cycle. Knowing the location difference of TDC and PPR trigger signals, the pressure trace was properly timed. The raw pressure signal of the pressure transducer (in Volts) was saved in a Microsoft Excel file for each point in a data matrix that had 7200 rows and a number of columns equal to number of cycles required to be saved. Later on, the analysis program calibrated the raw pressure signal from volts to an appropriate pressure quantity using calibration value. The intake plenum pressure was used to reference the original pressure signal. A 4th order Butterworth digital filter was used to reject the high-frequency noises of the signal. Details of pegging and filtering procedures are in Appendix D. The same program was used to acquire vibration of the engine structure on a cycle-by-cycle basis with 0.1 CAD resolution using accelerometer voltage output.

The engine mean value parameters for each operating point were saved in Excel files with "point number-UD.xls" format with "point number" is a consecutive number for all experimental points. The pressure trace was saved in an Excel file with "point number-P.xls" format, and accelerometer data was saved in "point number-K.xls" format.

2.4 Definitions of Parameters

In the following chapters, several engine and combustion parameters are used frequently. In some cases, there is a necessity to clarify the meaning of a parameter or the calculation method as it is necessary for repeating the experiments or using the experimental results to validate HCCI combustion.

2.4.1 Compression Ratio (CR)

The general definition of CR is the ratio of clearance volume (V_c) to the total volume of the cylinder as defined in [1].

$$\text{CR} = \frac{V_d + V_c}{V_c} \quad (2.1)$$

However Equation 2.1 requires a precise measurement of clearance volume V_c for an accurate estimation of CR. The special integrated one-piece design of the cylinder head/cylinder of the CFR engine makes it difficult to measure the clearance volume of the engine precisely. Arthur [116] filled the combustion chamber with a liquid through spark plug hole after running the engine to make the internal parts hot and expanded, and then measuring the required amount of liquid to fill the clearance volume, CR was calculated. Although this seems a precise technique and works for low compression ratios, at higher compression ratio a small deviation in the measurement of the clearance volume can cause a large error in CR calculation. On the other hand, as the cylinder head of the CFR engine in the current study was a special type of cylinder head with six access holes, calculating the CR based on the simple

cylindrical flat top shape of the geometry of the CFR engine also seemed to be inaccurate.

A precise motoring curve measurement and a modeling analysis was performed to determine the CR in any given position of the cylinder head. In the CFR engine, a dial gauge indicator is used to accurately position the cylinder head to cylinder sleeve as shown in Figure 2.2. After removing the guide plate ((6) in Figure 2.2) from the cylinder assembly, clearance volume was decreased to achieve the maximum height of the piston inside the cylinder head. At this position the dial gauge indicator was set at zero. The distance between the piston positioned at TDC and top of the combustion chamber was measured with inch pin gauges with precision of 2/10000 inch. The measurement showed a value of 0.168 inch (4.267 mm) for the distance between piston positioned at TDC and top of combustion chamber when dial gauge indicates zero. This position was the maximum CR achievable with the current configuration.

During the experiments at the beginning and at the end of each day of tests, cold and hot motoring pressure trace of the engine was measured for 100 consecutive cycles using a Labview DAQ program while the engine was motored using the dynamometer. Intake temperature before the intake valve, engine speed, and intake plenum pressure also were measured. The motoring curves were assigned to each day of experiments and each position of the dial gauge indicator. A validated engine model was used to simulate the combustion pressure trace with CR varied until the two matched. The CR used for this study is actually the effective CR that produced the same motoring curve that did the experiments. Description of the model used for CR estimation can be found in Appendix E. In all consecutive analysis, tables, and figures, CR is the effective CR that was estimated by the numerical model and it is not the geometrical CR that is normally calculated using Equation 2.1. Having all effective CR values calculated by the model, an equation was derived for estimation of effective CR from dial gauge indicator reading when the gap is

0.168 inch.

$$CR = 68.7d^2 - 50.0d + 18.3 \quad (2.2)$$

where d is dial gauge reading in inch (with 0.168 inch gap at dial gauge reading of zero) and CR is estimated by the model. A complete list of motoring points, initial conditions, and estimated CR can be found in Appendix E.

2.4.2 Relative Air/Fuel Ratio (λ)

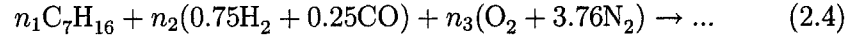
Several studies have been focused on estimation of air/fuel ratio as it is one of the essential parameters that describes the behavior of an IC engine. Air/fuel ratio can be determined indirectly from exhaust gas composition when the air and fuel flow measurement is not possible. A comparison of air/fuel ratio calculation by direct mass flow measurement and by exhaust gas analysis has been published by Lynch and Smith (1997) [125]. Cavina and Ponti (2003) [126] described a technique to estimate the air/fuel ratio from in-cylinder pressure frequency analysis. In a recent study, Mueller (2005) [127] defined a new parameter - oxidizer ratio - that was used to calculate stoichiometry ratio when the fuel molecule contains oxidizer or oxidizer contains fuel molecule.

Using a wide band air/fuel ratio meter that uses an oxygen sensor inside the exhaust flow is the direct method of measuring relative air/fuel ratio (λ) if conventional fuel is used. In this study, RG was used as an additive to the base fuel. As an oxygenated fuel, RG causes error in air/fuel ratio meter operation. Measuring air, fuel, and RG flow and calculating relative air/fuel ratio using Valence method was used. Valence method calculates the equivalence ratio (ϕ) based on the valences of all atoms involved in the combustion equation. Using valence values of carbon (+4), hydrogen (+1), nitrogen (0) and oxygen (-2), the equivalence ratio was calculated as:

$$\frac{1}{\lambda} = \phi = \frac{\sum V^+}{|\sum V^-|} \quad (2.3)$$

where λ is relative air/fuel ratio, ϕ is equivalence ratio, $\sum V^+$ and $|\sum V^-|$ are the summation of total positive valences and total negative valences of the

intake mixture, including both fuel and air, respectively. For example, for a mixture of n-Heptane, simulated RG (0.75% H₂, 25% CO), and air under the reactant equation of:



the λ is calculated as:

$$\frac{1}{\lambda} = \phi = \frac{44n_1 + 2.5n_2}{0.5n_2 + 4n_3} \quad (2.5)$$

where n_1 , n_2 , and n_3 are the molar flow rates of n-Heptane, RG, and air, respectively. Similarly, λ was calculated for other fuel and RG composition combinations.

2.4.3 EGR

EGR was calculated using volume concentration measurement of CO₂ upstream and downstream of the engine as indicated in Figure 2.7 EGR was calculated:

$$\text{EGR} = 100 \times \frac{\text{CO}_{2,up}}{\text{CO}_{2,down}} \quad (2.6)$$

2.4.4 RG Mass Fraction (RG blend fraction)

Reformer gas blend fraction was calculated using mass flow rate of the base fuel and mass flow rate of RG:

$$\text{RG}_{\text{mass,frac}} = 100 \times \frac{\dot{m}_{RG}}{\dot{m}_{RG} + \dot{m}_{fuel}} \quad (2.7)$$

where \dot{m}_{RG} and \dot{m}_{fuel} are RG mass flow and fuel mass flow rates, respectively.

2.4.5 Indicated Mean Effective Pressure (IMEP)

Indicated mean effective pressure (IMEP) was calculated using cylinder pressure trace and an equation from [1].

$$\text{IMEP} = \frac{\oint PdV}{V_d} \quad (2.8)$$

Where P is cylinder pressure trace in Pa, dV is rate of change of cylinder volume in m^3/s , V_d is displacement volume in m^3 , and $\oint PdV$ is the work per cycle of the engine integrated over compression and expansion cycles. IMEP was calculated for each individual cycle and then averaged over the range of cycles (usually 100) for each operating point.

2.4.6 Cyclic Variation (COV_{IMEP})

Several parameters can be used as indicators of cyclic variation. Cylinder maximum pressure value or cylinder maximum pressure timing, start of combustion, or rate of pressure rise inside the cylinder are some examples. Here the most direct parameter was used to quantify cyclic variation. As IMEP was averaged over 100 cycles for most of the operating points, coefficient of variation of IMEP was calculated as:

$$COV_{IMEP} = 100 \times \frac{Mean_{IMEP}}{\sigma_{IMEP}} \quad (2.9)$$

where $Mean_{IMEP}$ is the average of IMEP over 100 cycles and σ_{IMEP} is the standard deviation of IMEP over 100 cycles.

2.4.7 Thermal Efficiency (η_{th})

As the CFR engine is a high internal friction engine, the values for brake efficiencies of this engine are extremely low in comparison with current low-friction production engines. All calculations in this study are based on indicated values. First, the indicated power of the CFR engine was calculated using an equation from [1]

$$P_i = \frac{IMEP \cdot V_d \cdot N}{n_R} \quad (2.10)$$

where P_i is indicated power in W, IMEP is indicated mean effective pressure in Pa, N is the engine speed in rev/s, V_d is displacement volume in m^3 , and $n_R=2$ for a four-stroke engine. Then, indicated thermal efficiency (or indicated fuel conversion efficiency) was calculated by

$$\eta_{th} = 100 \times \frac{P_i}{\dot{m}_{fuel}LHV_{fuel} + \dot{m}_{RG}LHV_{RG}} \quad (2.11)$$

where η_{th} is indicated thermal efficiency in %, P_i is indicated power in kW, \dot{m}_{fuel} and \dot{m}_{RG} are fuel and RG mass flow rates in kg/s, and LHV is the lower heating value of the fuel or RG in kJ/kg.K.

2.4.8 Combustion Efficiency (η_c)

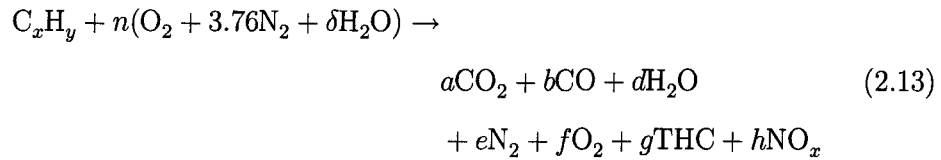
Combustion efficiency is an indicator of completeness of combustion being affected by the level of unburned fuel and carbon monoxide in the exhaust gas flow.

$$\eta_c = 100 \times \frac{\dot{m}_{HC}LHV_{HC} + \dot{m}_{CO}LHV_{CO}}{\dot{m}_{fuel}LHV_{fuel} + \dot{m}_{RG}LHV_{RG}} \quad (2.12)$$

where η_c is combustion efficiency in %, and \dot{m}_{HC} and \dot{m}_{CO} are mass flow rates of unburned hydrocarbons and CO inside the exhaust flow in kg/s.

2.4.9 Indicated Specific Emissions

All emissions were measured on a dry-basis after condensation of water from the exhaust gas sample as indicated in Figure 2.8. It is required to first convert all dry measurements to a wet value that accounts for the amount of water condensed from the exhaust gas sample. A combustion equation assuming no oxygenated fuel is:



To calculate indicated specific emissions, first number of the H_2O moles in ambient air was calculated

$$\delta = 4.773 \times \frac{P_{vap}}{P_{atm} - P_{vap}} \quad (2.14)$$

where δ is number of H_2O moles in air, P_{vap} is the vapor pressure in the room condition calculated using atmospheric pressure (P_{atm}), dry and wet bulb temperatures. Dry mole fraction of water then becomes

$$Y_{H_2O,Dry} = \frac{P_{@T_{sat}}}{P_{atm} - P_{vac}} \quad (2.15)$$

where $P_{@T_{sat}}$ is the pressure at saturation temperature of the sample line obtained from any classical thermodynamic text book, and P_{vac} is the sample line pressure which is normally vacuum gauge (P in Figure 2.8). Assume that the total products of combustion equals 1. Then the mole fraction of N_2 is calculated by subtracting all dry mole fractions from

$$Y_{N_2,Dry} = 1 - Y_{H_2O,Dry} - Y_{CO_2,Dry} - Y_{O_2,Dry} - Y_{CO,Dry} - Y_{NO_x,Dry} - Y_{THC,Dry} \quad (2.16)$$

where $Y_{i,Dry}$ is the dry molar concentration of species i, measured by emission analyzers. A nitrogen balance in combustion equation gives the number of moles of air (n) in the reactants

$$n = \frac{Y_{N_2,Dry} + 0.5Y_{NO_x,Dry}}{3.773} \quad (2.17)$$

$$Y_{H_2O,Wet} = 2 \times (n + 0.5\delta - (Y_{CO_2,Dry} + 0.5Y_{CO,Dry} + Y_{NO_x,Dry} + Y_{O_2,Dry})) \quad (2.18)$$

A carbon balance of the combustion equation gives wet H_2O molar concentration:

$$x = Y_{CO_2,Dry} + Y_{CO,Dry} + Y_{THC,Dry} \quad (2.19)$$

As the FID analyzer is a carbon counter, it was assumed that all carbons are connected to two hydrogen atoms, hence a hydrogen balance yields to

$$y = 2Y_{H_2O,Wet} + Y_{THC,Dry} \quad (2.20)$$

and the correction factor for change from dry to wet values is:

$$\alpha = 1 + Y_{NO_x,Dry} \quad (2.21)$$

To calculate the wet value of each species, it is required to divide the dry value by α .

The exhaust molecular weight is calculated using species individual molecular weight and calculated wet molar concentration

$$MW_{exhaust} = \sum Y_{i,Wet} MW_i \quad (2.22)$$

where i represents by all species of the combustion equation 2.13. Assuming no blow-by from the cylinder to crankcase and conservation of mass,

$$\dot{m}_{exhaust} = \dot{m}_{intake} = \dot{m}_{air} + \dot{m}_{fuel} + \dot{m}_{RG} \quad (2.23)$$

Exhaust molar flow is rate

$$\dot{n}_{exhaust} = \frac{\dot{m}_{exhaust}}{MW_{exhaust}} \quad (2.24)$$

and for example for the case of CO

$$\dot{m}_{CO} = Y_{CO,Wet} \times \dot{n}_{exhaust} \times MW_{CO} \quad (2.25)$$

and indicated specific CO

$$isCO = 3600 \times \frac{\dot{m}_{CO}}{P_i} \quad (2.26)$$

where \dot{m}_{CO} is CO mass flow rate in g/s, P_i is indicated power in kW, and isCO is indicated carbon monoxide emission in g/kW-hr.

2.4.10 Cylinder Pressure Trace Characteristics

Cylinder pressure trace -P- can be used for several other informative parameters that are indicators of rate of combustion or combustion timing. Among those Maximum cylinder pressure (P_{max}), and maximum cylinder pressure rate ($(dP/d\theta)_{max}$) were used for this study. Each parameter was averaged over 100 consecutive cycles.

2.4.11 Knock Indicators

Knock in an HCCI engine is an important phenomenon that defines the high power boundary of operation. The engine knocking characteristics is also highly related to chemistry of the fuel being used in the HCCI engine. Hence, a precise comprehensive study of knock characterization techniques and definition of the parameters to define the knock boundary and to quantify the knock level is unavoidable.

Knock Quantification Techniques

At least three major theories are available for knock in a SI engine presented by Cuttler et al (1988)[128].

- Autoignition theory: end gas undergoes a high pressure and temperature because of the flame propagation and it auto-ignites from one or more points. Resulting pressure wave crosses pressure wave of premixed flame and causes a back-and-forth pressure fluctuation.
- Detonation theory: Normal premixed flame changes its regime from subsonic deflagration to supersonic detonation, and
- Rapid-entrainment theory: normal premixed flame is accelerated and causes a high pressure rise rate.

A conventional SI engine combustion photography by Cuttler et al (1988) [128] and Konig et al (1990) [129] showed the existence of rapid entrainment condition, but a general acceptance is in place to believe that end gas autoignition is the most common cause of knock in SI engines. In fact, a combination of end gas autoignition causing a rapid pressure rise resulting to a structural vibration is more applicable to a general knock condition.

HCCI combustion which is usually characterized by fast heat release is a controlled knock without excessive vibration. With HCCI combustion, high rate of pressure rise happens frequently and there is not any definite boundary between knock and no-knock conditions. Combustion behavior changes gradually with increasing rate of pressure rise.

There are several methods available for knock detection and characterization. A comprehensive review paper by Puzinauskas (1992) [130] classified all available methods to simple pressure evaluation, frequency-domain pressure manipulation, and derivative-based method categories. Eleven different methods were chosen and examined in the study and advantages and disadvantages were discussed. Cuttler et al (1988) [128] or Benson et al (1983) [131] used

a pressure evaluation method and offered maximum cylinder pressure (P_{\max}) as a knock indicator. Identifying P_{\max} as a knock indicator is an easy way to detect and quantify knock, but it changes with engine operating parameters and makes it difficult to interpret.

Several investigators such as Cuttler et al (1988) [128], Konig et al (1990) [129], Benson et al (1983) [131], and, Arrigoni et al (1972) [132] examined frequency domain manipulation of cylinder pressure data to identify knock. Usually the pressure signal was band-pass filtered around the knock frequency. Then peak to peak amplitude or root mean square (RMS) of the band-pass filtered signal was used to determine a knock cycle. In addition, fast-Fourier transforms were used to show spectral content of pressure signal. Several researchers used derivative based method for knock detection. Checkel and Dale (1986-1989) [133, 134, 135] used a third derivative of pressure signal for knock characterization. In addition, some researchers such as Ando et al (1989) [136] and Michael et al (1996) [137] used rate of heat release for knock detection. In a study by Katranik et al (2006) [138], third derivative of pressure was used to predict start of combustion in diesel combustion similar to a knock detection method.

HCCI combustion is usually characterized by rapid pressure rise. HCCI engine operating sound changes when rate of pressure rise changes. At high rate of pressure rise and even before knock, a noise is noticeable. Further increase in rate of pressure rise (by increasing inlet air temperature, increasing compression ratio, decreasing air/fuel ratio, etc.) causes the engine noise to convert to a ticking sound which is actually high-frequency vibration of the engine structure. Rate of pressure rise is a determining factor in an HCCI engine and is used to identify non-knocking, transition, and knocking conditions. Even in a non-knocking condition, a closer look at pressure trace identifies small oscillations similar to knock. It is important to quantify knock, in an HCCI engine because even when there is not a severe, recognizable knock, engine operation noise is excessive, which is a concern for practicality. In the first

passenger car equipped with a dual mode SI-HCCI engine, this phenomenon was identified as a problem ([17]).

In this study, two sets of knock intensity parameters were used. For naturally aspirated operating modes, knock intensity parameters were extracted from pressure trace signals. Appendix F shows the details of calculations for ΔP_P and RMS_P . The other set of knock intensity parameters were calculated using the accelerometer analog output for supercharged data. Details of calculations of $P_{k.Acc.}$ and $RMS_{Acc.}$ is indicated in Appendix F.

All four selected parameters indicated a knock quantification parameter independent of the engine operating parameters (such as λ , EGR), compression ratio, and fuel properties. Based on the least square curve fitting of an exponential function around knock limit of $(dP/d\theta)_{max} = 8$ bar/CAD the following values were calculated for knock limit : $\Delta P_P = 1.63$ bar, $P_{k.Acc.} = 1.26$ V, $RMS_{Acc.} = 0.1741$ V, and $RMS_P = 0.0212$ bar. Averages of the knock quantification parameters over 100 consecutive cycles were used to determine the knock intensity of each operating point considering certain confidence interval limits that comes from cyclic variation of the parameter.

Heat Release Parameters

Direct heat release analysis was performed on filtered pressure traces using a well stirred single zone model with air as working fluid. Heat release analysis is usually performed to specific the combustion timing, combustion duration, rate of heat release and properties of double stage combustion. In conventional SI engines, usually mass fraction burn is calculated using the Rassweiler-Withrow technique [139]. However, as this method relies on flame propagation throughout the combustion chamber, its validity is questionable when used in the flameless HCCI combustion.

Details of the heat release model used here are described in Heywood [1]. The complete heat release equation that was derived from ideal gas law considering

constant R is:

$$\begin{aligned}
 \frac{dQ_{HR}}{d\theta} = & \\
 & \frac{\gamma}{\gamma-1} p \frac{dV}{d\theta} \\
 & + \frac{1}{\gamma-1} V \frac{dp}{d\theta} \\
 & + V_{cr} \left[\frac{T'}{T_w} + \frac{T}{T_w(\gamma-1)} + \frac{1}{bT_w} \ln \left(\frac{\gamma-1}{\gamma'-1} \right) \right] \frac{dp}{d\theta} \\
 & + \frac{dQ_{HT}}{d\theta}
 \end{aligned} \tag{2.27}$$

where:

$\frac{dQ_{HR}}{d\theta}$ is the gross total rate of heat release, $\frac{\gamma}{\gamma-1} p \frac{dV}{d\theta} + \frac{1}{\gamma-1} V \frac{dp}{d\theta}$ represents the sensible energy change and work transferred to the piston $V_{cr}[\dots] \frac{dp}{d\theta}$ is the heat transfer to the crevices, and $\frac{dQ_{HT}}{d\theta}$ is the heat transfer to the cylinder wall.

In this study the crevices effect (3rd term on the right hand side of the Equation 2.27) was neglected. To calculate the heat transfer to the the cylinder wall, the Woschni correlation for heat transfer ([140]) modified by Chang (2004) [141] for HCCI combustion was used. $\frac{dQ_{HR}}{d\theta}$ without crevices effect and heat transfer to the cylinder was called net (apparent) rate of heat release (NRHR). As crevices effect was neglected in this study, the summation of NRHR and heat transfer to the cylinder wall was called gross rate of heat release. Gross rate of heat release was integrated and normalized to calculate gross accumulative heat release (GHR). Gross accumulative heat release was used to define the combustion characteristics. Figure 2.12 compares the cylinder pressure trace for a specific case of n-Heptane HCCI combustion. The x-axis in Figure 2.12 is the same for all three plots and indicates crank angle degree (CAD) after TDC (aTDC); hence, the value of 0 on X-axis indicates TDC position. The NRHR plot in Figure 2.12 indicates a double-stage combustion for n-Heptane. Detailed combustion characteristics were defined using NRHR and GHR plots

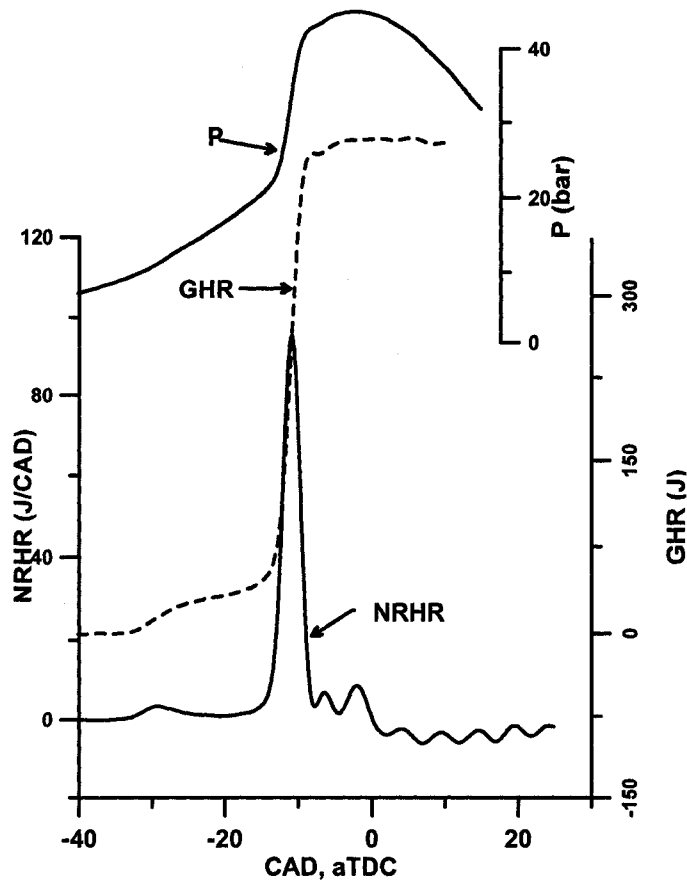


Figure 2.12: A comparison of pressure trace (P), net rate of heat release (NRHR), and gross accumulative heat release (GHR) for HCCI combustion of n-Heptane at $\lambda=1.98$, EGR=10%, CR=9.5, N=700 RPM

as indicated in Figure 2.13.

Start of combustion (SOC) was defined as the crank angle position where 10% of the maximum GHR has occurred as indicated in Figure 2.13-b. Crank angle rotation in CAD during which GHR goes from 10% to 90% of maximum was defined as combustion duration (CD) as indicated in Figure 2.13. For the fuels with double stage combustion - in this study n-Heptane-, further combustion characteristics were extracted from the NRHR plot as indicated in Figure 2.13-a. Maximum rate of heat release at the first stage or low-temperature heat release (LTR_{max}), maximum rate of heat release at the main stage of combus-

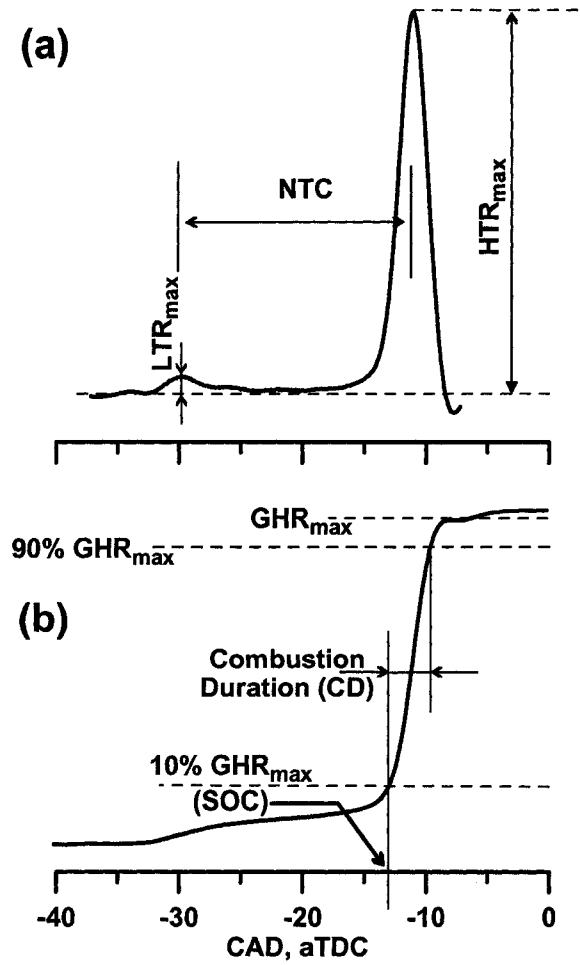


Figure 2.13: Combustion characteristics definition using NRHR and GHR plots, HCCI combustion of n-Heptane

tion or high-temperature heat release (HTR_{max}), and negative temperature coefficient length (NTC) were defined here as shown in Figure 2.13. Ratio of first to second stage rate of heat release was calculated by

$$LTR/HTR\text{-ratio} = 100 \times \frac{LTR_{max}}{HTR_{max}} \quad (2.28)$$

Actual SOC, CD, NTC, LTR_{max} , HTR_{max} , and LTR/HTR-ratio for each operating point were calculated on a cycle-by-cycle basis and averaged over 100 consecutive cycles considering confidence interval limits caused by cyclic vari-

ation.

2.5 Experimental Matrix and Procedures

A total of 1874 acceptable operating points were collected during this study with a range of fuels, CRs, and intake mixture temperatures. All operating points were numbered consecutively.

Experiments were designed here to achieve an acceptable operating range, but not optimized, as the purpose of the study was not to operate an experimental, knock-prone, high-internal-friction-CFR engine in an optimum manner. Instead the study was focused on the interaction of parameters, mainly effects of RG on HCCI combustion characteristics.

For each individual fuel, based on the autoignition characteristics, a range of intake mixture temperature, compression ratio, and engine speed were examined to obtain the widest operating region. On the other hand, RG addition was considered as a potential means of increasing or decreasing fuel resistance to autoignition; and hence, the initial condition without RG was slightly over-adjusted to compensate for the shifts occurring with RG addition. For each fuel, keeping engine speed, compression ratio, intake mixture temperature, and intake pressure constant, the engine operating region was obtained by varying EGR, λ , and RG blend fraction in certain steps to cover the whole engine map. The experimental procedure was conducted under certain steps:

- A certain fuel was selected.
- CR, $T_{\text{intake,mix}}$, P_{intake} , and N (speed) were fixed after a series of trial run based on previous studies.
- EGR was fixed at maximum attainable without excessive cyclic variation.
- RG blend fraction was selected zero at the beginning.

- λ was fixed at the minimum possible (rich) and data was taken consecutively keeping EGR and RG mass fraction constant and increasing λ with permissible steps by injector control
- RG mass fraction was increased by 10% and λ variation was repeated
- Getting to maximum RG blend fraction attainable, EGR was decreased by 10% and whole procedure was repeated.
- The procedure was continued until getting all possible EGR, RG mass fraction and λ possible combinations in the allowable engine operating region.

Other experimental procedures which were conducted are:

- SI to HCCI mode transfer procedures that were designed and performed to start and warm up the engine in natural gas SI mode and convert the operation gradually to any desired HCCI combustion with selected fuel, CR, and speed.
- Repeatability tests were performed to ensure the required repeatability of data on various incidents within a certain confidence interval.
- To quantify the effect of major engine input parameters such as speed and EGR level, on engine and combustion characteristics, a series of experiments designed with a factorial scheme was performed. Details of factorial design are discussed in Chapter 3.

2.6 Uncertainty Analysis

In these experiments, precautions were considered to minimize the human bias and equipment failure during the experiments. In several incidents, either human error or equipment failure caused a certain irregularity that could not be explained by the physics of the problem. Repeat experiments were performed

to confirm data errors and the erroneous set of data was replaced by the new set.

Ensuring minimum human and equipment errors, minimizing equipment nonlinearities and carefully calibration equipments is not enough to establish a well performed experiments with trustable results. Certain statistical and mathematical procedures were conducted to establish a level of accuracy and confidence interval for all engine and combustion parameters.

A combination of repeated measurement and estimation of small errors in equations were used to analyze the experimental results. Three basic error estimation categories have been used.

2.6.1 Error Estimation of the Primary Parameters

The first group are the basic direct measured parameters such as air mass flow, fuel mass flow, RG mass flow, temperatures, pressures and exhaust gas species dry volumetric concentrations. For these parameters, repeated measurement with internal error analysis was used. The question was "how many samples must be taken such that the sample mean \bar{x}_s becomes a true (population) mean \bar{x} within $\pm\delta$ at a confidence level (p%). A value of p=95% confidence limit was considered. Then, for example considering NO_x measurement in ppm, a typical standard deviation for NO_x analyzer was ± 2 ppm. At confidence limit of p=95%, a required mean sample standard deviation of ± 1 ppm and a t-value from t-student two-tailed table of $t=2.110$, number of required samples $n=18$. As a rule of thumb, a minimum sample number of $n=30$ is required to get closer to a normal distribution. Hence, for all experiments a minimum number of samples of $n=30$ (usually $n=50$) were collected. Then, using internal error analysis the error associated with direct measurement of the basic parameters to be laid on 95% confidence limit was considered as $\pm 2\sigma_s$, which σ_s is the sample (not population) standard deviation. Details of minimum sample size requirement calculation, and error analysis of primary parameters is in Appendix G.

2.6.2 Error Estimation of the Secondary Parameters

Using primary parameters, the secondary variables such as indicated specific emissions, λ , and RG blend fraction were calculated. Although it is possible to calculate the uncertainty for secondary parameters through internal error estimation using whole sample size of primary parameters to calculate secondary parameters, for the more precise error analysis, the secondary parameters uncertainties were calculated using an external error analysis method. Details of error estimation for this group of parameters is in Appendix G.

2.6.3 Error Estimation of Cyclic Related Variables

The third group of parameters were categorized as the parameters where variation is due to small deviations from the mean and also due to cyclic variation. IMEP, SOC, CD, NTC, and knock intensity are some of the examples of these parameters.

For example, consider SOC as a parameter that belongs to the third category. SOC was calculated using a heat release model through a series of mathematical manipulations on a cycle-by-cycle basis. For each operating point, 100 consecutive pressure traces were measured. From each cycle, one value for SOC was calculated. Hence, 100 values for SOC were obtained for each operating point. Then, SOC was averaged over 100 cycles and a mean value of SOC was reported for actual combustion timing of each operating point. Three various uncertainties or dispersions were calculated for a single parameter:

- A value of standard deviation for each SOC value of one cycle, σ_{SOC} For those parameters that were obtained using a long mathematical procedures, external error analysis was tedious, so dispersion was calculated using resampling techniques such as the bootstrap method (e.g. [142]).
- A value of standard deviation that relates to 100 consecutive SOC values, $\sigma_{SOC,cyclic}$ This value is likely showing the cyclic variation of each parameter.

- A value of dispersion that states the uncertainty of the mean of a series of SOCs using pooled standard deviation statistics, $\sigma_{SOC,pooled}$

Then, the final estimation of uncertainty is the largest value calculated using the three error estimation paths. Cyclic variation caused the largest uncertainty; and hence, it was used as the error bars in related plots. Detailed analysis of the error for the third type of parameters is in Appendix G.

2.7 Summary

An experimental facility for HCCI combustion engines was developed for this study. The measurements were conducted using a series of carefully calibrated sensors. Data was taken using computerized data acquisition techniques with National Instrument Labview programs. Certain procedures were followed to ensure the precision, accuracy, and repeatability of data taken. Finally, using several statistical techniques the uncertainty and confidence interval of measured parameters were determined.

Basic Operating Characteristics of HCCI Combustion Engine

This chapter analysis the basic operating characteristics of HCCI combustion in the CFR engine and the effect of parameters such as λ , EGR, CR, $T_{intake,mix}$ on engine mean value and combustion parameters. This analysis is used in later chapters as a baseline to isolate the effects of partial reforming.

HCCI basic combustion characteristics have been analyzed in several previous literatures. To discuss the possibility of combustion timing control with RG in an HCCI engine, effect of other influential parameters have to be studied first. The knowledge of the engine operating parameters and combustion characteristics behavior of engine input variables is essential to explore different aspects of partial fuel reforming.

3.1 Operating Region

The operating region in this study was defined based on λ and EGR. In an HCCI combustion engine, the combination of λ and EGR determine the location of the operating point in the load-efficiency map. For fixed values of compression ratio, intake temperature and engine speed, demand for a particular engine output can be met by varying combinations of λ and EGR.

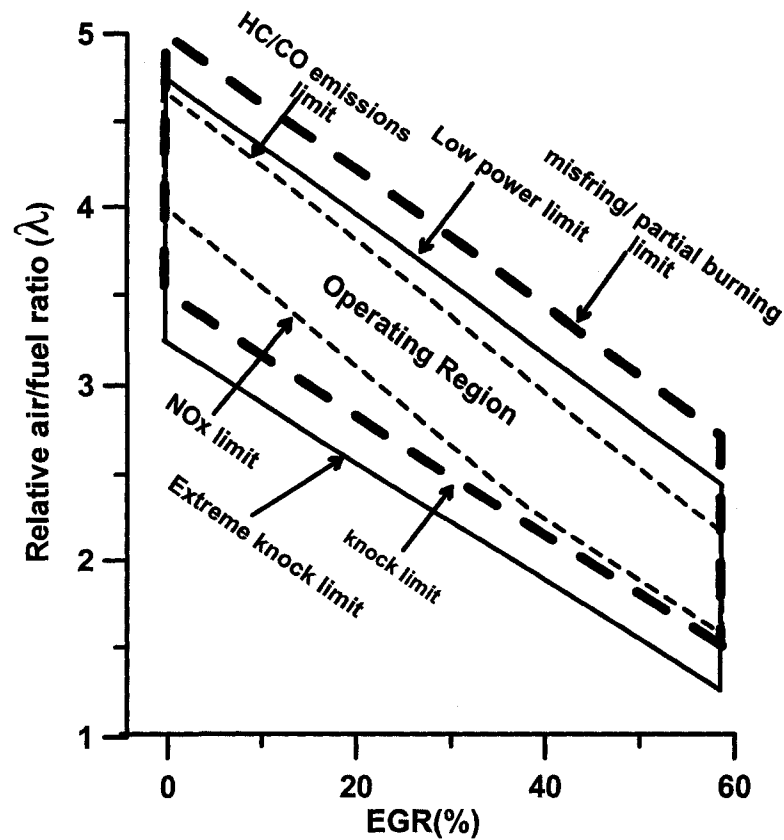


Figure 3.1: A typical λ -EGR operating region for HCCI combustion with various definitions of operating boundaries

Ideally, engine calibration will use the values which meet this load demand at the optimum efficiency available within the available operating range. Operating region boundaries can be defined based on limits of combustion stability, (such as misfire and knock limits), or on limits of acceptable exhaust emissions. Figure 3.1 is a typical HCCI operating region, shown schematically on a λ -EGR map. In HCCI operation map, at any constant compression ratio and intake temperature, any engine load demand can be obtained by several pairs of λ and EGR. Engine calibration can be performed to optimize any certain load for maximum efficiency. Three sets of boundaries are shown on Figure 3.1. Starting from the center of the operating region at any constant EGR,

NO_x starts to rise with a shift to richer mixture, (lower λ). The NO_x limit on operating range is arbitrarily set by NO_x emissions standards and generally becomes wider with higher EGR fraction. Shifting further towards richer mixture leads to a knock limit and then an extreme knock limit. Appendix F describes parameters which can be used to quantify knock and define the knock limits. In this work, operation was studied out to the extreme knock boundary as defined by limiting the maximum rate of pressure rise ($(dP/d\theta)_{\max}$) to 20 bar/CAD.

Starting again from the center of the operating region and shifting towards leaner conditions, (higher λ), tends to give higher CO and HC emissions. CO and HC emissions from HCCI combustion tend to be high enough to require exhaust gas after-treatment so an emissions-related operating region boundary would be defined considering emissions standards and the capability of exhaust after-treatment systems. At higher EGR fraction, the high CO/ HC limit tends to provide a narrower operating region due to decreased combustion temperature.

If the HCCI operating region is not limited on the lean side by CO / HC emissions, another possible limit is set by low power. This proved to be a technical barrier for the CFR engine used in this study. Under naturally aspirated HCCI conditions, the lean mixture limit was set by the inability of the engine to produce sufficient power to overcome the high internal friction of the CFR. For most engines, (which have lower internal friction than the CFR), the lean limit to HCCI operation is set by misfire and partial burn limits. This boundary can be defined using any cyclic variation parameter such as coefficient of variation of IMEP (COV_{IMEP}) exceeding a limit such as 5%.

In conventional combustion engines, the operating window is a multi-dimensional space defined by torque, manifold absolute pressure and speed, with limits set by standard emission levels, knock and fuel consumption. The desirable operating window is defined by parameters such as maximum torque, maximum thermal efficiency, or minimum cyclic variation, all with the condition that

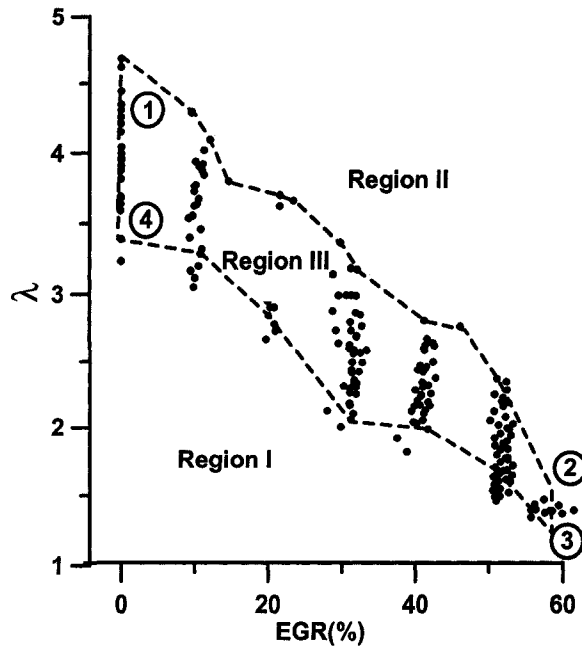


Figure 3.2: λ -EGR operating region of n-Heptane, supercharged HCCI combustion, initial conditions indicated in Table 3.2

emissions are maintained below acceptable limits. There are also other issues such as engine operating temperature, vibration and audible noise that may shift or limit the final operating window.

The operating window in this study was defined more simply than for a production engine because the purpose was to study combustion behavior over a wide range of conditions rather than to calibrate and optimize a production engine. As shown in Figure 3.2, the broadly defined HCCI operating region used in this study typically exhibits three major regions and four distinct boundaries. The actual operating window (Region III in Figure 3.2) was limited by a boundary shown by a dashed line and passing through four points (1-2-3-4-1).

Misfiring, Partial Burning and Low Load Limits

Region II that is defined by boundary 1-2 is called the misfiring/partial burning/ low power region. This boundary is at the lean side and low power of HCCI engine operating region. HCCI combustion is a flameless multi-site combustion and dilution limit is much wider than that of normal conventional combustion. HCCI combustion initiates at several and not all of the points inside the combustion chamber. By ignition of each set of points inside the combustion chamber, temperature and pressure increases and causes the ignition of the next set of points that have less access to fuel and/or oxygen or located on the cooler parts of the combustion chamber. Hence, certain amount of temperature rise is necessary to progress from the core zone toward the cylinder wall zones to ignite the whole air/fuel mixture. In the case of dilution with air, less temperature rise happens by the core zone mixture simply because of less energy content (at any constant EGR rates diluting the mixture happens by decreasing fuel flow rate at constant air flow rate). Hence, at a certain point, not all of the fuels are ignited, causing an increase in cyclic variation and extreme amount of HC and CO emissions. At such a condition, the pressure rise due to combustion is low. Then, further dilution of the mixture causes a complete misfiring and none of the fuel molecules ignites and possibly some of the fuel molecules undergo a fuel reforming rather than a complete or incomplete combustion.

The other phenomenon that is observed in such a situation at high EGR rates is a cyclic fluctuation of the engine operation between knock and misfiring. Misfiring in one cycle causes an extreme amount of HC in the exhaust that is being returned to the intake by EGR; and hence, on the next cycle a temporary rich air/fuel mixture is inside the cylinder. If the intake temperature is enough for combustion initiation, temporary rich mixture causes a fast and early combustion with high rate of pressure rise and engine severe knock.

Several factors can be used to determine the boundary limit of 1-2. High

cyclic variation, knock/misfiring fluctuation, extreme amount of HC and CO emission can be used as indicators to identify the boundary.

The boundary of 1-2 in Figure 3.2 is the main cause of practical difficulty in HCCI combustion application in idling condition. Idling requires a low power production just enough to overcome the engine internal friction in a stable low cyclic variation condition. In an HCCI engine, load control mostly happens by λ variation; hence, achieving low loads requires high λ . Increasing λ causes the operating region shifting toward boundary 1-2 in Figure 3.2. In normal production engines with low internal friction, this boundary happens well before idle load. Hence, idling of such an engine in HCCI mode usually is accompanied by high cyclic variation, partial burning, misfiring, and excessive amount of HC and CO emissions that causes a low combustion efficiency and a low thermal efficiency.

The CFR engine is a knock prone engine to tolerate knocking without any damage to the engine structure. This design enables the engine to operate at situations that can be easily destructive to a production engine. On the other hand, such a heavy design causes the engine to suffer from a high internal friction. Using torque measurement and Willans line method for engine friction estimation (described by Heywood [1]); the engine friction mean effective pressure (FMEP) of the engine was estimated of 2.16 bar for supercharged natural gas HCCI engine at 800 RPM at CR=19.0 and 1.90 bar for supercharged n-Heptane HCCI engine at 800 RPM and CR=11.5. These values are much higher than the typical engine friction. For example, Heywood in [1] reported the FMEP = 50 kPa for a six cylinder diesel engine at 800 RPM. The actual FMEP for one cylinder is much less than this. Using the equation that correlates the engine speed with FMEP for a four cylinder SI engine from the same reference FMEP=1.21 bar.

Having such an internal friction usually requires a large idling load. The power production in HCCI engine however is limited and by increasing λ toward Region II in Figure 3.2 at a certain point brake power produced by the engine is

not enough to overcome the internal friction and the engine starts to stall before getting to partial burning or misfiring boundary. Hence, the CFR engine HCCI operating range is even more restricted than a production light engine to the low power limit. Hence, the line 1-2 in Figure 3.2 that separates the engine operating window (Region III) from unacceptable operating (Region II) is a combination of misfiring, partial burning and low load points depending on the operating condition. An example of such an operating range is indicated in Figure 3.3 by pressure trace P_2 compared with a knocking cycle (P_1) and motoring pressure trace (P_3).

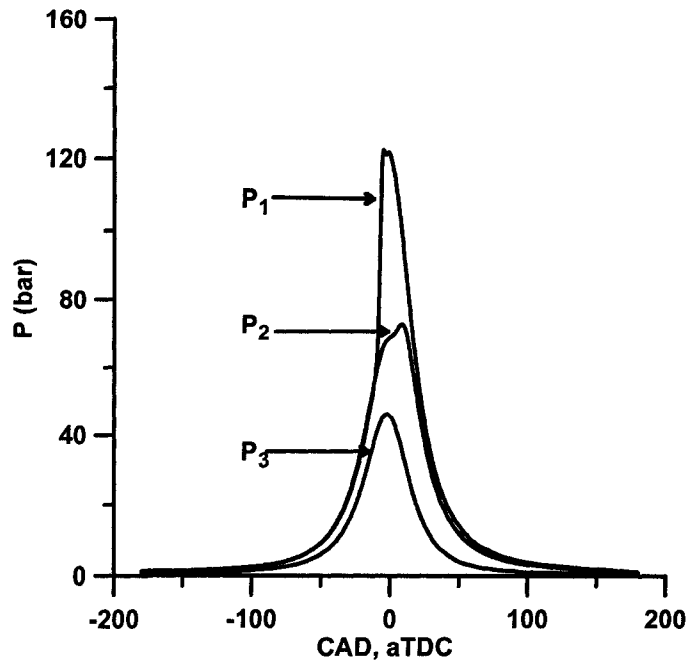


Figure 3.3: A comparison of pressure traces for operating points at boundaries, P_1 a knocking cycle, P_2 a misfiring cycle, and P_3 a motoring cycle, supercharged natural gas HCCI combustion, initial conditions indicated in Table 3.2

Maximum EGR Limit

Line 2-3 in Figure 3.2 defines the maximum EGR fraction of HCCI combustion. This line is defined by either maximum possible EGR fraction in which the combustion remains normal (cyclic variation below a certain limit) or by maximum achievable EGR at any certain operating condition. In this study, thermal effects of EGR was eliminated by keeping $T_{\text{intake,mix}}$ constant. At high EGR fractions, thermodynamic effects (higher heat capacity, lower ratio of specific heat in comparison with air) causes low after-compression temperature resulting in later less intense combustion. In addition, dilution effects of EGR reduces the chance of fuel molecules to intercept with oxidizer. All of these effects cause combustion inhibition even in the flameless HCCI combustion.

For the case of maximum EGR, increasing EGR fraction more than a certain levels narrows down the operating window to a single operating points that itself fluctuates between knock and misfiring boundaries. In fact, that certain EGR causes two lines of 1-2 and 3-4 crosses each other. At this situation, λ variation do not help to the engine operation. Changing the $T_{\text{intake,mix}}$ and/or CR can be helpful, but not useful for the current study.

The other type of EGR limit is dictated by fluid dynamics of the operation. As indicated in Figure 2.3, the EGR line connects the exhaust port to the engine manifold and EGR is driven by the fluid dynamics, which itself is a function of EGR valve (14 in Figure 2.3) position, exhaust back-pressure, intake manifold pressure, engine speed, and valve timing. At low speed of the CFR engine even at maximum EGR valve opening without exhaust back-pressure, the maximum attainable EGR fraction is limited.

Knock Limit

Line 3-4 in Figure 3.2 defines the knock boundary of the HCCI engine operation. HCCI combustion is characterized by rapid pressure rise. While rate of pressure rise in conventional combustion engines does not exceed 4-5

bar/CAD, HCCI combustion can easily produce a rate of pressure rise more than 10 bar/CAD. Moving toward the knocking boundary 3-4 in Figure 3.2, the rate of pressure rise increases. Defining a solid boundary similar to the one that is indicated in Figure 3.2 is arbitrary. This can be done by calculating knock frequency occurrence within the collected cycles by choosing a knock intensity parameter and certain knock limit. In this study, all operating points are indicated in plots, despite of various level of knock that they exhibit.

General Comments about the Operating Region

In this study all attainable operating points were considered for analysis because of limited nature of operating region. Hence, there are several high cyclic variation points and knocking points with various knocking intensities among the operational points that were indicated in the analysis. Although all these points were treated similar to normal operating points, if the knocking or partial burning/misfiring caused an especial situation, it has been mentioned and isolated from the normal points.

Several previous studies have been particularly focused on expanding the operating region of an HCCI engine using various techniques.

Urushihara et al (2003) [40] used various injection patterns in an HCCI direct injection gasoline engine to expand the operating region on the lean side. They found that injection of the fuel in negative valve overlap region can greatly widen the operating window.

Using a mechanical supercharger or a turbocharger Hyvönen et al (2003) [143] expanded the operating range of a VCR-HCCI engine on the high power side considerably.

Ogawa et al (2003) [32] used fuel chemistry alteration technique. With selective use of various fuels such as light naphtha and alcohol with various low-temperature oxidation properties, they expanded the operating range of an HCCI engine comparable to a naturally aspirated diesel engine.

AFR-EGR operating range of an HCCI engine with three distinct boundaries

Table 3.1: PRF fuel experimental matrix

Fuel	N (RPM)	T _{intake,mix} °C	CR
PRF0 (n-Heptane)	700	100	9.5/11.5
PRF20	700	100	11.5
PRF40	700	100	12.3
PRF60	700	140	14.4
PRF80	700	140	14.4
PRF100 (iso-Octane)	700	140	14.4/16.0

of knock, partial burn, and misfire was obtained using an improved probability density function model by Bhave et al (2005) [144]. The model used an excessive rate of pressure rise to identify the knocking points.

In 2007, Kuzuyama et al [145] used a combination of internal-external EGR and turbocharging to expand the operating region of an HCCI natural gas engine.

Ogawa et al (2007) [146] suggested that the combination a low octane number fuel with low compression ratio with direct injection of methanol can greatly expand the operating range of an HCCI engine.

Xu et al (2007) [147] summarized the major efforts in University of Birmingham to expand the operating range of the HCCI engine with partial fuel reforming on the lean side and external EGR and supercharging on the rich side.

CFR engine operating region at various combinations of the fuels, compression ratios, and intake mixture temperatures is indicated in Figure 3.4. Experimental points indicated in Figure 3.4 were obtained at N=700 RPM with various compression ratios and intake mixture temperature set points with and without partial reforming of the base fuel. The experimental matrix is indicated in Table 3.1.

As indicated in Figure 3.4 the general shape of the operating region is almost the same for all PRF fuels. These operating ranges are typical of HCCI combustion operating window. Each operating region starts at higher λ and decreases toward high EGR rates. The same trend was observed for operat-

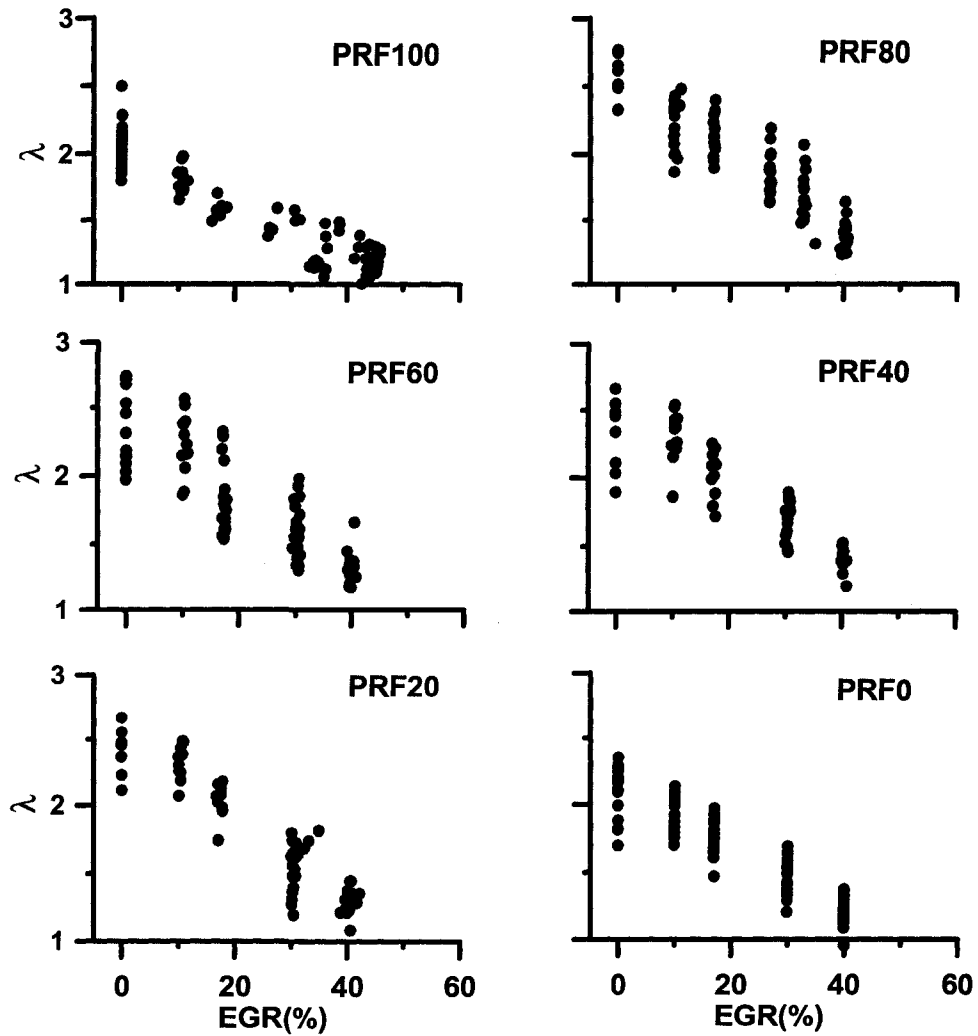


Figure 3.4: λ -EGR operating region with PRFs in the naturally aspirated mode, initial conditions indicated in Table 3.1

ing region of natural gas, n-Heptane (PRF0) and iso-Octane (PRF100) when operated in supercharged mode. Table 3.2 shows the experimental matrix for the cases of natural gas, n-Heptane, and iso-Octane HCCI combustion in the supercharged mode.

As a general representative of the operating region, the case of supercharged n-Heptane (middle plot on Figure 3.5) is magnified in Figure 3.2.

3.2 Influential Parameters' Effects on the Engine Operating Parameters and Combustion Characteristics

3.2.1 λ and EGR

Studies on λ and EGR Effects on HCCI Combustion

Effect of λ and EGR on HCCI combustion were discussed in several studies. EGR is an available combustion product and can be easily used and controlled. EGR dilution has been commercialized in both SI and CI engines mainly to decrease the combustion high temperature and to reduce the related NO_x emission. The maximum amount of EGR in conventional engines is restricted by the in-cylinder charge dilution limit dictated by flammability limits. These limits are much wider in an HCCI combustion engine.

In an HCCI engine, NO_x is naturally low and EGR has other applications. EGR decreases the peak cylinder pressure, and affects the ignition onset; hence, in an HCCI combustion engine, EGR is a diluent and a combustion controller. An HCCI engine can tolerate a high amount of EGR due to fast flameless combustion.

Hot EGR added to the intake replaces the air inducted into the cylinder; hence, λ is decreased. An intake mixture with a high EGR rate is richer than normal, but still is highly diluted. For example, for high EGR rates at Figure 3.2, λ values is near to stoichiometric, while the mixture is highly diluted with ex-

Table 3.2: Supercharged HCCI combustion engine experimental matrix

Fuel	N (RPM)	$T_{\text{intake,mix}}$ °C	CR
Natural gas	800	140	19.5
iso-Octane	800	100	14.4
n-Heptane	800	100	11.8

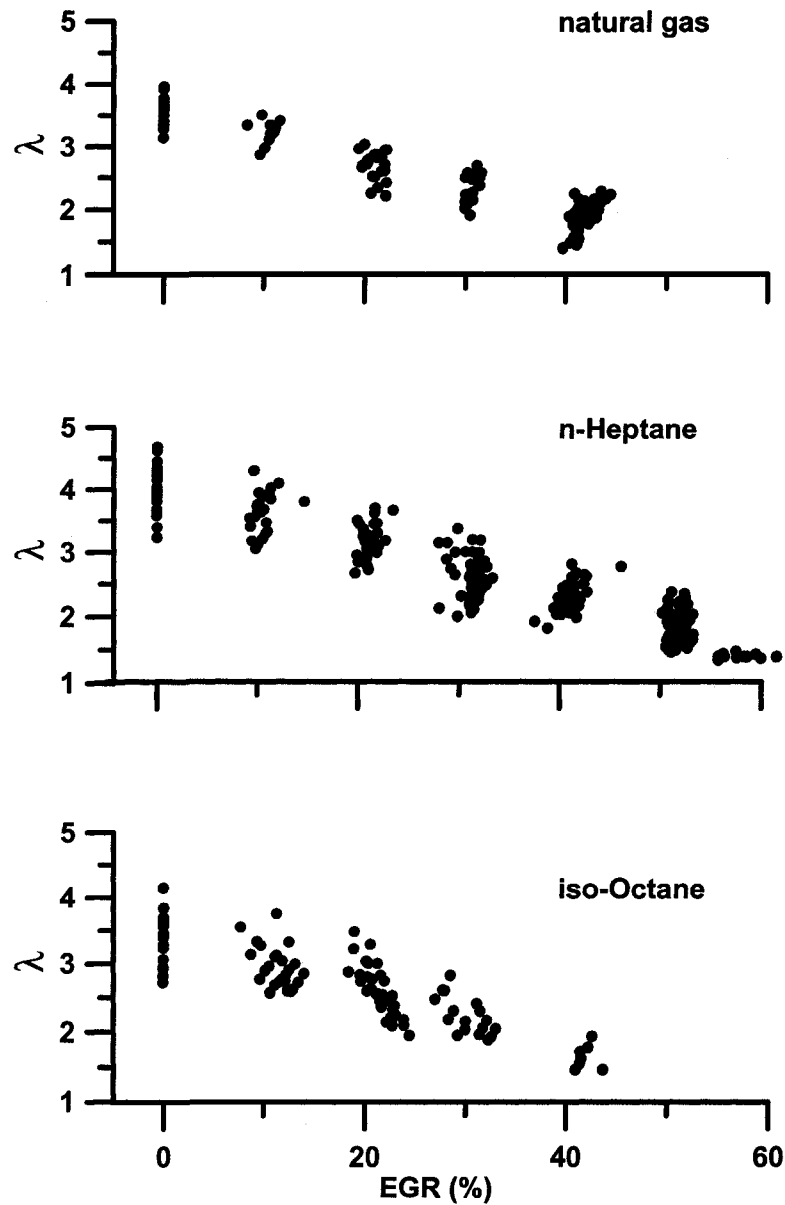


Figure 3.5: λ -EGR operating region with natural gas, n-Heptane and iso-Octane supercharged HCCI engine with and without partial reforming, initial conditions indicated in Table 3.2

ternal EGR. External or cold EGR is the type of EGR that enrouted directly from the exhaust system to the intake plenum. Most of EGR studies of HCCI

combustion used external EGR.

EGR contains tri-atomic molecules, H_2O and CO_2 ; hence, heat capacity is higher and ratio of specific heats (γ) is lower than that of the air, consequently the after-compression temperature is lower. The lower after-compression temperature directly affects the combustion timing in an HCCI engine, it tends to retard the ignition as mentioned by Olsson et al (2003) [148]. Some studies show slight dependency of SOC on the EGR rate (see Oakley et al (2001) [36]). EGR increases burn duration; hence, smoother and quieter operation is achieved. Several studies have reported that a lower peak pressure extended the high load operation limits of the HCCI engine. A numerical study investigated how each effect of EGR changes the operation parameters (see Zhao et al (2001) [30, 149]). The study identified five different effects of EGR: the charge heating effect, dilution effect, heat capacity effect, chemical effect, and stratification effect. It concluded that the charge heating effect advanced the autoignition, increased the heat-release rate, and shortened the combustion duration. The dilution effect was not responsible for phasing the autoignition, but extended the combustion duration and reduced the heat-release rate. The heat capacity effect, like the dilution effect, extended the burn duration. The chemical effect just slightly reduced the combustion duration at high EGR rates.

When EGR is used, no change in combustion efficiency has been reported by Morimoto et al (2001) [150], because the absolute combustion speed is fast enough to compensate the dilution effect. EGR does not have a major effect on pumping loss and in an acceptable operating range, slightly increases CO and HC emissions. Usually EGR has a maximum fraction limit. Beyond this limit, dilution effects and low concentration of O_2 in the charge, cause unstable combustion, misfiring, and a high amount of HC and CO emissions (e.g. line 2-3 in Figure 3.2).

Hot or internal EGR (IEGR) is the trapped residual of combustion in the cylinder. A 2-stroke engine has a higher amount of trapped residuals because

of poor scavenging process. HCCI first implemented in a 2-stroke engine by Onishi et al (1979) [11]. In a 4-stroke engine, different mechanisms create IEGR. Hot residual gases can be kept in a cylinder by relatively early closing of the exhaust valve. Re-opening the exhaust valve on the next intake stroke can create re-breathing of the hot exhaust gases from the exhaust manifold. Both methods have similar effects on the HCCI combustion's parameters as mentioned by Law et al (2000) [21].

IEGR's thermal effects on the next cycle's mixture is effective on combustion timing and characteristics (see Au et al (2001) [22]). When the chemical and dilution effects of IEGR and external EGR are the same, the former has more exaggerated thermal effects than the latter. IEGR's significantly higher temperature reduces the dependency of stable HCCI combustion on a high intake temperature, and such combustion is possible even with no intake heating (For example, see Hiraya et al (2002) [151]). This feature makes HCCI combustion more attractive for practical use.

The use of IEGR significantly improves combustion stability as mentioned by Law et al (2000) [21]. IEGR decreases the peak cylinder pressure, decreases the maximum rate of pressure rise, reduces combustion duration, retards ignition onset, and reduces NO_x emissions (see Zhao et al (2002) [152]). However, IEGR also increases CO and HC emissions and fuel consumption. IEGR significantly expands the HCCI engine's operating region. With a lower compression ratio or higher engine speed, more IEGR is necessary for stable combustion (see Hiraya et al (2002) [151]).

Some studies have used cooled EGR to eliminate EGR's thermal effects and to examine its dilution effects on HCCI combustion. The use of cooled EGR was found to slow down combustion, lower the peak pressure, and more expand the high limit of operation (see Morimoto et al (2001) [150]). One reason for using cooled EGR is to keep the density of the charge inducted in the cylinder as high as possible (see Christensen et al (2000) [27]). Cooled EGR can also be used in turbocharged or supercharged HCCI, in which an EGR line must be

connected to the intake system before the compressor. Hot EGR can damage the compressor.

When the combustion process is controlled by chemical kinetics, and the effects of turbulent and mixing are minimized, and the combustion process is naturally initiated, the mixture's quality is the most influential parameter on combustion. Because of the HCCI engine's un-throttled operation, λ can be directly altered by the fuel injection rate, and indirectly by the EGR, intake temperature changes, and intake pressure adjustment. As combustion initiates at many sites in the cylinder simultaneously, and the combustion rate is higher than that in conventional engines, an HCCI engine tolerates much higher dilution. On the other hand, due to the self-ignition nature of HCCI combustion, a lower amount of λ is restricted to near to stoichiometric at high loads, and no richer mixture can be used. An HCCI engine's operating region is much narrower near to a stoichiometric mixture and wider at leaner mixtures (see Figure 3.2).

Beyond its function as a load controller similar to that in a conventional engine, λ plays another important role – combustion phasing – in an HCCI engine. As the combustion in conventional engines is forced by injection or spark timing, the mixture quality is not as important as it is in the HCCI mode for combustion phasing. Enriching the mixture decreases the ratio of the specific heats (γ), and thus reduces the amount of disposable compression heating in the charge. Consequently, the mixture has to be compressed further to reach the ignition temperature. The ignition timing is therefore delayed as mentioned by Milevanovic and Chen (2001) [42] and Hiraya et al (2002) [151].

Burn duration increases with larger λ increases [153, 154]. NO_x has a peak when a stoichiometric mixture is used, but is still low enough not to be counted (see Li et al (2001) [155]). These results are the same as EGR's dilution effects. Lower fuel consumption – a result of an HCCI engine's ability to operate with a higher λ - is considered to be a valuable gain. However, the results of studies show that operation more near to the stoichiometric condition is more efficient

and produces lower CO and HC emissions, but HCCI engines usually operate at a high level of EGR, which is still a diluted mixture.

Effect of λ and EGR on Combustion Timing, Combustion Duration, and Pressure Characteristics

As described earlier, combustion timing was calculated using a single zone well stirred model with air as the working fluid using experimental pressure trace. Figure 3.6 indicates the combined effect of λ and EGR on SOC for the case of naturally aspirated PRF HCCI combustion.

SOC was defined in the current study (See Figure 2.13-b) such that low temperature heat release was included in SOC calculation. This effect is more considerable at low octane PRFs when LTR is more strong. During current study, the LTR_{max} never exceeded 5% of HTR_{max} ; hence, calculated SOC was insensitive to LTR timing.

Both λ and EGR affected SOC considerably with greater effect belonging to EGR. Increasing EGR fraction and/or increasing λ retarded combustion timing. Increase λ by 1 unit in all PRF cases, retarded combustion timing by an average of 5 CAD. The same trend was observed for supercharged cases with a very early combustion timing for n-Heptane case, as indicated in Figure 3.7. In supercharged cases, natural gas exhibited the latest combustion timing with SOC dependent to both λ and EGR, which was less sensitive to λ at low EGR rates. At high EGR rates for natural gas supercharged HCCI combustion, SOC was highly sensitive to λ . Sensitivity of SOC to λ increased from 4.8 CAD for 1 unit of λ in EGR=0% to 24.6 CAD for 1 unit of λ at EGR =40%. In average, increasing λ by 1 unit, retarded natural gas HCCI combustion by about 10 CAD. The same observation was made for iso-Octane supercharged HCCI combustion timing. Sensitivity of SOC to λ increased from 2.0 CAD for 1 unit of λ at EGR=0% to 16.3 CAD for 1 unit of λ at EGR =50%. In average, increasing λ by 1 unit retarded iso-Octane HCCI combustion by more than 5 CAD. For n-Heptane case SOC was insensitive to λ for all EGR cases. EGR

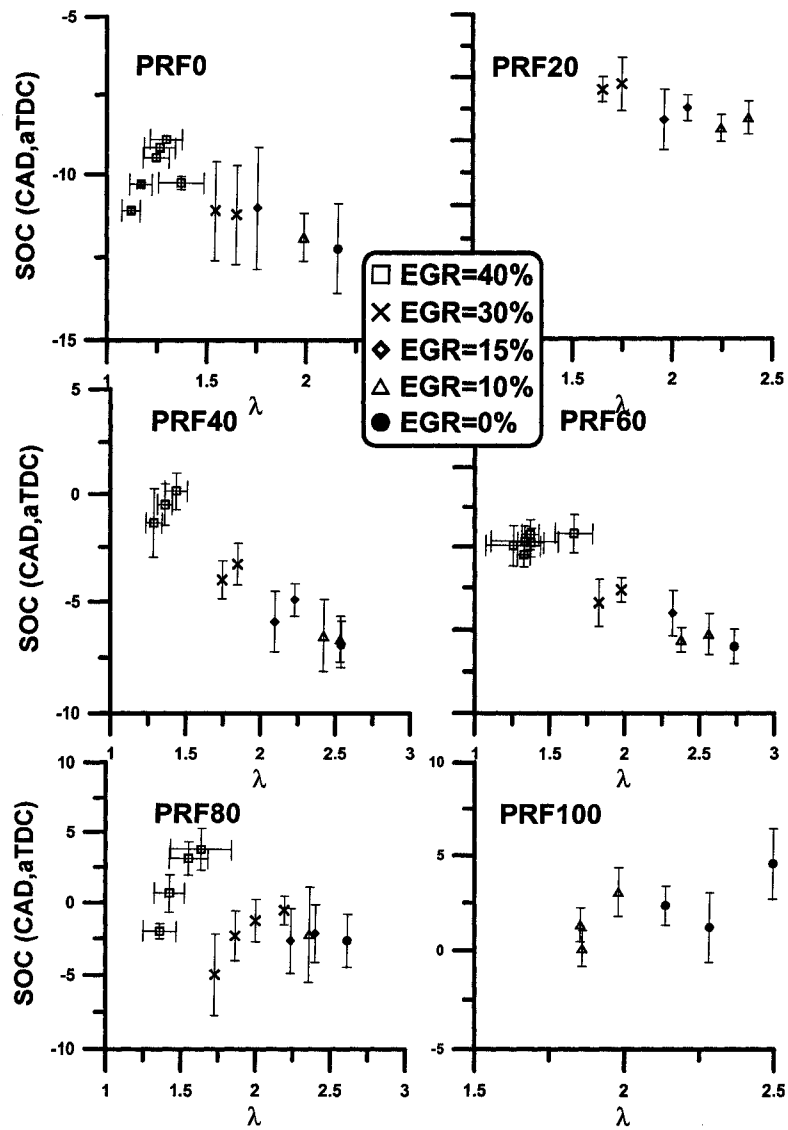


Figure 3.6: Effect of λ and EGR on combustion timing (SOC), HCCI combustion of PRFs in CFR engine, Experimental matrix indicated in Table 3.1, error bars indicate $\pm 2\sigma_{n-1}$

also showed no effect on SOC on low EGR fractions. At high EGR fractions, increasing EGR by 10% retarded SOC by 5 CAD.

Combustion duration (CD) was defined as the required crank angle rotation to complete from 10% to 90% of gross accumulative heat release. Fast HCCI

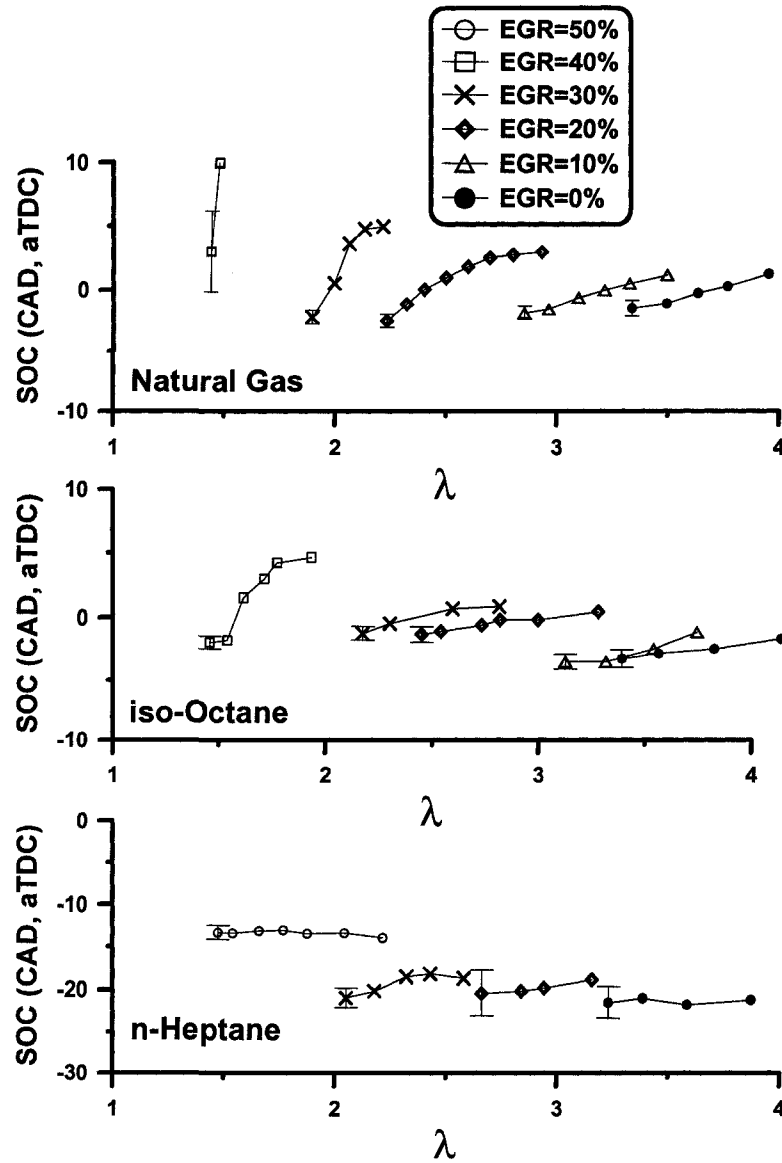


Figure 3.7: Effect of λ and EGR on start of combustion (SOC), Supercharged n-Heptane, iso-Octane, and natural gas HCCI combustion, initial conditions indicated in Table 3.2, error bars indicate $\pm 2\sigma_{n-1}$

combustion was observed for all PRFs with total combustion duration less than 5 CAD for most of the operating points. EGR did change CD considerably. CD increased by increasing λ as indicated in Figure 3.8 for PRFs and

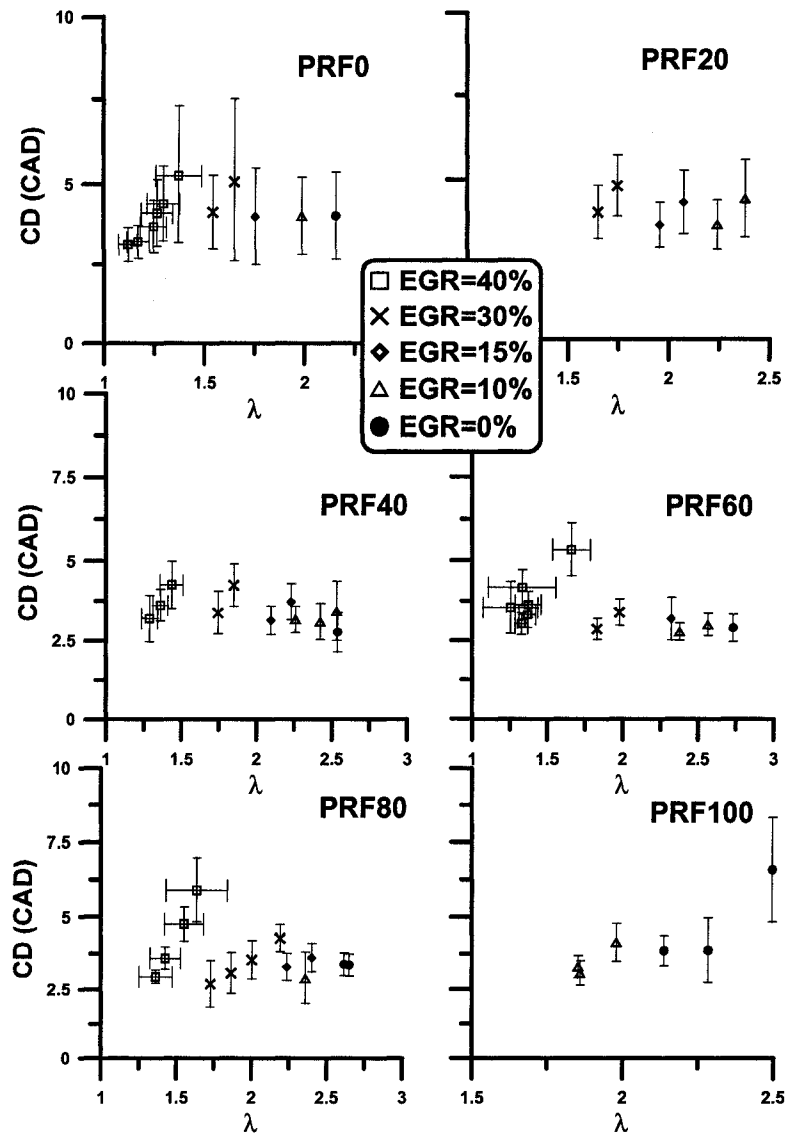


Figure 3.8: Effect of λ and EGR on combustion duration (CD), initial conditions indicated in Table 3.1, error bars indicate $\pm 2\sigma_{n-1}$

in Figure 3.9 for supercharged HCCI combustion. Increase in λ by 1 unit, increased combustion duration by an average value of 8 CAD for PRF case. Combustion duration for supercharged cases also showed the same trend. For the case of natural gas, combustion duration was longer than that of expected

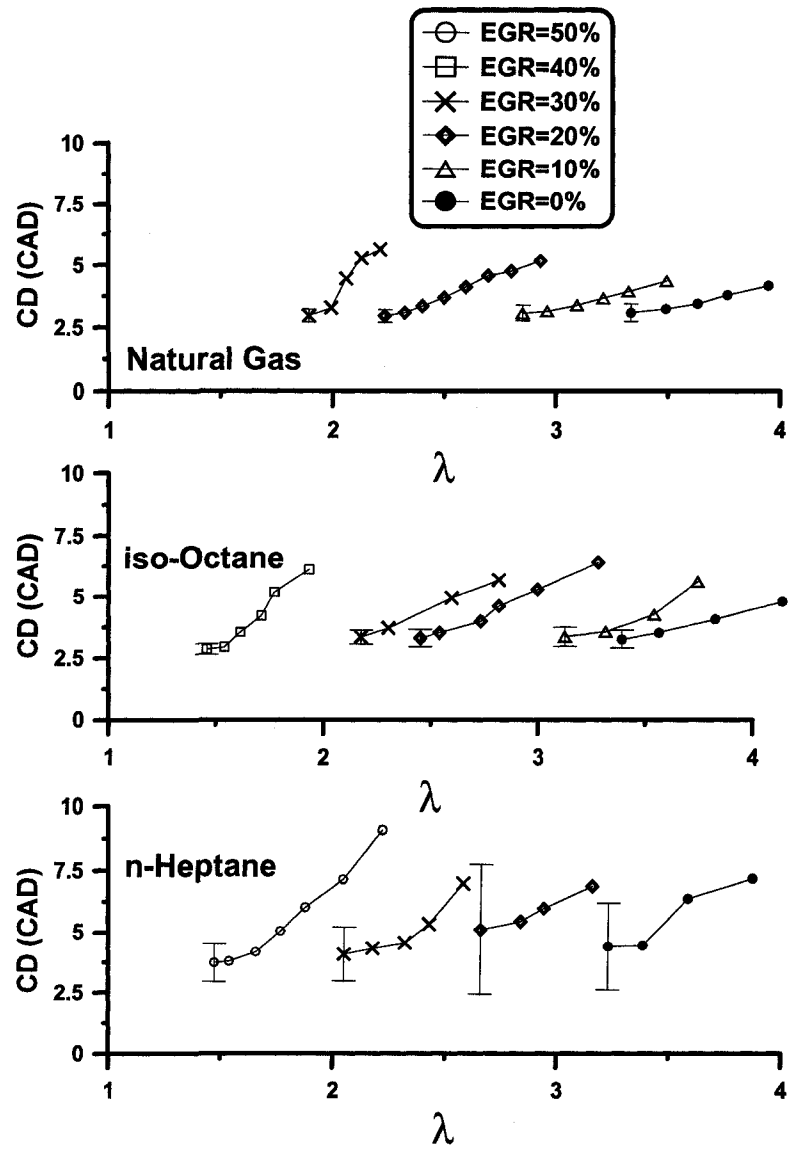


Figure 3.9: Effect of λ and EGR on combustion duration (CD), Supercharged HCCI combustion of natural gas, n-Heptane and iso-Octane, initial conditions indicated in Table 3.2, error bars indicate $\pm 2\sigma_{n-1}$

from a normal natural gas HCCI combustion because of the operation in the low power region. Increasing λ by 1 unit increased CD by an average of 4 CAD for supercharged cases. For the case of n-Heptane, low-temperature heat re-

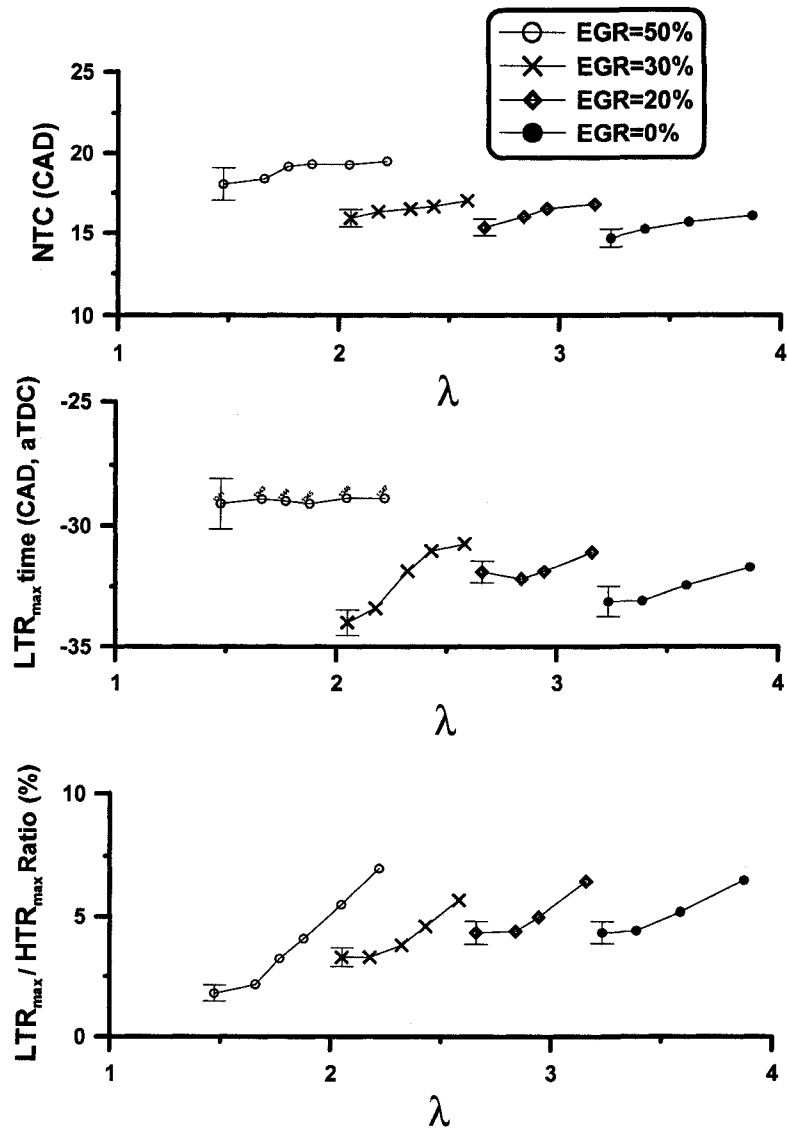


Figure 3.10: Effect of λ and EGR on low negative temperature coefficient (NTC), low-temperature reaction timing (LTR_{max}) and the ratio of low-temperature to high-temperature reaction that were defined in Figure 2.13, Supercharged n-Heptane HCCI combustion, initial conditions indicated in Table 3.2, error bars indicate $\pm 2\sigma_{n-1}$

least characteristics variation by λ and EGR is indicated in Figure 3.10.

EGR appeared to be ineffective on NTC, $LTR_{max,time}$, and LTR/HTR -Ratio.

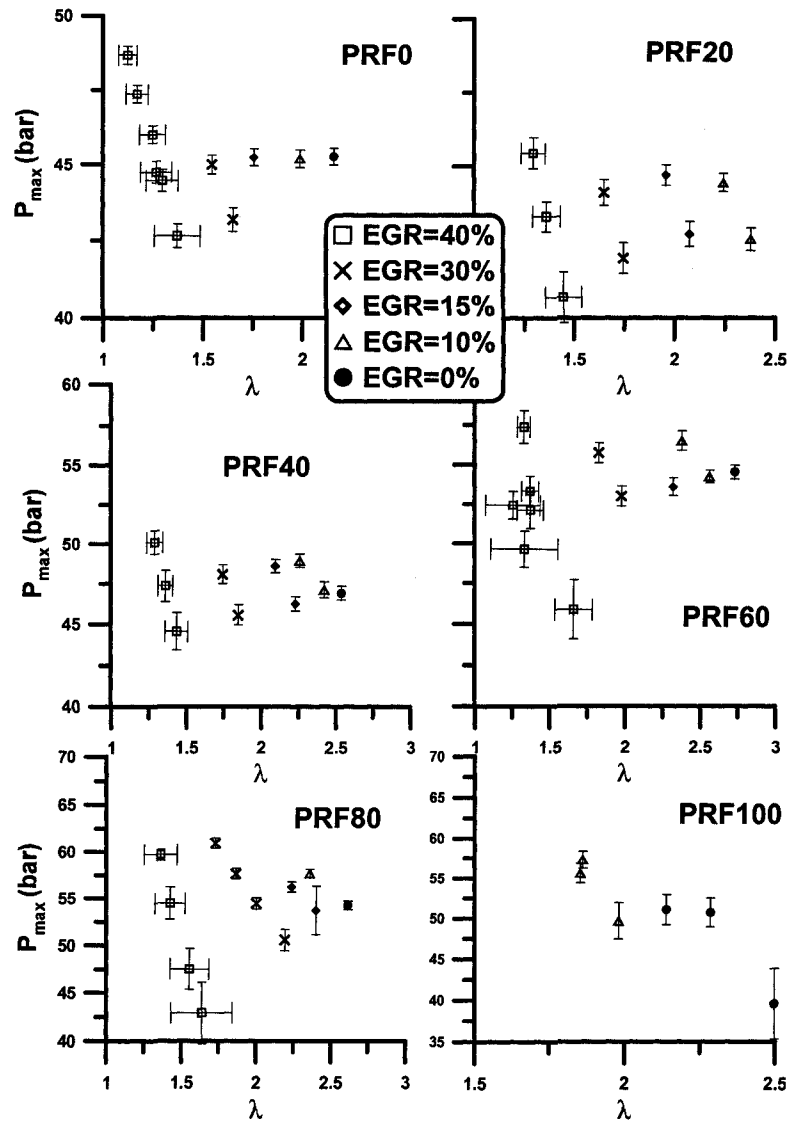


Figure 3.11: Effect of λ and EGR on cylinder maximum pressure P_{max} , initial conditions indicated in Table 3.1, error bars indicate $\pm 2\sigma_{n-1}$

λ also did not show significant effect on NTC and $LTR_{max,time}$, but it effectively changed LTR/HTR-Ratio. Increasing λ by 1 unit, increased LTR/HTR-Ratio by an average of more than 5%.

Combustion knock intensity also was affected by λ and EGR. Details of effects

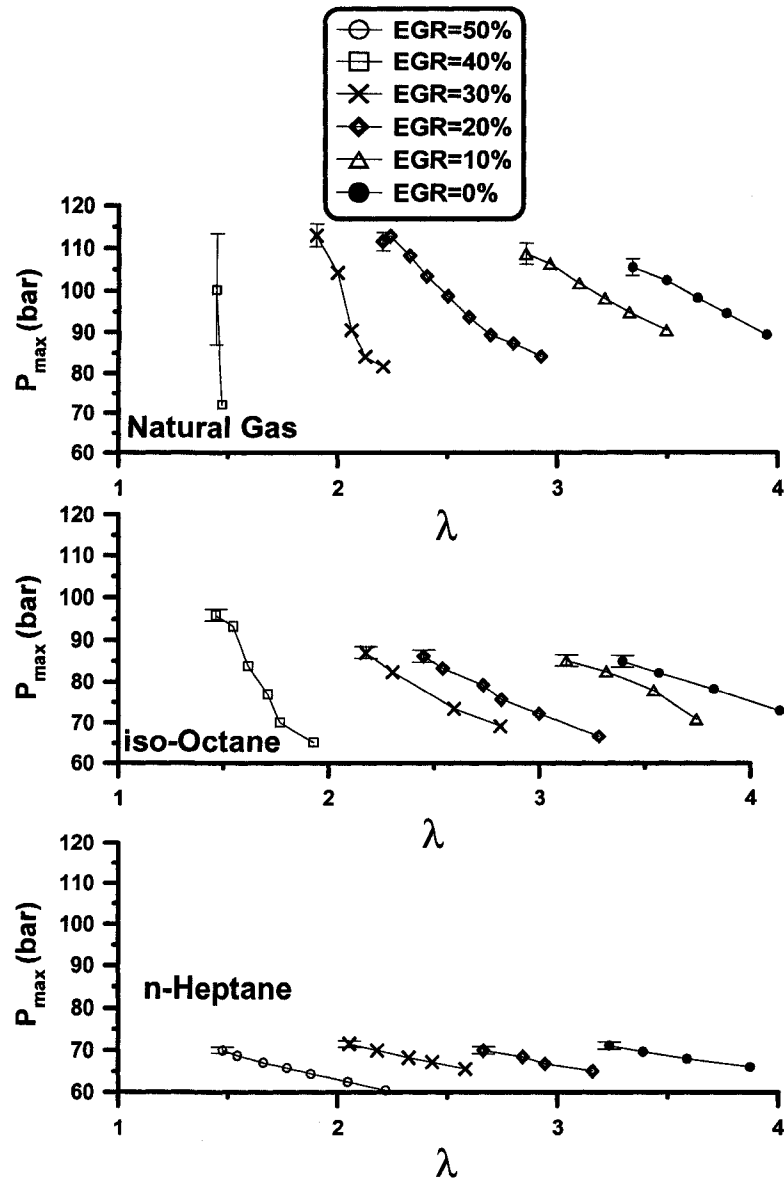


Figure 3.12: Effect of λ and EGR on maximum cylinder pressure - P_{max} - Supercharged HCCI combustion of natural gas, n-Heptane and iso-Octane, initial conditions indicated in Table 3.2, error bars indicate $\pm 2\sigma_{n-1}$

of λ and EGR on combustion intensity is presented in Appendix H (see section H.2).

P_{max} is a determining factor for the engine structural design. Normally diesel

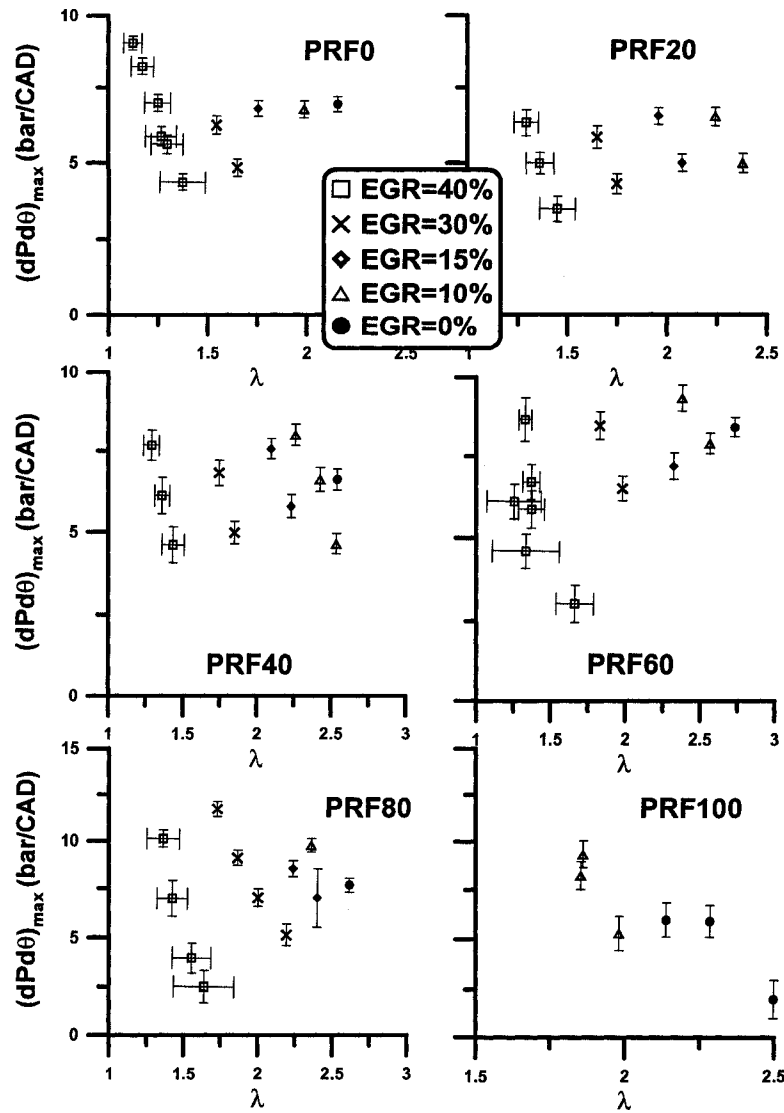


Figure 3.13: Effect of λ and EGR on cylinder maximum pressure rate $(dP/d\theta)_{max}$, initial conditions indicated in Table 3.1, error bars indicate $\pm 2\sigma_{n-1}$

engines operate at higher CR and P_{max} is higher than that of gasoline engine. P_{max} in HCCI combustion engine is higher than that of conventional engines because of the high rate of pressure rise. Sudden multi-site combustion of air/fuel mixture at relatively high CR and high $T_{intake,mix}$ causes high P_{max} ,

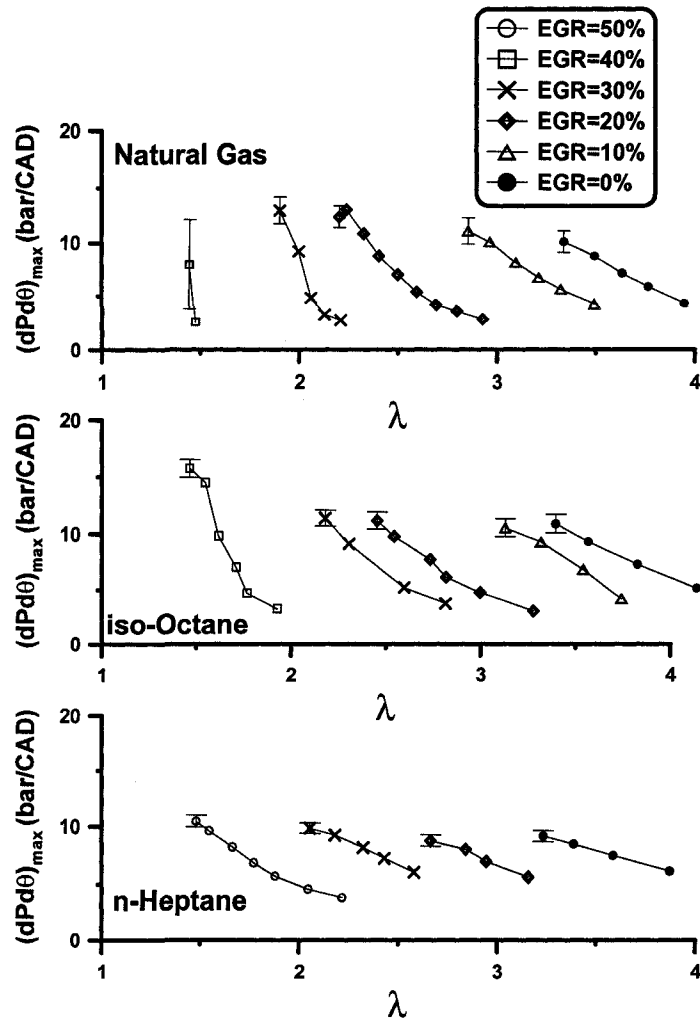


Figure 3.14: Effect of λ and EGR on cylinder maximum pressure rate $(dP/d\theta)_{max}$, Supercharged HCCI combustion of natural gas, n-Heptane and iso-Octane, initial conditions indicated in Table 3.2, error bars indicate $\pm 2\sigma_{n-1}$

which is a limiting factor for HCCI combustion engine applications.

P_{max} is a strong function of CR, EGR, and λ as indicated in Figure 3.11 and Figure 3.12 and was reduced by increasing λ and EGR. The average P_{max} in Figure 3.11 increased by increasing octane number of fuel because of using

higher CR for higher octane PRFs. Increasing EGR considerably decreased P_{\max} at any given constant λ with slower combustion. Increasing λ also decreased P_{\max} . 1 Unit of increase in λ reduced P_{\max} by an average of 25 bar for PRFs in the naturally aspirated mode. In the supercharged mode in Figure 3.12, for natural gas case, P_{\max} is higher than that of iso-Octane or n-Heptane cases because of higher CR and $T_{\text{intake,mix}}$. This was a limiting factor for moving the operation region of natural gas toward higher power operation. Increasing λ by 1 unit, reduced P_{\max} for natural gas HCCI combustion by an average of 30 bar, for iso-Octane HCCI combustion by an average of 25 bar, and for n-Heptane case by an average of 10 bar.

Figure 3.13 and 3.14 show the effects of λ and EGR on $(dP/d\theta)_{\max}$. Increasing λ by 1 unit, reduced $(dP/d\theta)_{\max}$ by an average of 15 bar/CAD for PRF HCCI combustion in the naturally aspirated mode. It also reduced $(dP/d\theta)_{\max}$ for natural gas HCCI combustion by 15 bar/CAD, for iso-Octane HCCI combustion by 9.5 bar/CAD, and for n-Heptane HCCI combustion by 7 bar/CAD.

Effect of λ and EGR on Power and Efficiency

The combination of λ and EGR determines the power output of an HCCI engine. Figure 3.15 indicates the indicated power of the HCCI engine using PRF fuels with experimental matrix indicated in Table 3.1.

Figure 3.15 indicates that despite of replacing some of the intake air by EGR, IMEP was increased considerably. The highest IMEP was achieved for each PRF fuel at maximum EGR fraction and minimum λ . This finding is similar to what Oakley et al [36] reported. Increasing EGR shifted the operating region (See Figure 3.4) toward richer intake mixture such that λ at maximum EGR was almost stoichiometric for all PRF fuels tested.

At any constant EGR rate for all PRFs, increasing λ decreased indicated power due to the energy content reduction inside the cylinder. Increasing λ by 1 unit, reduced IMEP by an average of 2.1 bar. This is a considerable power reduction considering the fact that internal friction in the CFR engine is more

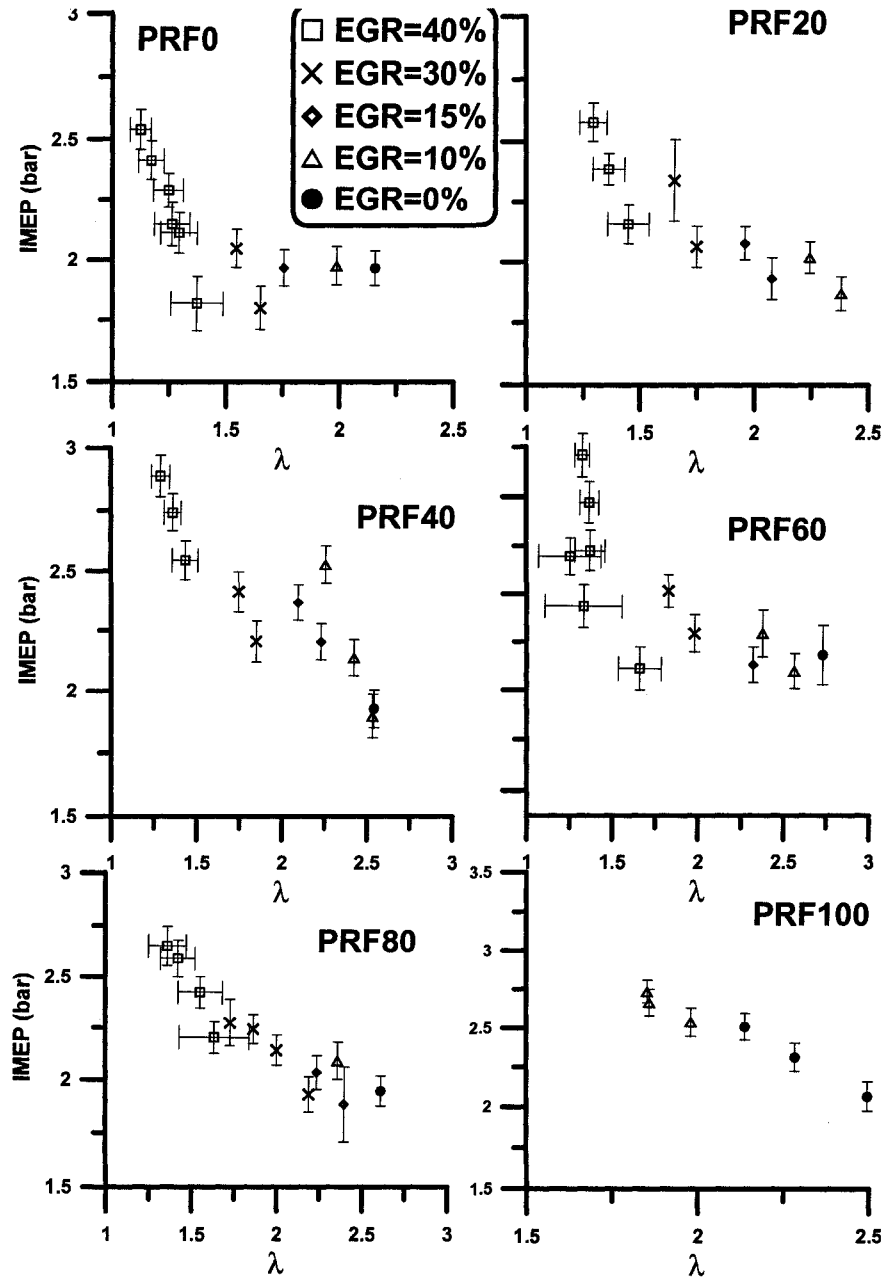


Figure 3.15: Effect of λ and EGR on indicated power, initial conditions indicated in Table 3.1, error bars indicate $\pm 2\sigma_{n-1}$

than 2 bar for most cases. In addition to use low octane PRFs, EGR fraction

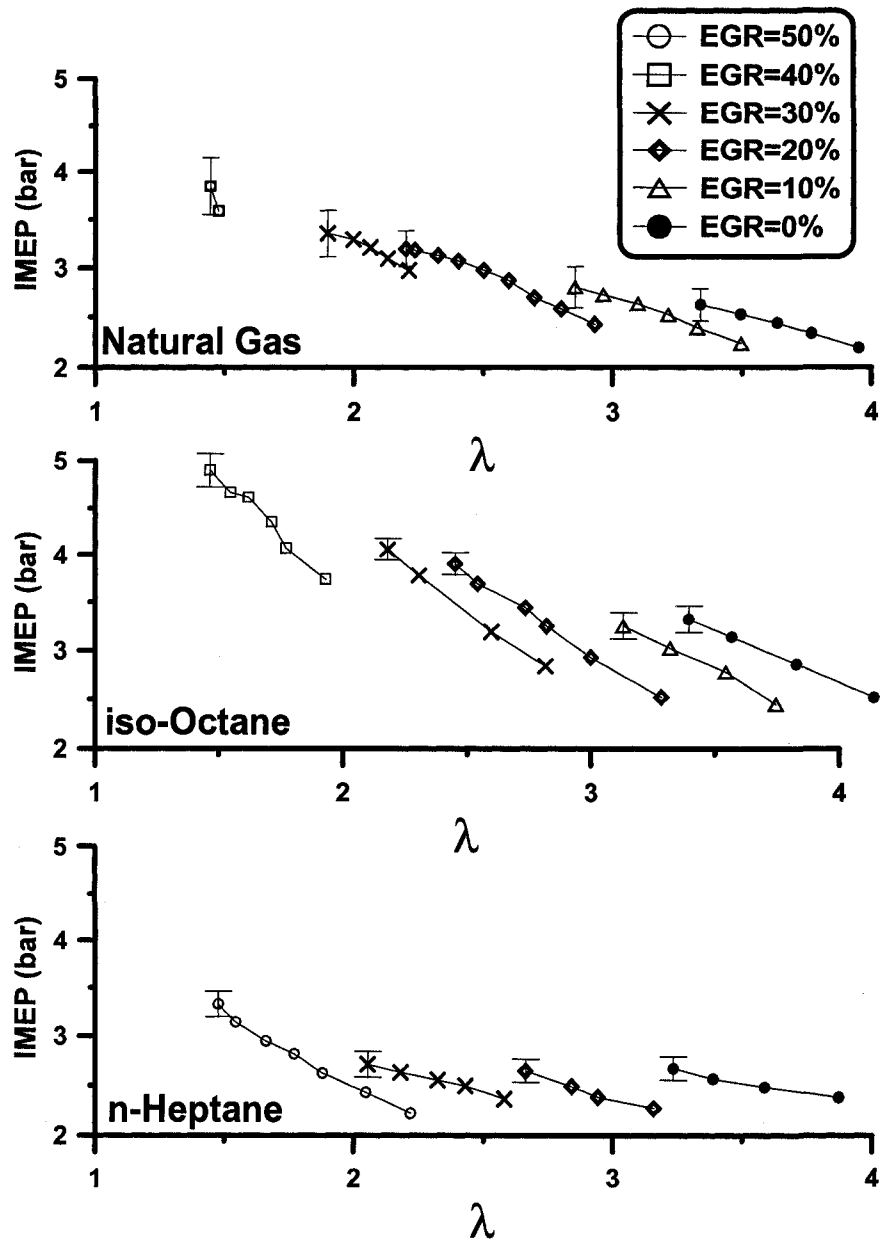


Figure 3.16: Effect of λ and EGR on indicated power, Supercharged natural gas, n-Heptane, and iso-Octane HCCI combustion, initial conditions indicated in Table 3.2, error bars indicate $\pm 2\sigma_{n-1}$

increase increases the indicated power with distinct steps, while at high octane

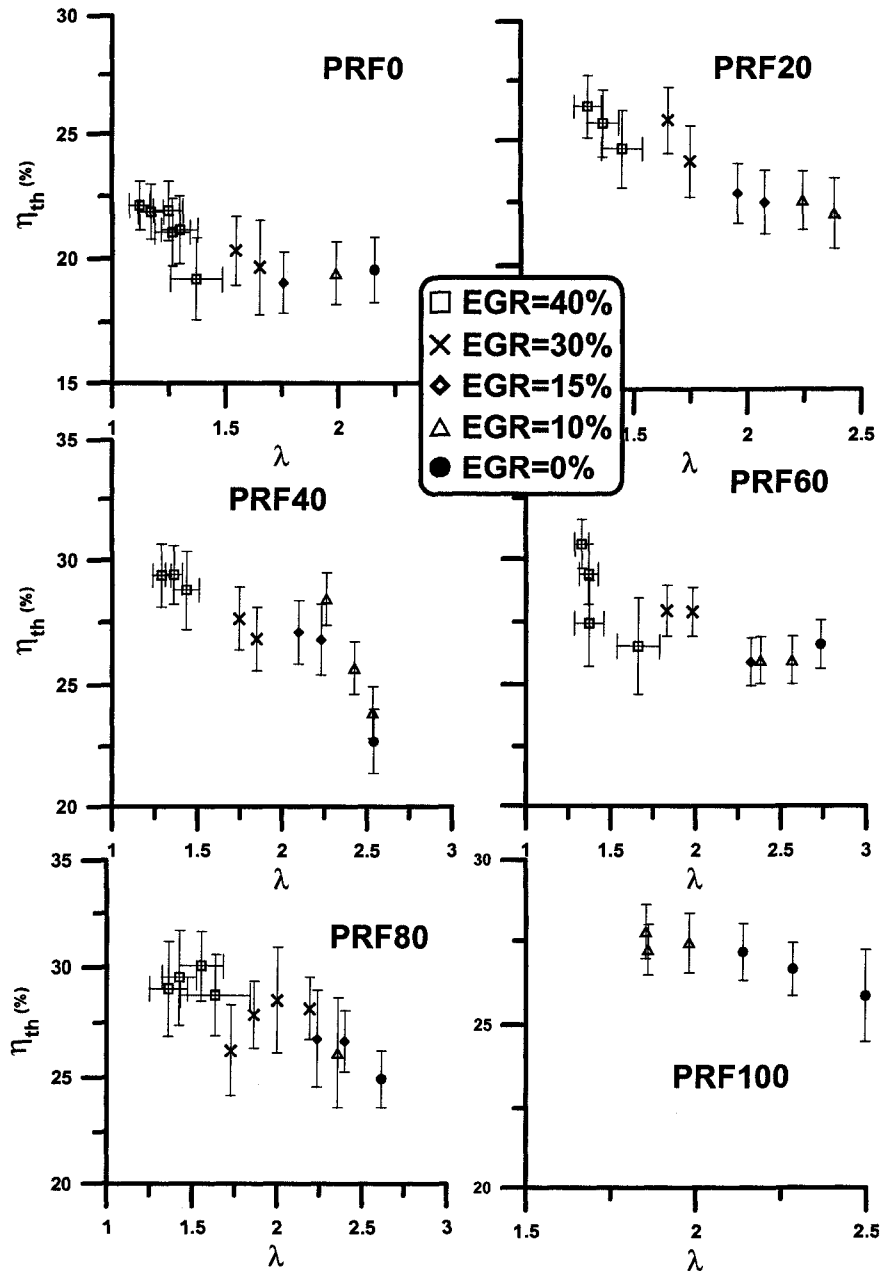


Figure 3.17: Effect of λ and EGR on indicated thermal efficiency, initial conditions indicated in Table 3.1, error bars indicate $\pm 2\sigma_{n-1}$

PRF fuels the EGR fraction lines collapsed on one single trend and it seemed

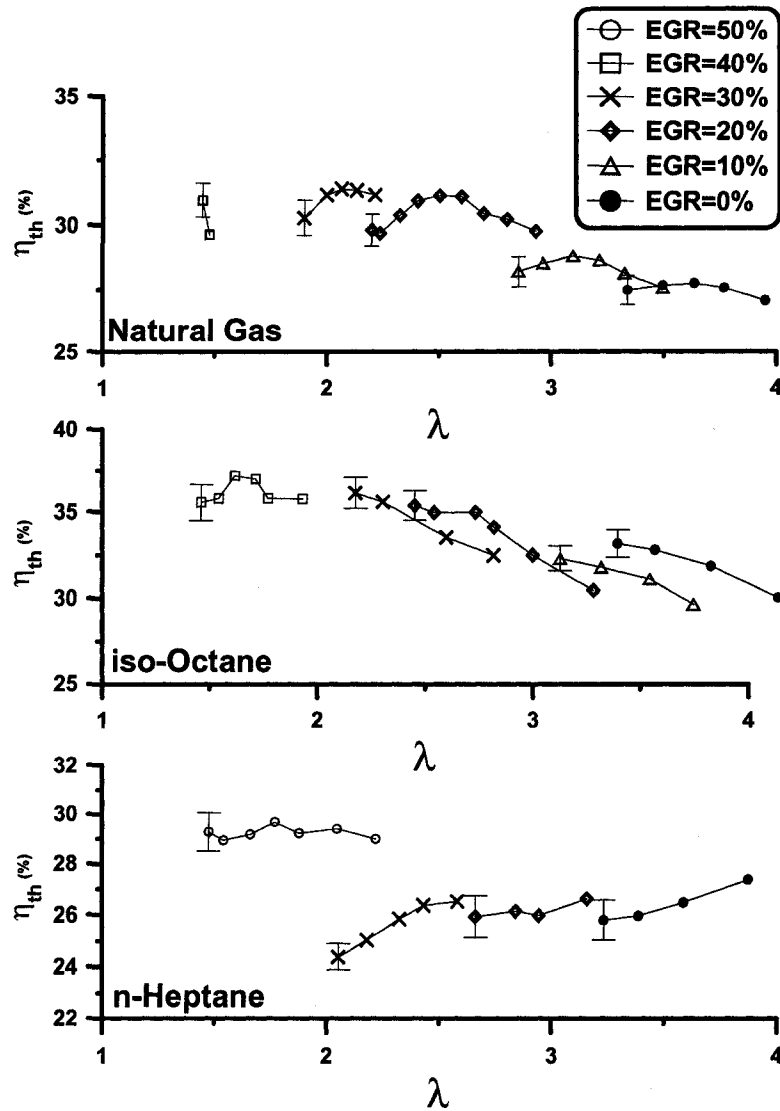


Figure 3.18: Effect of λ and EGR on indicated power, Supercharged HCCI combustion of natural gas, n-Heptane and iso-Octane, initial conditions indicated in Table 3.2, error bars indicate $\pm 2\sigma_{n-1}$

that indicated power is independent from EGR possibly because of extreme $T_{intake,mix}$ and CR at high octane PRFs.

The same observation was made for the supercharged HCCI combustion cases as indicated in Figure 3.16. Increasing λ decreased IMEP by more than 1.5

bar. Figure 3.16 indicates the reduction of indicated power by increasing λ and/or EGR and achieving maximum power possible at maximum EGR rate. In fact, keeping λ constant and increasing EGR would reduce the indicated power, but increasing EGR to achieve lower λ increased indicated power. Higher indicated power was associated with higher thermal efficiency as indicated in Figure 3.17 for PRF cases. The indicated thermal efficiency for all PRFs shown in Figure 3.17 was less than that of reported by other studies. As mentioned before, HCCI combustion in the CFR engine was not optimized for thermal efficiency. A proper combination of $T_{\text{intake,mix}}$, CR, and speed could increase the thermal efficiency to a higher level.

While indicated power was a function of EGR and λ at low PRFs, it was observed that indicated thermal efficiency (η_{th}) was directly a function of λ and independent from EGR. The required energy to increase the $T_{\text{intake,mix}}$ using an electrical heater was not considered for η_{th} calculation. η_{th} was found maximum near the knock boundary and minimum near the low load boundary. For all cases of natural gas, n-Heptane, and iso-Octane thermal efficiency was a strong function of λ and EGR. While maximum thermal efficiencies were achieved at maximum EGR rates for all fuels, on constant EGR lines, thermal efficiency trends behaved differently for each fuel. Further analysis of effect of λ and EGR on emissions and combustion efficiency are summarized in Appendix H (see section H.1).

Discussion on Combined Effect of λ and EGR on HCCI Combustion

EGR was applied externally; hence, the EGR temperature varied based on the exhaust temperature and EGR flow rate. (The higher the EGR flow rate, the higher the EGR temperature, because of considerable heat transfer in the long un-insulated EGR line.) In this study:

- As $T_{\text{intake,mix}}$ was kept constant, thermal effects of EGR on HCCI combustion was minimized. Any variation in EGR temperature was compensated by adjustment in after-heater air temperature automatically to

achieve constant $T_{\text{intake,mix}}$.

- In the naturally aspirated mode, increasing EGR replaced more of the intake air, so the mixture became rich. If there was a need to keep λ constant, the fuel flow rate was adjusted accordingly by decreasing fuel injector pulse width.
- In the supercharged mode, as the intake was supercharged by pressurizing (and not by an actual supercharger) the increase EGR alteration was done by exhaust back-pressure adjustment while the butterfly manual EGR valve was kept wide open. At constant intake boost pressure, adjusting exhaust back-pressure altered the EGR fraction.
- The operating range for most of the conditions during this study was limited such that conducting test points at constant λ while varying EGR was mostly impossible. Hence all presented figures indicate constant EGR lines and not constant λ lines.

The differences between EGR and λ adjustment technique in this study in comparison with previous studies explains the differences between results and observations.

Although testing the engine at constant λ lines was impossible as discussed, a virtual constant λ line can be considered to discuss the sole effect of EGR on HCCI combustion base-line tests. Among five EGR effects that were mentioned by Zhao et al (2001) [30], charge heating effect and stratification effect are negligible in this study as $T_{\text{intake,mix}}$ was kept constant in all operating points, and EGR was introduced in the intake plenum before the fuel injector, and well before the intake valve. At low CFR engine speed, a well mixed intake mixture at constant $T_{\text{intake,mix}}$ was expected. The other effects are dilution effect, heat capacity effect, and chemical effect.

A special case of the virtual λ constant line with EGR fraction increase is considered. In this case, air/fuel ratio was constant as EGR increased but

total in-cylinder energy content was reduced. In addition, replacing the air (mostly bi-atomic N_2) with EGR (tri-atomic H_2O and CO_2) increased heat capacity (C_p), decreased ratio of specific heat (γ); and hence, decreased after-compression temperature. As mentioned thermal effect was excluded so there was not any charge heating with EGR.

IMEP was decreased at any constant λ line because of lowering in-cylinder chemical energy as indicated in Figures 3.15 and 3.16. At the same time increasing λ at each constant EGR decreased IMEP for all fuels and operating conditions. However, thermal efficiency (η_{th}) did not behave the same way as IMEP on constant EGR lines. Reducing thermal efficiency on these constant EGR lines was a result of lowering combustion efficiency (See Figures H.5 and H.6) because of increasing HC and CO emissions (See Figures H.1, and H.2). For the case of natural gas and n-Heptane, although combustion efficiency and HC and CO emissions were behaved the same way as other fuels, increasing λ first increased and then decreased thermal efficiency in natural gas case and did not have significant effect or slightly increased thermal efficiency in n-Heptane case as indicated in thermal efficiency plot of supercharged cases in Figure 3.18. This can be described by looking at combustion timing (SOC) and combustion duration in Figures 3.7 and 3.9.

Increasing λ at any constant EGR line retarded combustion timing of natural gas supercharged HCCI combustion considerably and prolonged combustion timing. An optimum combustion timing happened at the mid range for each case. Too early combustion resulted in compression of combustion product, fast rate of heat release, high rate of heat transfer and releasing most of the chemical energy in compression stroke. Too late combustion also resulted in efficiency penalty. The optimum combustion timing resulted in an optimum thermal efficiency for the case of supercharged natural gas cases.

For n-Heptane case however, λ variation did not change the combustion timing at any constant EGR line. EGR was a dominant factor over λ for combustion timing control and as the EGR thermal effects were excluded a retardation of

combustion timing was observed because of EGR dilution effect. In this case, prolongation of combustion duration (CD) at any constant EGR rates while start of combustion (SOC) was constant caused an increase in efficiency by increasing λ . To summarize effect of λ and EGR on HCCI combustion timing:

- For most of the operating points combination of λ and EGR can effectively control combustion timing with the drawback of power and efficiency variation
- For most cases higher EGR fraction and higher λ values resulted in lower IMEP and thermal efficiency, and higher HC and CO emissions, smoother combustion (i.e. lower P_{\max} and $(dP/d\theta)_{\max}$).
- For specific cases of natural gas and n-Heptane HCCI combustion in this study, SOC and CD were determining factors on combustion efficiency. A combination of optimum SOC and CD produced the maximum thermal efficiency. Other effects were observed the same. Higher EGR and λ produced less abrupt combustion with smoother heat release.

3.2.2 Intake and Exhaust Pressure

HCCI combustion in the CFR engine exhibited a narrow operating range. Hence intake supercharging and exhaust back pressurizing were considered the way to obtain wider operating range while maintaining the EGR level. Supercharging equipments were discussed in Chapter 2, Figure 2.6, and Table 2.6.

Intake pressure affected HCCI combustion through several mechanisms. Increasing intake pressure increased total energy content of the cylinder at any constant λ , increased after-compression temperature, and increased volumetric efficiency. Exhaust pressure increase was responsible for EGR fraction increase and possibly internal residual increase as well as volumetric efficiency decrease.

Intake Pressure Effects

Two sample cases of n-Heptane and natural gas supercharged HCCI combustion was considered for intake pressure effect study. Details of operating condition are indicated in Table 3.3.

Case I: Natural Gas

The operating region for the natural gas HCCI engine with boosted intake is shown in Figure 3.19, which illustrates the HCCI operating window of λ , EGR, and IMEP. At the lean boundary, the limit is imposed by stalling due to low IMEP (when IMEP produced is less than FMEP) or by partial burning and misfiring (which is more common with higher EGR rates). Under these partial burn conditions, HC emission was increased considerably. The diamond symbols (\diamond) in Figure 3.19 indicate points chosen with an approximate constant λ to investigate the effects of intake system pressure.

Air mass flow to the engine was changed when the intake pressure was altered, so it was required to change the fuel flow rate to keep λ constant. Figure 3.20 shows an example of variation of air mass flow and fuel mass flow with intake absolute pressure.

Figure 3.21 indicates the pressure trace of an average cycle for the case of intake pressure increase. Keeping all influential parameters constant, pressure traces were changed considerably because of intake pressure and total in-cylinder energy content variation. Figure 3.21-b shows the diagnosis of the Figure 3.21-a.

Table 3.3: Operating conditions for supercharged natural gas HCCI combustion and n-Heptane to investigate intake boost pressure effects

Parameter	Natural Gas	n-Heptane
N(RPM)	800	800
$T_{\text{intake,mix}}$ ($^{\circ}\text{C}$)	140	110
Effective CR	19.0	11.5
Fuel Pressure (psi)	80	60
EGR (%)	0	$57 \pm 1.5\%$
λ	3.62 ± 0.03	1.38 ± 0.02
FMEP (bar)	2.16	1.90

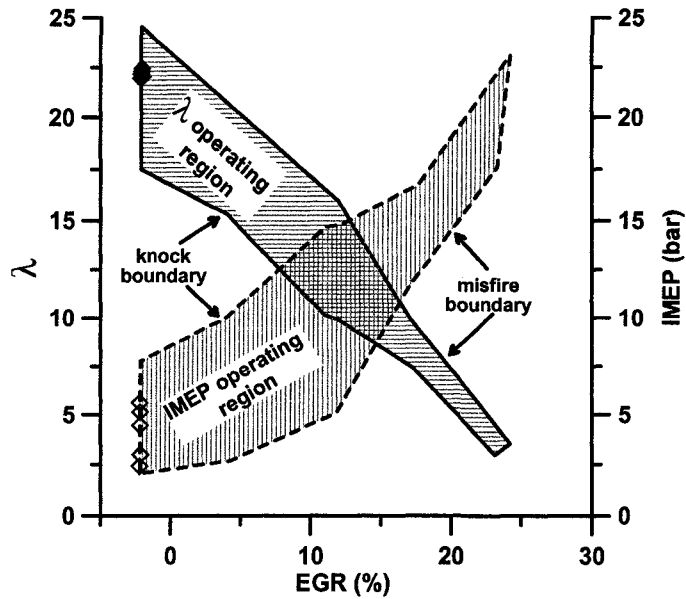


Figure 3.19: Supercharged HCCI combustion operating region with selected λ constant cases

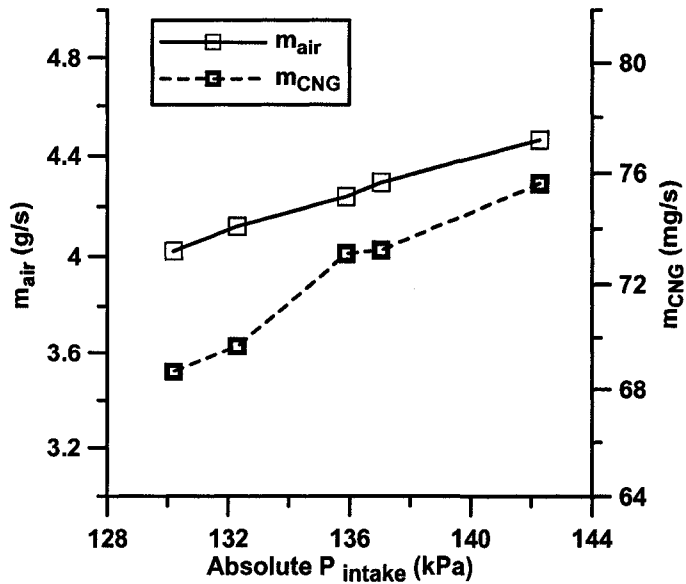


Figure 3.20: variation of air mass flow rate and natural gas flow rate with intake pressure keeping λ constant at 3.62, supercharged natural gas HCCI combustion, operating condition in Table 3.3

Increasing intake pressure at constant operating condition increased P_{\max} and $(dP/d\theta)_{\max}$ by increasing total amount of energy delivered to the engine at each cycle at constant λ . Although the relative ratio of air mass to fuel mass was constant, because of relative significant of number of moles of air inducted in comparison with number of moles of fuel, heat capacity of the mixture was reduced at constant λ . It resulted in higher after-compression temperature; hence, earlier and faster combustion. In addition, when combustion started, more available energy caused stronger combustion resulting in high P_{\max} and $(dP/d\theta)_{\max}$. Error bars on Figure 3.21-b shows the high cyclic variation of the natural gas case.

Boosting the intake pressure increased the mass and energy flows into the engine, leading to a proportionally higher IMEP / indicated power as shown in Figure 3.22. Figure 3.22 also shows that the relative cyclic variation of IMEP decreased as the power increased. The operating points chosen are near to the high λ /idling boundary, where the power output is low and even low

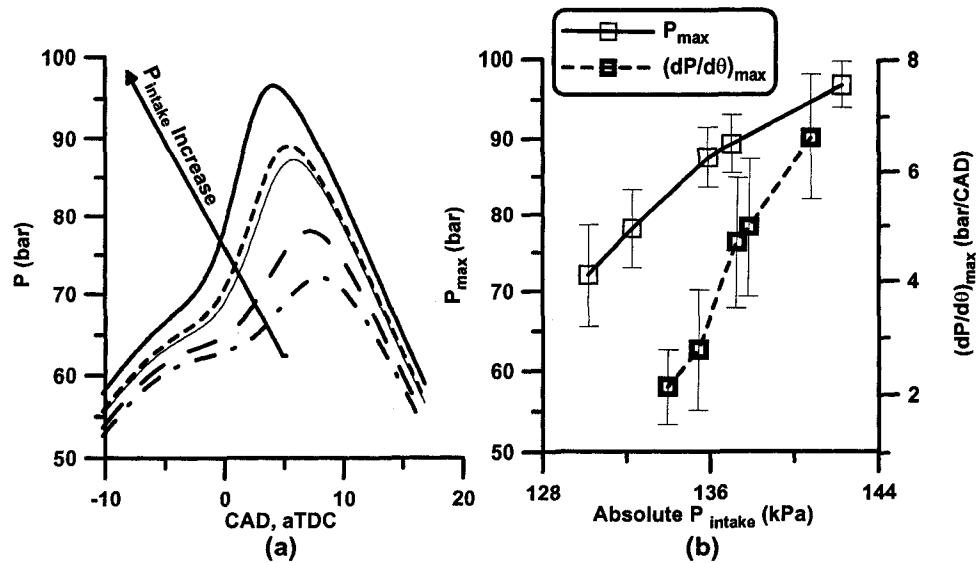


Figure 3.21: Effect of intake pressure on (a) pressure trace and, (b) P_{\max} and $(dP/d\theta)_{\max}$, HCCI combustion of natural gas, initial conditions indicated in Table 3.3, error bars indicate $\pm 2\sigma_{n-1}$

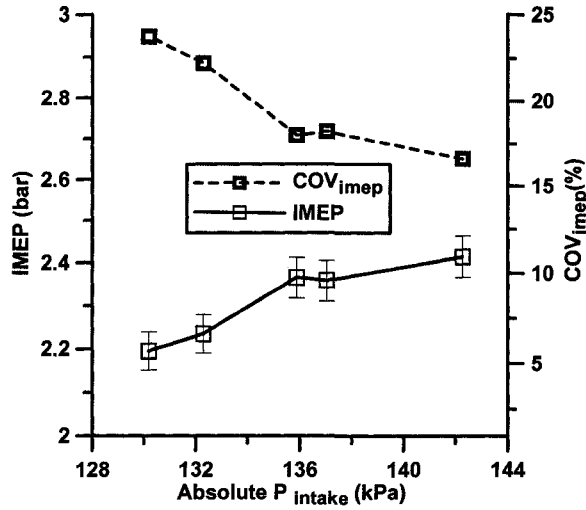


Figure 3.22: Effect of intake pressure on indicated power (IMEP) and cyclic variation (COV_{IMEP}), supercharged HCCI combustion of natural gas, initial conditions indicated in Table 3.3, error bars indicate $\pm 2\sigma_{n-1}$

pressure fluctuation resulted in a high relative value for coefficient of variation. However, for these conditions it is also notable that the decrease in relative

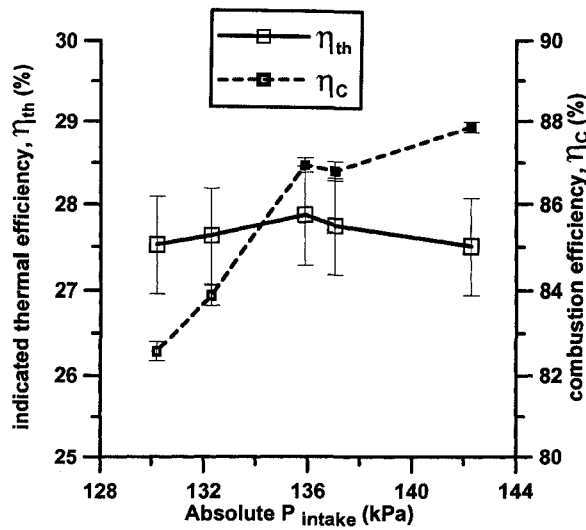


Figure 3.23: Effect of intake pressure on thermal (η_{th}) and combustion (η_c) efficiencies, supercharged HCCI combustion of natural gas, initial conditions indicated in Table 3.3, error bars indicate $\pm 2\sigma_{n-1}$

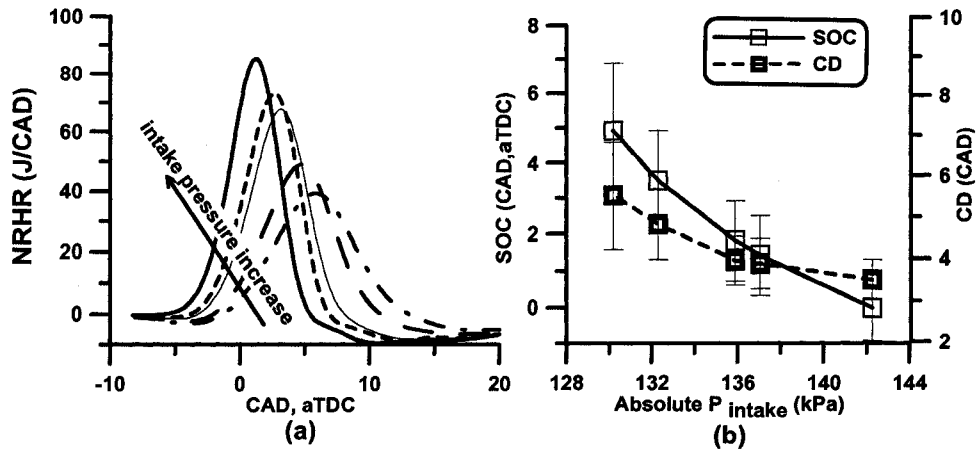


Figure 3.24: Effect of intake pressure on rate of heat release (RHR) top plot and start of combustion (SOC) and combustion duration (CD), super-charged natural gas HCCI combustion indicated in Table 3.3, error bars indicate $\pm 2\sigma_{n-1}$

IMEP fluctuation was much greater than the corresponding increase in IMEP, indicating a true reduction in combustion variability as intake pressure was boosted.

Thermal efficiency for these operating cases was low and almost constant with intake pressure as indicated in Figure 3.23. For these low-power experimental cases, the timing was not optimum and thermal efficiency was in the 27% range. For a well-optimized HCCI engine, indicated thermal efficiency is in the order of 50%. The constant thermal efficiency shows that combustion characteristics did not change considerably as intake pressure changed for a constant λ . The combustion efficiency, an indication of completeness of combustion, was generally low for these cases, falling in the 82% to 88% range. Higher combustion efficiency was associated with increasing intake pressure. It is postulated that higher energy flow to the engine led to higher gas temperatures, and thus, to more complete combustion. Figure 3.24-a indicates the net rate of heat release and diagnosis of gross accumulative heat release as SOC and CD in the Figure 3.24-b. Increasing intake pressure produced sooner and

faster combustion. Advance timing combustion was a result of increasing effective compression ratio that caused producing higher temperature sooner in the compression cycle. Then, more in cylinder internal energy caused a faster rate combustion resulted in a shorter combustion duration (smaller CD). An increase in intake pressure by 10 kPa, advanced combustion timing by 4 CAD, and reduced combustion duration by 1.6 CAD.

Case II: n-Heptane

n-Heptane, which is easily ignited at a lower compression ratio and with a less intake heating, was tested as a comparison with natural gas. The operating region is shown in Figure 3.25. The points chosen for examining variable intake pressure are indicated by diamond symbols (\diamond) in Figure 3.25.

Figure 3.25 also indicates the naturally aspirated λ -EGR operating region

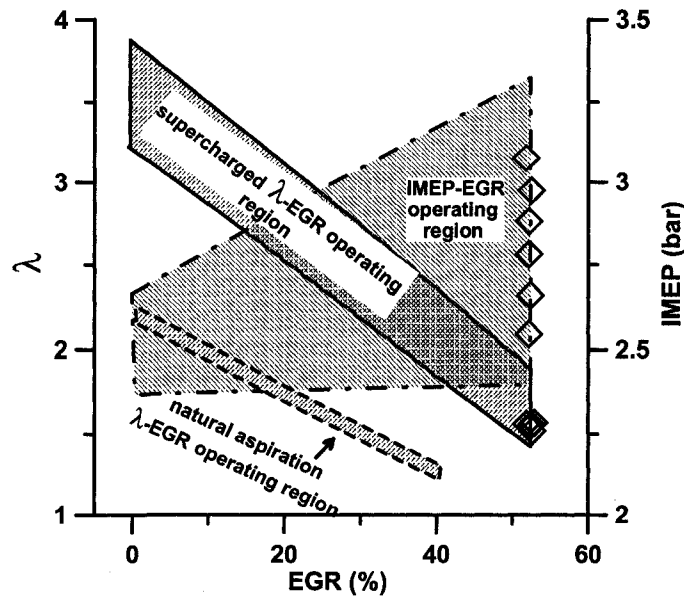


Figure 3.25: Supercharged HCCI combustion with n-Heptane, test points indicated in Table 3.3

compared to supercharged λ -EGR operating region. Increasing intake pressure shifted the operating region toward leaner mixtures and expanded it on the lean side. This was mainly because of low IMEP boundary limit in the

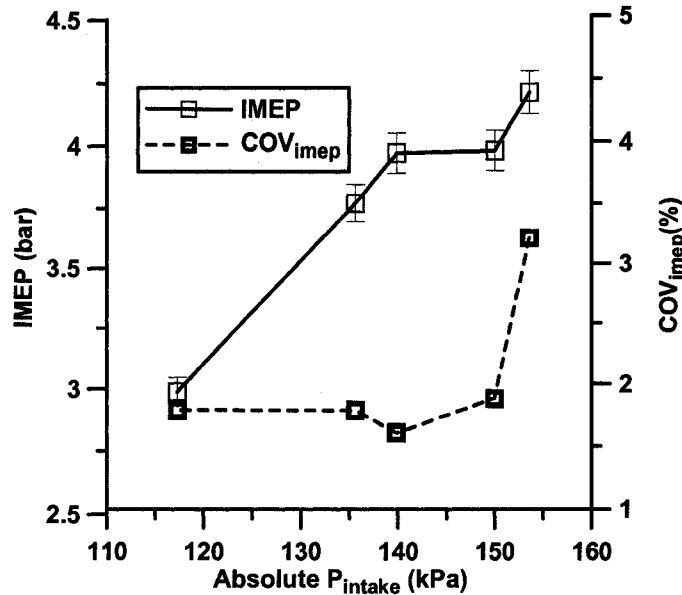


Figure 3.26: Effect of intake pressure on indicated power (IMEP) and cyclic variation (COV_{IMEP}), supercharged n-Heptane HCCI combustion indicated in Table 3.3, error bars indicate $\pm 2\sigma_{n-1}$

naturally aspirated mode.

The n-Heptane-fueled operating points used to examine intake pressure effects were chosen at the operating region boundary determined by high-dilution, with EGR about 60%, and $\lambda = 1.38$. These operating points suffer from partial burning and occasional misfiring in some cycles. Because significant amounts of unburned fuel are returned by the high EGR rate, misfiring cycles were followed by knocking cycles.

For the n-Heptane engine, raising the intake pressure produced a directly proportional increase in IMEP as shown in Figure 3.26.

The relative variation of IMEP was lower than in the natural gas engine, mostly because of the higher absolute value of IMEP at this operating condition.

Figure 3.27 indicates the pressure trace and diagnosis of pressure trace for the case of supercharged n-Heptane HCCI combustion. Similar to natural gas case, increasing intake pressure at constant EGR and λ conditions, increased

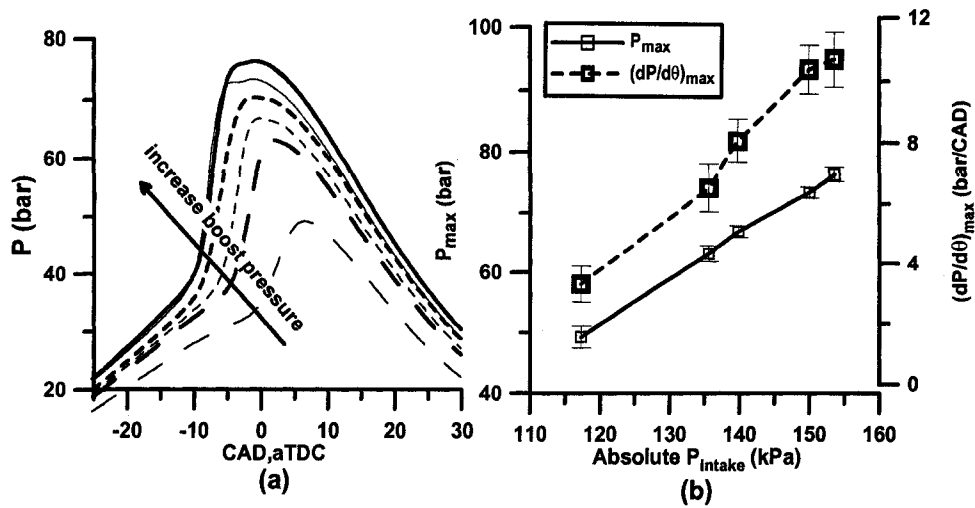


Figure 3.27: Effect of intake pressure on (a) pressure trace and (b) P_{\max} and $(dP/d\theta)_{\max}$, supercharged n-Heptane HCCI combustion, initial conditions indicated in Table 3.3, error bars indicate $\pm 2\sigma_{n-1}$

effective compression ratio, increased after-compression temperature, and advanced pressure trace timing. Higher P_{\max} and $(dP/d\theta)_{\max}$ was observed also as a result of intake pressure increase.

Figure 3.28 indicates effect of intake pressure on heat release characteristics of n-Heptane HCCI combustion. Increasing intake pressure advanced heat release timing and increased maximum rate of heat release on the main stage (Figure 3.28-a). It also advanced combustion timing and shortened combustion duration (Figure 3.28-b). It also shortened NTC length and did not affect LTR/HTR ratio considerably (Figure 3.28-c).

To summarize, pressurizing the intake plenum of the CFR engine operated in HCCI mode provided a simple research method for operating the high-internal-friction CFR engine at a sufficiently lean mixture, that it could exhibit a true lean limit due to misfiring and partial burn cycles rather than the friction-limited, low IMEP boundary exhibited for naturally aspirated cases.

The direct effects of increasing intake pressure on power and efficiency were also studied for both natural gas and n-Heptane operation. Keeping all in-

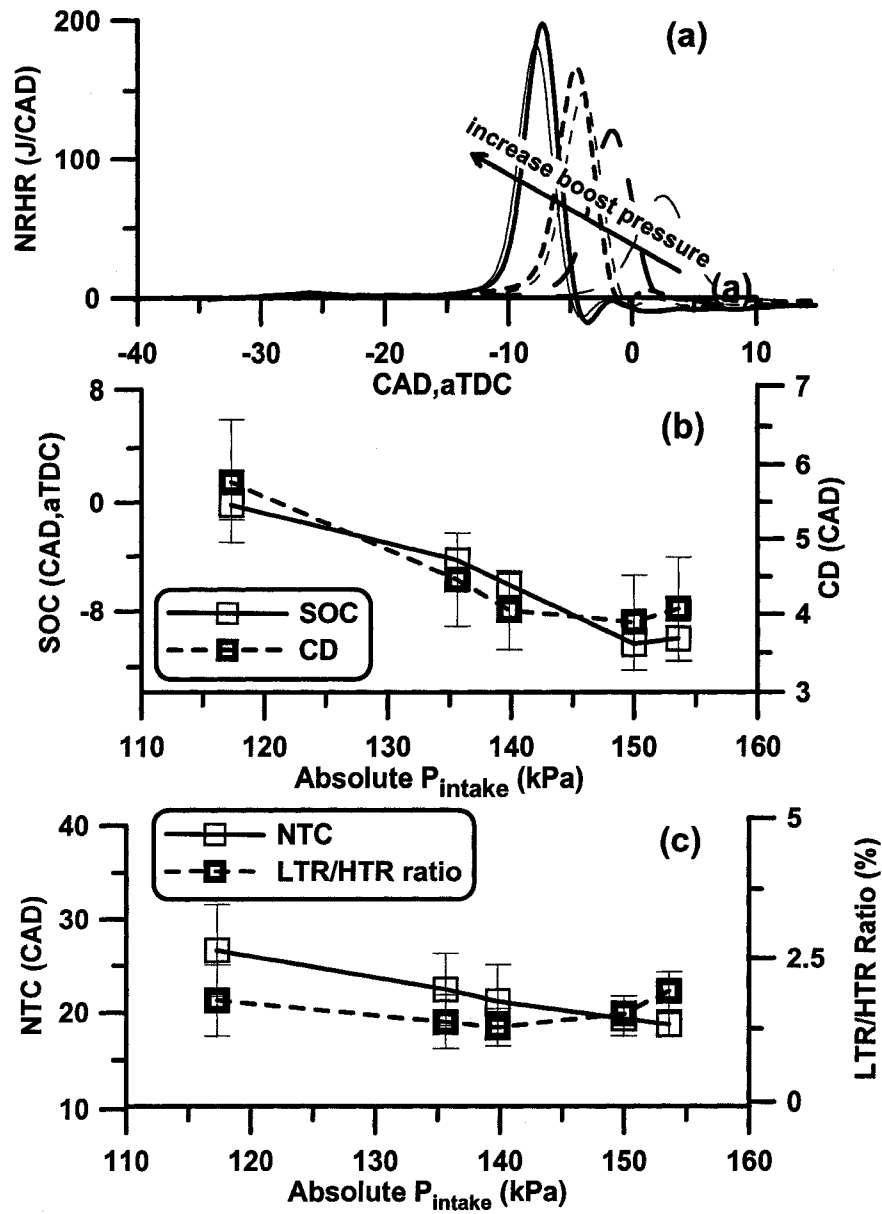


Figure 3.28: Effect of intake pressure on the (a) net rate of heat release (NRHR), (b) combustion timing (SOC) and duration (CD), and (c) negative temperature coefficient length (NTC) and (LTR/HTR-Ratio), supercharged n-Heptane HCCI combustion, initial conditions indicated in Table 3.3, error bars indicate $\pm 2\sigma_{n-1}$

fluent parameters of compression ratio, intake mixture temperature, EGR rate, and λ constant, increasing the intake pressure produced proportionately higher indicated power for both cases. Indicated thermal efficiency for both fuels did not change consistently with supercharging. In addition, both fuels showed a significant increase in combustion efficiency due to the higher energy flow to the engine and higher combustion temperature. For both cases, increasing intake pressure advanced combustion timing and shortened combustion duration. P_{\max} and $(dP/d\theta)_{\max}$ increased and maximum rate of heat release increased with higher intake pressure. Effect of intake pressure on combustion characteristics was similar to the effect of $T_{\text{intake,mix}}$ increase.

Exhaust Pressure Effects

During supercharged HCCI combustion tests, while keeping intake pressure constant, exhaust back-pressure was adjusted to alter EGR rates. Exhaust back-pressure variation possibly contributed to internal residual fraction variation. Internal residual or internal EGR is one of the most influential parameters on HCCI combustion. Various level of exhaust back-pressure also causes the alteration of pumping loss and volumetric efficiency and consequently thermal efficiency. To quantify the effects of exhaust back-pressure while keeping other influential parameters a test was designed and performed. Using iso-octane as the fuel, the exhaust pressure was altered between 93.33 to 179.81 kPa.

Figure 3.29 indicates the effect of exhaust pressure on several engine and combustion parameters of supercharged HCCI combustion.

As indicated in Figure 3.29 most of the engine operating parameters and combustion/heat release characteristics were not affected by exhaust back-pressure variation. The slight variation of the parameters can be mostly described by slight λ variation that is shown in Figure 3.29. The only parameters that their change were drastically and could not explained by λ variation were exhaust temperature and emissions.

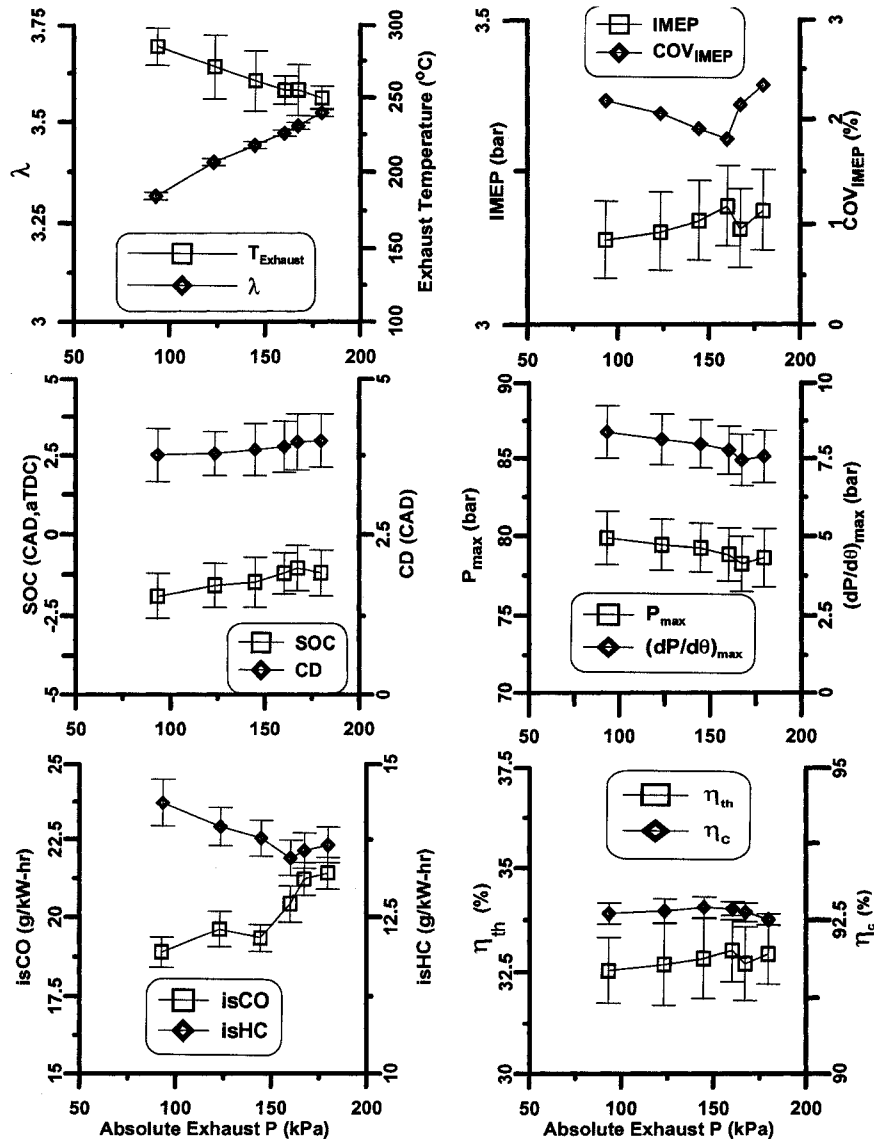


Figure 3.29: Effect of exhaust pressure on supercharged iso-Octane HCCI combustion, initial conditions indicated in Table 3.2, $P_{\text{intake}} = 142.80 \pm 1.1 \text{ kPa}$, error bars indicate $\pm 2\sigma_{n-1}$

Exhaust temperature was increased considerably by increasing exhaust pressure. This effect was not related to the combustion and expansion stroke temperature directly as all other engine operating parameters were constant.

Exhaust temperature rise was related directly to the exhaust system pressure that can be explained by an isentropic pressure rise in the isolated exhaust system. HC and CO emissions were also changed considerably by exhaust back-pressure variation. HC slightly decreased by increasing exhaust pressure. HC emission relies on after-compression oxidation during expansion stroke. Higher exhaust pressure and temperature resulted in more HC oxidation.

Effect of exhaust back-pressure on the engine and combustion parameters were negligible in the range that was examined on the CFR engine. Low speed CFR engine with late exhaust valve open event did not allow a significant increase in the residual. Hence, while keeping intake pressure constant for supercharged case and varying back-pressure to obtain desired external EGR, no significant change in the engine operating parameters was observed from exhaust back-pressure alteration.

3.3 Factorial Design Tests for Significants of CR, EGR, $T_{\text{intake,mix}}$, and Speed

To demonstrate the capability of the experimental design techniques on evaluating HCCI combustion base-line tests, a factorial experimental design with four variables of CR, EGR, $T_{\text{intake,mix}}$, and speed each at two levels were chosen. Theory, definitions, and required design technique for a full factorial design were obtained from Box, Hunter and Hunter (2005) [156], Montgomery (1996) [157], and Anderson and Whitcomb (2000) [158]. The latter is a simple practical tool for design of experiments that comes with a trial version of an experimental design software of Design-Ease[®] by Stat-Ease, Inc. The software used to analyze the factorial design test of HCCI combustion data. Table 3.4 indicates the main variables and chosen levels for each variable.

In a full factorial test, choosing the appropriate variables and level for each variable is an important step. The important parameters that affect HCCI combustion parameters were discussed already namely as fuel octane quality,

compression ratio (CR), EGR, λ , speed (N), and $T_{\text{intake,mix}}$. Among these parameters, fuel octane quality was fixed and n-Heptane was chosen for the factorial design study. As mentioned, operating region was narrow even at a low octane fuel in a supercharged intake condition. Hence, combination of two λ level with other parameters was impossible without either excessive knock and/or misfiring/partial burning in some of the design points. Hence, λ -which is one of the most important influential parameter- was discarded from the factorial tests and was kept constant for all operating conditions for the value of $\lambda = 2.70 \pm 0.03$.

Choosing the level of variables also is important and has a direct effect on the outcome of the analysis. Keeping λ and fuel octane quality constant (n-Heptane) imposed an automatic constraint on CR and $T_{\text{intake,mix}}$. Covering 20% of the possible range, CR levels were chosen as 9.3 and 11.8, and $T_{\text{intake,mix}}$ levels were chosen of 80 and 100 °C arbitrary. EGR levels of 20% were chosen as 20% and 30%. Considering a factorial test that covers the 4 variables and all possible first order interactions $2^4 = 16$ test runs were completed. Using Design-Ease[®], the test runs were ordered randomly. The levels of variables were represented by coded values of +1 for the high and -1 for the low value.

Several responses were considered for the analysis. Here combustion timing (SOC) was chosen as a sample response of Y_1 . For the case of SOC as the response Y_1 , the effect for each variable (A, B, C, D) and their first order

Table 3.4: Main variables and their levels for full factorial design tests

Factor	Name	Unit	Low level(-)	High Level(+)
A	Speed (N)	RPM	800	1000
B	$T_{\text{intake,mix}}$	°C	80	100
C	CR	-	9.3	11.8
D	EGR	%	20	30

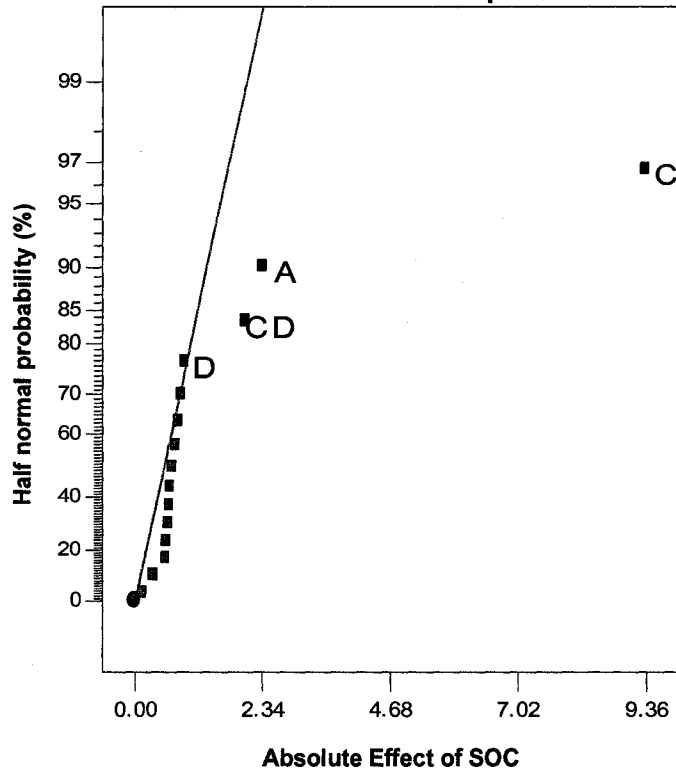


Figure 3.30: Half-normal probability of main effects and interaction for SOC (response Y_1), two-level factorial design tests, n-Heptane HCCI combustion indicated in Table 3.4

interactions (AB, AC, AD, BC, BD, CD) were calculated by:

$$\text{Effect}_{\text{SOC}} = \frac{\sum Y_+}{n_+} - \frac{\sum Y_-}{n_-} \quad (3.1)$$

Plotting the absolute value of each effect on a half-normal plot identified the significant variables in the statistical sense as shown in Figure 3.30.

In this case, for SOC (response Y_1) three variables of C (CR), A (speed), and CD (CR-EGR interaction) were identified to be significant with a much stronger effect belonging to C. In most engineering problems, interactions are not likely to happen. Here the CR-EGR interaction was kept in the the model for further analysis. Avoiding hierarchy of the model variable D (EGR) was also added to the model. Table 3.5 indicates the result of analysis of variance

(ANOVA) using Design-Ease[®]. From the model F-value of 59.1318 it can be concluded that there was only 0.01% chance that such a large F-value could occur due to noise. Value $F > 0.0500$ indicate model terms that were significant, A, C, and CD. The hierarchical term D which was added after manual regression was insignificant as expected. Then, the coded value model for predicting SOC based on the coded value of significant parameters is:

$$\text{SOC} = -0.76 - 4.65C + 1.13A - 1.053CD \quad (3.2)$$

The coded model shown in Equation 3.2 indicates that the most significant effect belongs to CR with highest coefficient in the equation. To confirm the validity of the model Equation 3.2 was used to predict SOC as a function of coded values of A, C, and CD. Checking the normal distribution of the residual (Figure 3.31) confirmed the validity of the model of identifying the significance of the influential parameters on combustion timing.

The statistical analysis of a response (SOC) to a set of influential parameters (CR, speed, EGR, $T_{\text{intake,mix}}$) at certain high and low levels as shown in Table 3.4 indicated the significant effect of CR among other variables on HCCI combustion timing. It was discussed that CR has similar effect to $T_{\text{intake,mix}}$ on combustion timing, but in this specific case $T_{\text{intake,mix}}$ effect was insignificant in comparison with CR, speed, and CR-EGR interaction effects.

Speed was more significant than other parameters, but less than that of CR.

Table 3.5: Analysis of variance (ANOVA) for testing the significance of model for SOC

Source	Sum of Squares (SS)	Degree of Freedom	Mean Square (MS)	F value	Prob > F
Model	392.7857	4	98.19643	59.1318	< 0.0001
A	22.2784	1	22.2784	13.41558	0.0037
C	350.4384	1	350.4384	211.0266	< 0.0001
D	3.4225	1	3.4225	2.060957	0.1789
CD	16.6464	1	16.6464	10.02411	0.0090
Residual	18.267	11	1.660636		
Cor Total	411.0527	15			

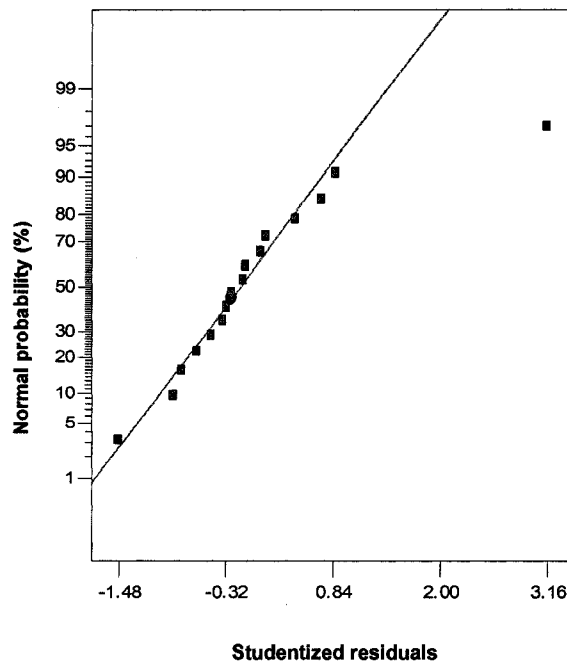


Figure 3.31: normal probability plot of the residual of predicted values by coded model and actual values of SOC (response Y_1), n-Heptane HCCI combustion indicated in Table 3.4

The reason is that SOC was calculated on the CAD basis. Beyond thermal and mixing effect of engine speed on HCCI combustion timing (less time for heat transfer and more mixing at higher speed) as SOC was calculated on a CAD basis, increasing the engine speed keeping all other influential parameters would advance the combustion timing. Calculating SOC on a time basis, for example from start of compression or intake valve close event, would have solved this issue.

As mentioned, it is unlikely to see strong interaction effect of parameters in most engineering problems. Here is this specific case interaction of two parameters CD (CR-EGR) was relatively significant with respect to other parameters. Further investigation using an interaction plot was required as indicated in Figure 3.32.

Figure 3.32 indicates that CR-EGR interaction existed in this case. At low

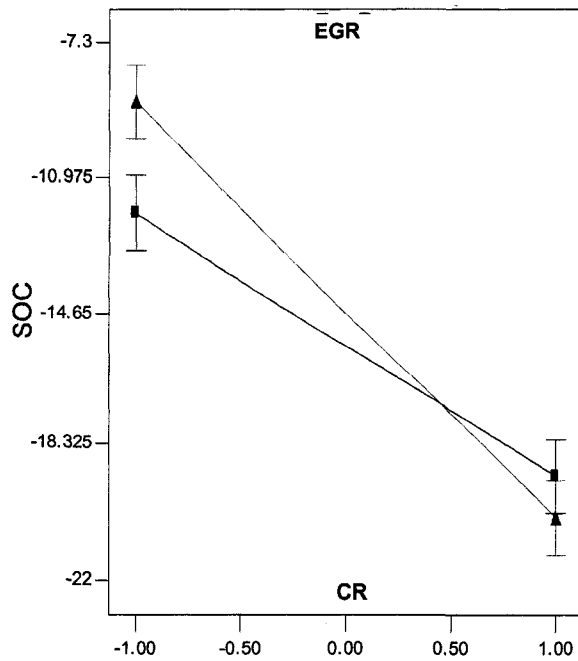


Figure 3.32: Interaction plot for combined effect of CR and EGR on SOC for coded values, n-Heptane HCCI combustion indicated in Table 3.4, ▲ is high EGR (coded value =+1, EGR =30%) and ■ is low EGR (coded value =+1, EGR =20%)

CR (coded value =-1, CR=9.3) increasing EGR retarded combustion timing while at high CR (coded value=+1, CR=11.8) increasing EGR slightly advanced combustion timing or did not have any effect as error bars have overlap at high CR. The error bar was calculated using least significant difference (LSD) by $LSD = t_{critical} S_{pooled} \sqrt{2/n}$. At low CR, EGR can postpone the combustion timing through dilution effect, and at relatively high CR, dilution had negligible effect on combustion timing because of extreme condition (high after-compression temperature) produced by relatively high CR. The CR-EGR interaction had minor effects.

If the coded model of SOC is normalized using the largest coefficient in the Equation 3.2, the normalized coefficient for the coded model are:

Table 3.6: Absolute Normalized coefficients for coded value models of two-level factorial design indicated in Table 3.4

Response	A (Speed)	B (T _{intake,mix})	C(CR)	D(EGR)	CD(CR-EGR)
IMEP	-	0.67	1.00	0.83	-
η_{th}	0.75	0.47	1.00	-	-
η_c	-	-	0.88	1.00	0.52
isHC	1.00	-	0.80	-	-
isCO	0.31	0.33	0.72	1.00	0.38
P _{max}	0.16	-	1.00	0.41	-
(dP/d θ) _{max}	0.22	-	0.71	1.00	-
SOC	0.24	-	1.00	-	0.22
CD	-	-	1.00	0.80	-
LTR _{time}	-	1.00	0.96	0.50	-
NTC	1.00	-	0.71	0.55	-
$\frac{LTR}{HTR}$ ratio	0.56	0.56	-	1.00	-
Pk _{Acc.} -	-	0.64	1.00	0.39	-
RMS _{Acc.} -	-	0.51	1.00	0.31	-

- CR: $\frac{4.65}{4.65} = 1.00$
- N (RPM): $\frac{1.12}{4.65} = 0.24$
- CR-EGR interaction: $\frac{1.05}{4.65} = 0.22$

comparing the normalized coefficient of the coded value indicates the relative significance of the effect of the variable on the response (in this case SOC). The same analysis can be applied to other engine and combustion parameters to find the most influential variable at the proposed level of a two-level factorial design test. Doing the same analysis and checking the models for validation by analysis of variance and checking the normality of residuals, result of the analysis for normalized coefficient of the models is indicated in Table 3.6. Table 3.6 confirms several aspects of HCCI combustion. CR was considerably effective and the most dominant factor on IMEP, η_{th} , P_{max}, SOC, CD, Pk_{Acc.}, and RMS_{Acc.}. Higher relative difference between two-level in the factorial design test can lead to a systematic bias error of an observation. Engine speed dominantly affected isHC and NTC. For isHC speed has negative effect, i.e.

increasing speed from low to high decreased isHC, that is the direct result of more mixing and less time for the heat transfer. Speed effect on CAD related parameters such as NTC is an indirect effect of calculation of the time-based parameters on a CAD basis.

EGR was the dominant variable affecting η_c , isCO, $(dP/d\theta)_{\max}$, and LTR/HTR-Ratio. isCO was the only response that all variables had relative influence on it and none of them had a clear dominant effect. This could be the result of complex nature of CO formation in the combustion chamber. EGR decreased rate of combustion by decreasing rate of pressure rise $(dP/d\theta)_{\max}$ dominantly. The second factor after EGR is CR that changes the rate of pressure rise.

Effects of $T_{\text{intake,mix}}$ were found to be insignificant for most cases. The reason could be the chosen level of $T_{\text{intake,mix}}$. The 20 °C difference was not enough to show any significant effect. $T_{\text{intake,mix}}$ showed a dominant effect over LTR_{time} that is the result of higher after-compression temperature in the early stages of combustion.

Knock intensities of accelerometer oscillations (Pk_{Acc} , and RMS_{Acc}) were affected by CR, $T_{\text{intake,mix}}$, and EGR. This order was expected as increasing CR directly increased after-compression temperature and rate of pressure rise, also increasing $T_{\text{intake,mix}}$ increased combustion rate and advanced combustion timing. Increasing EGR reduced combustion rate and decreased combustion intensity.

3.4 Summary

In the current chapter, several observations have been made on HCCI combustion base-line tests for various octane quality fuels and engine operating conditions. A combination of fuel octane quality, CR, speed, $T_{\text{intake,mix}}$, intake pressure, EGR fraction, and relative air/fuel ratio λ determined HCCI combustion base-line characteristics.

The operating region for the HCCI engine was limited between low load/misfiring/partial

burning boundary and knock boundary. The operating region for naturally aspirated case was extremely narrow and could not be used for further analysis aiming at constant λ and/or EGR lines. Supercharging HCCI engine expanded the operating range to a wider band and shifted the operating region toward leaner regions by increasing in-cylinder total energy.

At any fixed fuel octane quality, CR, and speed; HCCI combustion was affected by a combination of λ -EGR. The best operating condition in terms of maximum power, efficiency, minimum emissions, and the best combustion characteristics were at maximum EGR fraction when the relative air/fuel ratio is near to stoichiometric at the vicinity of the knocking boundary. Moving toward lean region by increasing λ and/or EGR increased cyclic variation, reduced power and efficiency while reduced knock intensity.

SOC can be indirectly controlled by λ and EGR variation with the penalty of moving operating condition to an undesired location inside the operating window. It was found that λ is an affective parameter for HCCI combustion control. Increasing λ by 1 unit, retarded combustion timing by an average of 5 CAD for most cases of naturally aspirated PRF HCCI combustion and increased combustion duration by an average of 8 CAD for naturally aspirated PRF HCCI combustion and 4 CAD for supercharged HCCI combustion. While λ was effective on combustion timing control, IMEP suffered from increasing λ by 1 unit by about 2.1 bar which is a considerable power reduction for HCCI combustion in the CFR engine.

Statistical tools were used to analyze HCCI combustion characteristics. In the current study, a two-level factorial design was used to find the most significant variable among speed, CR, $T_{\text{intake,mix}}$, and EGR on engine and combustion characteristics. Most of the finding through analysis of variance and building a linear coded model can be explained by HCCI combustion phenomenon physics. It was found that CR is the most influential parameter on HCCI combustion.

Chapter 4

Reformer Gas Application in n-Heptane HCCI Combustion Timing Control

Partial content of this chapter has been published as a peer reviewed Society of Automotive Engineering (SAE) technical paper in 2007 [159] and in a conference presentation in ASME internal combustion engine fall technical conference in 2005 [160].

This chapter specifically focuses on Homogeneous Charge Compression Ignition (HCCI) combustion of low octane Primary Reference Fuels (PRFs) with double-stage combustion and investigates the effects of Reformer Gas (RG) blending on engine and combustion parameters using heat release analysis of experimental results and chemical kinetics modeling tool.

n-Heptane is one of the binary mixture of Primary Reference Fuel (PRF) with assigned octane number of 0 and is used widely to test the octane quality of fuels in ASTM standard tests with CFR engine.

According to Ryan and Lestz (1980) [161], n-Heptane has the fastest laminar burning velocity among other conventional hydrocarbons such as iso-Octane and methane. n-Heptane is a well known fuel and its autoignition chemical kinetic mechanisms were extensively studied. (e.g. Cox and Cole (1985) [102], Benson (1981) [97], Warnatz (2000) [162]). For internal combustion engine

applications, autoignition was studied because of knock phenomenon (e.g. Hu and Keck (1987) [103], Leppard (1990) [91], Westbrook et al (1991) [100]). Several chemical kinetics mechanisms have been offered such as a detailed comprehensive reaction set for n-Heptane by Curran et al (1998)[104] offering 25 various classes of reactions. Normally, in the engine temperature and pressure operating conditions, n-Heptane exhibits a double-stage combustion that includes both high and low temperature reactions. While high temperature heat release reactions are well developed for n-Heptane, the low temperature kinetics still needs improvement. Since the effect of RG blending appears to be mostly on low temperature regime for the case of n-Heptane, a detailed mechanism for the first stage of heat release would be beneficial for a precise description of RG blending effects.

n-Heptane is used as a representative of diesel fuel, because it is relatively simple to model and boiling point temperature is lower than that of regular diesel fuel. In an early diesel Homogenous Charge Compression Ignition (HCCI) study, Gray et al (1997) [29] used n-Heptane as a diesel fuel. Peng et al (2003) [153] studied the air/fuel ratio and Exhaust Gas Recirculation (EGR) effect on n-Heptane HCCI combustion and considered it as a diesel fuel. Diesel HCCI is a crucial subject for HCCI research and development. Natural high compression ratio (CR), capability of injecting fuels at high pressure with any desired injection timing and duration, and high auto-ignitability of diesel fuels compared with gasoline fuels, make diesel engines a suitable choice for a dual mode HCCI/CI (Compression Ignition) engine. In fact, some types of diesel engines are taking the benefits of HCCI combustion in limited operating modes by an early injection of diesel fuel into the cylinder, forming a homogenous premixed charge. It has been found that low cetane number fuels are more suitable for HCCI combustion, while modern diesel engines are using more higher cetane number fuels. While the concept of a dual fuel dual mode engine seems attractive, the feasibility is questionable because of practical issues related to carrying two fuels onboard. Hence, RG blending of a diesel type fuel (in this

case n-Heptane) to achieve a controllable wide range HCCI combustion is an important step toward dual mode HCCI/CI engine.

Few studies have been focused on the effect of Reformer Gas (RG) blending on n-Heptane HCCI combustion. Eng, Leppard, and Sloane (2002) [114] studied effects of POx (partial oxidation) RG on n-Heptane HCCI combustion and iso-Octane at two conditions of external EGR and internal EGR (via exhaust re-breathing technique). They found that thermal stratification caused by hot exhaust gases re-breathed into the cylinder influenced n-Heptane HCCI combustion dominantly, and POx had no or little effect on controlling combustion timing. In the external EGR case when the temperature was not a dominant factor, adding 15% POx to the mixture caused a strong suppression in the early stages of combustion and combustion timing was retarded. The experimental setup and procedure in Eng et al [114] was different from the current study. In the Eng et al [114] study, intake temperature was adjusted (increased) when RG was increased while in the current study intake mixture temperature ($T_{\text{intake,mix}}$) was kept constant. Also in Eng et al [114], the fueling rate was kept constant while increasing RG fraction (so it was RG enrichment). In the current study, λ was kept constant (and hence it was RG blending). These major differences made the comparison of results impossible. In the current study, as EGR was applied externally and intake mixture temperature ($T_{\text{intake,mix}}$) was kept constant, RG blending effectively postponed combustion timing in a wide range while keeping all other influential parameters constant. RG acted as a strong octane number enhancer retarding combustion timing. Variation of RG composition did not change the outcome considerably. Decreasing H_2 fraction in RG from 75% to 50% (of H_2/CO mixture), slightly reduced RG effectiveness on combustion timing retardation.

4.1 Effect of RG on Low Octane PRF HCCI Combustion in the Naturally Aspirated Mode

4.1.1 Operating Region

Three data sets were collected for low octane HCCI combustion, two sets for n-Heptane and one set for PRF20 (80% n-Heptane, 20% iso-Octane). Selected initial and engine operating conditions for three data sets are indicated in Table 4.1. The operating region for n-Heptane HCCI combustion in the naturally aspirated mode and at two different compression ratios with and without RG blending are indicated in Figure 4.1. Data Set I and data Set II of data in Table 4.1 were tested both with n-Heptane at the same speed and $T_{\text{intake,mix}}$, but CR was different at two conditions. Without RG blending, operating region of the lower CR (Set I) was much wider than that of higher CR (Set II). Increasing CR pushed the knock boundary in and limited the operating region from the rich side by increasing knock intensity, and slightly expanded the operating region on the lean side, because of the higher after-compression temperature at higher CR (when keeping $T_{\text{intake,mix}}$ constant).

At CR=9.5 (Set I) adding RG expanded the operating region on the rich side of the operation toward the leaner mixtures, because of the anti-knock quality of RG that suppressed the autoignition and reduced knock intensity. On the lean side however, at CR=9.5 (Set I) the operating range was more limited with RG addition, mainly because of the misfiring and partial burning caused by high resistance of RG to autoignition. In the case of CR=11.5 (Set II), because of higher CR and higher after-compression temperature, RG extended HCCI

Table 4.1: Operating conditions of n-Heptane and PRF20 naturally aspirated HCCI combustion

Data Set	Set I	Set II	Set III
PRF	0	0	20
CR	9.5	11.5	11.5
$T_{\text{intake,mix}}$ (°C)	100	100	100
Speed (RPM)	700	700	700

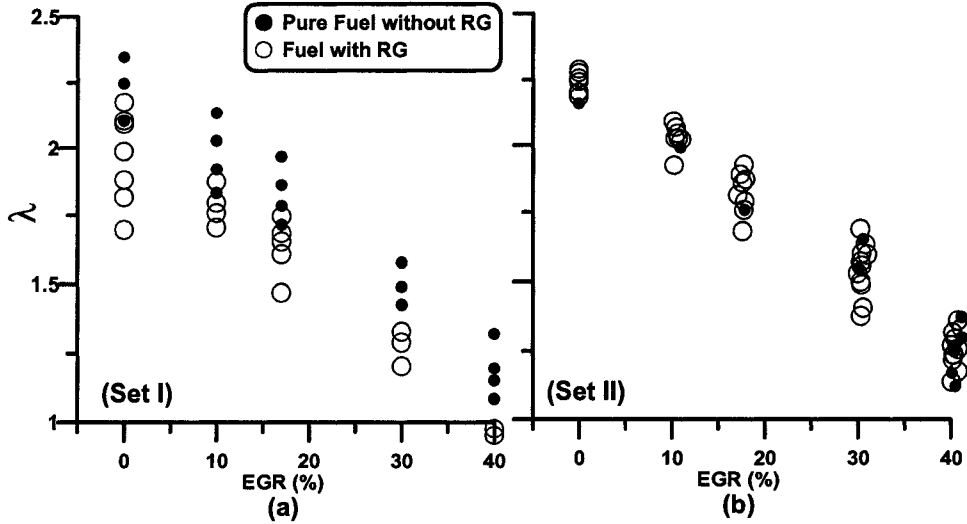


Figure 4.1: EGR- λ operating region for (a) data Set I and (b) data Set II indicated in Table 4.1, n-Heptane HCCI combustion in the naturally aspirated mode

combustion on both rich and lean sides of the operating region. Note that the overall operating region for higher CR case (Set II- Figure 4.1-b) was located

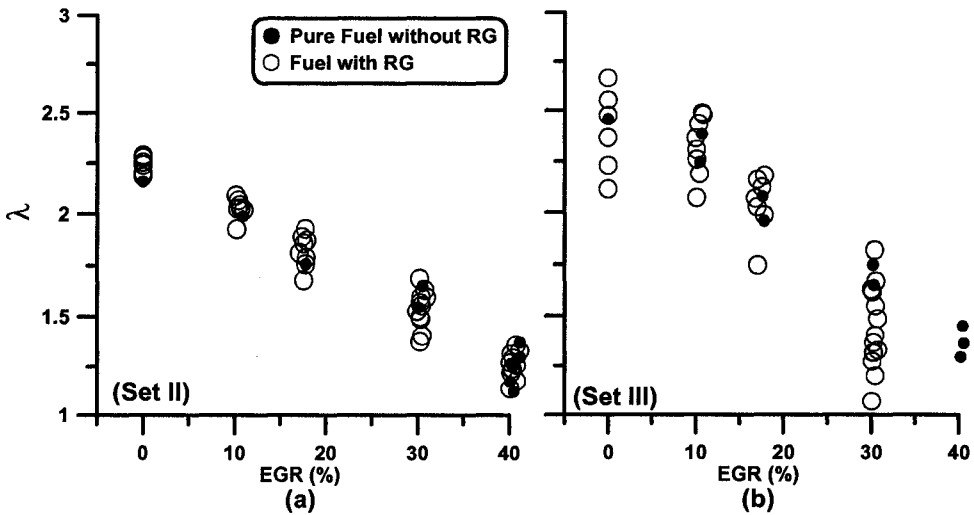


Figure 4.2: EGR- λ operating region for (a) Set II and (b) Set III of data indicated in Table 4.1, n-Heptane and PRF20 HCCI combustion in the naturally aspirated mode

Table 4.2: Selected constant λ cases from Table 4.1

Label	Selected from Data Set	λ	EGR (%)
A	I	2.09 ± 0.00	0.0 ± 0.0
B	II	1.24 ± 0.02	40.2 ± 0.2
C	III	1.63 ± 0.01	30.1 ± 0.1

at the overall leaner mixtures.

The comparison of the operating region for the same $T_{\text{intake,mix}}$ and CR, but different octane number is presented in Figure 4.2 where effects of RG blending is demonstrated on n-Heptane and PRF20 HCCI combustion.

PRF20 exhibited an operating region toward much leaner mixtures than that of n-Heptane at the identical initial and operating conditions. As thoroughly discussed, the lean limit of the operation in naturally aspirated mode was limited by low load and not by partial burning. Adding iso-Octane to n-Heptane (to make PRF20) at any constant air induction rate (constant EGR in naturally aspirated mode) caused a slightly higher energy content creating an opportunity for further shifting toward lean limit. While PRF20 operating range was extremely limited between severe knock and low load, adding RG expanded the operating range considerably in both lean and rich limits of the operation because of anti-knock quality of RG on the rich side.

For further analysis, three sets of data with approximate constant λ were chosen from each data set from Table 4.1 that are indicated in Table 4.2.

4.1.2 Combustion Timing, and Combustion Duration

Increasing RG blend fraction retarded combustion timing and slightly prolonged combustion duration as indicated in Figure 4.3. For the case A, the SOC timing variation was 6.2 CAD per 10% RG, for case B it was 6.6 CAD per 10% RG, and for the case C it was 5.2 CAD per 10% RG. The results show that despite of fundamental differences between groups of data, the slope of SOC variation with RG blend fraction, relatively remained constant for all cases. Increasing iso-Octane fraction in the fuel (migrating from PRF0 to

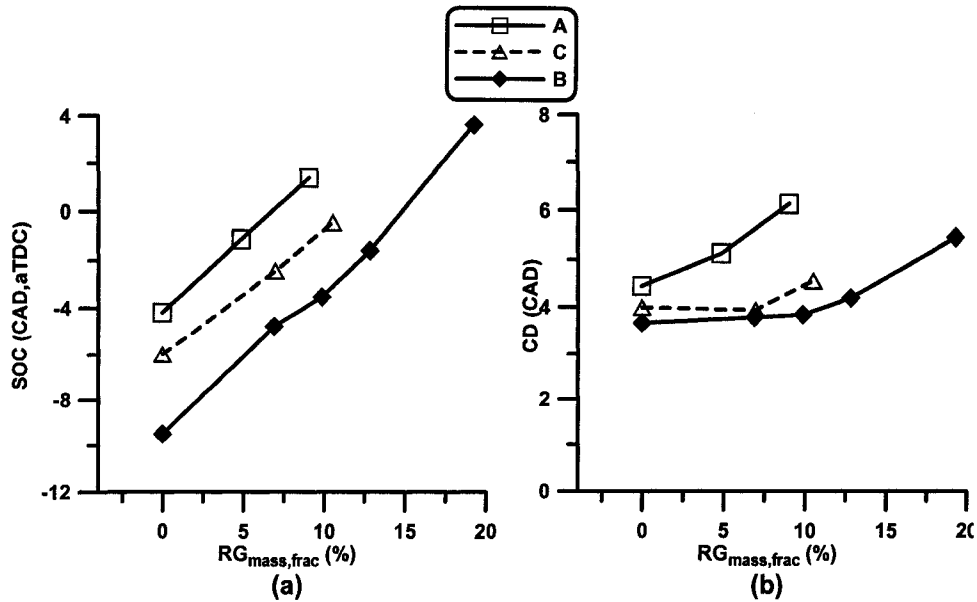


Figure 4.3: Effect of RG blend fraction on (a) start of combustion and (b) combustion duration, initial conditions indicated in Table 4.2

PRF20) slightly decreased the effectiveness of RG on SOC control. Based on Figure 4.3, RG blending at constant initial conditions for low octane PRF0 and PRF20 showed that an average increase of RG blend fraction by 10%, could advance the combustion timing by an average of 6 CAD. In comparison with other SOC control methods, for example, the same 6 CAD retardation of combustion timing for the case of naturally aspirated PRF0 HCCI combustion at EGR=40% was required an increase in λ of 1.2 (see Figure 3.6). The λ increase by 1.2 unit, would reduce the power (IMEP) by 3.3 bar and move the operating points out of the acceptable operating region.

Combustion duration was also slightly prolonged by RG blend fraction increase. Increase in RG blend fraction by 10%, prolonged combustion duration by an average of 1 CAD. Note that as the low temperature heat release for all cases was less than 5% of total heat release, and start of combustion was considered as 10% of total heat release, negative temperature coefficient (NTC) prolongation did not have a considerable translation in combustion duration

prolongation.

4.1.3 Pressure Trace Characteristics

For all cases of A to C of Table 4.2, P_{\max} and $(dP/d\theta)_{\max}$ decreased at constant λ lines when RG blend fraction increased. Increase in RG blend fraction by 10%, decreased P_{\max} by an average of more than 3 bar and decreased $(dP/d\theta)_{\max}$ by an average of about 2 bar/CAD. Note that both P_{\max} and $(dP/d\theta)_{\max}$ are strong functions of λ and the same reduction of P_{\max} and $(dP/d\theta)_{\max}$ would require the increase in λ by 1.2 unit, resulting to power reduction, cyclic variation and shifting the operating point toward outside operating region boundaries. Decreasing combustion intensity (or P_{\max} and $(dP/d\theta)_{\max}$ reduction) while maintaining power makes the HCCI combustion of low octane fuels quite possible. Low octane fuels (in this case n-Heptane and PRF20) were quite easy to auto-ignite. At high load side, their prone to auto-ignition causes very fast combustion that is destructive for engine structure and associates with noise pollution.

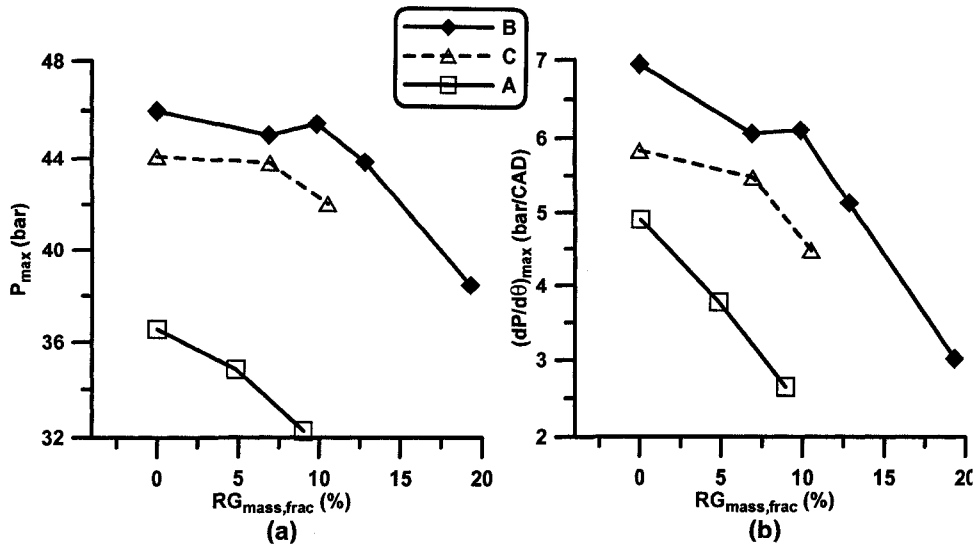


Figure 4.4: Effect of RG blend fraction on (a) P_{\max} and (b) $(dP/d\theta)_{\max}$ emissions of cases in Table 4.2

4.1.4 Engine Operating Parameters

Effect of RG blend fraction on indicated power and cyclic variation of three cases of Table 4.2 are shown in Figure 4.5. RG blend fraction increase at constant λ did not change IMEP of case A while for case B and C, IMEP increased. COV_{IMEP} was minimal and remained unchanged.

As λ (and hence energy flow to the engine) were constant, IMEP trends also were observed in indicated thermal efficiency (η_{th}) trends. For case A, η_{th} was constant and for cases B and C it was increased by increasing RG blend fraction as shown in Figure 4.6. Overall in this case, RG blending altered combustion timing without any significant change in IMEP or slightly IMEP improvement by more optimized combustion timing. The thermal efficiency slightly increased by about 1% in the case A and 2% in the case B. Assuming a 78% reforming efficiency and replacing 10% of n-Heptane with RG, an efficiency drop of less than 1% is expected for RG blend fraction =10%, that was compensated by more optimized combustion timing for the cases of A and B. Combustion efficiency slightly decreased for all cases when RG blend

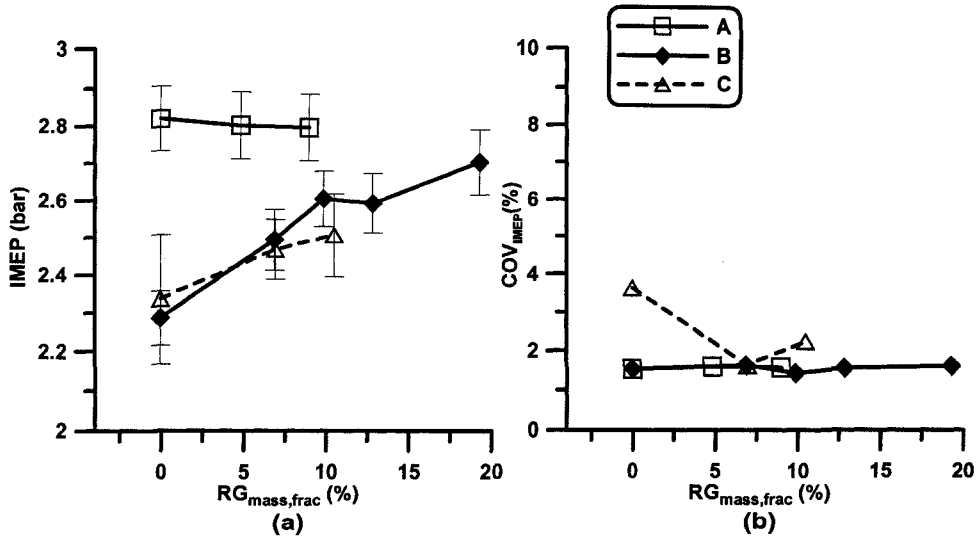


Figure 4.5: Effect of RG blend fraction on (a) IMEP and (b) COV_{IMEP} , initial conditions indicated in Table 4.2, error bars indicate $\pm 2\sigma_{n-1}$

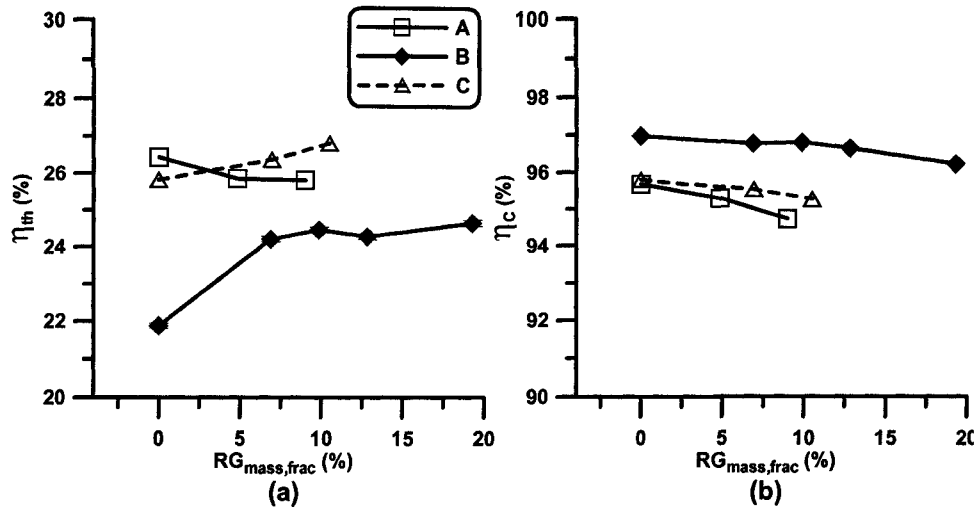


Figure 4.6: Effect of RG blend fraction on (a) η_{th} and (b) η_c , initial conditions indicated in Table 4.2

fraction increased because of relative constant HC emissions and increasing CO emissions as shown in Figure 4.7.

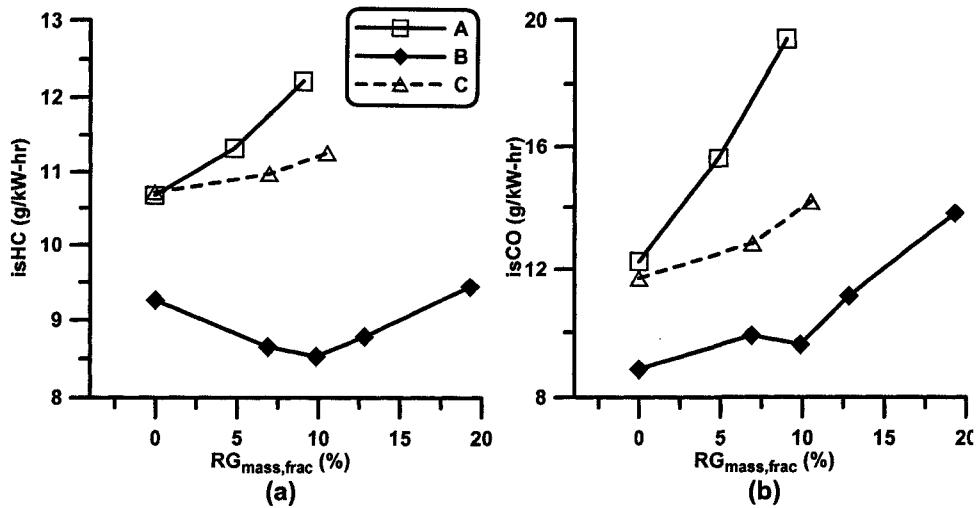


Figure 4.7: Effect of RG blend fraction on (a) HC and (b) CO emissions, initial conditions indicated in Table 4.2

4.2 Effect of RG on Supercharged n-Heptane HCCI Combustion

Limited operating range of the n-Heptane HCCI combustion in the CFR engine in the naturally aspirated mode caused the limited available data to be used for analysis and modeling. Boosting intake pressure produced a much wider operating region and capability of exploring RG effect on HCCI combustion of low octane fuel (in this case n-Heptane) in a reasonable wide range.

4.2.1 Operating Region

Supercharged n-Heptane HCCI combustion experiments were performed at $N=800$ RPM, $T_{\text{intake,mix}}=110$ °C, $CR=11.8$, and an average intake boost pressure of 50 kPa. The operating range of the pure n-Heptane was limited between knock and misfiring boundaries. Adding RG expanded the operating region as indicated in Figure 4.8. Effect of RG blending on operating region limits of the supercharged case was slightly different from naturally aspirated cases (See

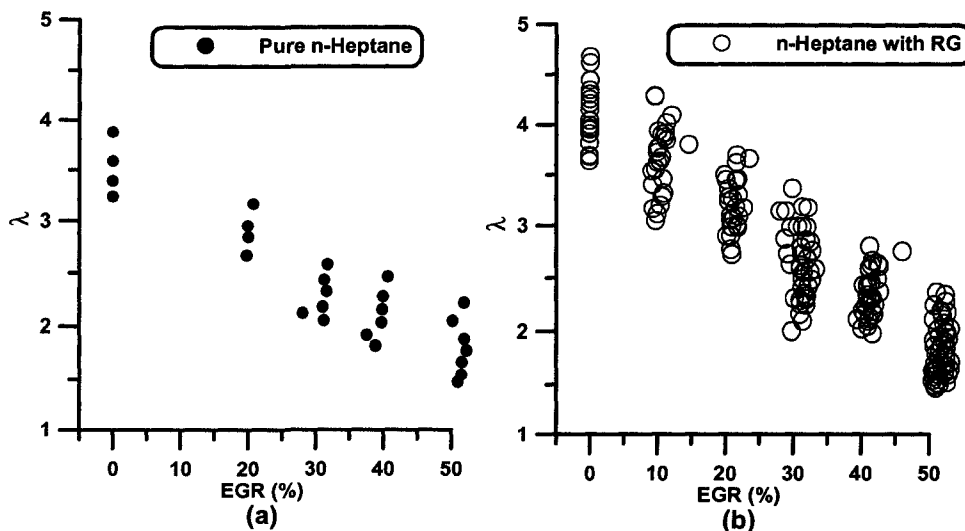


Figure 4.8: λ -EGR operating region for n-Heptane HCCI combustion at elevated intake pressure (a) without RG blending and (b) with RG blending, $N=800$ RPM, $T_{\text{intake,mix}}=110$ °C, $CR=11.8$

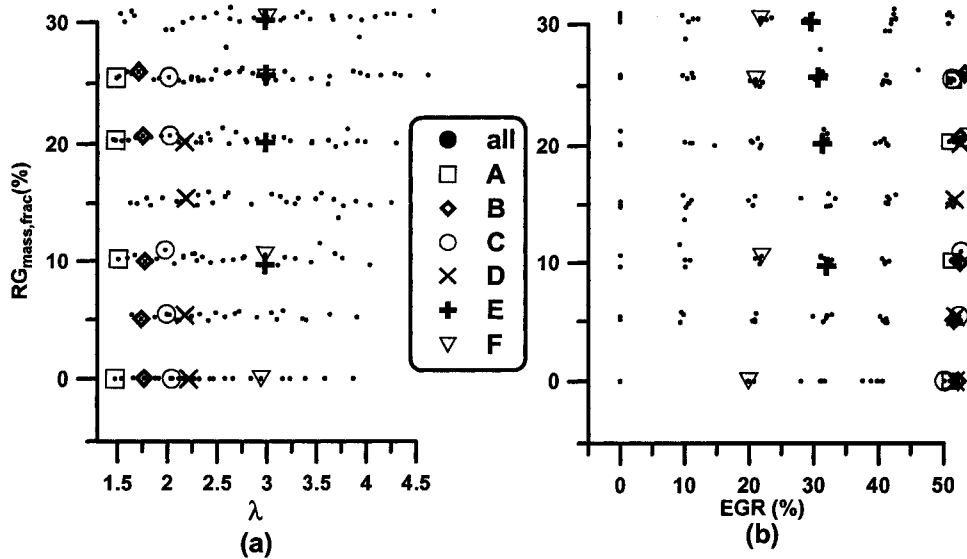


Figure 4.9: (a) RG- λ and (b) RG-EGR operating regions with indication of constant λ groups of data indicated in Table 4.3, $N=800$ RPM, $T_{\text{intake,mix}}=110$ °C, $CR=11.8$

Figures 4.1 and 4.2). The differences between RG effects on operating region boundaries always depends on the base line operating region and the location of initial operating points that were considered for RG blending within the operating limits. The baseline HCCI combustion operating region determines the RG effect on shifting operating region boundaries. For all cases of n-Heptane and PRF20, RG shifted the rich boundary for case I of data (Figure 4.1), did not change operating region boundaries for Case II and Case III (Figure 4.2),

Table 4.3: Selected λ -EGR constant data groups, supercharged n-Heptane HCCI combustion at $N=800$ RPM, $CR=11.8$, $T_{\text{intake,mix}}=110$ °C

Label	λ	EGR (%)
A	1.49 ± 0.01	51.1 ± 0.3
B	1.75 ± 0.02	52.4 ± 0.6
C	2.19 ± 0.02	52.0 ± 0.4
D	2.31 ± 0.01	31.4 ± 0.7
E	2.98 ± 0.00	30.9 ± 1.0
F	2.98 ± 0.02	21.1 ± 0.9

and shifted the operating region of supercharged HCCI combustion toward the lean boundary (Figure 4.8). The difference between naturally aspirated operating region and supercharged operating region for n-Heptane was more intense initial condition in the supercharged case. After-compression temperature was higher in supercharged case than that of naturally aspirated case assuming that both have the same $T_{\text{intake,mix}}$. At higher initial temperature, the significance of the low temperature heat release was reduced resulting to the difference between naturally aspirated and supercharged modes.

Figure 4.9 shows the operating region of RG- λ and RG-EGR. As shown, there is not any limit to apply RG at various EGR and λ levels, as supercharged HCCI combustion operating region was wide enough to not be limited by low load in the lean side. A series of data points were chosen with constant λ for further analysis as indicated in Figure 4.9.

Summary of λ constant groups are indicated in Table 4.3. Each group is labeled with capital A to G letters. Most of the possible constant λ cases were chosen from high EGR fractions as operating region was large enough to group a series of constant λ data. The variation between λ and EGR within each group was shown by an uncertainty value indicated by \pm sign. The symbols were assigned to each group of data remains the same for the rest of the analysis.

4.2.2 Combustion Timing, Combustion Duration, and other Heat Release Characteristics

Combustion timing and duration were affected by RG blend fraction increase in a similar way to the naturally aspirated points as indicated in Figure 4.10. SOC was retarded by adding RG at various λ and EGR.

Figure 4.10 shows the ineffectiveness of λ on combustion timing control of n-Heptane. For each constant EGR fraction, changing λ did not change combustion timing and the timing was identically a function of EGR fraction. This is also indicated in the base-line experiments with n-Heptane HCCI combus-

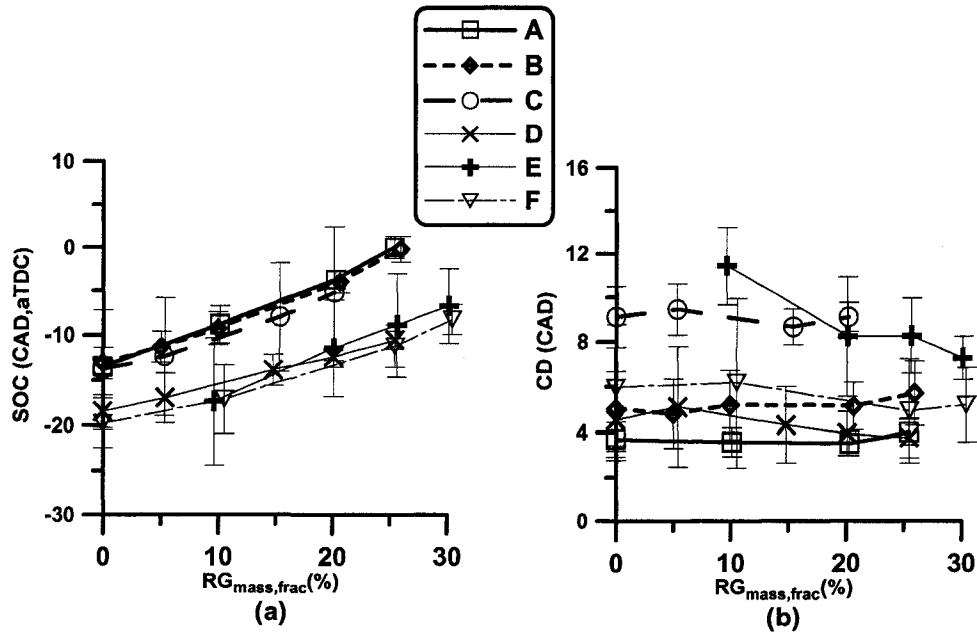


Figure 4.10: Effect of RG blend fraction on (a) start of combustion and (b) combustion duration at constant λ and EGR for data indicated in Table 4.3, error bars indicate $\pm 2\sigma_{n-1}$

tion without RG blending in Figure 3.7. In addition, drastic changes in EGR fraction from 50% to 30% or 20% changed the combustion timing in a range of 4-5 CAD while increasing RG blend fraction from 0% to 30% changed combustion timing in a range of 14-15 CAD as indicated in Figure 4.10-a. Increase in RG blend fraction by 10%, retarded combustion timing by an average of 4.4 CAD for all cases. This was slightly less than naturally aspirated case in which 10% RG blend fraction increase, retarded combustion timing by 6 CAD. Higher after-compression temperature for supercharged case and less intensive low temperature heat release is the reason for less effectiveness of RG blending over combustion timing in supercharged case.

While λ had minimum effect on combustion timing, effect of λ was more obvious on combustion duration as indicated in Figure 4.10-b. RG was ineffective on combustion duration and no obvious trends were observed for CD when RG

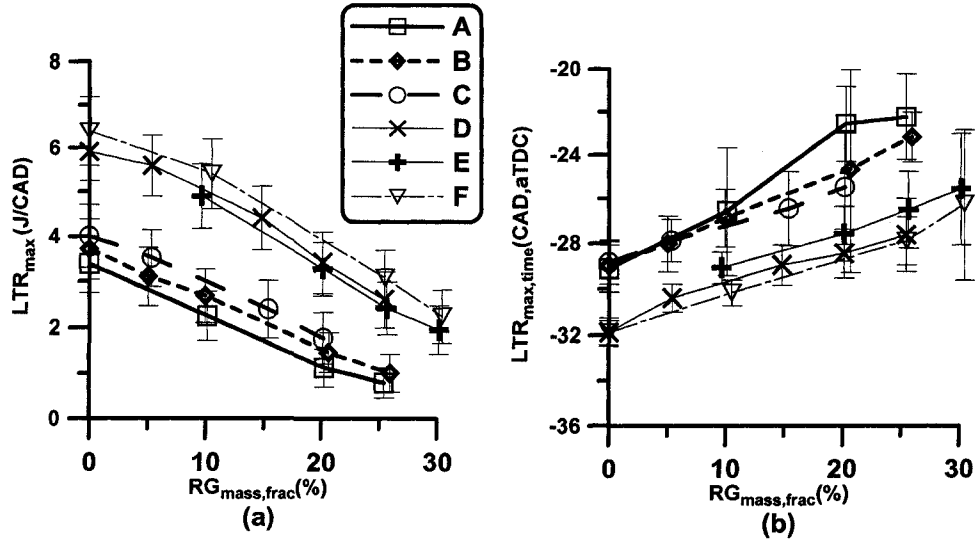


Figure 4.11: Effect of RG blend fraction on (a) maximum low-temperature heat release, LTR_{max} , and (b) maximum low-temperature heat release timing, $LTR_{max,time}$ at constant λ and EGR for data indicated in Table 4.3, error bars indicate $\pm 2\sigma_{n-1}$

blend fraction was changed. This is again due to the fact that RG is effective on low temperature heat release which was less than 5% for all cases (lower than 10% heat release threshold considered for SOC definition).

Figure 4.11 indicates the peak of low-temperature heat release, LTR_{max} , and timing of the peak of low-temperature heat release, $LTR_{max,time}$. LTR_{max} was relatively strong function of EGR and weak function of λ . Change of LTR_{max} relative to RG blend fraction variation was quite drastic in comparison with both λ and EGR effects. Increasing RG blend fraction by 10% decreased LTR_{max} for about 15%. Adding RG to the n-Heptane/air mixture, reduced the first stage heat release considerably. However, $LTR_{max,time}$ variation was not drastic as LTR_{max} , because the starting of the heat release was mostly a function of temperature and pressure and RG effects on low-temperature heat release happened during the early chain branching reactions.

Figure 4.12 similar to Figure 4.11 indicates effect of RG on main stage of combustion characteristics, i.e. peak high-temperature heat release HTR_{max} and

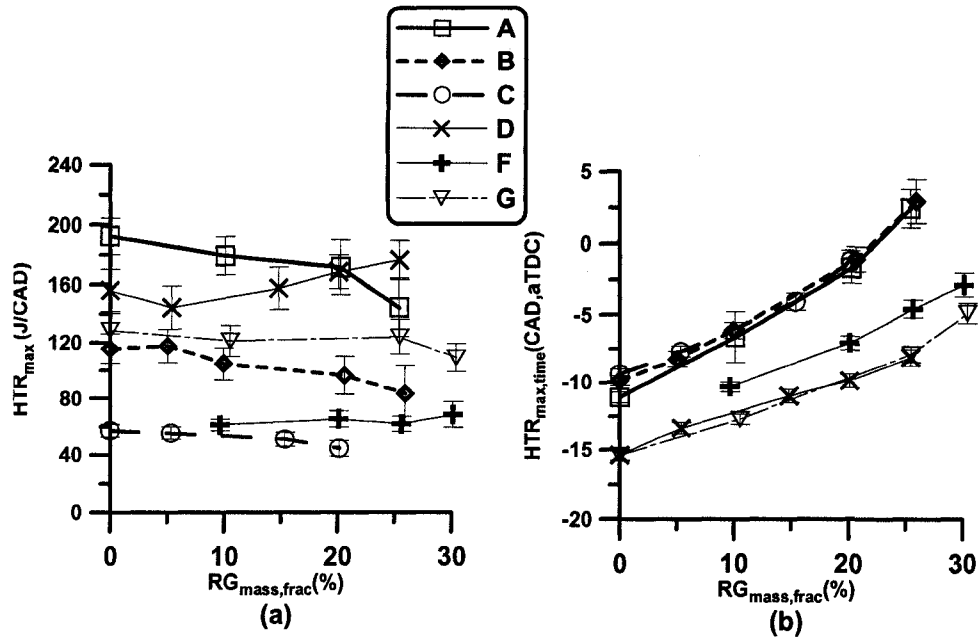


Figure 4.12: Effect of RG blend fraction on (a) maximum high temperature heat release, HTR_{max} and (b) maximum high temperature heat release timing, $HTR_{max,time}$ at constant λ and EGR for data indicated in Table 4.3, error bars indicate $\pm 2\sigma_{n-1}$

$HTR_{max,time}$. Maximum rate of heat release at the main stage of combustion, HTR_{max} , was not affected by RG addition. As LTR_{max} was less than 5% of HTR_{max} for most of the operating points, suppressing of the LTR_{max} by RG, did not exhibit a considerable effect on HTR_{max} . However, $HTR_{max,time}$ was retarded considerably by increasing RG blend fraction independent of λ and with less dependency to the EGR. The shift in $HTR_{max,time}$ was parallel for all λ -EGR constant lines.

Increasing RG blend fraction reduced LTR_{max} , hence the required energy for the main stage of combustion had to be compensated by more compression that took more time and retarded the main stage of combustion considerably. In a fuel with double-stage combustion behavior, the main combustion timing is highly dependent to the energy released at the first stage and concentration of the radical pools created after the first stage. Any small change in energy

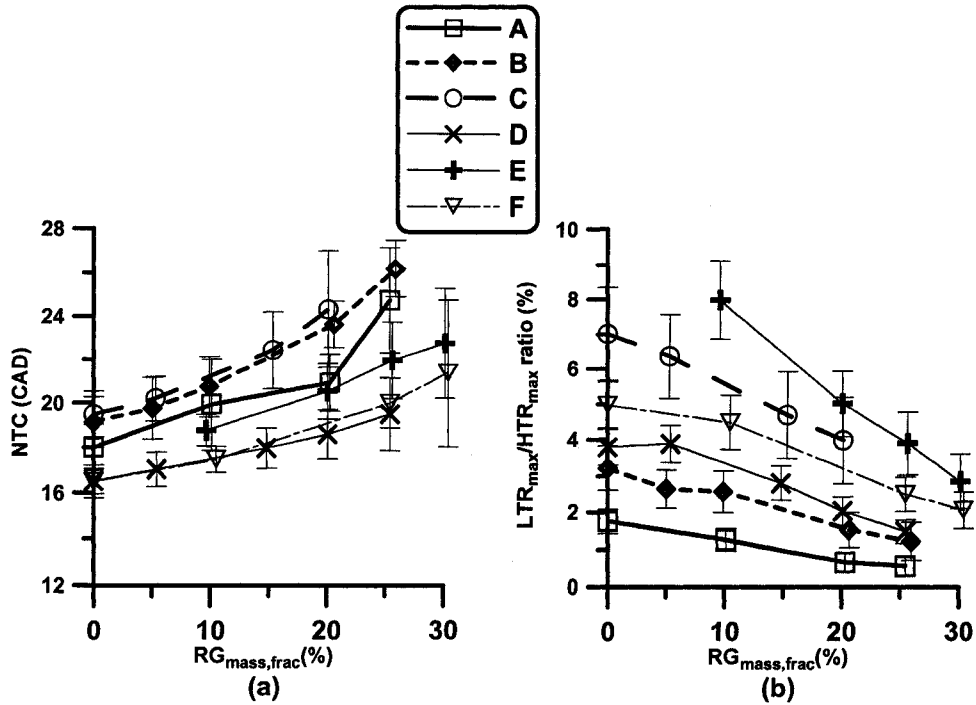


Figure 4.13: Effect of RG blend fraction on (a) negative temperature coefficient and (b) ratio of the first to second stage maximum heat release at constant λ and EGR for data indicated in Table 4.3, error bars indicate $\pm 2\sigma_{n-1}$

or radical pool concentration can change the ignition delay for the main stage of combustion, as the time is required to build up the radical pools increases. Having a relatively independent $LTR_{max,time}$ from RG blend fraction and retardation of $HTR_{max,time}$ by RG blend fraction increase, resulted to longer NTC (that was defined as the required crank angle revolution in CAD to complete the combustion from $LTR_{max,time}$ to $HTR_{max,time}$) as indicated in Figure 4.13-a. Suppression of LTR_{max} in the early stage of combustion by RG also reduced the LTR/HTR-Ratio considerably as indicated in Figure 4.13-b.

Figure 4.14 indicates the effect of RG blend fraction on pressure traces of case B in Table 4.3. Increasing RG blend fraction retarded and reduced peak cylinder pressure and decreased rate of pressure rise. In this specific case, at constant λ and EGR, increasing RG blend fraction retarded combustion peak

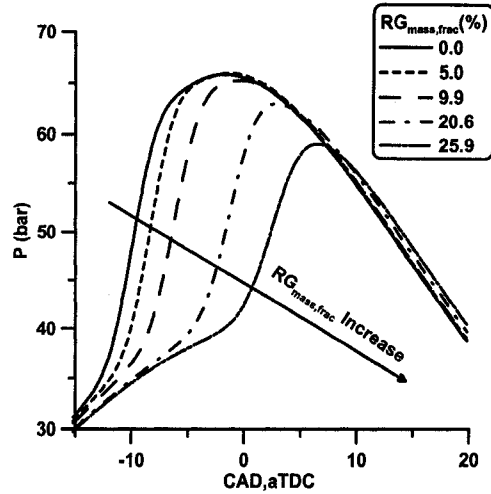


Figure 4.14: Effect of RG blend fraction on pressure traces of data group B in Table 4.3, error bars indicate $\pm 2\sigma_{n-1}$

pressure from -1.6 CAD,aTDC at RG blend fraction =0% to 6.4 CAD,aTDC at RG blend fraction =25.9%, reduced peak pressure from 65.8 bar to 59.2 bar, decreased maximum rate of pressure rise from 6.7 bar/CAD to 4.1 bar/CAD. Retardation of peak pressure and more optimized combustion timing in this case resulted to increasing indicated power, IMEP from 2.81 bar to 3.48 bar leading to efficiency increase from 29.6% to 36.4%.

For the same case of group B of Table 4.3, effect of RG on net rate of heat release, NRHR and gross accumulative heat release, GHR are indicated in Figure 4.15. The low-temperature heat release -LTR- region is magnified in Figure 4.15-a. As indicated, increasing RG blend fraction decreased first stage heat release, retarded second stage heat release, and reduced maximum rate of heat release at the second stage. The same observation can be made on the GHR plot (Figure 4.15-b). The suppression of the first stage heat release by adding RG to the intake mixture can be seen in GHR plot. It is also notable that while increasing RG blend fraction decreased the peak of net heat release rate (see Figure 4.15-a), it does not have the same effect on GHR curves. Accumulated gross heat releases were the same for all RG blend fraction values.

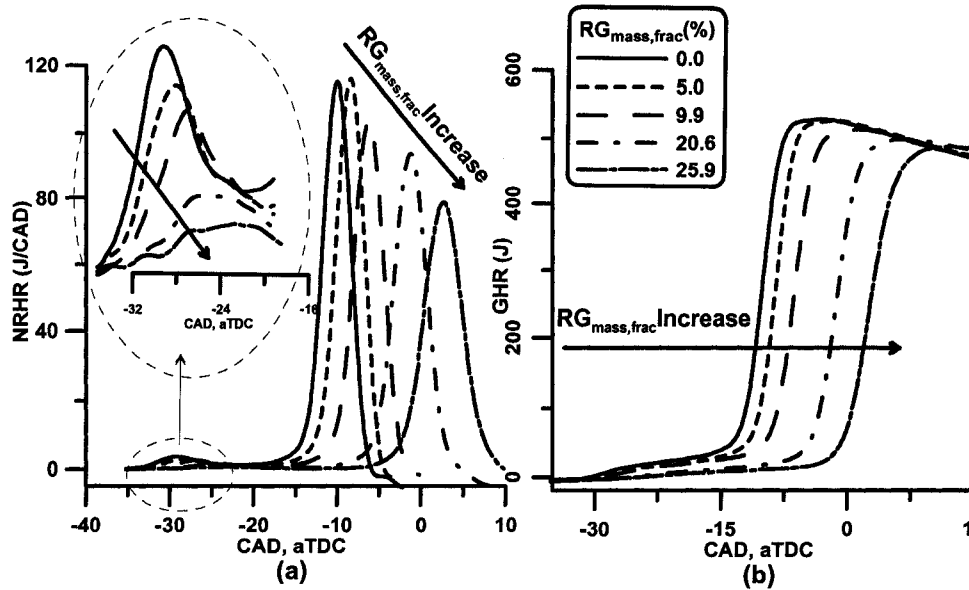


Figure 4.15: Effect of RG blend fraction on (a) net rate of heat release and (b) gross accumulative heat release of data group B in Table 4.3, error bars indicate $\pm 2\sigma_{n-1}$

As the operating points of group B were chosen such that they have an approximate constant λ and EGR, the energy content of the fuel mixture was the same for all operating points. The only difference is on thermal efficiency difference. Hence maximum values of GHR were nearly the same.

4.2.3 Pressure Trace Characteristics

Effect of RG on P_{\max} and $(dP/d\theta)_{\max}$ is indicated in Figure 4.16. All of the operating points were located under rate of pressure rise of 10 bar/CAD. Similar to naturally aspirated case (Figure 4.4), increasing RG blend fraction decreased both P_{\max} and $(dP/d\theta)_{\max}$ at constant λ and EGR for some of the data groups of Table 4.3. More precisely, increasing RG blend fraction decreased P_{\max} and $(dP/d\theta)_{\max}$ of groups A, B, and C of data in Table 4.3, but had limited or no effect on the rest of constant λ cases. For those cases that RG reduced P_{\max} , 10% RG blend fraction increase, reduced P_{\max} by about 2.5 bar

and $(dP/d\theta)_{\max}$ by 0.7 bar/CAD. These results were significantly lower than the naturally aspirated cases in which increasing RG blend fraction by 10% decreased P_{\max} by 3 bar and $(dP/d\theta)_{\max}$ by 2.5 bar/CAD. The reduction in naturally aspirated cases was because of narrow operating range and knocking condition. High rate of pressure rise was increased by knocking and RG was effective on reducing knock intensity. In the supercharged case however, most of the cases were chosen in the lean region that there were not extensive knocking and hence, RG blending did not change the rate of pressure rise considerably. This was also seen in Figure 4.10 in which effect of RG blending on combustion duration was negligible.

Effect of RG on knocking intensity of the combustion is indicated in Figure 4.17. Knocking intensity is indicated with two parameters of $P_{k.Acc.}$ and $RMS_{Acc.}$. Combustion knocking has similar trend to P_{\max} and $(dP/d\theta)_{\max}$ in

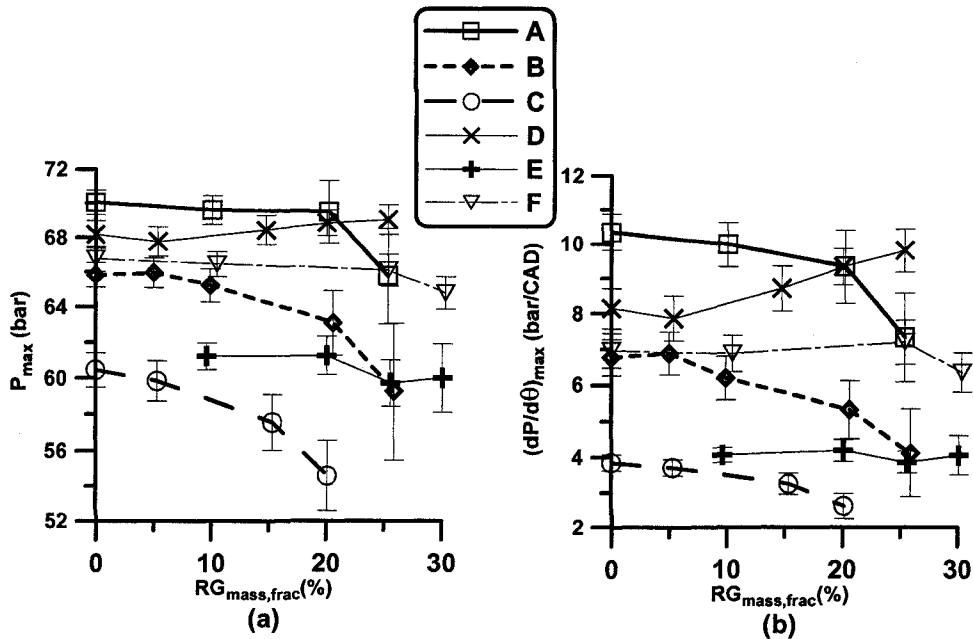


Figure 4.16: Effect of RG blend fraction on (a) cylinder maximum pressure and (b) cylinder maximum pressure rise rate at constant λ and EGR for data indicated in Table 4.3, error bars indicate $\pm 2\sigma_{n-1}$

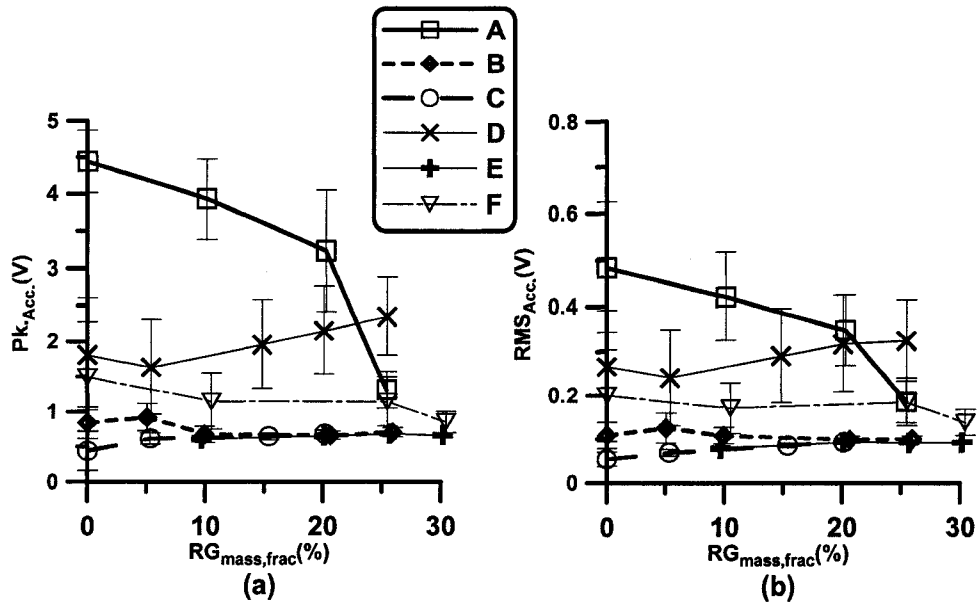


Figure 4.17: Effect of RG blend fraction on knock intensity parameters of (a) average maximum peak-to-peak accelerometer voltage and (b) average root mean square of accelerometer voltage at constant λ and EGR for data indicated in Table 4.3, error bars indicate $\pm 2\sigma_{n-1}$

Figure 4.16. Due to the nature of knocking (it may appear several times among non-knocking cycles), the error bars of knocking intensities are large as they calculated based on the standard deviation of means of values among 100 consecutive collected cycles. For most of the operating points, as the operation was around lean limit, knocking oscillation indicated by accelerometer output was minimum. For those points located at high side of power, increasing RG blend fraction decreased knock intensity considerably.

4.2.4 Engine Operating Parameters

Figure 4.18 shows the relation of RG blend fraction with IMEP and COV_{IMEP} at constant λ and EGR. Similar to naturally aspirated cases (Figure 4.5), increasing RG blend fraction increased IMEP and did not change cyclic variation considerably. 10% increase in RG blend fraction caused an average of 0.25

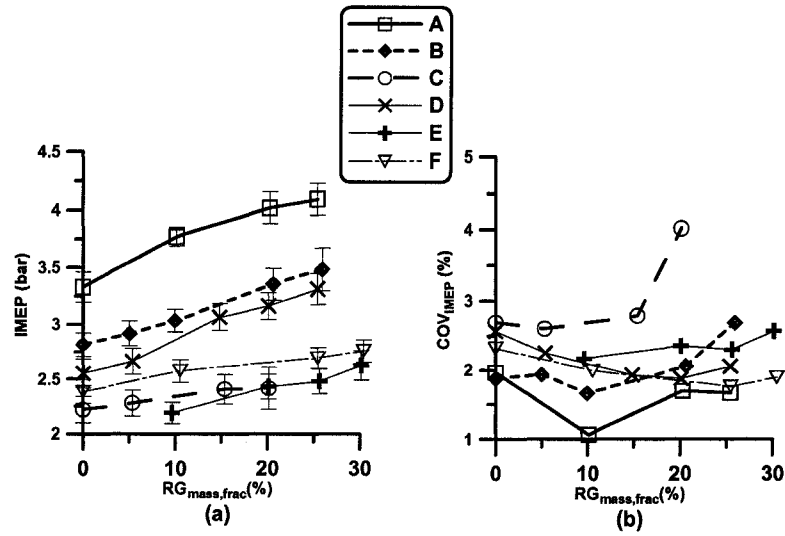


Figure 4.18: Effect of RG blend fraction on (a) IMEP and (b) COV_{IMEP} at constant λ and EGR for data indicated in Table 4.3, error bars indicate $\pm 2\sigma_{n-1}$

bar increase in IMEP, because of more optimized combustion timing. This caused increase in thermal efficiency (η_{th}) by an average of 2.8% for 10% RG

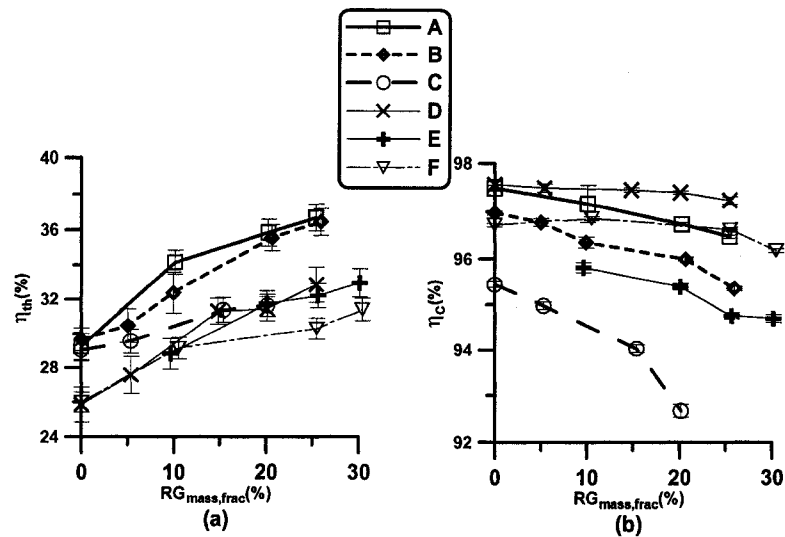


Figure 4.19: Effect of RG blend fraction on (a) η_{th} and (b) η_c at constant λ and EGR for data indicated in Table 4.3, error bars indicate $\pm 2\sigma_{n-1}$

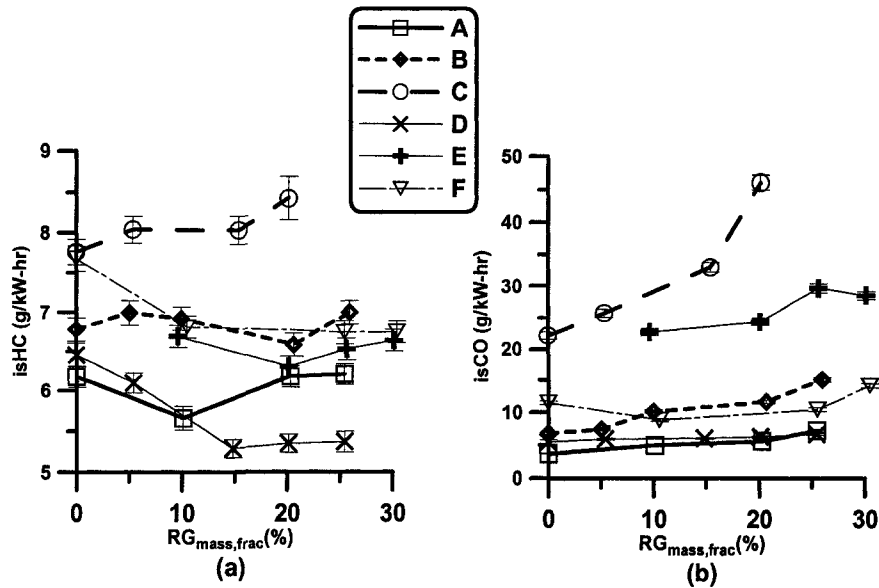


Figure 4.20: Effect of RG blend fraction on (a) indicated specific HC and (b) indicated specific CO at constant λ and EGR for data indicated in Table 4.3, error bars indicate $\pm 2\sigma_{n-1}$

blend fraction increase as indicated in Figure 4.19-a. 10% RG blending by mass contributes to less than 1% total energy loss due to reforming. Hence, RG blending overall caused thermal efficiency gain. The maximum achieved efficiency was the highest indicated thermal efficiency obtained during this study. It was around the values that was expected from highly efficient HCCI combustion. The values of thermal efficiency was expected to be increased by RG blend fraction increase as IMEP was increased at constant λ -EGR rates (constant energy input to the engine).

Combustion efficiency remained almost constant or slightly decreased by increasing RG blend fraction as indicated in Figure 4.19-b very similar to naturally aspirated case in Figure 4.6.

Approximate constant combustion efficiency with RG blend fraction variation is explained by approximate indicated specific HC and CO emissions in Figure 4.20. Both emissions remained constant or slightly increased when RG blend

fraction was increased. As replacing a high carbon fuel such as n-Heptane with a low carbon fuel such as RG reduced number of carbon atoms per mole in the combustion, constant HC emissions or slightly increased HC emission can be translated to high unburned fuel emissions. Increasing RG blend fraction increased unburned fuel fraction even further. CO increase was a direct result of the presence of CO in the main fuel (RG has 25% by volume CO in this case).

4.3 RG Composition Effects

Simulated RG was provided from high pressure tanks for the purpose of this study. In practice, RG composition varies depending on the base fuel, reforming technique, and reforming condition such as type of catalyst, temperature, and pressure.

Many reformer studies have focused on producing RG with H₂ content of 99.9% for the purpose of fuel cell applications. However, for IC engine application the type and condition of reforming can be more flexible as both H₂ and CO are flammable gases and contain chemical energy. As two possible extreme cases, two RG composition were considered for further analysis as indicated in Table 4.4.

In addition to H₂ and CO, RG always includes some inert gases such as CO₂, N₂, water vapor and other negligible combustion products. This can always be compensated by part of the EGR used during this study. For example, at

Table 4.4: A comparison of selected RG composition properties

Property	RG 75/25	RG 50/50
Composition (Volume %)	75% H ₂ / 25% CO	50% H ₂ / 50% CO
Composition (Mass %)	18%H ₂ / 82%CO	7%H ₂ / 93%CO
Composition (Energy)	72.5%H ₂ / 27.5%CO	48%H ₂ / 52%CO
Molecular Weight (kg/kmol)	8.5	15
Lower Heating Value (kJ/kg)	29,800	17,700
Stoichiometric air/fuel ratio	3.2	4.8

Table 4.5: Initial conditions for two cases of RG 75/25 and RG 50/50, n-Heptane HCCI combustion

RG Com- position	CR	$T_{\text{intake,mix}}$	Intake absolute pressure	Speed	EGR
50/50	11.8	100	144.1 ± 0.4	800	52.3 ± 1.8
75/25	11.8	100	143.9 ± 0.3	800	51.7 ± 1.0

RG blend fraction =10% and a stoichiometric mixture for n-Heptane HCCI combustion, 10% of fuel mass and less than 0.7% of intake mixture is occupied by RG. If it is assumed that RG is a product of partial oxidation with air, and 75% of RG mixture is inert gases, the total amount of EGR that has to be counted for inert gas part of RG is 0.5% of intake mixture. Hence, in this case 0.5% of EGR (as EGR is also quantified by % intake mixture) is considered as inert gas fraction of RG.

Two RG compositions of RG 75/25 and RG 50/50 was used for the case of n-Heptane (see Table 4.4). The operating region of n-Heptane HCCI combustion blended with two compositions of RG is indicated in Figure 4.21 with initial conditions indicated in Table 4.5.

RG 75/25 cases exhibited wider operating range than that of RG 50/50. Constant λ -RG pairs of points as indicated in Figure 4.21-a have been selected for comparison.

Figure 4.22 shows that pairs of constant λ -RG blend fraction have similar IMEP considering the cyclic variation of IMEP indicated by error bars. Note that the trend of IMEP versus RG blend fraction in Figure 4.22 is not a true representative of the effect of RG blending on IMEP as both RG and λ were changed simultaneously. However, for each pairs of RG 75/25 and RG 50/50 points, λ , RG, and all other initial conditions are relatively constant. Figure 4.22 shows that for RG 75/25 cases, indicated power was slightly lower than those of RG 50/50 points at identical λ and RG blend fraction. The small difference in the initial point that has been shown with RG blend fraction =0% is due to experimental repeatability errors. For the rest of pairs of points,

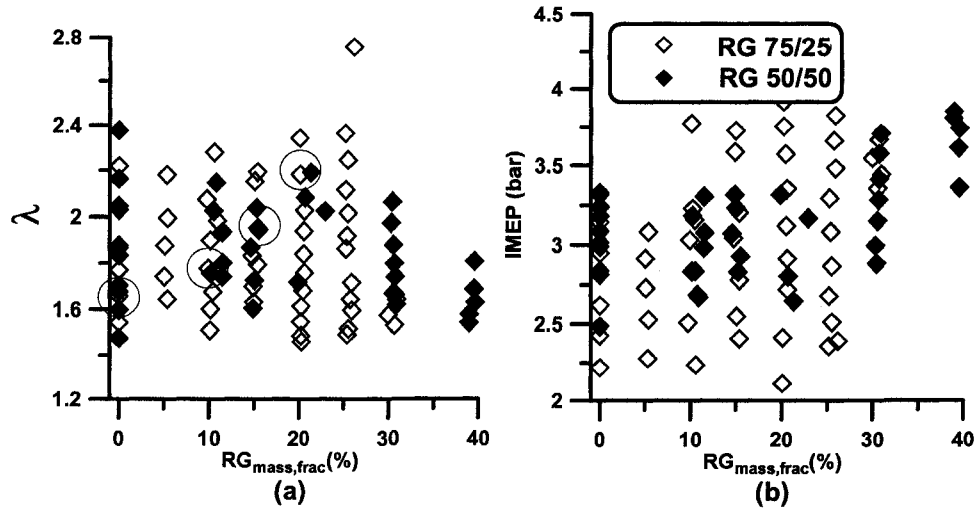


Figure 4.21: n-Heptane fueled supercharged HCCI combustion enriched with RG (a) λ -RG and (b) IMEP-RG operating windows, initial conditions indicated in Table 4.5

the difference in IMEP came from difference in fuel energy utilization as shown in Figure 4.23.

Figure 4.23 shows that efficiencies for both RG 50/50 and RG 75/25 cases for

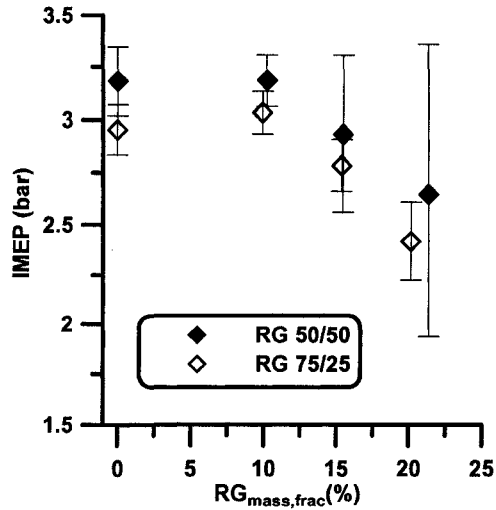


Figure 4.22: IMEP variation for the cases of λ -RG constant, initial conditions indicated in Table 4.5, error bars indicate $\pm 2\sigma_{n-1}$

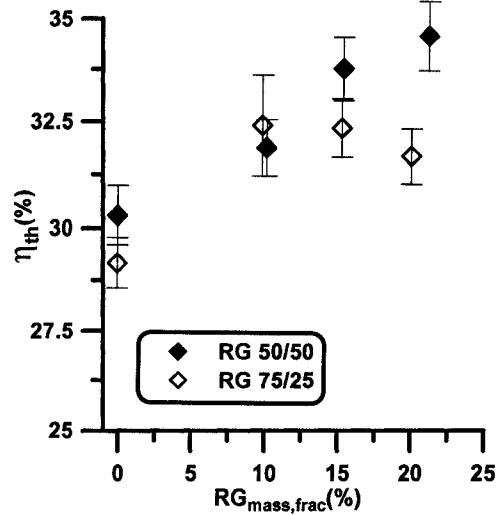


Figure 4.23: Effect of RG composition on indicated thermal efficiency of n-Heptane HCCI combustion, initial conditions indicated in Table 4.5, error bars indicate $\pm 2\sigma_{n-1}$

n-Heptane increases while increasing RG blend fraction and decreasing λ . Except for the maximum RG blend fraction case for RG 75/25 that efficiency was reduced. This was caused by high cyclic variation and misfiring and partial burning at high RG blend fraction for the case of RG 75/25.

Figure 4.24-a and -b shows the effect of RG composition on start of combustion and combustion duration. Similar effects were observed for both RG composition cases with more stronger effect on combustion timing variation belonging to RG 75/25. Note that retardation of combustion timing by RG blend fraction increase in Figure 4.24 cannot be used as a basis of combustion timing retardation (as λ is just constant for each pair of RG 75/25 and RG 50/50 points). Figure 4.24 shows that for the same amount of RG blending and at any constant λ , combustion timing retardation is more strong for the case of RG 75/25. The difference between combustion phasing retardation became more obvious at high RG blend fraction. For example, at RG blend fraction =10%, RG 75/25 combustion timing was about 3 CAD more retarded than RG 50/50 combustion timing, while it was about 5 CAD more

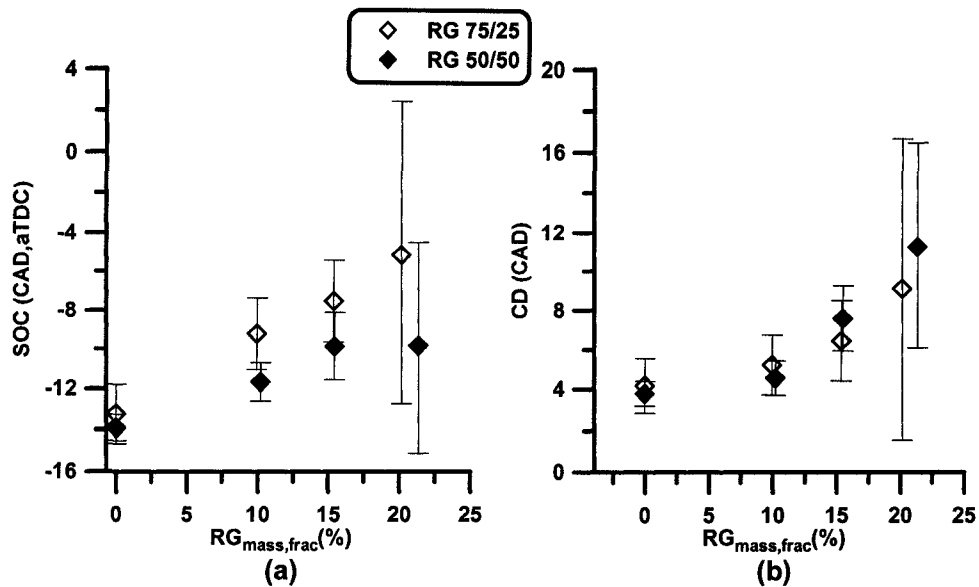


Figure 4.24: Effect of RG composition on (a) start of combustion and (b) combustion duration of n-Heptane HCCI combustion, initial conditions indicated in Table 4.5, error bars indicate $\pm 2\sigma_{n-1}$

retarded for RG blend fraction = 20%. This shows that RG 75/25 was more effective on combustion timing retardation. A sudden increase in HC emission and drop in thermal efficiency at high RG blend fraction for the case of RG 75/25 is explained by more effectiveness of combustion timing retardation. At high RG blend fraction, large combustion timing retardation, caused very low combustion temperature, misfiring, partial burning, and excessive cyclic variation. Figure 4.24 also shows that despite of variation of RG composition, combustion duration (CD) remained relatively constant for both cases of RG 75/25 and RG 50/50. As start of combustion was considered as 10% of heat release, alteration of combustion timing could not cover the low temperature heat release which was less than 5% for all experimental cases examined in this study as indicated in Figure 4.25.

Figure 4.25 indicates the difference between heat release characteristics alteration of two cases of RG 75/25 and RG 50/50. Figure 4.25-a shows that increasing RG blend fraction almost had no effect on timing of first stage heat

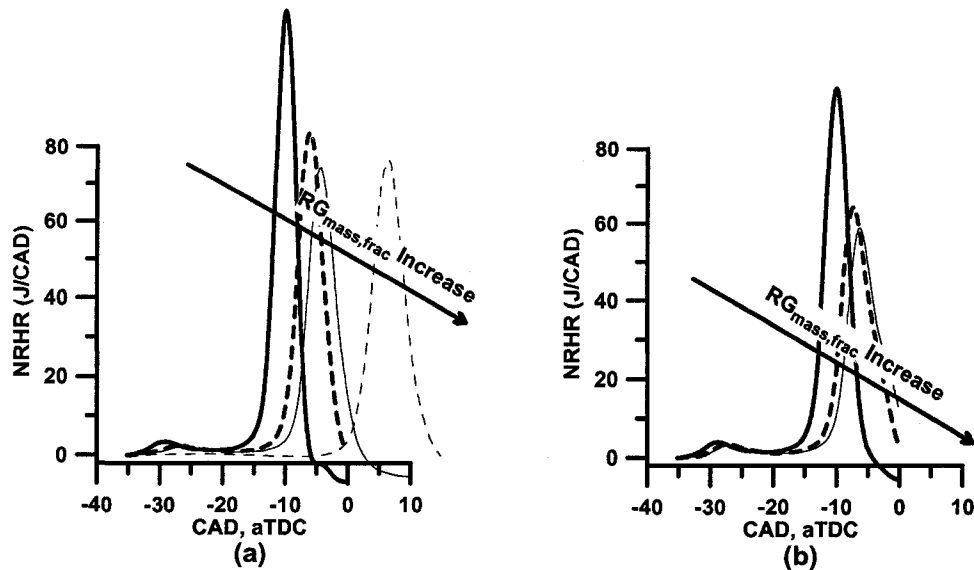


Figure 4.25: Effect of RG composition on net rate of heat release for (a) RG 75/25 and (b) RG 50/50 for n-Heptane HCCI combustion, initial conditions indicated in Table 4.5, error bars indicate $\pm 2\sigma_{n-1}$

release. Maximum heat release rate at the second stage was reduced. Negative temperature coefficient (NTC) region was extended, and second stage of heat release was retarded. The same observation is made in Figure 4.25-b for the case of RG 50/50. The difference lies on the amount of retardation on the second stage of heat release. For the case of RG 50/50, retardation of high-temperature heat release was significantly less than that of RG 75/25 case.

Experimental results showed that both RG compositions of RG 75/25 and RG 50/50 had similar effects on HCCI combustion, i.e. retardation of combustion timing. The amount of retardation in the RG 50/50 case was less than that of RG 75/25. If RG is used as a control agent, the current engine control systems are capable of adjusting SOC by alteration of RG fraction blended with the base fuel on a cycle-by-cycle basis, compensating for variation of H_2 content in RG.

Figure 4.26-a shows the effect of RG composition on unburned hydrocarbons emissions. Despite of similar λ and IMEP for each pair of data points, RG

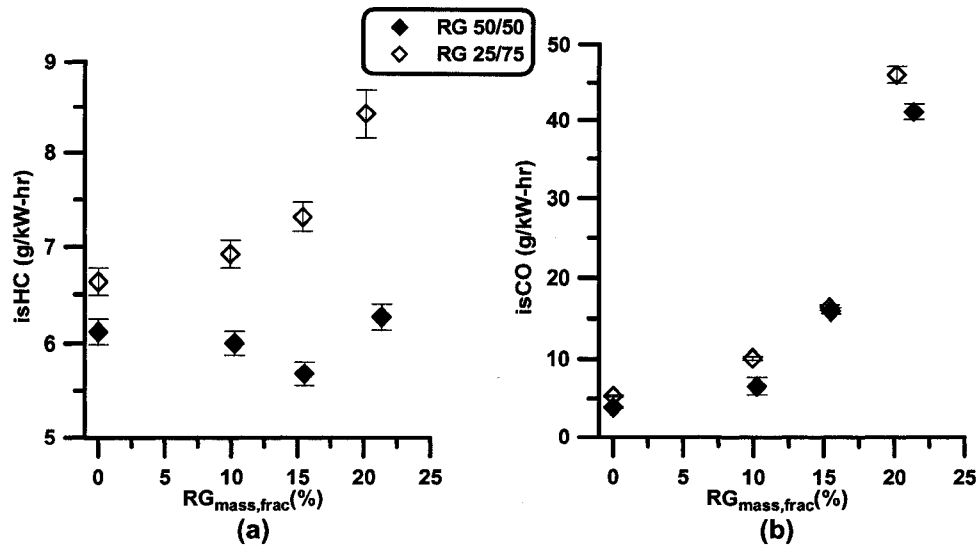


Figure 4.26: Effect of RG composition on (a) HC and (b) CO emissions of HCCI n-Heptane combustion, initial conditions indicated in Table 4.5, error bars indicate $\pm 2\sigma_{n-1}$

75/25 cases produced much higher HC emissions than that of RG 50/50 that was caused by later combustion timing by RG 75/25. While HC of RG 75/25 was much higher than that of RG 50/50, CO trends were similar for two RG composition cases as indicated in Figure 4.26.

4.4 Modeling Analysis

4.4.1 Description of Chemical Kinetic Model

A Matlab based stand alone chemical kinetic model was developed for investigation of RG effects on reactions of natural gas and n-Heptane in an HCCI engine. Chemical Kinetic model description, equations, heat transfer sub-models, and other related information are in a series of publications by Kongsereparp and Checkel ([163, 164, 165, 166]).

The model was named as ChemComb and was capable of simulation of one complete cycle of an HCCI combustion engine in two configurations of single

zone (SZM) and multi-zone (MZM). The initial conditions of the model are determined either by pressure and temperature, and equivalence ratio (ϕ) at intake valve close event, or mass flow rates of intake mixture.

In the cited reference there are examples of ChemComb-SZM and ChemComb-MZM validations, using pressure trace and engine operating parameters from the current CFR engine data. It was shown that ChemComb-MZM is capable of predicting a true pressure trace similar to the experiments with precise prediction of combustion timing, P_{\max} , $(dP/d\theta)_{\max}$, IMEP, and other engine operating parameters. Recursive nature, using a novel approach to determine initial condition, estimating inhomogeneity schemes, and optimizing coefficients of rate of reactions for each point enabled ChemComb-MZM to have a predictive quality, which makes it a favorable choice for design purposes.

In the current study, ChemComb was used to reveal the chemistry and thermodynamic of combustion up to the point of ignition. Using ChemComb-MZM for this purpose is over-rated and is not computationally efficient. Hence, ChemComb-SZM package was used to model the experimental point emphasizing that the model was used for the early stages of combustion.

ChemComb-SZM was found to be relatively accurate for predicting start of combustion in the range of cyclic variations of experimental results. Due to its single zone nature (having one zone and no inhomogeneity schemes for temperature, residuals, and ϕ), ChemComb-SZM over predicts P_{\max} , $(dP/d\theta)_{\max}$, IMEP, and other engine parameters. It cannot predict combustion duration (CD) accurately. However, as the purpose of modeling analysis was focused on the early stages of combustion, using ChemComb-SZM was accurate and computationally economic.

4.4.2 Effect of RG on n-Heptane HCCI Combustion Timing

As described, ChemComb-SZM was relatively accurate for predicting start of combustion in the range of cyclic variations of experimental results for n-

Heptane HCCI combustion. The n-Heptane chemical kinetic mechanisms used for this study was adopted from a semi-reduced chemical kinetic mechanism developed by Golovichev [167] with 290 reactions and 57 species.

4.4.3 Comparison of Simulation and Experiments

Data set F of experimental data was chosen from Table 4.3 for further analysis. Experimental pressure traces were compared to pressure traces predicted by ChemComb-SZM. For each operating points, as pressure traces were collected by 100 consecutive cycles, three cycles were chosen. These three cycles are the cycles that have maximum P_{\max} , minimum P_{\max} , and median P_{\max} , respectively. For simplicity, these cycles were named P_{\max} (maximum P_{\max}), P_{\min} (minimum P_{\max}), and P_{median} (median P_{\max}).

Figures 4.27, 4.28, 4.29, and 4.30 show examples of the comparison of experimental pressure traces with ChemComb-SZM in the early stages of combustion. Each figure contains the three P_{\max} , P_{\min} , and P_{median} . Figure 4.31 shows that SOC prediction of ChemComb-SZM is within or at the vicinity of cyclic variation error of experimental SOC.

4.4.4 Detailed Analysis using ChemComb-SZM

Figure 4.32 shows the cylinder temperature and pressure traces predicted by ChemComb-SZM for data set F in Table 4.3. Experimental results showed the combustion retardation of 3.7 CAD for 10% RG blending. The ChemComb-SZM results showed the combustion retardation of 3.1 CAD for 10% RG blending. Considering the single zone nature of the model and combustion variability of the experiments, the results were in the acceptable range. In Figure 4.32-a, the temperature during the late stages of compression and early stages of low temperature heat release is magnified. As shown with arrows in the magnified section of Figure 4.32, before the low-temperature heat release, compression temperature of high RG blend fraction operation points was

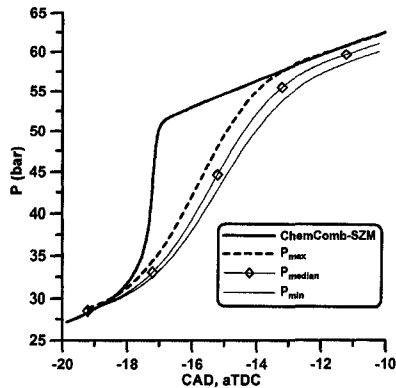


Figure 4.27: Comparison of experimental pressure traces of point 1, data set F with ChemComb-SZM, Experiment: supercharged n-Heptane HCCI combustion, $N=800$ RPM, $CR=11.8$, $T_{intake,mix}=100$ °C, Intake pressure =143 kPa, $\lambda=2.94$, $EGR=19.9\%$, RG blend fraction =0.0%

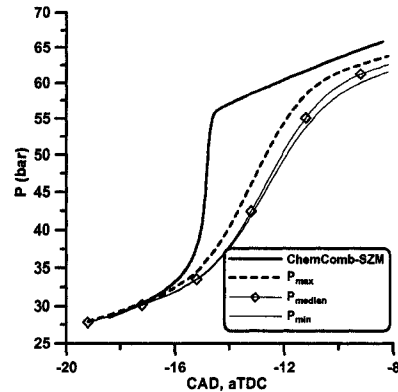


Figure 4.28: Comparison of experimental pressure traces of point 2, data set F with ChemComb-SZM, Experiment: supercharged n-Heptane HCCI combustion, $N=800$ RPM, $CR=11.8$, $T_{intake,mix}=100$ °C, Intake pressure =143 kPa, $\lambda=2.98$, $EGR=21.9\%$, RG blend fraction =10.5%

higher than that of low RG blend fraction . This was associated with higher ratio of specific heats of RG blended points. This effect was similar to that of natural gas HCCI combustion temperature profile blended with RG (see Figure 6.32). The subsequent behavior with n-Heptane differs from natural gas. After low-temperature combustion initiation, the temperature profile flipped over and high RG blend fraction points was associated with lower combustion temperature that was an indication of suppression of first stage heat release by RG. Because of combustion suppression by RG, main stage combustion was retarded considerably as indicated in Figure 4.32-a and -b similar to the experimental results.

Low temperature heat release behavior is monitored by looking at key species concentrations during LTR and NTC. Figure 4.33 shows the typical mole fraction of the key intermediate hydroxyl (OH), hydrogen peroxide (H_2O_2), and formaldehyde (CH_2O) radicals. Using any of these species demonstrates the

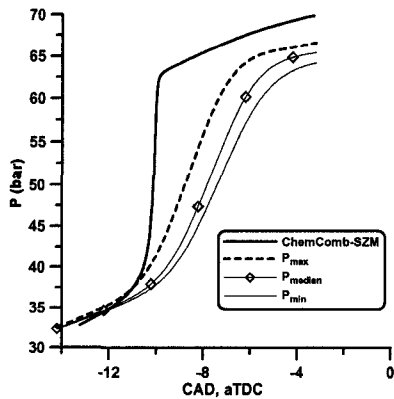


Figure 4.29: Comparison of experimental pressure traces of point 3, data set F with ChemComb-SZM, Experiment: supercharged n-Heptane HCCI combustion, $N=800$ RPM, $CR=11.8$, $T_{\text{intake,mix}}=100$ °C, Intake pressure =143 kPa, $\lambda=2.98$, $EGR=20.9\%$, RG blend fraction =25.4%

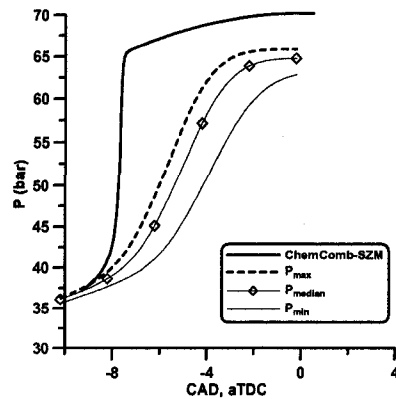


Figure 4.30: Comparison of experimental pressure traces of point 4, data set F with ChemComb-SZM, Experiment: supercharged n-Heptane HCCI combustion, $N=800$ RPM, $CR=11.8$, $T_{\text{intake,mix}}=100$ °C, Intake pressure =143 kPa, $\lambda=3.00$, $EGR=21.7\%$, RG blend fraction =30.4%

variation of low-temperature heat release characteristics during and after LTR. Figure 4.34 shows the effect of RG on mole fraction of CH_2O and H_2O_2 . Increasing RG blend fraction decreased both molar fraction of intermediate radical species and retarded the timing of radical production. For the case of CH_2O in Figure 4.34-a, two cases of high RG blend fraction exhibited an increasing trend of CH_2O mole fraction during NTC that could be resulted from non-optimized combustion mechanisms for high RG blend fraction cases. Figure 4.35 shows the similar trend for OH mole fraction. In Figure 4.35-a increasing RG blend fraction decreased OH mole fraction considerably and retarded the maximum mole fraction. Consequently, the main stage of combustion was retarded as indicated in Figure 4.35-b.

As an example of reaction rates, in the main mechanisms used in ChemComb-SZM ([167]), reaction 122 is the main source of H_2O_2 production during NTC.

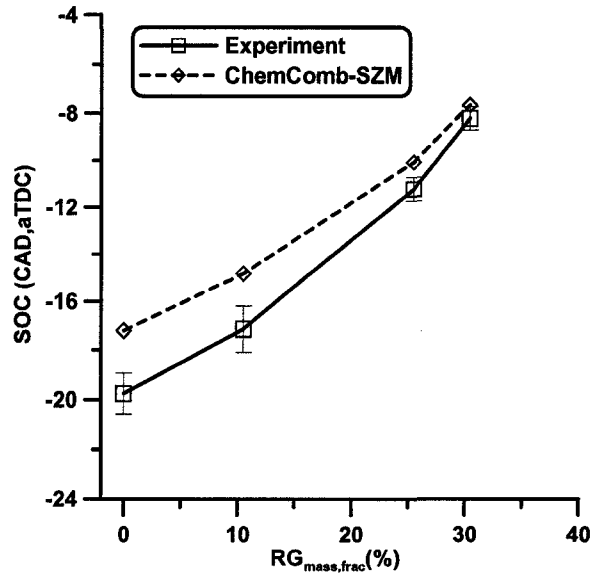


Figure 4.31: A comparison of combustion timing (SOC) prediction by ChemComb-SZM with actual experimental combustion timing for data set F in Table 4.3, error bars indicate $\pm 2\sigma_{n-1}$

Equation 4.1 shows reaction 122.

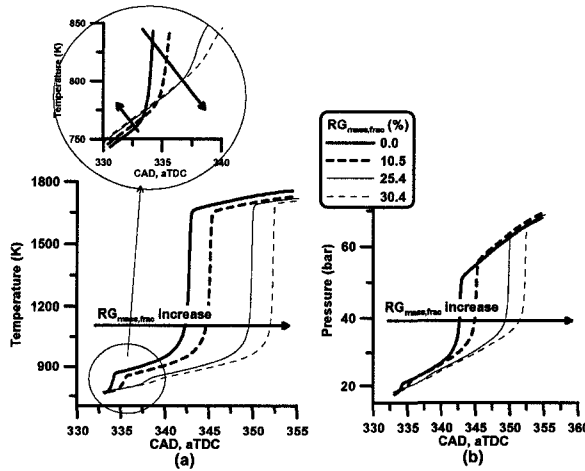
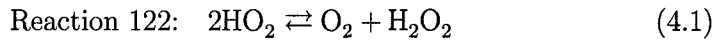


Figure 4.32: ChemComb-SZM simulation results for (a) in-cylinder temperature during and after compression, and (b) predicted pressure for data set F in Table 4.3

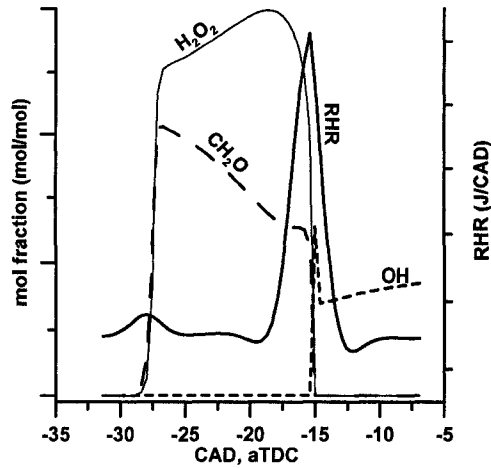


Figure 4.33: Typical mole fraction traces of key species of OH, H_2O_2 , and CH_2O compared with net rate of heat release in n-Heptane HCCI combustion

Reaction 123 is the main reaction responsible for H_2O_2 destruction that is indicated in Equation 4.2.

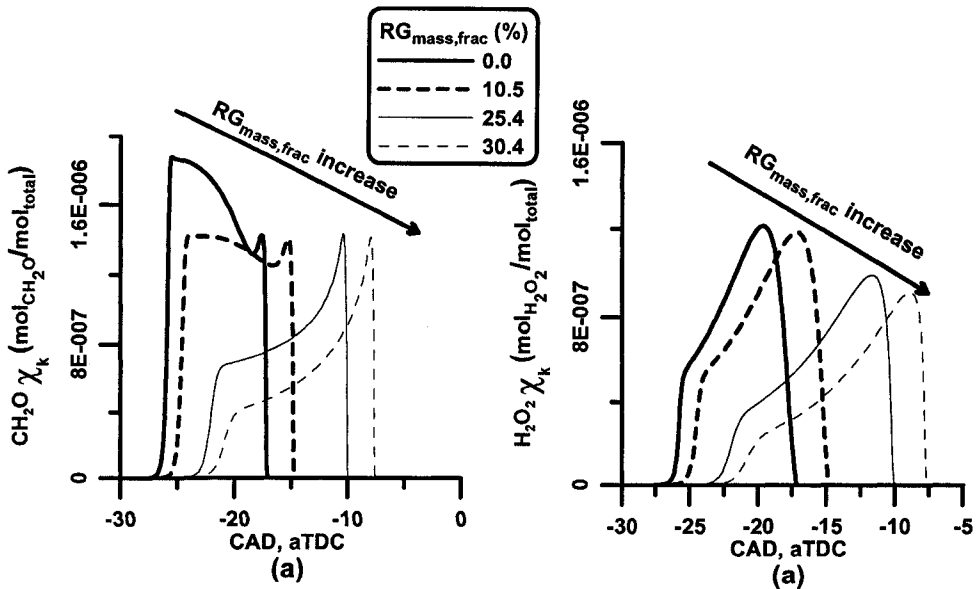
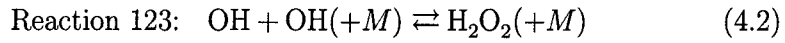


Figure 4.34: Effect of RG on mole fraction of (a) Formaldehyde (CH_2O), and (b) hydrogen peroxide (H_2O_2), n-Heptane HCCI combustion simulated by ChemComb-SZM for data set F in Table 4.3

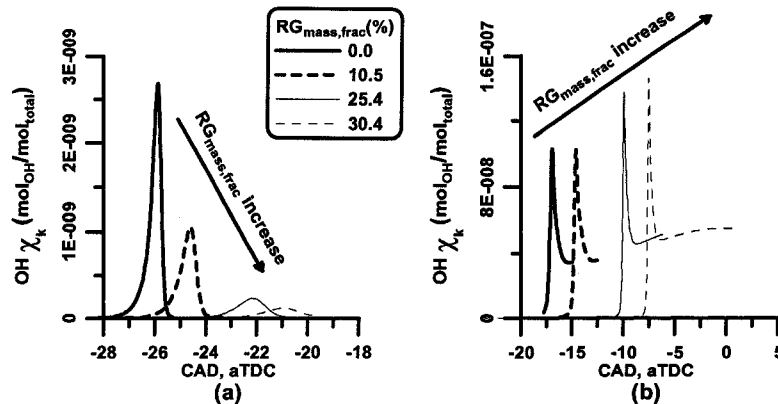


Figure 4.35: Effect of RG on mole fraction of OH during (a) low-temperature heat release, and (b) early stage of high temperature heat release, n-Heptane HCCI combustion simulated by ChemComb-SZM for data set F in Table 4.3

Figure 4.36 shows the effect of RG on the $[H_2O_2]$ rate of production ($d[H_2O_2]/dt$) for the main H_2O_2 production reaction (Equation 4.1), the main H_2O_2 destruction reaction (Equation 4.1), and total rates (that is the summation of all production and destruction reactions for H_2O_2).

Figure 4.36 shows that the dominant effect of RG blend fraction increase was increasing both production and destruction rates for the intermediate radicals. The same observation can be made for formaldehyde radicals. Note that the X-axis in Figure 4.36 is temperature and advancing the peak production and destruction rates for H_2O_2 does not mean that they happened earlier in the cycle. In fact, looking at Figure 4.32-a shows that any certain temperature happened later in the cycle. Figure 4.36-c that increasing production and destruction rates of reactions are in the favor of destruction rates as increasing RG blend fraction caused an overall faster destruction of H_2O_2 radicals.

The key reaction changes happened during LTR. Looking at LTR stage for both hydroxyl and hydrogen peroxide radicals, the concentrations of both radicals were decreased during LTR (see Figures 4.34-b and 4.35-a). While mole fractions of OH and H_2O_2 were decreased during LTR, the ratio of maximum

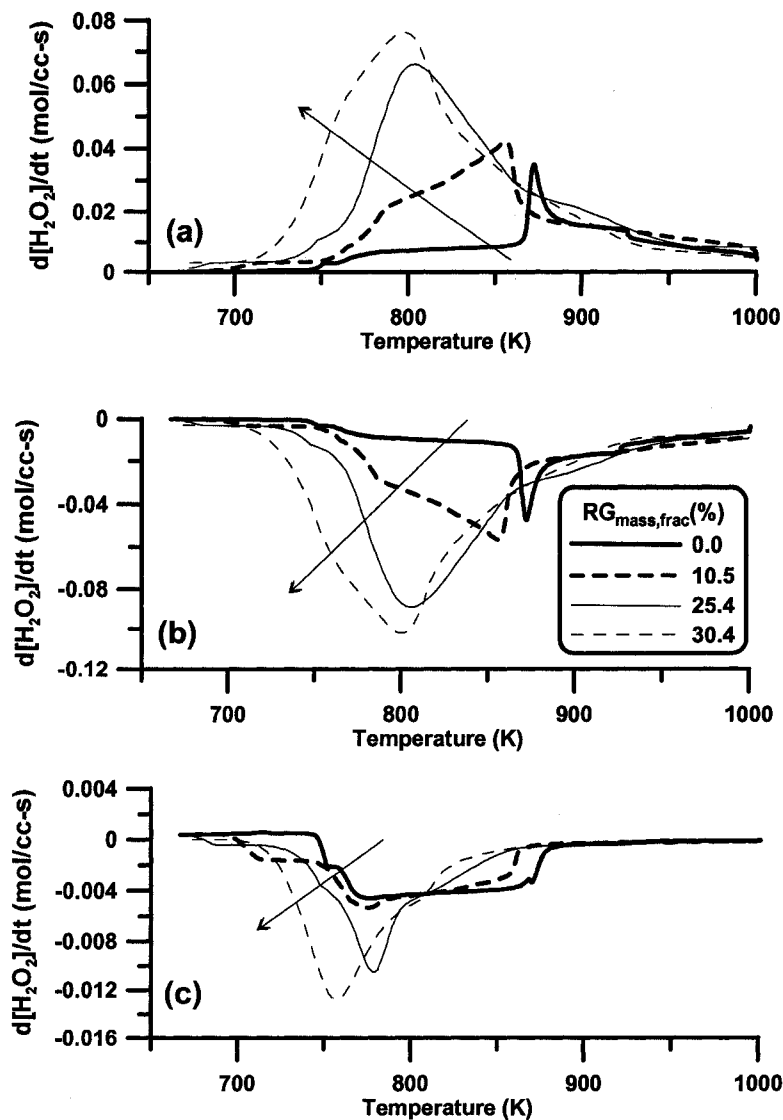


Figure 4.36: Effect of RG on the reaction rates of H₂O₂, (a) production rate for reaction 122 (Equation 4.1), (b) production rate for reaction 123 (Equation 4.2), and (c) total production rate (from all 19 reactions), n-Heptane HCCI combustion simulated by ChemComb-SZM for data set F in Table 4.3

OH mole fraction over maximum H₂O₂ mole fraction also were decreased considerably. This ratio shifted progressively from [OH]=0.94 [H₂O₂] to [OH]=0.08 [H₂O₂] as RG blend fraction went from 0% to 30% as shown in Figure 4.37. RG

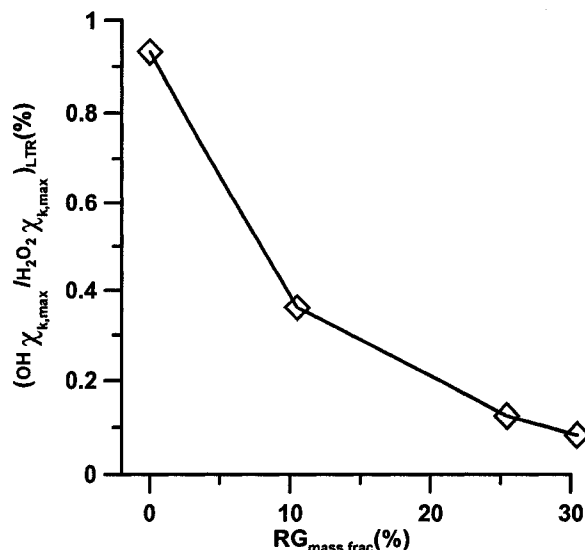
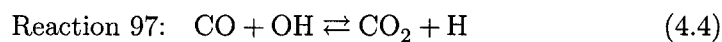
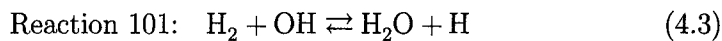


Figure 4.37: Effect of RG on the ratio of maximum mole fraction during LTR for OH over H₂O₂

during LTR replaces most of the OH by H₂O₂ radicals through the following series of reactions:



Produced H quickly combines with OH, forms HO₂, and then with another H atom forms H₂O₂. OH is a highly active radical at low-temperatures, while both HO₂ and H₂O₂ are almost inert during LTR. Converting highly reactive OH radicals to less reactive HO₂ and H₂O₂ resulted to lower chain branching reactions during LTR that led to less heat release during NTC and retardation of HTR. These results are in agreement with findings of previous modeling and chemical kinetic studies such as [168] and [169].

4.4.5 Detailed Analysis of Effect of RG Composition on HCCI Combustion Timing

All six cases of constant IMEP-RG blend fraction in Figure 4.21 were examined using ChemComb-SZM. Figure 4.38 shows the comparison of SOC for two cases of RG 75/25 and RG 50/50 and experimental results versus modeling estimation of SOC. ChemComb-SZM was able to predict most of the experimental SOC within the cyclic variation limits for both cases. For the case of RG 50/50, experimental results showed 2.4 CAD retardation in combustion timing with 10% RG and ChemComb-SZM predicted 1.7 CAD in SOC retardation. For the case of RG 75/25, experimental results showed 5.5 CAD in SOC retardation for 10% RG blend fraction increase and ChemComb-SZM predicted 5.1 CAD in combustion timing retardation. Figure 4.39 shows the mass fraction of hydrogen peroxide H_2O_2 as a function of CAD and RG for

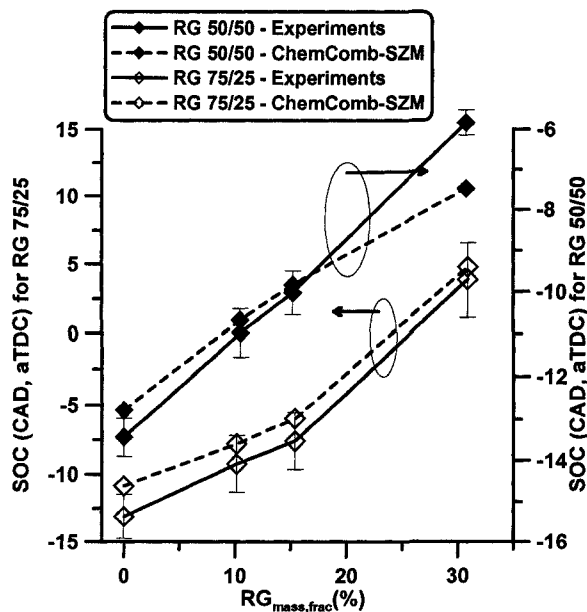


Figure 4.38: A comparison of SOC prediction by ChemComb-SZM and experimental results for two cases of RG 75/25 (left Y-axis) and RG 50/50 (right Y-axis), error bars indicate $\pm 2\sigma_{n-1}$

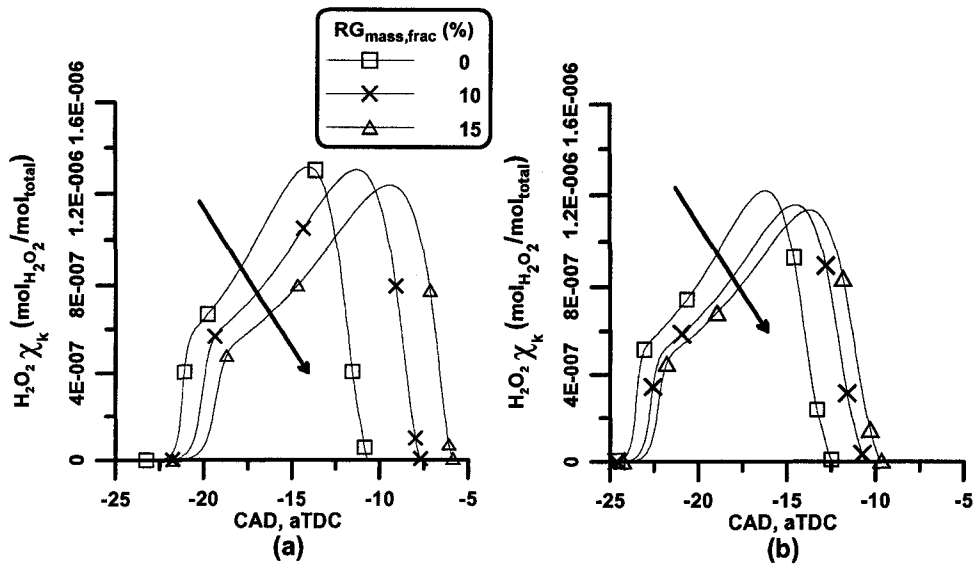


Figure 4.39: Effect of RG composition on H_2O_2 mole fraction for (a) RG 75/25 and (b) RG 50/50 cases

both cases of RG 75/25 and RG 50/50. Increasing RG blend fraction for both cases of RG 75/25 in Figure 26-a and RG 50/50 in Figure 26-b shows that mole fraction of intermediate radicals were reduced using both RG compositions. The suppression of intermediate radical of H_2O_2 was less for the case of RG 50/50. Less radical pool suppression in RG 50/50 case, caused the less delayed combustion. Based on H_2O_2 radical concentration indicated in Figure 4.39, the combustion timing indicated by timing of maximum H_2O_2 molar concentration was retarded by 5 CAD for RG 75/25 and less than 3 CAD for RG 50/50 case. The modeling analysis confirmed the retardation of combustion timing by RG enrichment for both RG compositions of RG 75/25 and RG 50/50. As Figure 4.38 shows, RG 75/25 is more effective on combustion timing retardation that was in agreement with findings of Shudo et al (2004,2007) [107, 169] where they examined different effect of RG on HCCI combustion of DME. Increasing H_2 fraction in RG in those cases also increased effectiveness of combustion retardation using RG in double-stage combustion of DME. The results are also in agreement with the results of a numerical study done by

Subramanian et al (2007) [168]. Using a detailed chemical kinetic mechanisms and a reduced chemical kinetic mechanism they concluded that at temperatures around 600K, the presence of CO lengthens the n-Heptane HCCI ignition delay by 5%-10%, while H₂ addition lengthens the ignition delay by 10%-15%. Both H₂ and CO have the properties of the suppression of radical pools. In the chemical kinetic mechanism used, reaction 97 (Equation 4.4) and reaction 101 (Equation 4.3) are responsible for OH radical consumptions by CO and H₂, respectively (Reaction numbers are referred to original chemical kinetics mechanism by Golovichev [167]). Similar to what has been discussed in [169], Reaction 101 is 3-6 times faster than Reaction 97 in the temperature ranges of 700K-1000K when the low-temperature oxidation happens. Migrating from RG 75/25 to RG 50/50 is in the favor of reaction 97 and radical consumption by RG was reduced. The similarity of combustion suppression of H₂ and CO makes it quite favorable as a mean of combustion timing control for fuels with double-stage combustion. Practically it means that small variation of onboard fuel reformer output due to operational variations is negligible in combustion timing control effect of RG.

4.5 Summary

Effect of RG on the operating region of n-Heptane HCCI combustion was studied in two operating modes of naturally aspirated and supercharged with two RG compositions of RG 75/25 and RG 50/50.

In the naturally aspirated mode at moderate intake pressure and temperature, dominant chemical effects caused a shifting in the operating window boundary. RG pushed back the knock boundary toward the higher indicated power regions. In this case, increasing RG blend fraction while keeping all other influential parameters constant, retarded combustion timing, increased combustion duration and reduced combustion intensity. Increasing RG blend fraction by 10%, retarded combustion timing by 6 CAD. Based on the base-line engine

tests, the same retardation of combustion timing would require the increase in λ by 1.2 unit that would reduce IMEP by 3.3 bar. The retardation of combustion timing by 6 CAD with 10% RG blending, increased thermal efficiency (η_{th}) and IMEP by 1-2%. The efficiency drop for 10% reforming is less than 1% of total cycle energy. Hence, reforming provided a wide combustion timing variation with no loss or slight gain in IMEP and efficiency (as the result of more optimized combustion timing). The increase in RG blend fraction by 10% also decreased P_{max} by 3 bar and $(dP/d\theta)_{max}$ by 2.5 bar/CAD.

In the supercharged mode, most of the effects were similar to naturally aspirated mode. The retardation of combustion timing and all subsequent effects were observed. However, the shifting of the operating region was toward lean side instead of rich side due to the difference of operating parameters between naturally aspirated and supercharged modes. At the elevated intake pressure, the amount of energy delivered to the engine in each cycle was higher causing the operating region to shift more toward lean side in comparison with naturally aspirated mode. The operational boundary was limited by misfiring/partial burning instead of low load limit in the naturally aspirated case. RG blending caused more stable combustion in the lean side overcoming unstable combustion and caused the shifting of the lean boundary. In the naturally aspirated mode, the low power boundary could not be shifted any more. Looking at the experimental rate of heat release, increasing RG blend fraction at constant λ and EGR, reduced the first stage of heat release, prolonged NTC and retarded the timing of HTR. The difference between after-compression temperature of naturally aspirated and supercharged modes caused a less strong low temperature heat release for supercharged case that resulted to slightly less effectiveness of RG blending on combustion timing control. Similar to naturally aspirated mode, the retardation of combustion timing for the case of supercharged was estimated 4.4 CAD for 10% RG blend fraction increase. It was shown in the base-line tests that λ was not effective on n-Heptane HCCI combustion timing control.

It was found that n-Heptane with low (0) octane and high (54) cetane is not a suitable fuel for HCCI combustion. Once autoignition starts, the ignition delay is short and the combustion timing is too advanced. To obtain proper HCCI combustion, the fuel must be ignited easily, (like n-Heptane or another fuel with strong double-stage autoignition behavior), and the combustion duration must be long enough to create an optimum combustion timing, (unlike n-Heptane). The high cetane number of fuels like n-Heptane is favorable for use in a diesel engine because it provides a short ignition delay. However, unless it is combined with fuel properties that also provide long combustion duration, the implementation of a dual mode diesel/HCCI engine is problematic. This study has shown RG blending with a high cetane fuel to be effective at maintaining the possibility of autoignition initiation while also retarding and extending the combustion timing toward more optimized phasing. This indicates that partial reforming of diesel and diesel-like fuels provides a path towards practical CI/HCCI dual mode engines.

Both two extreme cases of RG compositions of RG 75/25 and RG 50/50 had similar effect on n-Heptane HCCI combustion timing retardation, except that retardation of combustion timing was less for the case of RG 50/50. Both H_2 and CO had LTR reaction suppression while H_2 was more effective and increasing CO fraction in RG reduced the effectiveness of RG on combustion timing retardation. Increase of RG blend fraction by 10% for RG 75/25 case, retarded combustion timing by 5.5 CAD, while it retarded combustion timing by 2.4 CAD for a similar case of RG 50/50.

Single zone chemical kinetic model (ChemComb-SZM) confirmed the experimental results. Increasing RG blend fraction, increased the temperature during the compression. After LTR initiation, the temperature profile flipped over and higher RG blend fraction was associated with lower temperature indicating the suppression of heat release during LTR. Looking at important radical mole fraction during LTR and NTC, it showed that all radical concentrations were decreased by RG enrichment. Both production and destruction

rates for H_2O_2 increased, and total overall reaction rates increase was in favor of destruction rate producing less H_2O_2 radical at any given temperature. RG replaced the highly active OH radicals during LTR by less reactive H_2O_2 and CH_2O and hence overall LTR heat release was decreased.

Using RG to control HCCI combustion timing of n-Heptane (and generally any low octane fuel with multiple stages combustion) was confirmed. RG was an effective combustion timing controller and an octane number enhancer agent in this study. The effectiveness of RG on combustion timing retardation and enhancing octane number was related to the engine operating conditions (supercharged or naturally aspirated) and RG composition (H_2 content of RG). While keeping all other influential parameters constant, RG can potentially alter the combustion timing toward more optimized timing increasing indicated thermal efficiency. n-Heptane was the most suitable fuel for RG blending HCCI combustion timing control in this study.

Reformer Gas Application in Combustion Timing Control of iso-Octane

Partial content of this chapter has been published as a peer reviewed Society of Automotive Engineering (SAE) technical paper in 2007 [170].

This chapter specifically focuses on Homogenous Charge Compression Ignition (HCCI) combustion of high octane Primary Reference Fuels (PRFs) and investigates the effects of Reformer Gas (RG) blending on engine and combustion parameters using heat release analysis of experimental results. iso-Octane (PRF100) and PRF80 were used as the test fuels.

iso-Octane is referred to 2,2,4-trimethylpentane among several possible isomers of C_8H_{18} . It is one of the standard fuel which is used in binary mixture of standard PRF. With octane number of 100, it has high resistance to autoignition and its HCCI combustion is difficult to achieve. For example, Christensen et al (1997) [171] operated iso-Octane HCCI engine at nominal compression ratio (CR) of 21 and intake temperature between 40 °C and 120 °C and λ between 3 and 9. Gnanam et al (2006) [172] operated iso-Octane HCCI engine at compression ratio of 20 and intake temperature of 120-150 °C.

Fundamental combustion studies have been done on iso-Octane as a simple

reference fuel. For example, Ryan et al (1980) [173] studied its burning velocity and showed that iso-Octane laminar burning velocity is normally less than n-Heptane, methane, and propane and more than methanol. Also, Curran et al (2002) [174] developed a comprehensive oxidation mechanism for iso-Octane. HCCI combustion of high octane fuels is a favorable topic of HCCI research as it represents the actual condition of a gasoline spark ignition (SI) engine operated in HCCI mode. HCCI combustion is known for high thermal efficiency. Part load low efficiency is the SI engine's downside. Hence operating a SI engine at part load in the HCCI mode to achieve high thermal efficiency is the main practical target. In this study, iso-Octane and high PRFs such as PRF80 was investigated as representatives of gasoline fueled HCCI engine.

5.1 Effect of RG on High Octane PRF HCCI Combustion in the Naturally Aspirated Mode

5.1.1 Operating Region

As indicated in [170], three data sets were examined in the naturally aspirated mode to illustrate effects of octane number and compression ratio. A mixture of 75% H₂ and 25% CO was used as the simulated RG mixture for these sets of experiments. The initial and operating conditions for three sets of data are indicated in Table 5.1.

Among all operating points, Set I of data with higher octane number (100) and highest CR had the most limited operating region as indicated in Figure 5.1.

Table 5.1: Operating conditions of naturally aspirated iso-Octane and PRF80 HCCI combustion

Data Set	Set I	Set II	Set III
PRF	100	100	80
CR	16.0	14.4	14.4
T _{intake,mix} (°C)	140	140	140
Speed (RPM)	700	700	700

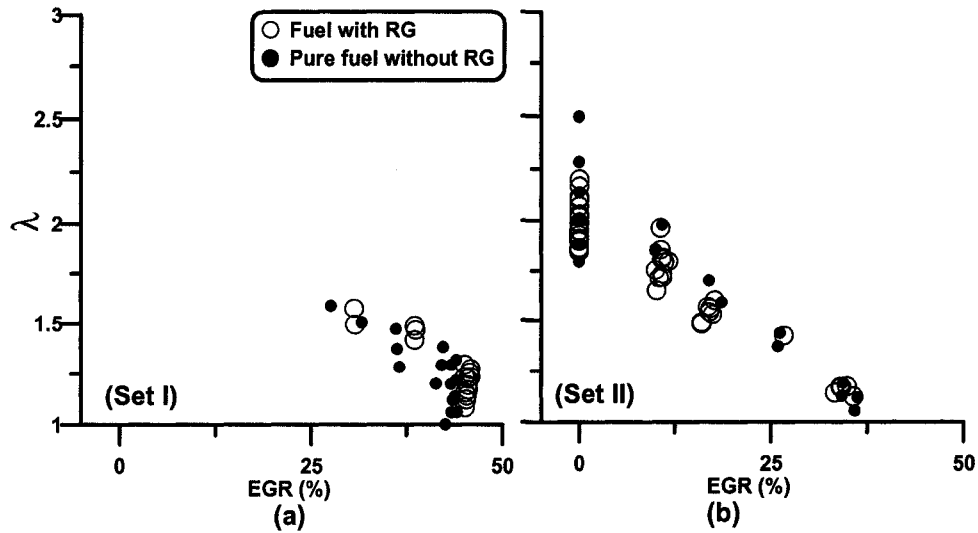


Figure 5.1: EGR- λ operating region for (a) Set I and (b) Set II of data indicated in Table 5.1, iso-Octane HCCI combustion, naturally aspirated mode

The operating regions for iso-Octane (PRF100) was extremely limited as shown in Figure 5.1 for both CRs. For high CR of 16.6, the minimum possible EGR fraction for any possible operation was about 25%. Even high EGR fraction did not expand operating region. As cited from previous studies, a proper HCCI engine operation fueled with high octane fuels such as iso-Octane is achievable only at very lean mixtures ($\lambda > 3$). This high value of λ was impossible to achieve as CFR engine suffered from high internal friction and needed a minimum amount of energy to operate at a constant speed. Decreasing CR from 16 to 14.4 expanded the operating region on the rich side.

Decreasing octane number of the base fuel from 100 to 80 (going from Set II to Set III) expanded the operating region even further and shifted the operating region toward leaner mixtures as indicated in Figure 5.2.

Both Figures 5.1 and 5.2 indicate that adding RG to high octane fuel HCCI combustion did change the operating region boundaries. No considerable shifts on operating region boundaries were observed on operating region location

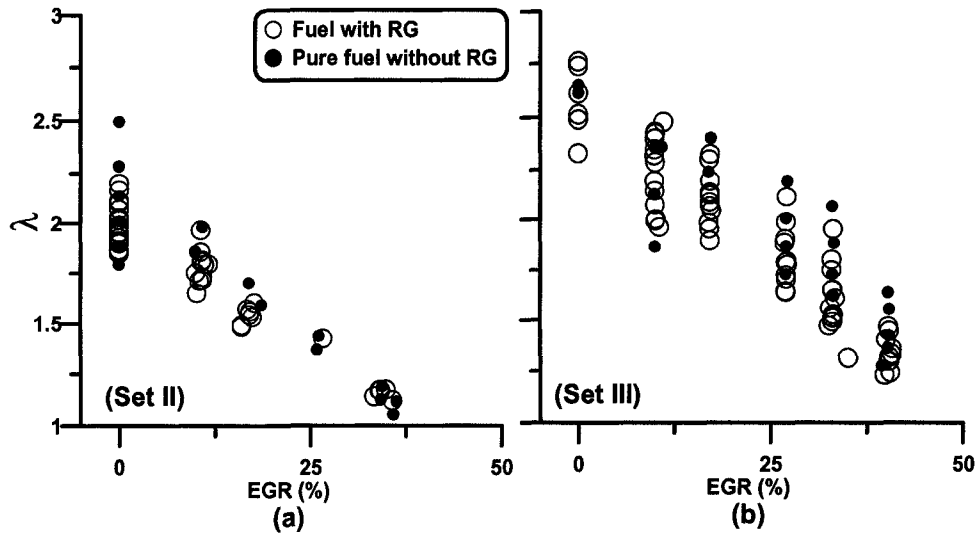


Figure 5.2: EGR- λ operating region for (a) Set II and (b) Set III of data indicated in Table 5.1, PRF100 and PRF80 HCCI combustion, naturally aspirated mode

inside λ -EGR map. It has been shown already that there is a certain operating region shifting when RG was blended with natural gas or low octane fuels such as n-Heptane. Even though octane number is not a proper indication of HCCI combustion behavior, the limits of knocking, misfiring, and low load was greatly a function of octane number and other initial conditions such as $T_{\text{intake,mix}}$ and CR. RG exhibited a similar octane number to iso-Octane and PRF80 and operating region did not change considerably. Extremely limited operating region using high octane fuels caused a limited number of data points to be collected at constant λ and EGR for further analysis. Three sets of data point with an approximate constant λ and EGR retrieved from iso-Octane (PRF100) and PRF80 data points (Sets II and III in Table 5.1). Table 5.2 summarizes the constant λ -EGR cases.

5.1.2 Comparison of RG Effect on PRF100 and PRF80

Combustion Timing, Combustion Duration, and Pressure Characteristics

Relatively constant indicated power and pressure characteristics were an indication of constant combustion timing and duration by RG blend fraction increase for PRF100. Figure 5.3 shows that increasing RG blend fraction did not have a significant effect on start of combustion (SOC) and combustion duration (CD) of PRF100 base fuel. For PRF80 the same Figures shows that increasing RG blend fraction retarded combustion timing and prolonged combustion duration. Increasing RG blend fraction by 10% for PRF80 case

Table 5.2: Selected constant λ -EGR cases from Table 5.1

Label	selected from Data Set	PRF	λ	EGR (%)
A	II	100	2.01 ± 0.02	0.0 ± 0.0
B	II	100	1.86 ± 0.00	0.0 ± 0.0
C	III	80	1.63 ± 0.02	33.1 ± 0.2

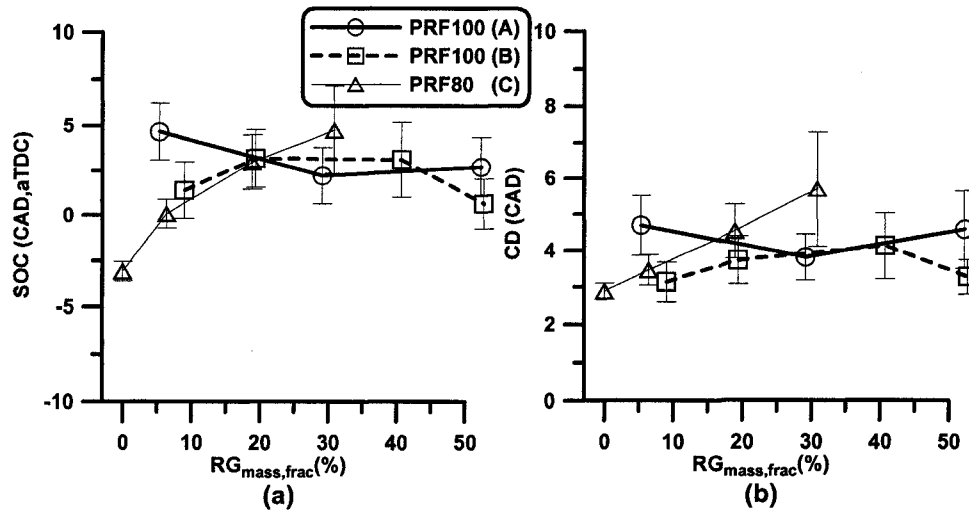


Figure 5.3: A comparison of effect of RG blend fraction on (a) start of combustion SOC and (b) combustion duration CD, PRF100 and PRF80 HCCI combustion for constant λ -EGR cases indicated in Table 5.2, error bars indicate $\pm 2\sigma_{n-1}$

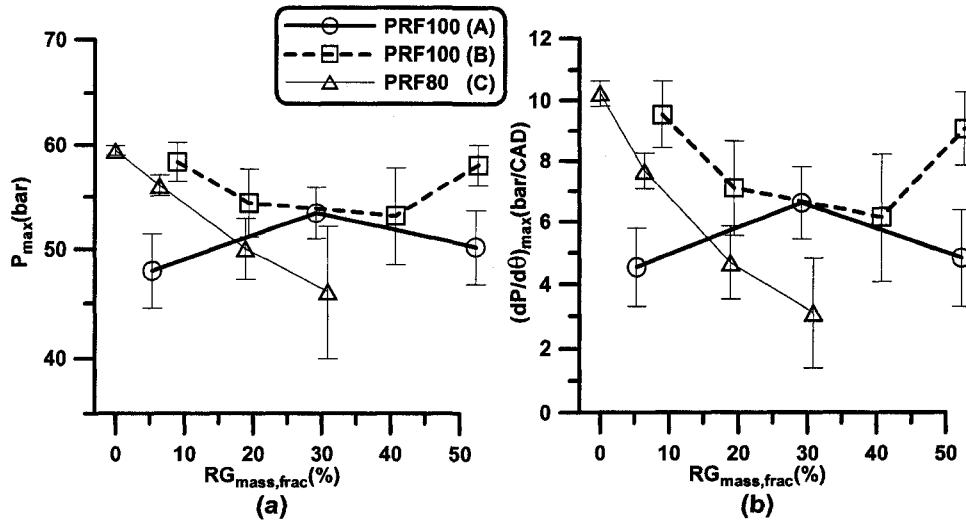


Figure 5.4: A comparison of effect of RG blend fraction on (a) P_{\max} and (b) $(dP/d\theta)_{\max}$, PRF100 and PRF80 HCCI combustion for constant λ -EGR cases indicated in Table 5.2, error bars indicate $\pm 2\sigma_{n-1}$

retarded combustion timing by 2.4 CAD and prolonged combustion duration by 0.9 CAD.

P_{\max} and $(dP/d\theta)_{\max}$ for PRF100 did not change significantly because of RG blend fraction variation relative to uncertainty error bars that comes from cyclic variation (Figure 5.4). However, for PRF80 having 20% n-Heptane that replaced iso-Octane in PRF binary mixture, caused that both P_{\max} and $(dP/d\theta)_{\max}$ decreased, because of RG blend fraction increase at constant λ and EGR very similar to n-Heptane cases. Increasing RG blend fraction for PRF80 case decreased P_{\max} by 4 bar and $(dP/d\theta)_{\max}$ by 2.2 bar/CAD.

Power, Efficiency, and Emissions

Similarity of octane number of RG and high octane fuels of PRF100 and PRF80 caused no change in operating region boundaries while using RG. Given a limited sets of constant λ and EGR in Table 5.2, Effect of RG blend fraction increase on indicated power was different on the base PRF100 and PRF80 fuels.

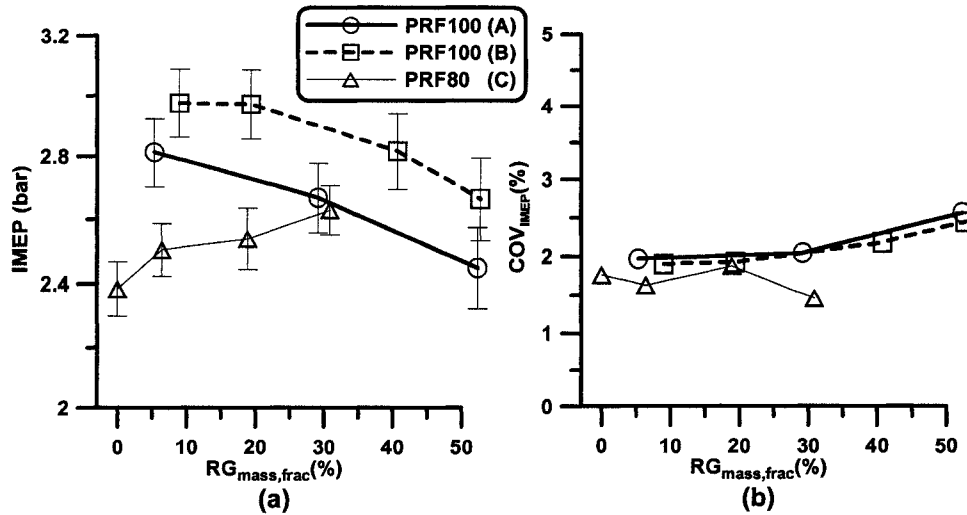


Figure 5.5: A comparison of effect of RG blend fraction on (a) indicated power and (b) cyclic variation of PRF100 and PRF80 HCCI combustion for constant λ -EGR cases indicated in Table 5.2, error bars indicate $\pm 2\sigma_{n-1}$

Even though the effects are mostly negligible in comparison with uncertainties as indicated in Figure 5.5, increasing RG blend fraction at constant λ and EGR slightly reduced IMEP for PRF100 and increased IMEP for PRF80. Increasing RG blend fraction by 10% decreased IMEP for PRF100 by 0.07 bar and increased it for PRF80 by 0.07 bar. No effect was observed on combustion stability. Higher IMEP of set B of data is because of richer air/fuel mixture in comparison with set A. Set C had lowest indicated power as EGR was much higher than that of Sets A and B. The difference between PRF100 and PRF80 was replacing some of iso-Octane by n-Heptane. n-Heptane increased low-temperature heat release characteristics. This small change had a drastic effect of RG on indicated power of the engine. Having small amount of n-Heptane, IMEP was increased by increasing RG blend fraction instead of decreasing in iso-Octane case.

Figure 5.6 shows the difference between effect of RG blend fraction on thermal and combustion efficiencies of PRF100 and PRF80 fuels. The changes in efficiencies were still not significant in both cases. The thermal efficiency in

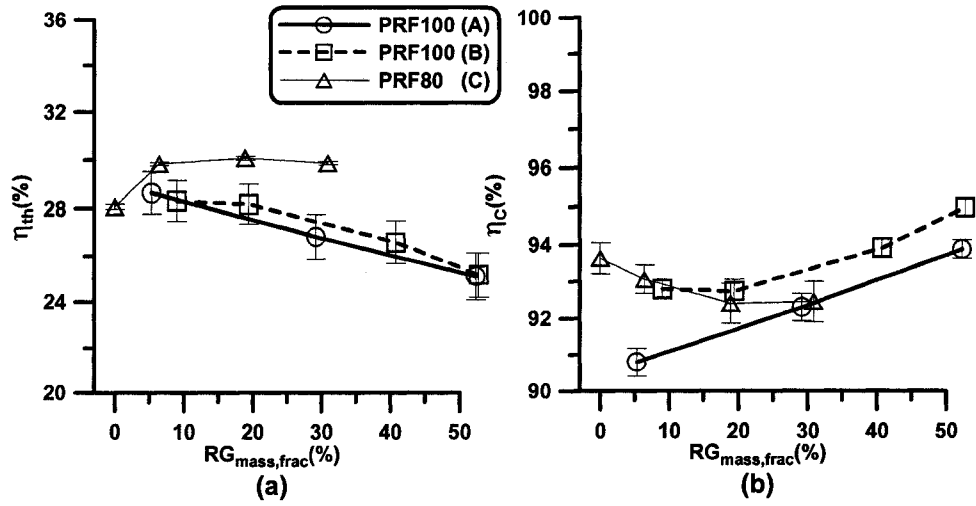


Figure 5.6: A comparison of effect of RG blend fraction on (a) indicated thermal efficiency η_{th} and (b) combustion efficiency η_c , HCCI combustion of PRF100 and PRF80 for constant λ -EGR cases indicated in Table 5.2, error bars indicate $\pm 2\sigma_{n-1}$

PRF100 cases were independent of λ and slightly decreased with RG blend fraction increase. For PRF80 case, thermal efficiency slightly increased first and remained constant. Combustion efficiency behaved differently. It increased by RG blend fraction increase for PRF100 and slightly decreased in PRF80 case.

No significant difference in IMEP and thermal efficiency by RG blend fraction variation indicates that combustion characteristics remained relatively constant. While combustion characteristics were remained constant, replacing a high carbon/hydrogen ratio fuel (iso-Octane) with RG that contains 83% by mass CO caused a slight reduction in HC and an increased in CO emissions (Figure 5.7). For both η_{th} and η_c , PRF80 behaved differently from PRF100. Increasing η_{th} and decreasing η_c for PRF80 were similar to n-Heptane cases (see Chapter 4) and decreasing η_{th} and increasing η_c were similar to natural gas cases (see Chapter 6).

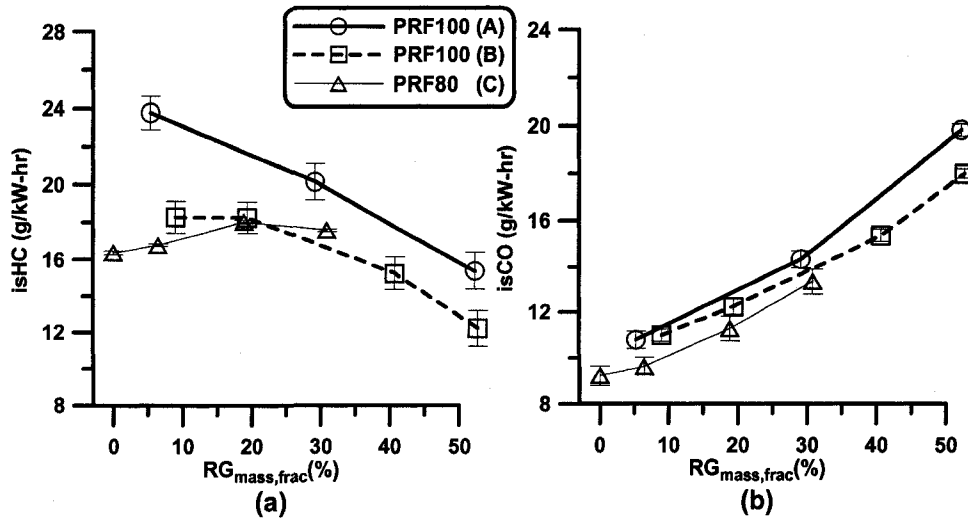


Figure 5.7: A comparison of effect of RG blend fraction on (a) indicated specific HC and (b) indicated specific CO, HCCI combustion of PRF100 and PRF80 for constant λ -EGR cases indicated in Table 5.2, error bars indicate $\pm 2\sigma_{n-1}$

5.2 Effect of RG on Supercharged iso-Octane HCCI Combustion

In the naturally aspirated mode most of the operating points were limited to near knock boundaries at which the combustion temperature was high. High combustion temperature reduced chemical effects of RG blending, which is in agreement with findings of Eng et al (2002) [114] in which two strategies were examined for EGR. Effect of RG was minimum when EGR was applied through exhaust re-breathing technique in comparison with the case that cold external EGR was applied. Supercharging the intake system of CFR engine created the opportunity of the operation of the engine near misfiring/partial boundaries where the combustion temperature was low and RG was more effective.

5.2.1 Operating Region

Wider operating region of iso-Octane HCCI combustion in the supercharged condition caused that RG blending shifted the operating region toward richer mixtures pushing back knocking boundary. In this case, a simulated RG mixture of 50% H₂ and 50% CO (RG 50/50) were used to resemble an actual gasoline fuel processor output. The effect was more obvious at low EGR rates. At maximum EGR of 40%, no RG blending was possible due to excessive combustion instability.

RG blending was more possible at low EGR rates as indicated in Figure 5.9-a. Adding RG increased autoignition resistance of the fuel mixture that could be tolerated at low EGR fractions. Increasing RG also limited the operating region in term of λ range as indicated in Figure 5.9-b. Increasing RG blend fraction in the fuel mixture limited the operating region at both rich and lean sides. At the rich side high RG blend fraction caused a fast combustion (after

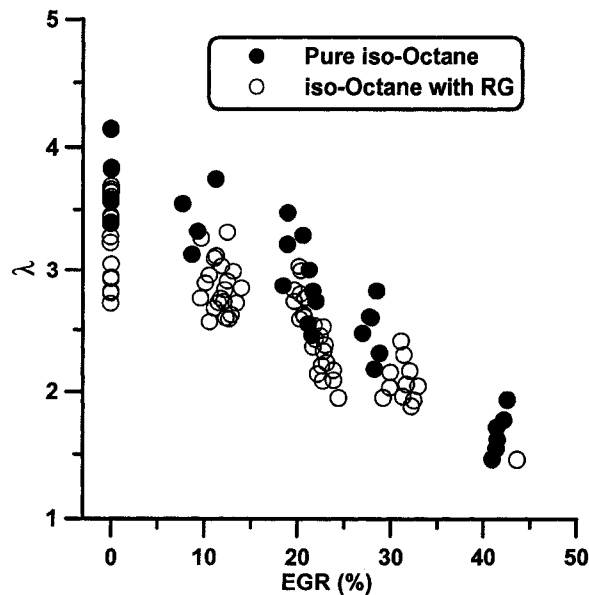


Figure 5.8: λ -EGR operating region for iso-Octane HCCI combustion in the supercharged mode with and without RG blending, N=800 RPM, $T_{\text{intake,mix}} = 100$ °C, CR=14.4

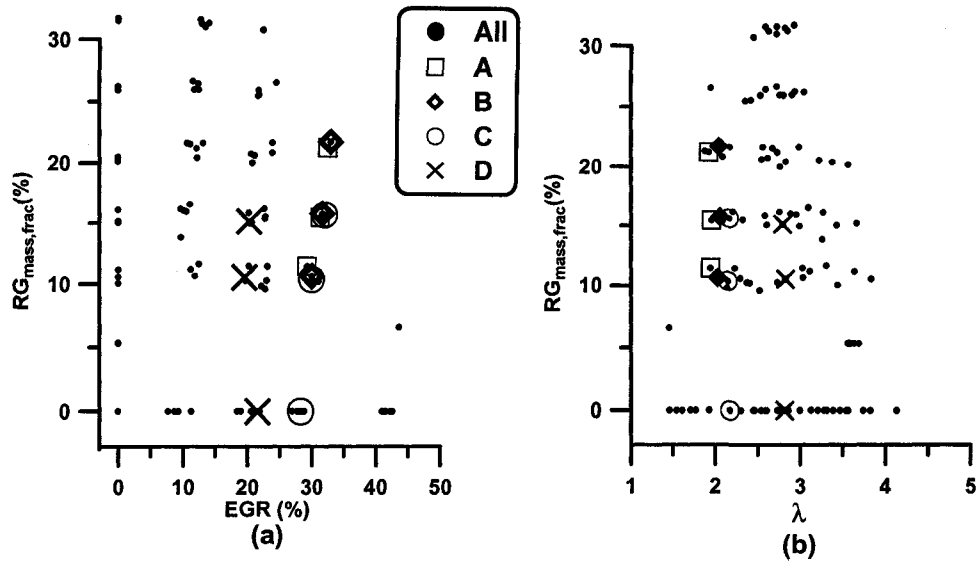


Figure 5.9: (a) RG-EGR and (b) RG- λ operating regions with indication of constant λ -EGR groups of data indicated in Table 5.3

initiation), and at the lean side misfiring and partial burning caused by high autoignition resistance of RG/fuel mixture.

A series of constant λ and EGR cases were chosen for further analysis. The changing of λ range while increasing RG blend fraction (See Figure 5.9-b) caused that limited cases were available. Table 5.3 shows λ -EGR constant cases. The selected groups of constant λ and EGR operating points are indicated in Figure 5.9.

Table 5.3: Selected λ -EGR constant groups of data, supercharged HCCI combustion of iso-Octane at N=800 RPM, CR=14.4, $T_{\text{intake,mix}} = 100 \text{ }^\circ\text{C}$

Label	λ	EGR (%)
A	1.94 ± 0.01	31.0 ± 1.6
B	2.04 ± 0.01	31.5 ± 1.5
C	2.16 ± 0.01	30.1 ± 1.9

5.2.2 Combustion Timing, Combustion Duration, and Pressure Characteristics

Effect of RG blend fraction was retardation of combustion timing for the cases of Table 5.3 while no obvious effect was observed on combustion duration that was suffering from high cyclic variation at high RG blend fraction rate. Increase in RG blend fraction by 10% retarded iso-Octane HCCI combustion by 3.2 CAD and reduced combustion duration by 1.4 CAD. From Table 5.3, the group C was selected for a detailed observation. Figure 5.11 indicates the pressure traces of the group C of data close to TDC. Increasing RG blend fraction postponed the pressure trace, decreased P_{\max} and reduced rate of pressure rise. Postponing the pressure trace from its original position in which P_{\max} was located around TDC did not contribute to more optimized combustion with high indicated thermal efficiency (see Figure 5.16). IMEP did not increase significantly by retardation of the pressure trace. Incomplete combustion caused by RG blend fraction increase, balanced the gain of more optimized combus-

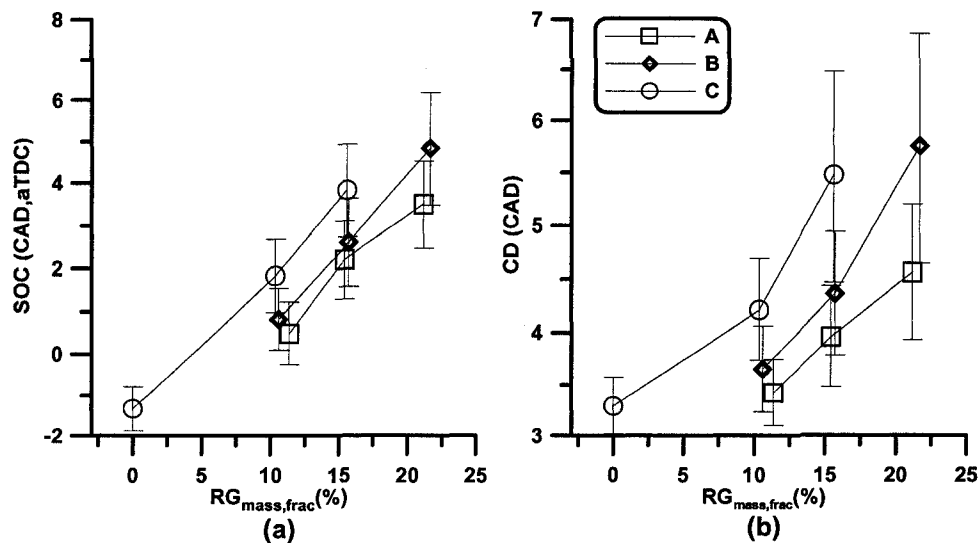


Figure 5.10: Effect of RG blend fraction on (a) start of combustion and (b) combustion duration for constant λ -EGR groups of data indicated in Table 5.3, error bars indicate $\pm 2\sigma_{n-1}$

tion timing. As it was indicated in n-Heptane case (Chapter 4), increasing RG blend fraction did not increase HC and CO as much as it did for iso-Octane case.

Heat release curves of set C of data in Table 5.12 shows that increasing RG blend fraction decreased the peak of NRHR, retarded $NRHR_{max}$ timing and retarded the timing of GHR and reduced the rate of GHR rise (Figure 5.12). Single stage combustion of iso-Octane is indicated in the same Figure.

P_{max} and $(dP/d\theta)_{max}$ decreased considerably by increasing RG blend fraction for the cases of Table 5.3 (Figure 5.13). Increase in RG blend fraction by 10% decreased P_{max} by 11.5 bar and $(dP/d\theta)_{max}$ by 4.5 bar. At high RG blend fraction values, the cyclic variation uncertainty for the average value that is indicated by error bars increased considerably indicating that combustion stability decreased at high RG blend fraction. This could be caused by high autoignition resistance of RG that caused partial burning.

For all cases of Table 5.3, increasing RG blend fraction decreased both knock

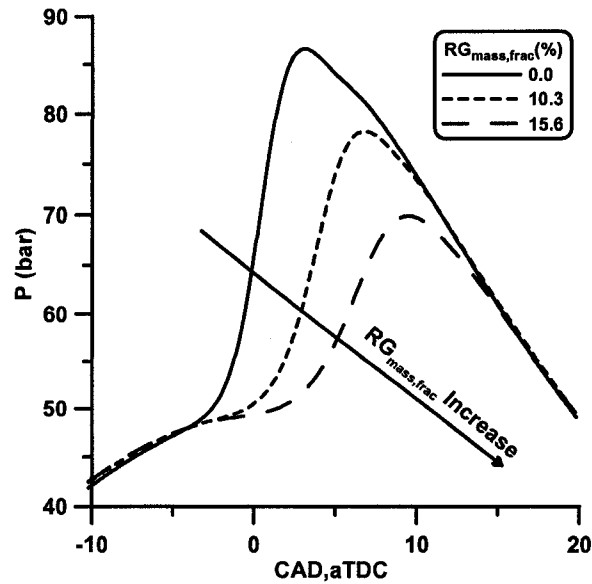


Figure 5.11: Effect of RG blend fraction on pressure traces of data group C in Table 5.3

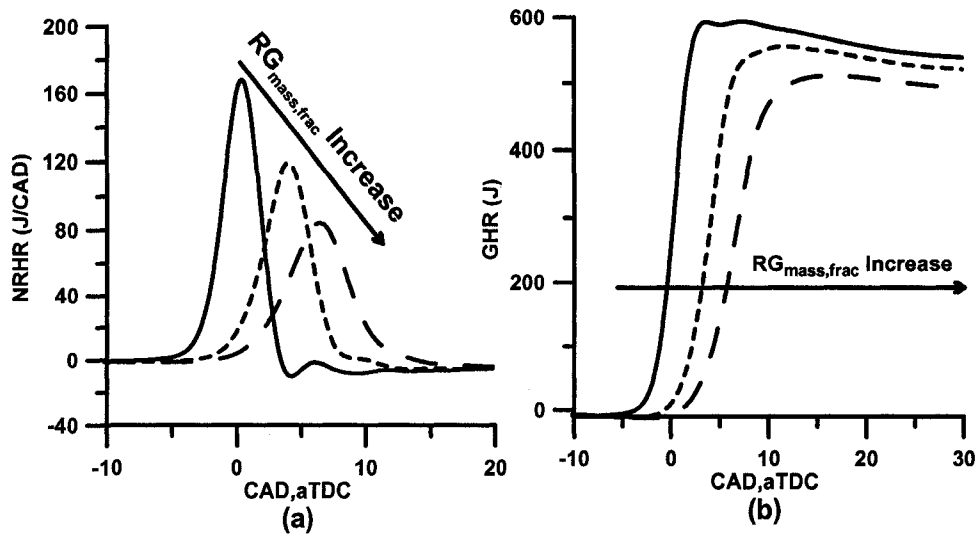


Figure 5.12: Effect of RG blend fraction on (a) net rate of heat release (NRHR) and (b) gross accumulative heat release (GHR) of data group C in Table 5.3

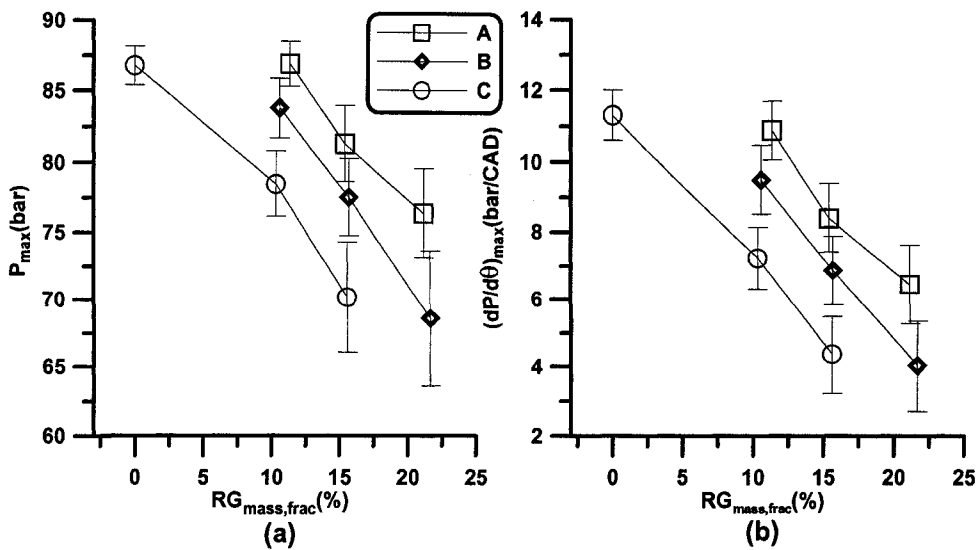


Figure 5.13: Effect of RG blend fraction on (a) P_{max} and (b) $(dP/d\theta)_{max}$ for constant λ -EGR groups of data indicated in Table 5.3, error bars indicate $\pm 2\sigma_{n-1}$

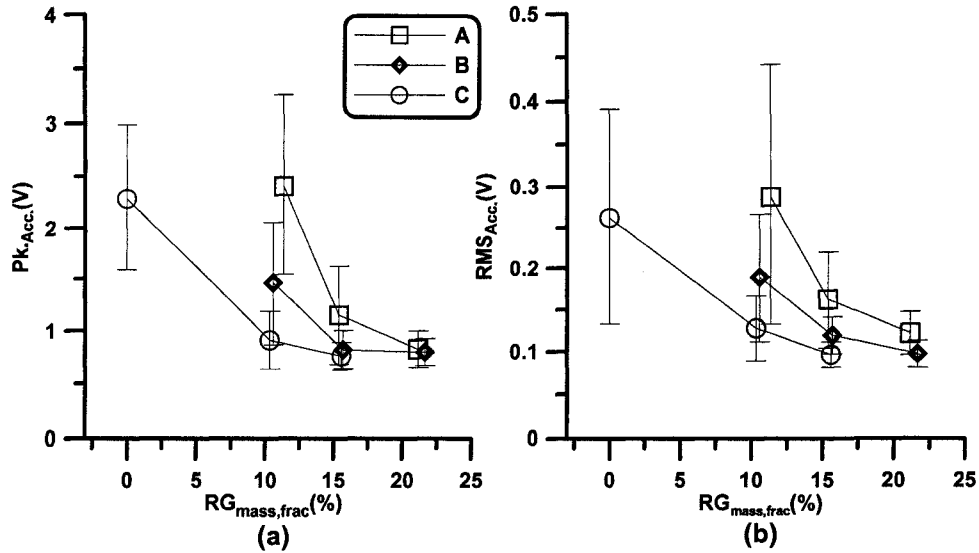


Figure 5.14: Effect of RG blend fraction on knocking intensity indicators of (a) Pk_{Acc} and (b) RMS_{Acc} for constant λ -EGR groups of data indicated in Table 5.3, error bars indicate $\pm 2\sigma_{n-1}$

intensity parameters of Pk_{Acc} and RMS_{Acc} while decreasing their cyclic variation considerably. At low RG blend fraction rate, the operating points were fluctuating between knock and no knocking cycles considerably that caused large uncertainty errors to appear on the plots of Figure 5.14.

5.2.3 Power, Efficiency and Emissions

Variation of RG blend fraction while keeping λ and EGR constant did not change the indicated power of supercharged iso-Octane HCCI combustion considering the cyclic variation of IMEP (Figure 5.15). Cyclic variations were minimum and remained unchanged by RG blend fraction variation.

RG blend fraction variation did not show a considerable effect on thermal and combustion efficiencies (Figure 5.17). A slight reduction in combustion efficiency was observed for most cases which was caused by higher HC and CO emissions (Figure 5.17).

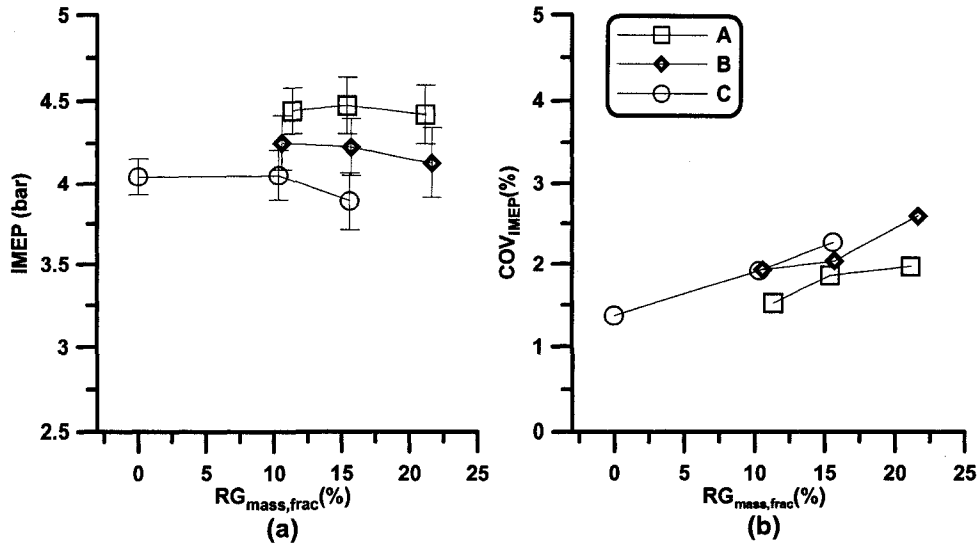


Figure 5.15: Effect of RG blend fraction on (a) indicated power and (b) cyclic variation for constant λ -EGR groups of data indicated in Table 5.3, error bars indicate $\pm 2\sigma_{n-1}$

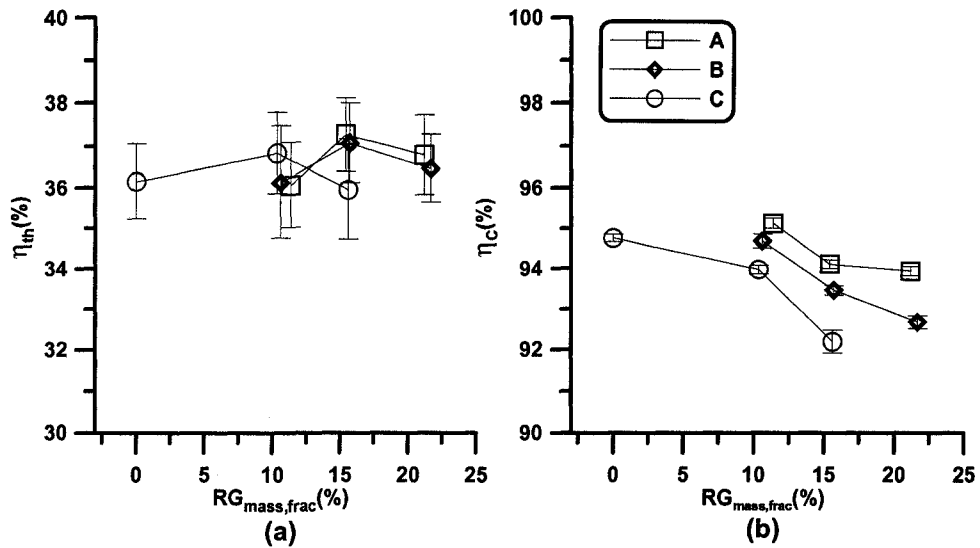


Figure 5.16: Effect of RG blend fraction on (a) indicated thermal efficiency η_{th} and (b) combustion efficiency η_c for constant λ -EGR groups of data indicated in Table 5.3, error bars indicate $\pm 2\sigma_{n-1}$

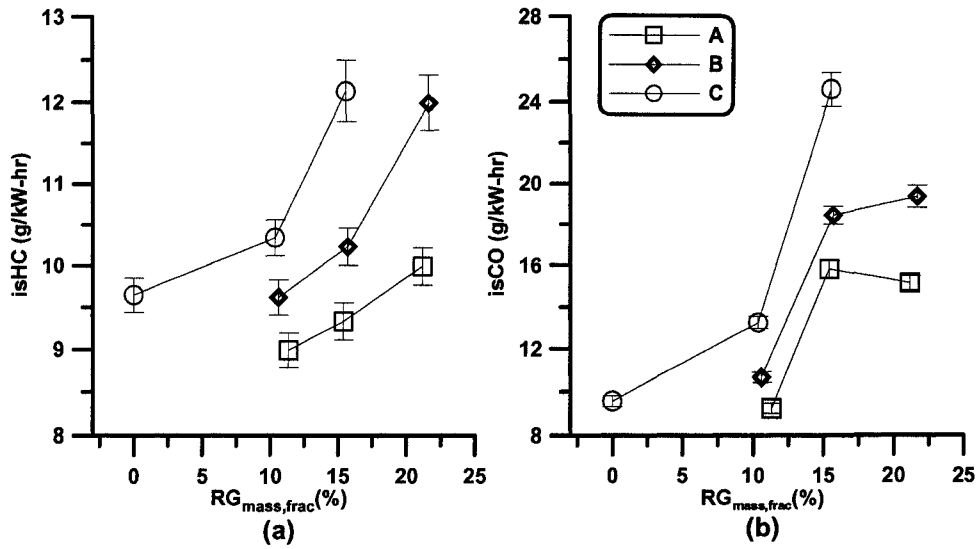


Figure 5.17: Effect of RG blend fraction on (a) indicated specific HC and (b) indicated specific CO emissions for constant λ -EGR groups of data indicated in Table 5.3, error bars indicate $\pm 2\sigma_{n-1}$

5.3 RG Composition Effects

The operating of iso-Octane HCCI combustion blended with two compositions of RG is indicated in Figure 5.18. Similar to natural gas case, the λ -RG operating regions for two cases of RG 75/25 and RG 50/50 did not overlap, while a series of constant IMEP points could be identified as indicated by circles in Figure 5.18-b. Figure 5.19 shows the λ difference between selected pairs of IMEP constant, RG constant of Figure 5.18-b. Rate of change of λ for two cases of RG 75/25 and RG 50/50 is similar. Figure 5.20 shows the difference between indicated thermal efficiency for two cases of RG 75/25 and RG 50/50 blending of iso-Octane HCCI combustion. Considering that IMEP for each pair of constant RG points were constant and λ was leaner for RG 50/50 cases, higher thermal efficiency of RG 50/50 cases is justified. Variation of start of combustion verses RG composition is indicated in Figure 5.21. Both RG compositions indicated a similar effect on start of combustion of HCCI combustion of iso-Octane. As effect of RG on HCCI combustion of iso-Octane

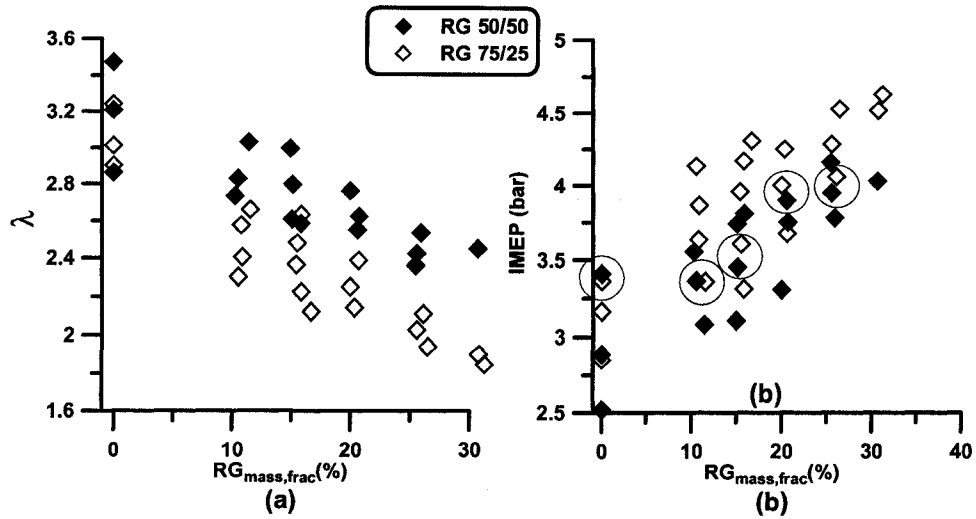


Figure 5.18: Supercharged iso-Octane HCCI combustion blended with RG 75/25 and RG 50/50 (a) λ -RG and (b) IMEP-RG operating windows

is a balance between thermodynamic alteration and chemical kinetic variation, very similar effects were observed for both cases of RG 75/25 and RG 50/50. For the cases of IMEP constant pair of points (Figure 5.18), RG 50/50 points

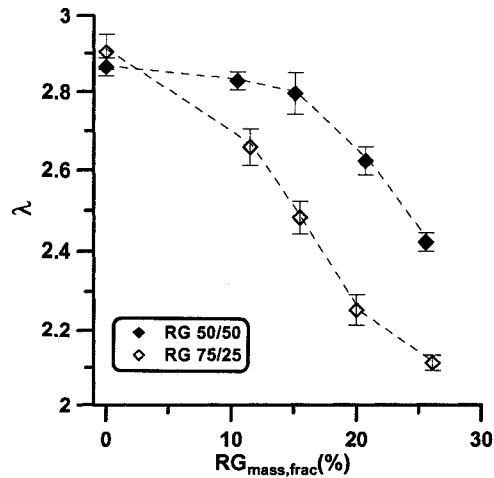


Figure 5.19: Demonstration of λ difference for selected pairs of constant IMEP in Figure 5.18, constant RG blend fraction points, supercharged iso-Octane HCCI combustion, error bars indicate $\pm 2\sigma_{n-1}$

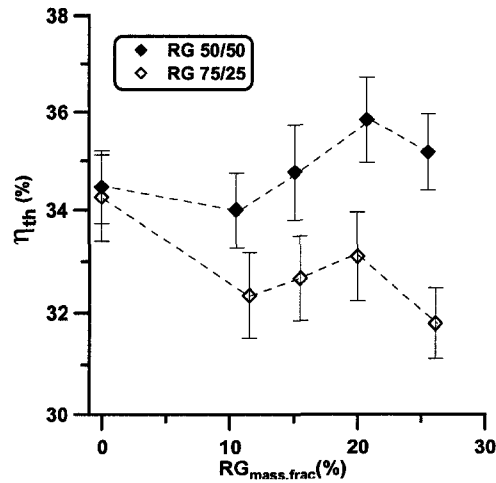


Figure 5.20: Effect of RG composition on indicated thermal efficiency of iso-Octane HCCI combustion, error bars indicate $\pm 2\sigma_{n-1}$

were operated slightly leaner than RG 75/25 (Figure 5.19). Higher thermal efficiency of RG 50/50 cases in Figure 5.20 was because of the less energy content of the fuel at the same load due to slightly more optimized combustion timing for RG 50/50 case (Figure 5.21). While the effects of RG on iso-

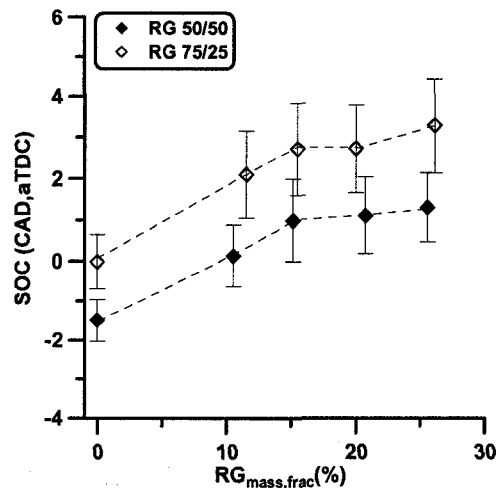


Figure 5.21: Effect of RG composition on change of start of combustion (SOC) of iso-Octane HCCI combustion, error bars indicate $\pm 2\sigma_{n-1}$

Octane HCCI combustion was minimum, migration from RG 75/25 to RG 50/50 did not have any considerable effects on engine operating parameters and combustion characteristics.

5.4 Summary

Effect of RG on high octane PRF HCCI combustion was negligible compared with natural gas or low octane PRF HCCI combustion. Similarity of octane number of RG and iso-Octane minimized octane enhancing/inhibiting effects. For the case of iso-Octane HCCI combustion in the natural aspirated mode, initial conditions were relatively severe ($CR=14.4$, $T_{\text{intake,mix}}=110\text{ }^{\circ}\text{C}$), hence RG blending with iso-Octane did not affect HCCI combustion characteristics or engine operating parameters. However, adding n-Heptane to iso-Octane and making PRF80 blend (20% n-Heptane by volume) improved multiple-stage autoignition property and decreased fuel octane number. Hence, RG was more effective on combustion timing alteration. Blending PRF80 with 10% RG 50/50 in the naturally aspirated mode retarded combustion timing by 2.4 CAD, increased combustion duration by 0.9 CAD, decreased P_{max} by 4 bar and decreased $(dP/d\theta)_{\text{max}}$ by 2.2 bar. Effects were similar to n-Heptane in which combustion was retarded by RG blending.

For the supercharged iso-Octane HCCI combustion, RG was effective on combustion timing alteration. Increasing RG blend fraction by 10% retarded iso-Octane HCCI combustion timing by 3.2 CAD, increased combustion duration by 1.4 CAD, decreased P_{max} by 11.5 bar, and decreased $(dP/d\theta)_{\text{max}}$ by 4.5 bar/CAD.

RG effectiveness on high octane fuel was sensitive to operating condition. In the naturally aspirated mode, as the operating points located near the rich boundary and initial conditions were relatively severe, RG had no effect on iso-Octane HCCI combustion. With similar conditions, increasing double-stage autoignition property of the fuel (migrating from iso-Octane to PRF80) in-

creased RG effectiveness. In the supercharged mode, operating points were located near the lean boundary and hence, RG blending was effective on iso-Octane HCCI combustion. Less intense initial conditions contributed to strengthen double-stage iso-Octane autoignition and increased RG effectiveness on iso-Octane HCCI combustion timing control.

Improvement of Natural Gas HCCI Combustion using Reformer Gas

Partial content of this chapter has been published in a peer reviewed Society of Automotive Engineering (SAE) technical paper in 2006 [175] and in a conference presentation in Combustion Institute/ Canadian Section (CICS) technical meeting in 2006 [176]. This chapter describes the effect of reformer gas (RG) on natural gas Homogeneous Charge Compression Ignition (HCCI) combustion. The chapter briefly reviews the previous works on natural gas HCCI combustion, importance of natural gas applications, and emphasizes on the effect of RG on natural gas HCCI combustion in two cases of naturally aspirated and supercharged mode. In addition, two various compositions of RG are examined to investigate the effect of RG composition on natural gas HCCI combustion.

In comparison with gasoline, natural gas has a very high octane number (≈ 120) and high autoignition temperature ($\approx 600^\circ$). Composed mostly of methane, natural gas is one of the fuels that exhibit relatively pure, single-stage autoignition. Other fuels have stronger low-temperature reaction and the required enthalpy for main stage combustion is obtained from low-temperature heat release after compression to a moderate pressure and temperature level.

In contrast, the methane molecule resists destruction by free radicals and produces negligible low-temperature reaction and heat release. Hence, in natural gas HCCI engines the high-temperature required for autoignition must be obtained by extreme levels of charge heating and/or compression. This leads inherently to a high rate of heat release once reaction starts and, in consequence, the air/fuel mixture must be highly diluted with air and/or EGR to avoid heavy knock. These facts make natural gas HCCI combustion even more difficult than with other fuels since methane already has a lower volumetric energy density in comparison with liquid fuels.

Although natural gas HCCI combustion is difficult to achieve, for practical reasons, it is an attractive option. Several high power industrial stationary engines are fueled by natural gas. Most of these engines are operating in relatively constant maximum power condition and constant speed. As the capital cost of these engines are high, engine modifications to implement HCCI combustion in their narrow operating range is reasonable. Hence, despite of inherent difficulties of natural gas HCCI combustion, it is discussed here as a special case.

Several natural gas HCCI combustion engines have been demonstrated. For example, Christensen et al (1997) [171] modified a 6-cylinder diesel engine to run in HCCI mode as a single cylinder engine using a compression ratio of 21 and intake temperature of 120 °C. Successful HCCI operation was demonstrated over $\lambda \simeq 2.2 - 3.5$. The same group (Christensen et al (1998) [48]) demonstrated a supercharged HCCI engine with compression ratios of 19 and 17 and intake temperatures of 150 °C and 170 °C, respectively. For most natural gas HCCI engines, the compression ratio and intake temperature were high and the engines were modified standard diesel engines.

Previous studies have shown the effect of using hydrogen or RG blending to control natural gas HCCI combustion timing. For example, Peucheret et al (2004) [110] and (2005) [58] demonstrated an on-board fuel reformer using a catalytic reforming technique and (Exhaust Gas Recirculation) EGR to op-

erate a natural gas HCCI engine with a moderate compression ratio. It was found that the presence of 10% H₂ in EGR enhanced the HCCI combustion.

6.1 Effects of RG on Naturally Aspirated Natural Gas HCCI Combustion

6.1.1 Operating Region

Table 6.1 summarizes the operating conditions for the case of naturally aspirated wide open throttle mode. For the low engine speed and at no exhaust back-pressure, maximum EGR attainable was quite low and about 5% for most of the operating points. The maximum EGR rates without exhaust back pressure was dictated by fluid dynamics and valve timing. As indicated in Table 6.1, three different Compression Ratios (CR)s were used for the natural gas HCCI engine. For all partial reforming cases, RG was a simulated mixture of 75% H₂ and 25% CO that is a typical output of a steam reformer using natural gas as the base fuel.

Figure 6.1 shows the effect of RG blending on operating region of natural gas HCCI engine. As the $T_{\text{intake,mix}}$ was constant for all three sets, it seems that set III with CR=16.5 had the optimum operation that exhibited maximum IMEP and minimum COV_{IMEP} . For Set III in Table 6.1, number of attainable operating points were not limited; and hence, Set II was chosen for further analysis due to availability of more operating points. Figure 6.1 also indicates that natural gas HCCI combustion even at extreme condition of $T_{\text{intake,mix}} = 140$ °C and high CR was highly limited. Most of the operating points shown

Table 6.1: Initial conditions for natural gas fueled HCCI combustion operated in the naturally aspirated mode

Data Set	Set I	Set II	Set III
CR	18.5	17.0	16.5
$T_{\text{intake,mix}}$ (°C)	140	140	140
Speed (RPM)	470	470	700

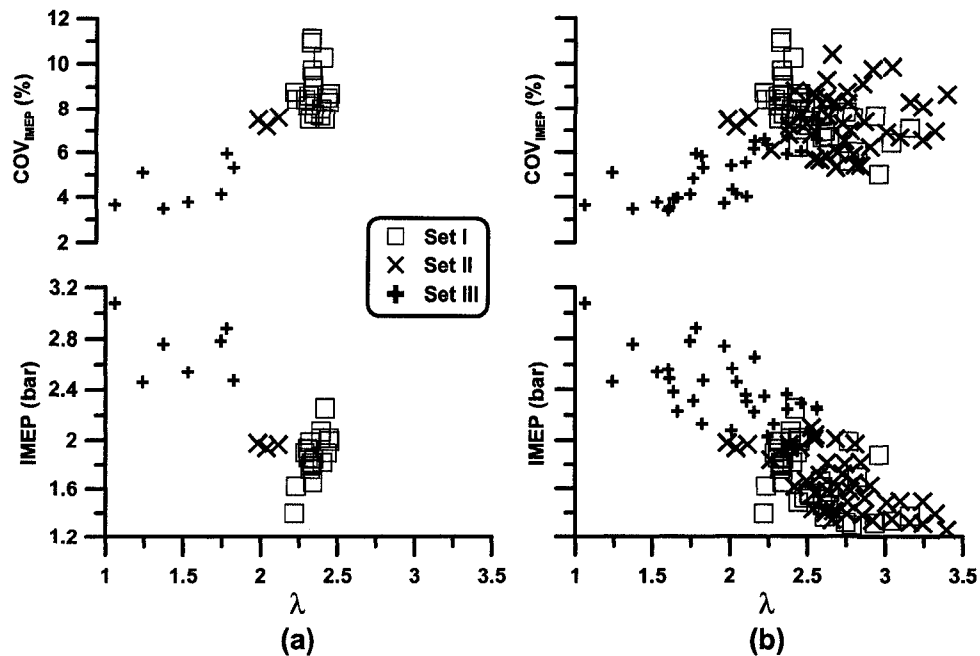


Figure 6.1: IMEP- λ operating region with indication of cyclic variation comparing (a) pure natural gas (b) natural gas blended with RG both at three sets of experiments indicated in Table 6.1, natural gas HCCI combustion in the naturally aspirated mode with wide open throttle

in Figure 6.1-a had severe knock and or low indicated power output. The engine speed of 470 RPM was achieved by idle operation of the engine at low friction condition of low speed. Figure 6.1 also indicates that partial reforming of natural gas with RG expanded the operating region toward leaner mixture and increased number of possible operating points. Figure 6.2 indicates the expansion and shifting of the operating region with RG blending of the base fuel. Increasing RG blend fraction from 0% to 60% shifted the operating region from $\lambda_{\min}=1.98$ at RG blend fraction =0% to $\lambda_{\min}=2.65$ at RG blend fraction =60%. The widths of the possible operating points between heavy knocking and low load operation also was increased from $\Delta\lambda=0.13$ at RG blend fraction =0% to $\Delta\lambda=0.73$ at RG blend fraction =60%.

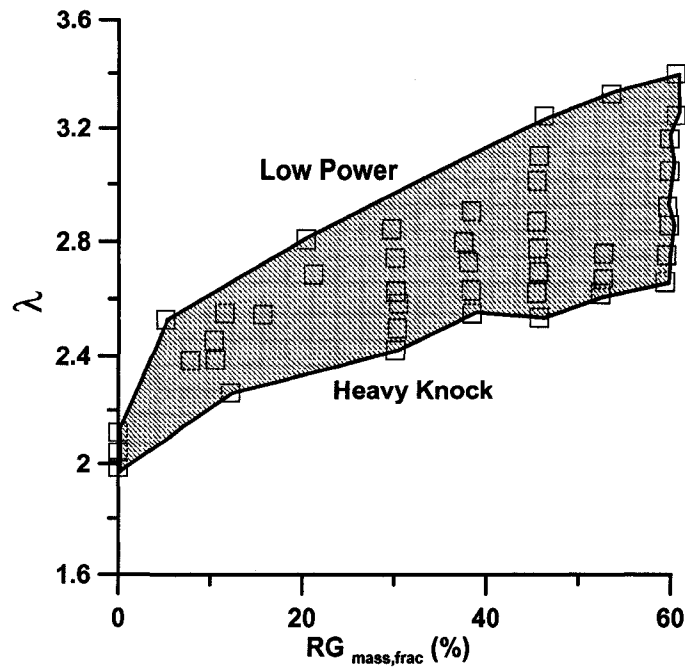


Figure 6.2: Effect of RG blend fraction increase on operating region of HCCI combustion of natural gas for Set II indicated in Table 6.1, EGR=5.5%

6.1.2 Combustion Timing and Duration

Figure 6.3 shows that increasing RG blend fraction along constant λ lines advanced combustion timing and shortened combustion duration. Increasing RG blend fraction by 10% advanced combustion timing of natural gas HCCI combustion in the naturally aspirated mode in an average by more than 1.3 CAD and reduced combustion duration by 0.4 CAD. Considering the short natural gas HCCI combustion duration, the reduction was more than 20% for 10% RG blending. Combustion timing advancing by RG blending can be translated into the lower intake heating requirement. The increase in intake temperature can potentially be compensated by RG addition as natural gas HCCI combustion requires high intake temperature. For example, Olsson et al (2002) [177] examined pure H_2 addition on natural gas HCCI combustion engine that was operated in the supercharged mode. It was reported that at

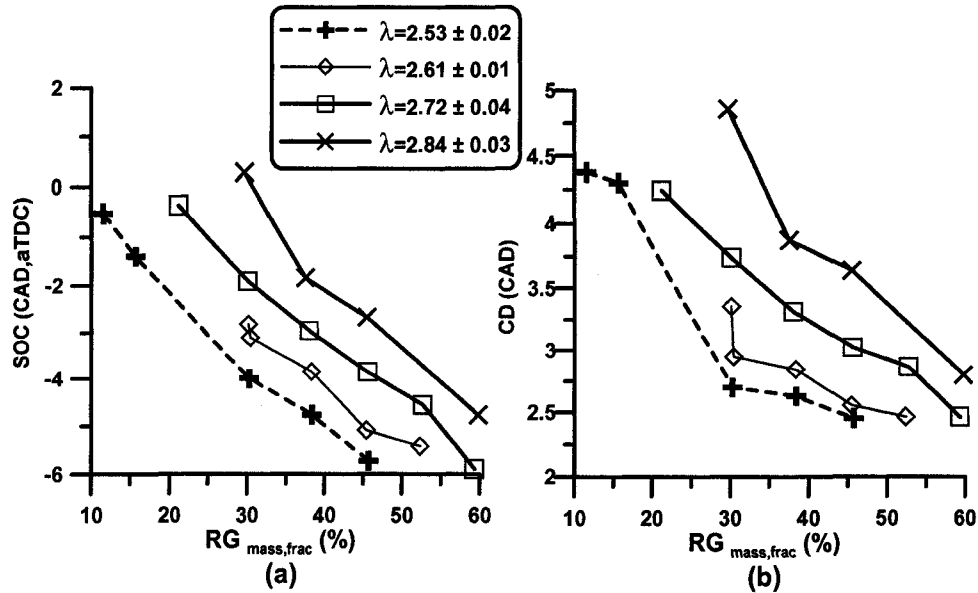


Figure 6.3: Effect of RG blend fraction on (a) combustion timing (SOC) and (b) combustion duration (CD) at constant λ lines, EGR=5.5%, Set II in Table 6.1

IMEP= 3 bar, increasing H_2 mass fraction from 0% to 50%, reduced intake heating requirement from more than 90 °C to about 40 °C.

6.1.3 Pressure Trace Characteristics

Figure 6.4 indicates effect of RG blend fraction increase on maximum pressure (P_{max}) and maximum pressure rise rate ($(dP/d\theta)_{max}$). As expected increasing RG blend fraction at any constant λ lines increased both P_{max} and $(dP/d\theta)_{max}$ considerably. Increasing RG blend fraction by 10%, increased $(dP/d\theta)_{max}$ by an average of 1.8 bar/CAD and P_{max} by an average of 1.1 bar. P_{max} and $(dP/d\theta)_{max}$ increase caused by earlier combustion timing. Compression of more combustion product by early combustion caused more intense combustion. Rate of pressure rise for all of the points were high. For most cases, a rate of $(dP/d\theta)_{max} = 10$ bar/CAD is considered as the border line for maximum rate of pressure rise. In this case, almost all of selected

points exhibited a maximum rate of pressure rise more than the conventional limit of 10 bar/CAD. Natural gas HCCI combustion at severe initial conditions of CR=17.0 and $T_{\text{intake,mix}}=140\text{ }^{\circ}\text{C}$ exhibited an abrupt combustion. For the CFR engine, this high rate of pressure rise is tolerable for a short period. A permanent operation of the engine to such a severe combustion condition damages engine structure. As with NO_x , λ has the dominant effect. Hence, expanding the operating region toward leaner mixture reduced P_{max} and $(dP/d\theta)_{\text{max}}$, while for a given λ , increasing RG blend fraction increased P_{max} and $(dP/d\theta)_{\text{max}}$. If an acceptable level of $(dP/d\theta)_{\text{max}} = 10$ bar/CAD was considered, the only operating points would be at $\lambda=2.8$ with RG blend fraction less than 35%.

RG blend fraction increase also changed the timings of P_{max} and $(dP/d\theta)_{\text{max}}$ substantially. As indicated in Figure 6.5 timing of both P_{max} and $(dP/d\theta)_{\text{max}}$ advanced con-

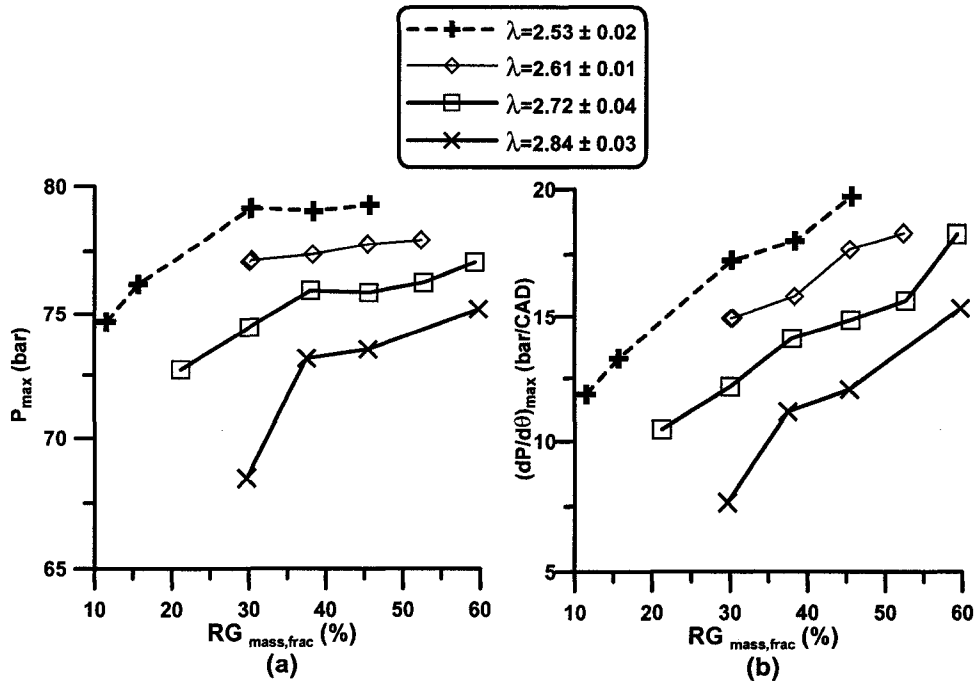


Figure 6.4: Effect of RG blend fraction on (a) P_{max} and (b) $(dP/d\theta)_{\text{max}}$ at constant λ lines, EGR=5.5%, Set II in Table 6.1

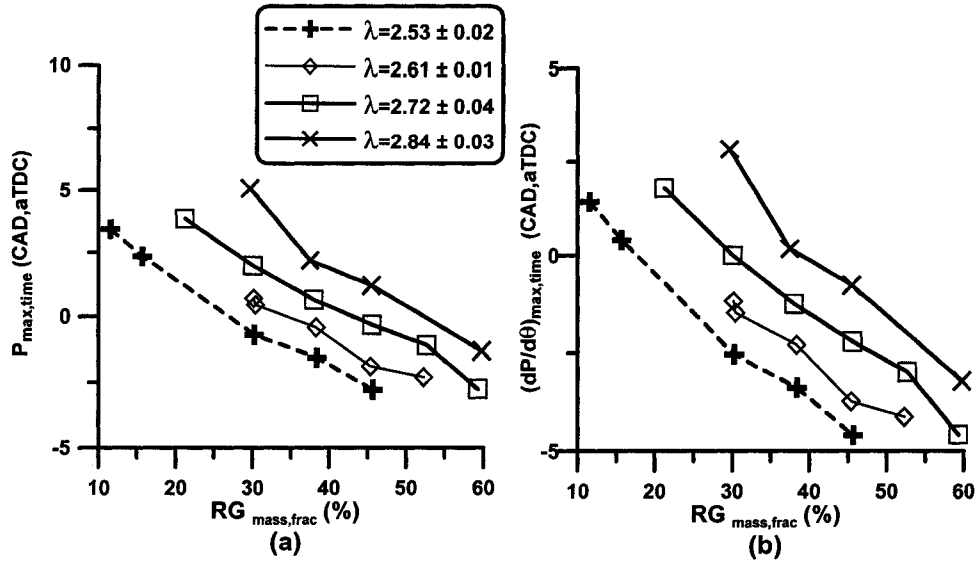


Figure 6.5: Effect of RG blend fraction on (a) P_{\max} timing and (b) $(dP/d\theta)_{\max}$ timing at constant λ lines, EGR=5.5%, Set II in Table 6.1

siderably as the result of RG blend fraction increase at constant λ lines.

The tendency of RG to shift the allowable operating range towards leaner mixtures, while also advancing the peak pressure timing, explains the significant drop in exhaust temperature shown by Figure 6.6 as the result of longer time for expansion of combustion products.

6.1.4 Engine Operating Parameters

As natural gas HCCI combustion engine at wide open throttle and in the naturally aspirated mode exhibited an extreme narrow operating window, a selected group of operating points with constant EGR and constant λ was difficult to collect. A selected group of constant λ lines for data Set II in Table 6.1 were considered for further analysis. The uncertainty in the value of λ comes from the variation in λ value among each group of constant λ lines.

Figure 6.7-a shows the effect of increasing RG blend fraction on IMEP reduction and COV_{IMEP} increase. Keeping λ constant and increasing RG blend fraction decreased IMEP. As λ was constant, the flow of energy into the engine

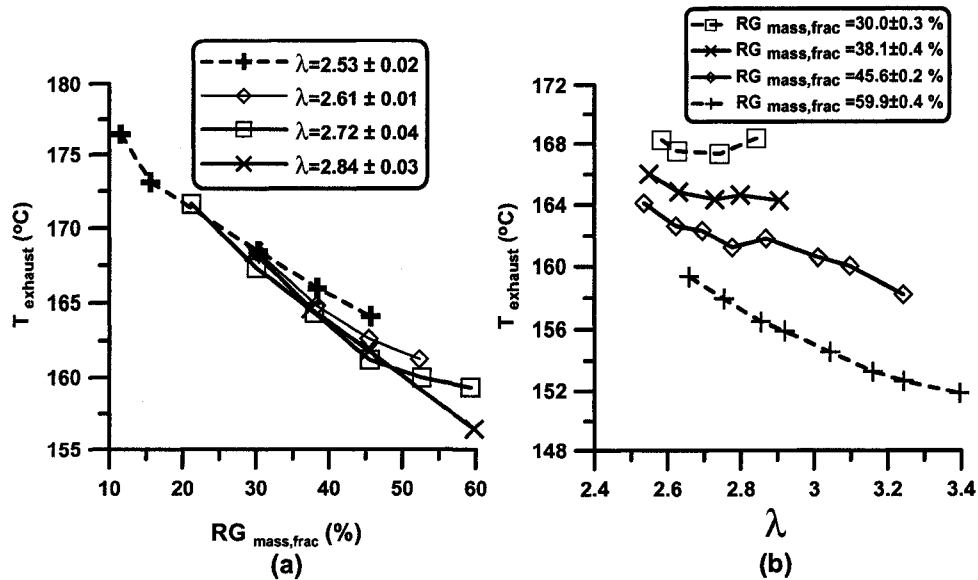


Figure 6.6: Effect of RG blend fraction on (a) T_{exhaust} at constant λ lines and (b) T_{exhaust} at constant RG blend fraction lines, EGR=5.5%, Set II in Table 6.1

was constant. Hence, IMEP reduction was a result of less efficient combustion. The efficiency drop resulted from early combustion timing by RG blend fraction increase. Higher cyclic variation (Figure 6.7-b) was an indication of less robust combustion by RG blend fraction increase. The operating points in this case were at the edge of knocking and misfiring points. All operating points exhibited fast rate of pressure rise and some level of knocking was presented in all cycles. Increasing RG blend fraction advanced combustion timing and increased instability in combustion by increasing knocking intensity. Keeping λ constant and replacing natural gas with RG did not change energy flow to the engine considerably as both fuels are in gaseous state and air flow to the engine was not changed drastically. IMEP reduction and COV_{IMEP} increase could be because of less efficient fuel utilization with RG blend fraction increase (see Figure 6.8-a). Thermal efficiency was decreased because of increase in RG blend fraction. This was not a result of combustion efficiency reduction or emission increase as indicated in Figure 6.8-a. At this condition, the engine

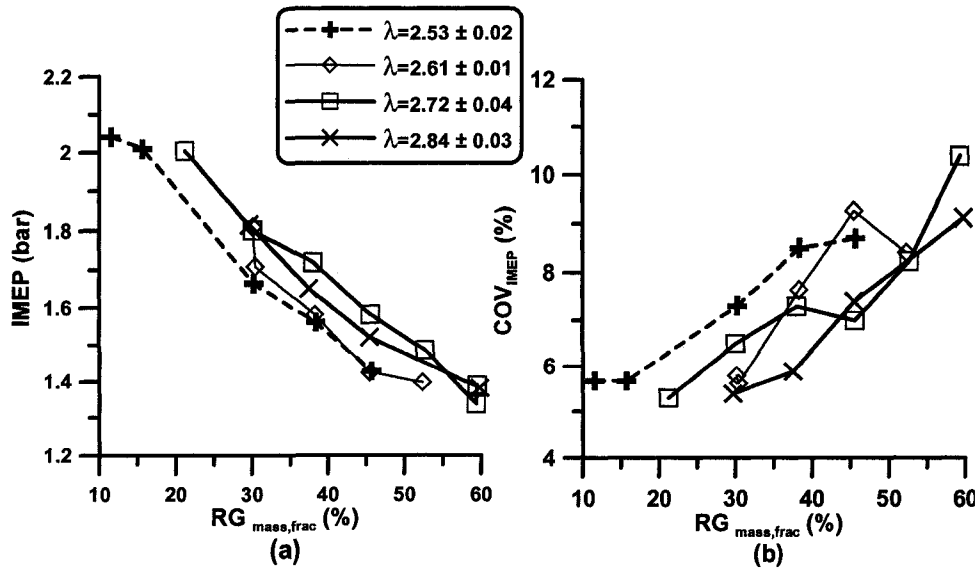


Figure 6.7: Effect of RG blend fraction on (a) indicated power (IMEP) and (b) cyclic variation COV_{IMEP} at constant λ lines, EGR=5.5%, Set II in Table 6.1

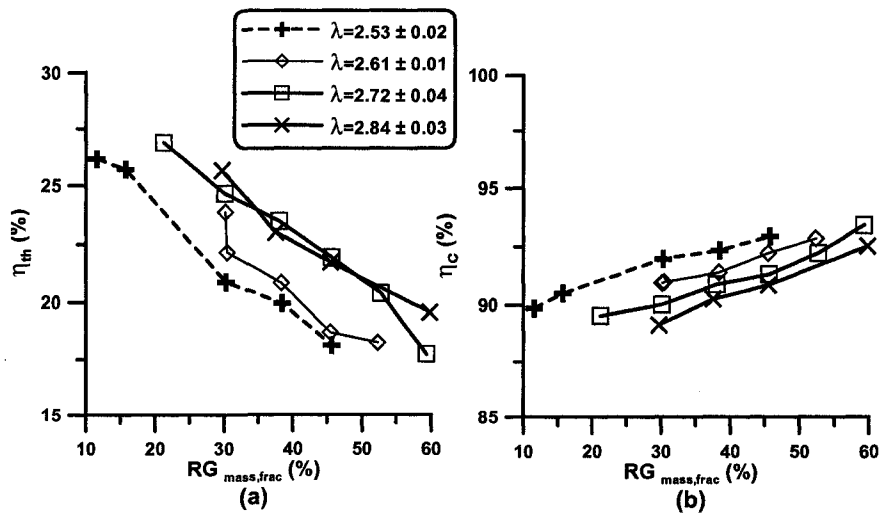


Figure 6.8: Effect of RG blend fraction on (a) indicated thermal efficiency (η_{th}) and (b) combustion efficiency (η_c) at constant λ lines, EGR=5.5%, Set II in Table 6.1

converted more fuel to combustion product as combustion efficiency increased by increasing RG blend fraction, but the fuel utilization suffered from non-optimized combustion timing and combustion duration.

Figure 6.9 shows the relation of engine emissions to RG blend fraction at constant λ lines. Keeping λ constant and increasing RG blend fraction decreased HC and increased CO emissions considerably. Decreasing HC emissions was a function of both λ and RG blend fraction, while increasing CO emissions was independent of λ and related to RG blend fraction .

Natural gas HCCI combustion at high CR and $T_{\text{intake,mix}}$ exhibited a narrow operating range between knock and low load. Most of the operating points had knock and high rate of pressure rise, which could not be considered a practical HCCI engine. In most of the fuels and operating conditions during this study NO_x was almost zero. However, in this specific case extreme amount of NO_x was observed during the experiments because of knocking in several cycles. Knock caused the disturbance of thermal boundary layer and less heat transfer to the cylinder wall and considerable increase in mixture temperature

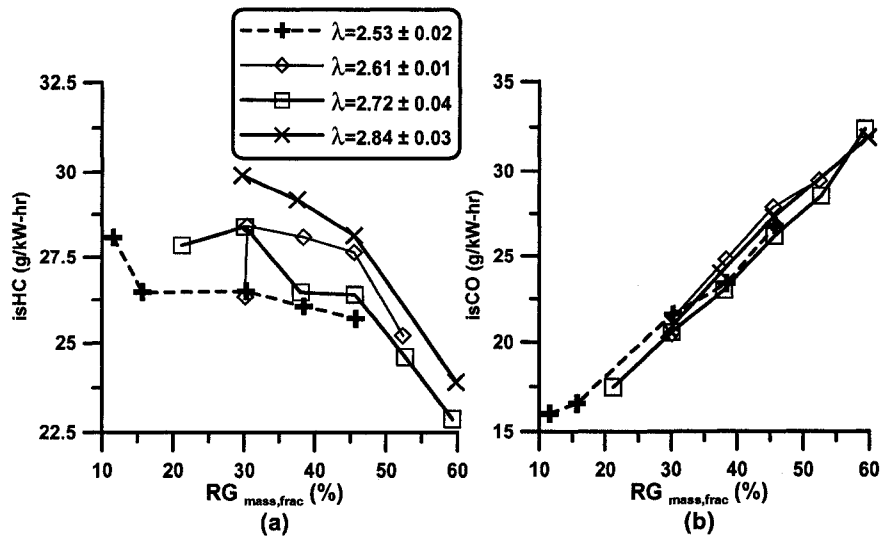


Figure 6.9: Effect of RG blend fraction on (a) indicated specific HC (isHC) and (b) indicated specific CO (isCO) at constant λ lines, EGR=5.5%, Set II in Table 6.1

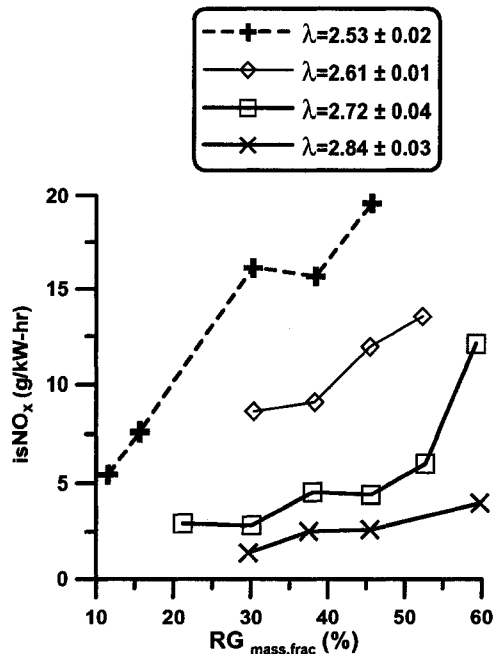


Figure 6.10: Effect of RG blend fraction on indicated specific NO_x (isNO_x) at constant λ lines, HCCI combustion of natural gas in naturally aspirated mode with wide open throttle, EGR=5.5%, Set II in Table 6.1

during and after combustion. In addition, knock produced hot spots inside the cylinder that caused advanced combustion timing that resulted in high rate of pressure rise and high knock intensity.

Figure 6.10 shows isNO_x increase by increasing RG blend fraction. This was one of the rare cases in the current study that NO_x was considerable.

Figure 6.11 indicates the possibility of the achievement of an acceptable HCCI combustion with minimum NO_x using high dilution. Increasing RG blend fraction increased NO_x as indicated in both Figure 6.10 and Figure 6.11. On the other hand, at any certain RG blend fraction constant line, increasing λ had a certain dilution limit. For example, when at constant line of RG blend fraction =30%, maximum λ attainable was 2.84, for RG blend fraction =60%, it was $\lambda=3.39$. Increasing the possibility of the lean operation reduced NO_x considerably.

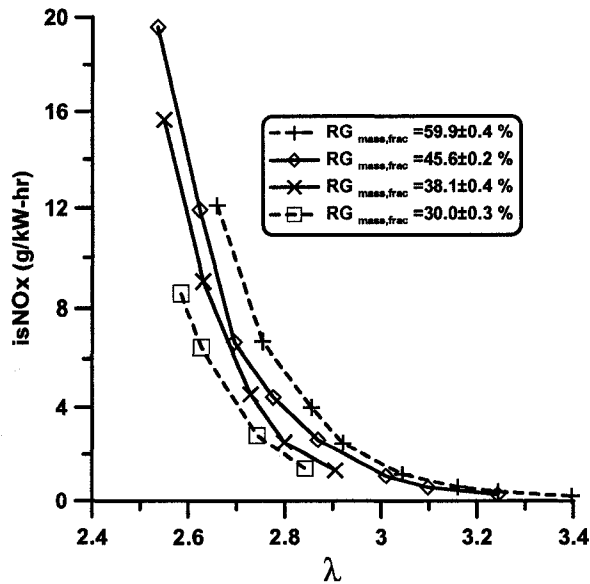


Figure 6.11: Effect of λ and RG blend fraction on indicated specific NO_x (isNO_x) at constant RG blend fraction lines, HCCI combustion of natural gas in naturally aspirated mode with wide open throttle, EGR=5.5%, Set II in Table 6.1

6.2 Effects of RG on Supercharged Natural Gas HCCI

As discussed, limited operating region of naturally aspirated cases did not exhibit a relatively true HCCI combustion with low NO_x. Most of the operating points in the naturally aspirated mode had high rate of pressure rise and certain amount of knocking was observed. Supercharging HCCI engine expanded the operating region and created the possibility of further analysis inside the wider operating window with more acceptable HCCI combustion operating points toward the lean side of the operating window. For supercharged case, the operating region was chosen close to the misfiring and partial burning boundary and for all operating points, isNO_x was near zero.

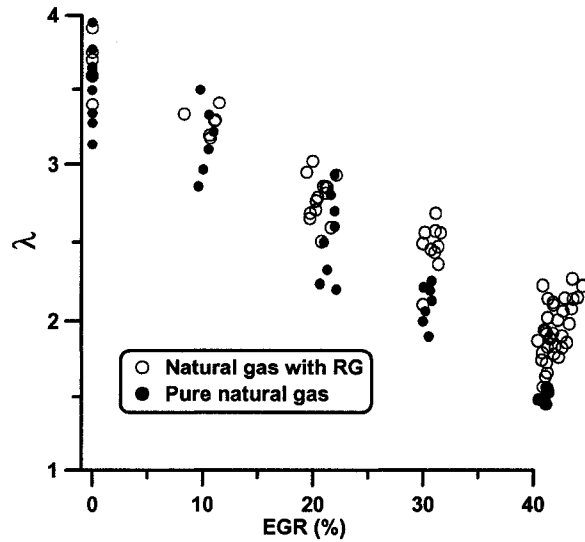


Figure 6.12: The operating region of supercharged natural gas HCCI combustion (●) and natural gas HCCI combustion blended with RG (○)

6.2.1 Operating Region

Supercharged natural gas HCCI combustion experiments were performed at steady state conditions with $CR=19.5$, $N=800$ RPM, and $T_{\text{intake,mix}}=140$ °C. RG composition was chosen as 75% H_2 and 25% CO (RG 75/25) and RG blend fraction was altered from 0% to about 40%. Figure 6.12 shows operating points of natural gas HCCI combustion with and without RG blending. It shows that all RG blended points were located on the lean side of the operating region. All operating points are indicated in Figure 6.13 in terms of λ and EGR. Figure 6.13-a and Figure 6.13-b are two views of a three-dimensional space of λ -EGR-RG blend fraction operating region. All possible RG blend fraction at high and low EGR and/or λ were examined. Increasing EGR increased the possibility of application of higher RG blend fraction. As RG limits the operating region at knock boundary at any constant λ , increasing EGR reduced the knock intensity and pushed back the knock boundary to achieve higher RG blend fraction rates. Increasing RG blend fraction at any constant $T_{\text{intake,mix}}$ limited the operating region as indicated in Figure 6.13-a. For example, at RG blend

fraction =0%, air/fuel ratio was achieved between $\lambda = 1.38 \pm 0.01$ and $\lambda = 3.95 \pm 0.02$ while at RG blend fraction =40% the only possible air/fuel ratio was $\lambda = 2.13 \pm 0.03$. Knock and partial burning boundaries for λ got closer when RG blend fraction increased because of faster combustion caused by high RG blend fraction at rich side and reducing total auto-ignitability of the fuel (natural gas and RG) on the lean side.

Figure 6.13- a and -b also indicate five groups of approximate constant λ / constant EGR points for further analysis. The groups of data were indicated by labels from A to E and details specifications are in Table 6.2.

6.2.2 Combustion Timing, Combustion Duration, and Pressure Characteristics

Figure 6.14 shows heat release analysis as combustion timing (SOC) and combustion duration (CD). Similar to naturally aspirated case, by increasing RG blend fraction, SOC was advanced and CD was reduced. Increasing RG blend

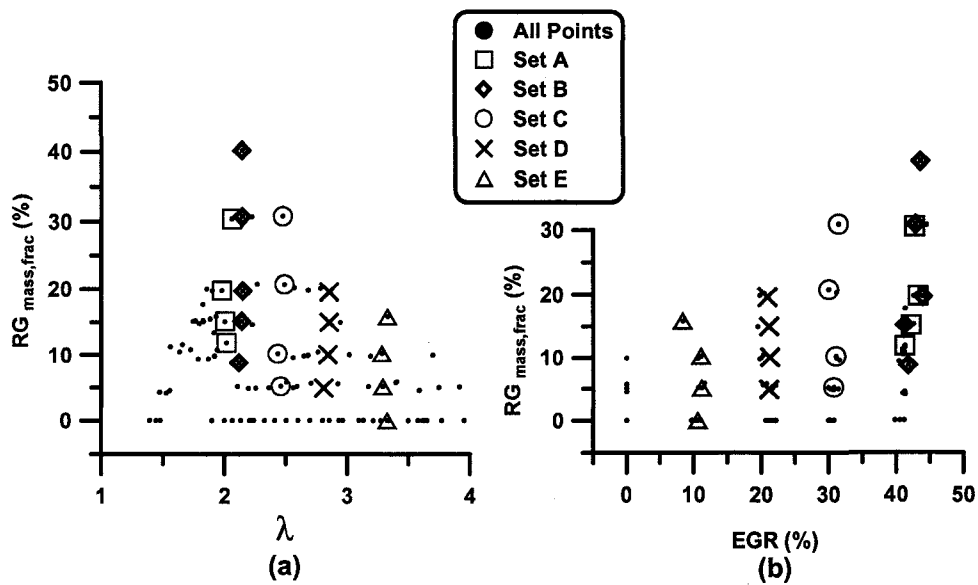


Figure 6.13: The operating window of RG-blended supercharged natural gas HCCI combustion in (a) RG- λ and (b) RG-EGR spaces with indication of constant λ -EGR groups of Table 6.2

Table 6.2: Selected groups of constant λ /constant EGR operating points from supercharged natural gas HCCI combustion with RG, N=800 RPM, $T_{\text{intake,mix}}=140$ °C, CR=19.5, labeled in Figure 6.13

Label	EGR	λ	RG blend fraction range
A	42.5 ± 0.8	2.02 ± 0.04	7.7 % to 21.3 %
B	42.7 ± 1.1	2.13 ± 0.01	8.7% to 40.1 %
C	30.8 ± 0.6	2.46 ± 0.02	5.1% to 30.7%
D	21.1 ± 0.1	2.84 ± 0.02	4.8% to 19.5%
E	10.3 ± 1.3	3.31 ± 0.02	0% to 15%

fraction by 10% advanced combustion timing by average of 3.5 CAD that exhibited a larger effect on combustion timing advancing compared with that of naturally aspirated case. As naturally aspirated case was operated around knocking limit and advance combustion timing, further advancing of combustion timing by RG was limited due to the saturation of early combustion timing. The combustion duration was reduced to about 1 CAD and remained at the same value by increasing RG blend fraction .

P_{max} and $(dP/d\theta)_{\text{max}}$ for supercharged case were similar to naturally aspirated case when RG blend fraction increased. Both P_{max} and $(dP/d\theta)_{\text{max}}$ were increased by increasing RG blend fraction as shown in Figure 6.15. Increasing

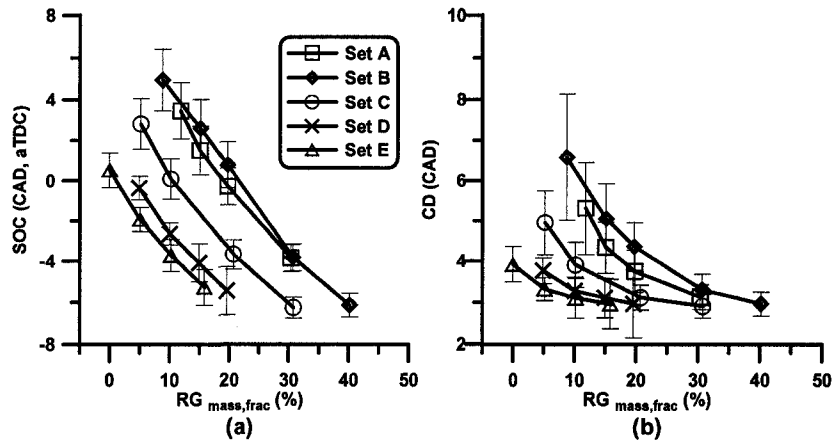


Figure 6.14: Effect of RG blend fraction on (a) SOC and (b) CD, HCCI combustion of cases A to E in Table 6.2, error bars indicate $\pm 2\sigma_{n-1}$

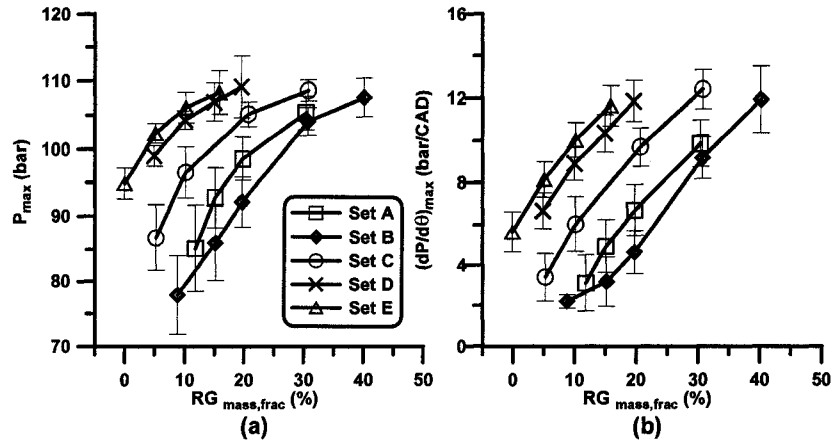


Figure 6.15: Effect of RG blend fraction on (a) P_{\max} and (b) $(dP/d\theta)_{\max}$, HCCI combustion of cases A to E in Table 6.2, error bars indicate $\pm 2\sigma_{n-1}$

RG blend fraction by 10%, increased P_{\max} by 8.5 bar and $(dP/d\theta)_{\max}$ by 3.4 bar/CAD. This was higher than correspondent values for naturally aspirated case of 1.1 bar and 1.8 bar/CAD respectively. RG was more effective on combustion timing advancing, hence, effect of RG was also larger on increasing P_{\max} and $(dP/d\theta)_{\max}$. Knock intensity was low for most of the operating points. As indicated in Figure 6.16, increasing RG blend fraction decreased both knock intensity parameters that were measured and calculated using the accelerometer.

For further analysis of constant λ lines of Table 6.2, data labeled B was chosen. Figure 6.17 shows the median pressure traces for 100 consecutive cycles for set B of data in Table 6.2. The Figure indicates that increasing RG blend fraction deviated combustion from adverse condition. While at $T_{\text{intake,mix}} = 140$ °C and $CR=19.5$, HCCI combustion of natural gas in supercharged mode was impossible without RG blending, median cylinder pressure was shifted considerably toward TDC, when RG blend fraction increased from 8% to 40%. The pressure trace curve indicating RG blend fraction =8% showed a partial burning, while RG blend fraction =40% exhibited a complete combustion with slight knocking.

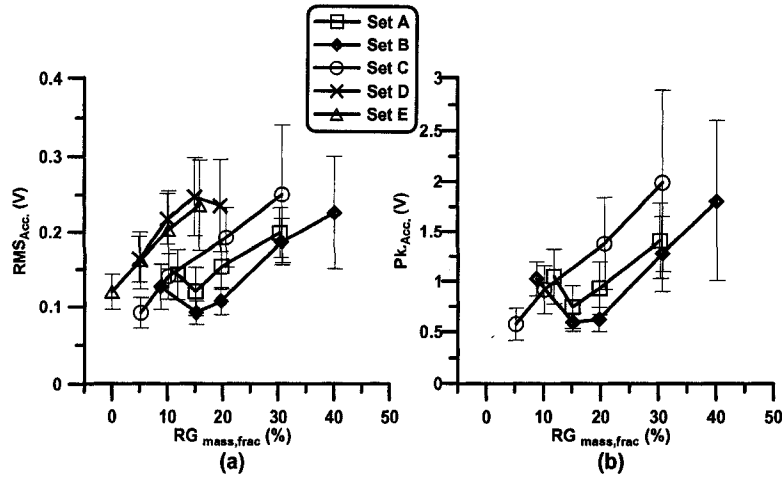


Figure 6.16: Effect of RG blend fraction on knock intensity parameters of (a) RMS_{Acc.} and (b) Pk_{Acc.}, HCCI combustion of cases A to E in Table 6.2, error bars indicate $\pm 2\sigma_{n-1}$

Figure 6.18 shows heat release characteristics of the constant λ case of data group B in Table 6.2. Increasing RG blend fraction, increased maximum rate of heat release (RHR_{max}), advanced timing of RHR_{max}, sharpened the slope of accumulative gross heat release (GHR) and advanced the location of GHR as

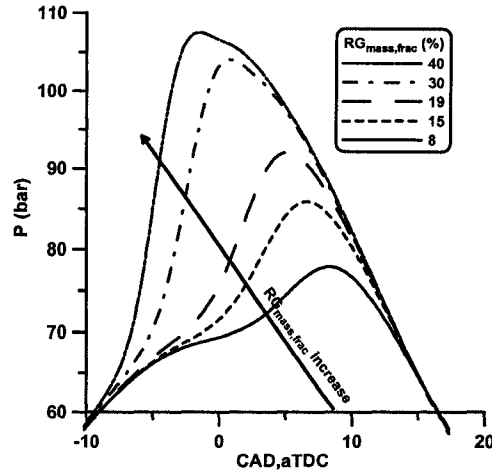


Figure 6.17: Effect of RG blend fraction increase on pressure traces of constant λ cases of Table 6.2, data group B, Supercharged natural gas HCCI combustion

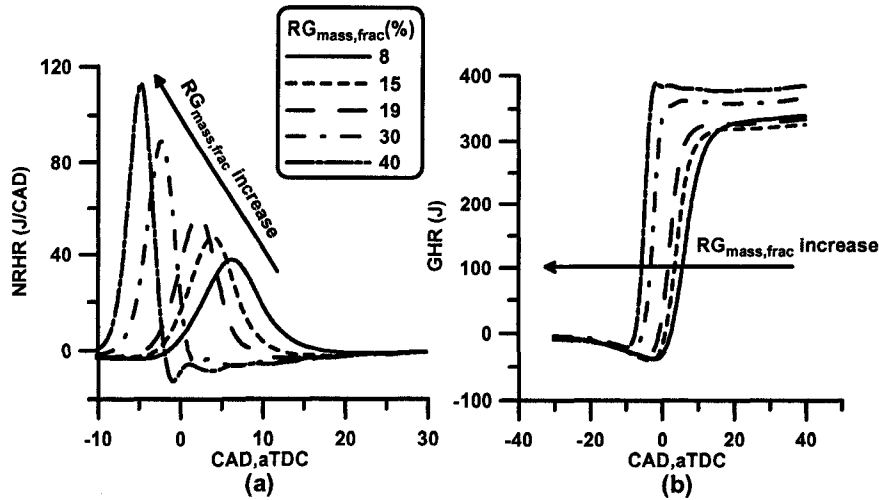


Figure 6.18: Effect of RG blend fraction increase on (a) net rate of heat release (NRHR) and (b) gross accumulative heat release (GHR) of constant λ cases of Table 6.2, data group B, Supercharged natural gas HCCI combustion

all indicated in Figure 6.18-a and -b.

6.2.3 Power, Efficiency, and Emissions

Figure 6.19 shows the indicated power and cyclic variation for cases of Table 6.2. Increasing RG blend fraction at any constant λ line did not have any significant effect on indicated power. Cyclic variation remained minimum for most of the cases. This observation was slightly different from what has been observed under naturally aspirated conditions. In that case as shown in Figure 6.7, increasing RG blend fraction at any constant λ line decreased IMEP and increased COV_{IMEP} . In the naturally aspirated mode, the operating points were chosen to be at the rich side of operating region with high rate of heat release and high $(dP/d\theta)_{max}$. Cyclic variation was minimum and increasing RG blend fraction shifted the operating points further into the knocking region, causing IMEP reduction by advancing combustion timing.

In supercharged case, the operating points were located inside the operating region mostly toward misfiring boundary because of intentional avoidance from

high P_{\max} . Increasing RG blend fraction at any constant λ , advanced combustion timing, resulted to thermal efficiency loss and combustion efficiency gain. The balance resulted in constant IMEP.

The same observation was seen in thermal efficiency behavior (see Figure 6.20-a). RG blend fraction variation reduced thermal efficiency. Combustion efficiency (Figure 6.20-b) was increased by increasing RG blend fraction independent of λ and EGR.

Combustion efficiency is a function of HC and CO emissions. As indicated in Figure 6.21, both HC and CO emissions were decreased by increasing RG blend fraction. While HC behavior as a function of RG blend fraction was similar to naturally aspirated case, CO showed reverse behavior as it actually increased in naturally aspirated case (see Figure 6.9-b). The nature of the changes for cases of naturally aspirated and supercharged also was different. In naturally aspirated cases, HC alteration by RG blend fraction was also a function of λ , while it showed an independent behavior versus λ and EGR in

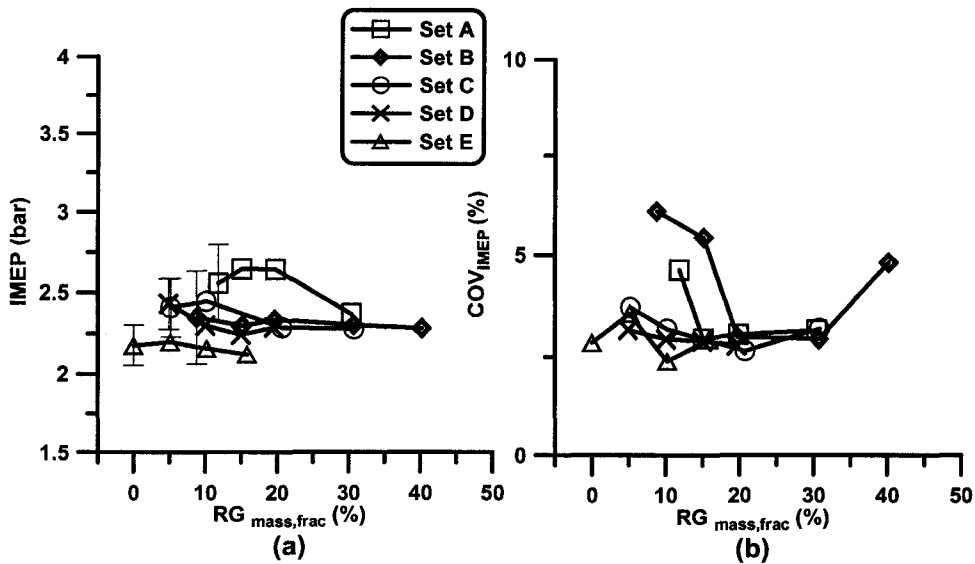


Figure 6.19: Effect of RG blend fraction on (a) IMEP and (b) COV_{IMEP} for HCCI combustion of cases A to E in Table 6.2, error bars indicate $\pm 2\sigma_{n-1}$

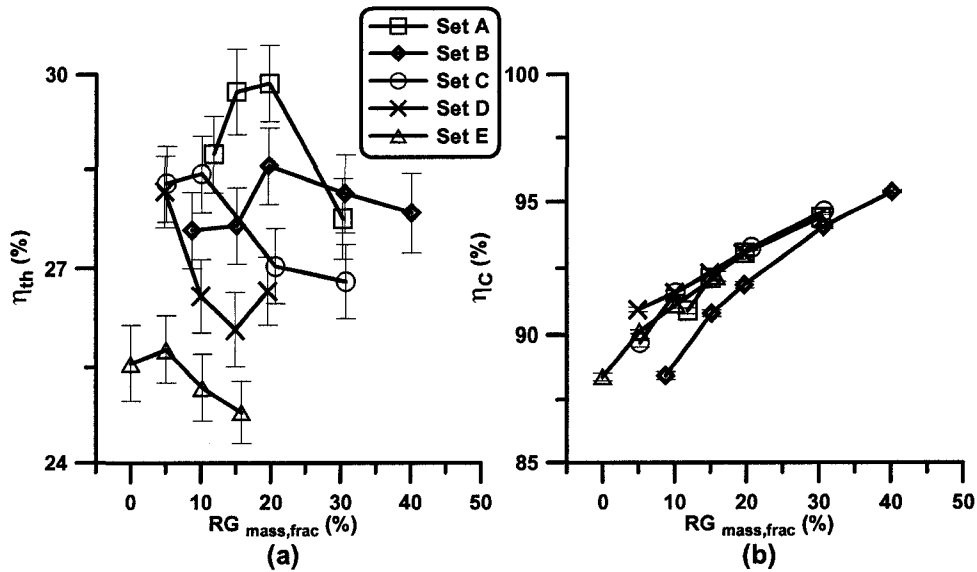


Figure 6.20: Effect of RG blend fraction on (a) indicated thermal efficiency (η_{th}) and (b) combustion efficiency (η_c), HCCI combustion of cases A to E in Table 6.2, error bars indicate $\pm 2\sigma_{n-1}$

supercharged case.

Increasing RG blend fraction shifted the operating region for both cases of naturally aspirated and supercharged toward more advanced combustion timing, higher P_{max} and $(dP/d\theta)_{max}$ and replacement of a hydrocarbon (natural gas) with H_2/CO (RG) mixture. The only difference was location of selected points. In naturally aspirated cases, the points were located in the rich side of the operating window. Increasing RG blend fraction replaced the base fuel (hydrocarbon) with less carbon content fuel (RG), also increased combustion temperature further and decreased HC emissions. In this case, increasing P_{max} and increasing CO content of fuel increased escaped fuel to crevices and doubled CO emissions when RG blend fraction increased to 60% (see Figure 6.9-b). However, in supercharged case increasing RG blend fraction shifted the operating point from lean side toward the inside the acceptable window by advancing combustion timing. Both HC and CO emissions decreased as indicated in Figure 6.21. The findings were similar to another study done

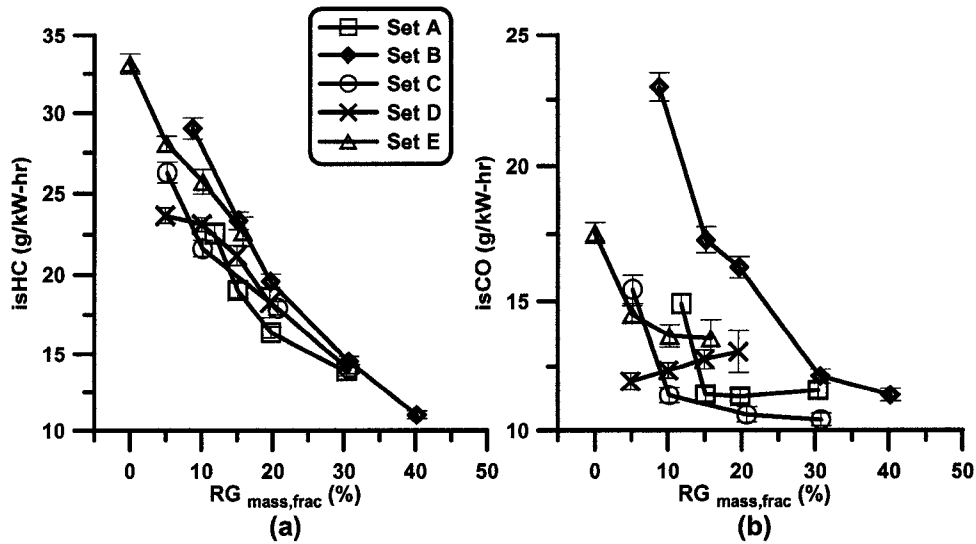


Figure 6.21: isHC (left) and isCO (right) for HCCI combustion of cases A to E in Table 6.2 as functions of RG blend fraction, error bars indicate $\pm 2\sigma_{n-1}$

by an actual fuel reformer in a closed-loop system utilizing EGR reformer gas (REGR) by Yap et al (2002,2006) [111, 113]. Although the experimental setup was different from this study (intake temperature was adjusted when adding RG), they reported that adding REGR advanced combustion timing of natural gas HCCI combustion. For example, at IMEP=2.4 bar, increasing H₂ fraction by 10% advanced combustion timing by about 5 CAD at the same intake temperature. Adding 10% H₂ reduced intake heating requirement by about 20 CAD.

6.3 RG Composition Effects

Details of RG composition selection has been discussed in Section 4.3. Two RG compositions of RG 75/25 and RG 50/50 were used for natural gas HCCI combustion (see Table 4.4). As previous results were based on RG 75/25, a series of tests were conducted on supercharged natural gas HCCI combustion using RG 50/50. The tests were conducted on the similar initial and operating conditions as indicated in Table 6.3.

The migration from RG 75/25 at constant fueling rate requires increasing RG mass flow rate to keep λ constant. For example, with natural gas fueling rate of 100 mg/s and air mass flow rate of 3 g/s, to keep λ constant at 1.75, RG 75/25 mass flow rate is 10 mg/s and RG 50/50 mass flow rate is 16 mg/s. Although mass flow rate of RG 50/50 is higher than that of RG 75/25, the energy flow to the engine is slightly lower because of the reduced LHV of RG 50/50 on a mass basis.

Similarly, consider cases of constant λ and RG blend fraction with two different RG compositions. If the natural gas fueling rate is constant, less RG 50/50 is needed than RG 75/25 to keep λ constant. Hence, the energy flow to the engine is lower in the RG 50/50 case at constant λ and RG blend fraction. Note that the trends indicated in Figures do not represent only the effect of RG blend fraction increase, because as RG blend fraction changes, the air/fuel ratio also changes. The operating range for natural gas HCCI combustion blended with two compositions of RG indicated in Figure 6.22.

Figure 6.22-a shows that the λ -RG operating window RG 75/25 was shifted further toward the lean side for RG 75/25 in comparison with the RG 50/50 case. The expansion of operating region toward the lean side with RG was due to less octane quality of RG compared with natural gas. In this study, effect of RG (both composition) on natural gas HCCI combustion was advancing combustion timing. Advanced combustion timing on the lean side of operating region compensated the retarded combustion timing by high λ values. Hence, the lean side of the operating region pushed back further.

It was more possible to operate the engine with high RG blend ratio using

Table 6.3: Initial conditions for two cases of RG 75/25 and RG 50/50, natural gas HCCI combustion

RG Com- position	CR	$T_{\text{intake,mix}}$	Intake absolute pressure	Speed	EGR
50/50	19.5	140	149.6 ± 0.0	800	30.6 ± 0.5
75/25	19.5	140	143.7 ± 0.2	800	30.2 ± 0.9

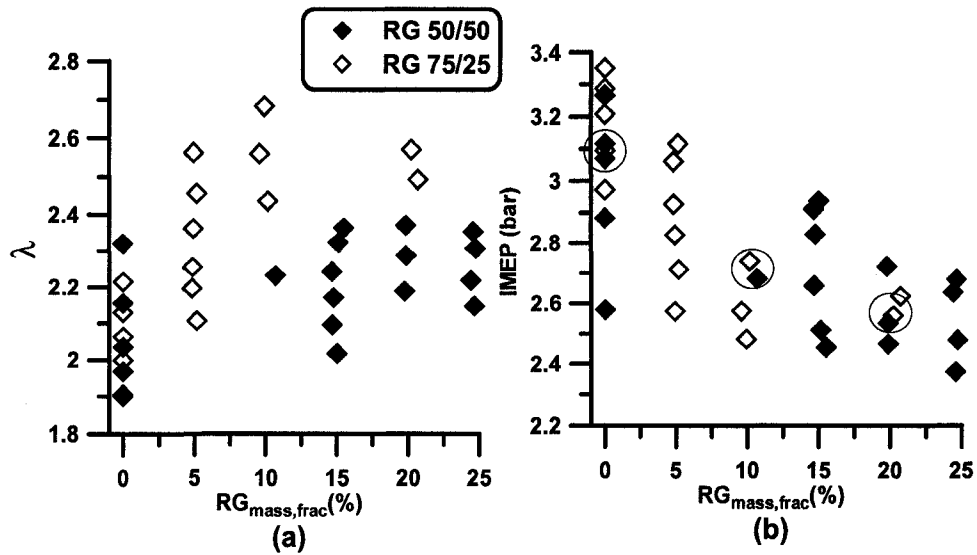


Figure 6.22: Natural gas fueled supercharged HCCI combustion with RG blending: (a) λ -RG and (b) IMEP-RG operating windows

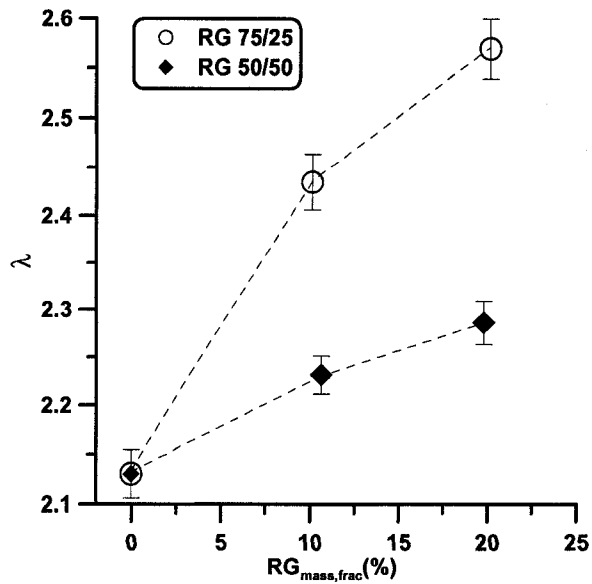


Figure 6.23: Demonstration of λ difference for selected pairs of constant IMEP, constant RG blend fraction points in Figure 6.22, error bars indicate $\pm 2\sigma_{n-1}$

RG 50/50 than with RG 75/25 (Figure 6.22). Both H₂ and CO have similar octane numbers although no certain octane numbers were reported. From an autoignition point of view, H₂ has more autoignition resistance than CO; hence, replacing RG 50/50 with RG 75/25 increased the resistance of the mixture to autoignition and limited the maximum RG blend fraction.

In Figure 6.22-b, the indicated power operating range was almost identical on the boundaries. This operating region shows minimum number of overlap for operating points that have the same initial conditions (λ and EGR). This makes the interpretation of the results difficult as HCCI combustion timing is a complex function of several engine operating parameters, including λ and EGR. For this purpose, three pairs of constant IMEP cases were chosen for further analysis. These three cases were indicated by circles in Figure 6.22-b. The λ variation for selected pairs of operating points is indicated in Figure 6.23.

While the value of λ differs between the cases of RG 75/25 and RG 50/50 there is a similar increasing λ as RG blend fraction is raised as shown in Figure 6.23. Figure 6.24 indicates the difference between indicated thermal efficiencies of RG 75/25 and RG 50/50 cases. The RG 75/25 cases showed a higher thermal efficiency. (Note that intake heating requirements and reforming efficiency was not considered in indicated fuel conversion efficiency calculations.)

Figure 6.25-a shows the difference between unburned hydrocarbon emissions for two cases of RG 75/25 and RG 50/50 for natural gas HCCI combustion. Natural gas blending with RG 75/25 showed less HC emissions than the RG 50/50 case. CO emissions behaved differently. The RG 50/50 case showed higher CO emissions which increased progressively with RG blend fraction increase and λ increase compared with RG 75/25 case as indicated in Figure 6.25-b.

Figure 6.26 indicates the effect of changing RG and λ on natural gas HCCI combustion timing. The error bars on combustion timing points are cyclic variation of SOC for 100 consecutive cycles with 95% confidence limit interval.

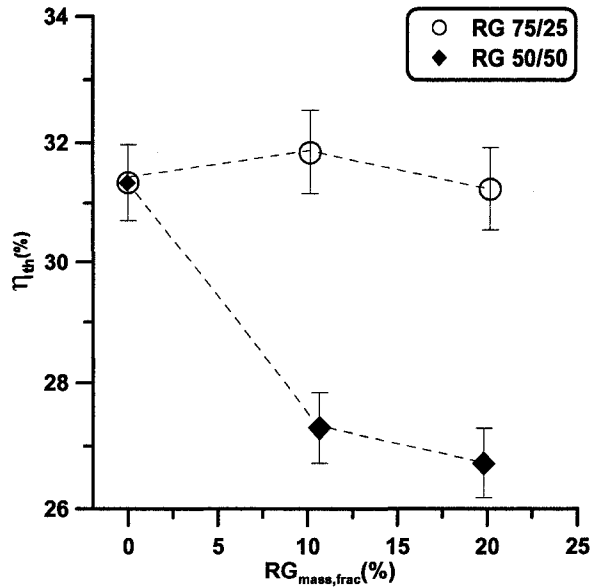


Figure 6.24: Effect of RG composition on indicated thermal efficiency for constant RG blend fraction points in Figure 6.22, error bars indicate $\pm 2\sigma_{n-1}$

Despite having the same RG blend fraction for each pair of data and identical change of λ , advancing combustion timing by RG increase was slightly sharper

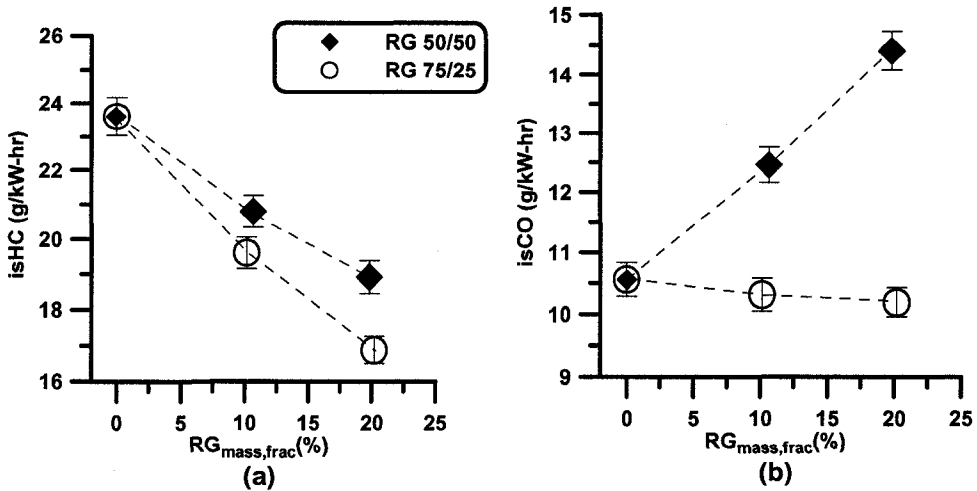


Figure 6.25: Effect of RG composition on (a) indicated specific HC and (b) indicated specific CO for constant RG blend fraction points in Figure 6.22, error bars indicate $\pm 2\sigma_{n-1}$

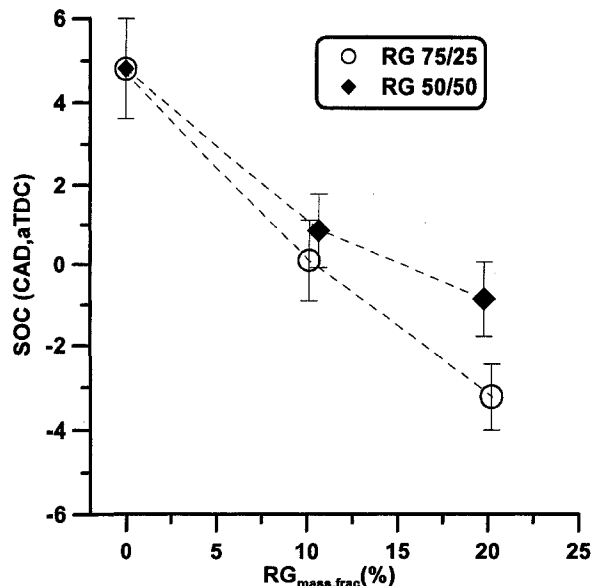


Figure 6.26: Effect of RG composition on (change of start of combustion (SOC) for constant RG blend fraction points in Figure 6.22, error bars indicate $\pm 2\sigma_{n-1}$

for the case of RG 75/25 than for RG 50/50. Considering that for the cases of RG 75/25, λ was leaner than the RG 50/50 case, and leaner air/fuel ratio caused later combustion, RG 75/25 was more efficient on advancing combustion timing. The indicated thermal efficiency of the engine was higher in RG 75/25 case at constant IMEP (Figure 6.24) because of leaner air/fuel ratio for RG 75/25 at any pair of constant IMEP with RG 50/50 (Figure 6.23).

6.4 Modeling Analysis

6.4.1 Effect of RG on Natural Gas HCCI Combustion Timing

The same chemical kinetic model that was used for n-Heptane HCCI combustion modeling, also was used for natural gas HCCI combustion in the single zone mode (ChemComb-SZM). For natural gas HCCI combustion simulation, the GRI mechanisms with 325 reactions and 53 species was used [178].

6.4.2 Comparison of Simulation and Experiment

Data set B of experimental data was chosen from Table 6.2 for further analysis. Figures 6.17 and 6.18 show the pressure traces and heat release characteristics of data set B. For each operating point, as pressure traces were collected by 100 consecutive cycles, three cycles were chosen. These three cycles are the cycles that have maximum P_{\max} , minimum P_{\max} , and median P_{\max} , respectively. For simplicity, these cycles were named P_{\max} (maximum P_{\max}), P_{\min} (minimum P_{\max}), and P_{median} (median P_{\max}).

Figures 6.27, 6.28, 6.29, and 6.30 show examples of the comparison of experimental pressure traces with ChemComb-SZM. Each figure contains three cycles of P_{\max} , P_{\min} , and P_{median} . The ChemComb-SZM pressure traces became more comparable with experimental pressure traces as RG blend fraction increased. This was because of the high rate of pressure rise and fast combustion at high RG blend fraction that is similar to the known behavior of a

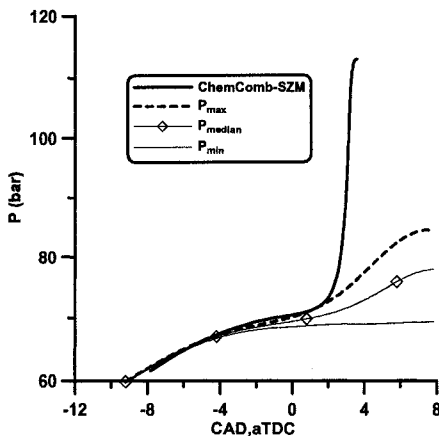


Figure 6.27: Comparison of experimental pressure traces of point 1, data set B with ChemComb-SZM, Experiment: supercharged natural gas HCCI combustion, $N=800$ RPM, $CR=19.5$, $T_{\text{intake,mix}}=140$ °C, Intake pressure =143 kPa, $\lambda=2.11$, $EGR=41.8\%$, RG blend fraction =8.7%

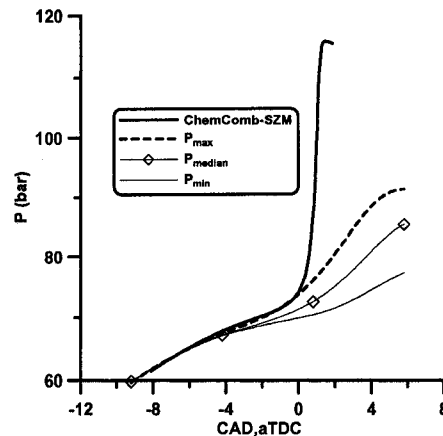


Figure 6.28: Comparison of experimental pressure traces of point 2, data set B with ChemComb-SZM, Experiment: supercharged natural gas HCCI combustion, $N=800$ RPM, $CR=19.5$, $T_{\text{intake,mix}}=140$ °C, Intake pressure =143 kPa, $\lambda=2.14$, $EGR=41.3\%$, RG blend fraction =15.1%

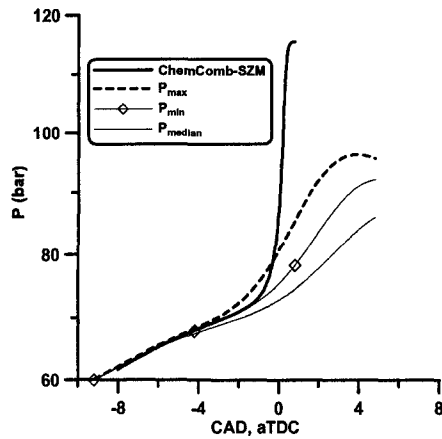


Figure 6.29: Comparison of experimental pressure traces of point 3, data set B with ChemComb-SZM, Experiment: supercharged natural gas HCCI combustion, $N=800$ RPM, $CR=19.5$, $T_{\text{intake,mix}}=140$ °C, Intake pressure =143 kPa, $\lambda=2.15$, $EGR=43.9\%$, RG blend fraction =19.7%

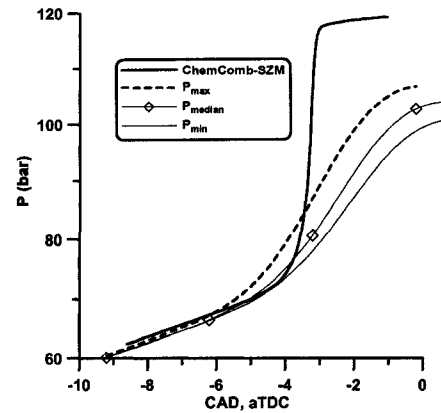


Figure 6.30: Comparison of experimental pressure traces of point 4, data set B with ChemComb-SZM, Experiment: supercharged natural gas HCCI combustion, $N=800$ RPM, $CR=19.5$, $T_{\text{intake,mix}}=140$ °C, Intake pressure =143 kPa, $\lambda=2.14$, $EGR=42.8\%$, RG blend fraction =30.7%

single zone model.

Figure 6.31 shows that SOC prediction of ChemComb-SZM is within or at the vicinity of cyclic variation error of experimental SOC. As mentioned, SOC was predicted more accurately at higher RG blend fraction. The experimental results showed an average of 4.0 CAD combustion timing advancing with 10% RG fraction blend increase, and the ChemComb-SZM predicted an average of 2.8 CAD per 10% RG blend fraction increase.

6.4.3 Detailed Analysis using ChemComb-SZM

Figure 6.32 indicates the temperature and heat capacity variation of selected cases. The pressure trace curves of those selected cases are indicated in Figures 6.27 to 6.30.

Figure 6.32 shows that increasing RG blend fraction at constant λ and EGR had a thermal effect on compression stroke. Increasing RG blend fraction

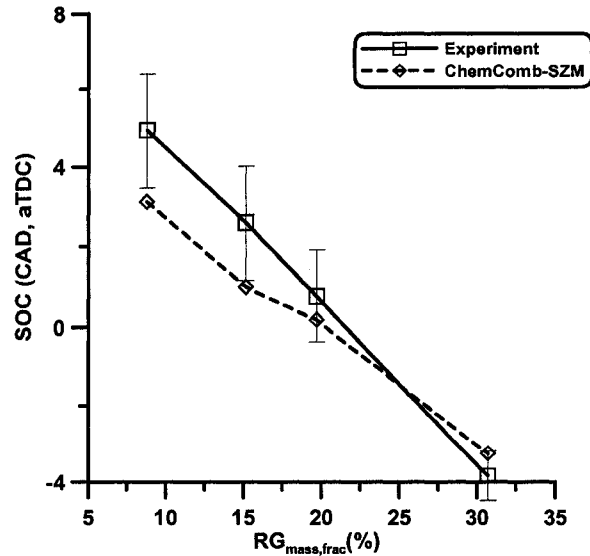


Figure 6.31: A comparison of combustion timing (SOC) prediction by ChemComb-SZM with actual experimental combustion timing for set B of data in Table 6.2, error bars on experimental SOC show the cyclic variation, error bars indicate $\pm 2\sigma_{n-1}$

shows a clear increase in after-compression temperature right before combustion initiation (Figure 6.32-a). The combustion initiation temperature was almost identical for all cases around 1080 K, but increasing RG blend fraction caused that temperature happened earlier in the cycle leading to an advanced combustion timing. For example, at -12 CAD,aTDC, increasing RG blend fraction from 8.7% to 30.7%, increased combustion temperature by about 25K. Figure 6.32-b shows that the ratio of specific heat is considerably higher for the cases of high RG blend fraction even before combustion initiation. For example at 1000 K, increasing RG blend fraction from 8.7% to 30.7%, increased ratio of specific heats by 0.002 unit. Note that the X-axis in Figure 6.32-b is temperature instead of CAD (compared to Figure 6.32-a).

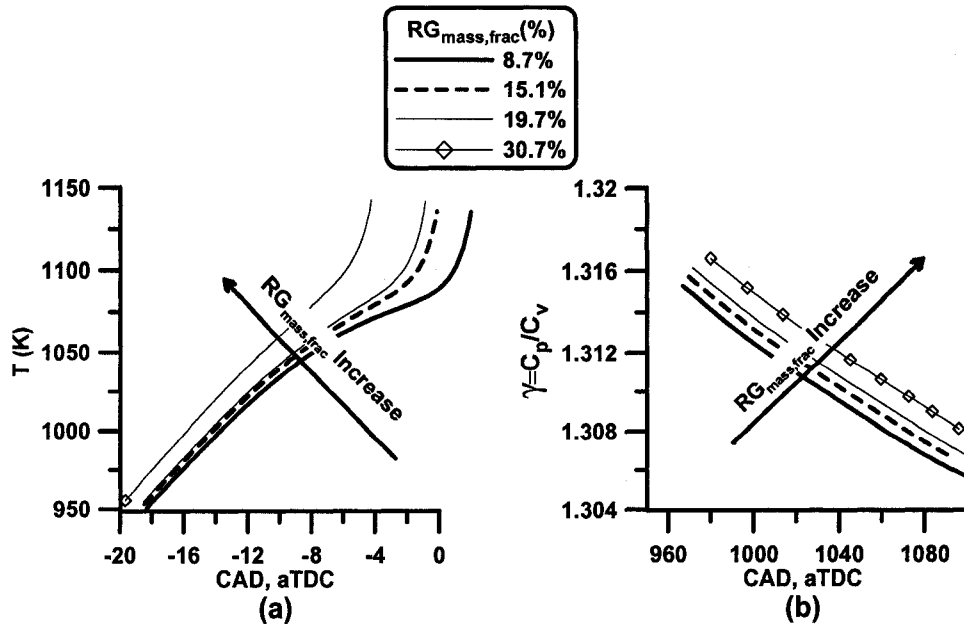


Figure 6.32: Effect of RG blend fraction on (a) temperature trace and (b) heat capacity trace, HCCI combustion of natural gas for case B of Table 6.2 simulated by ChemComb-SZM

6.4.4 Effect of RG Composition on HCCI Combustion Timing

Figure 6.33 shows the effect of RG composition on natural gas HCCI combustion timing obtained by experiments and simulated by ChemComb-SZM. For RG blend fraction increase by 10%, experimental results showed 1.3 CAD combustion timing advancing for RG 50/50 and 4.0 CAD for RG 75/25. ChemComb-SZM predicted 1.4 CAD combustion timing advancing for RG 50/50, and 4.2 CAD for RG 75/25 by 10% increase in RG blend fraction. Note that avoiding confusion, different Y-axis were assigned for RG 75/25 and RG 50/50 cases.

Figure 6.34 shows effect of RG composition on variation of ratio of specific heat. The change in the ratio of specific heat for the case of RG 75/25 is larger than that of RG 50/50. For example, at $T=1020K$, increasing RG blend fraction

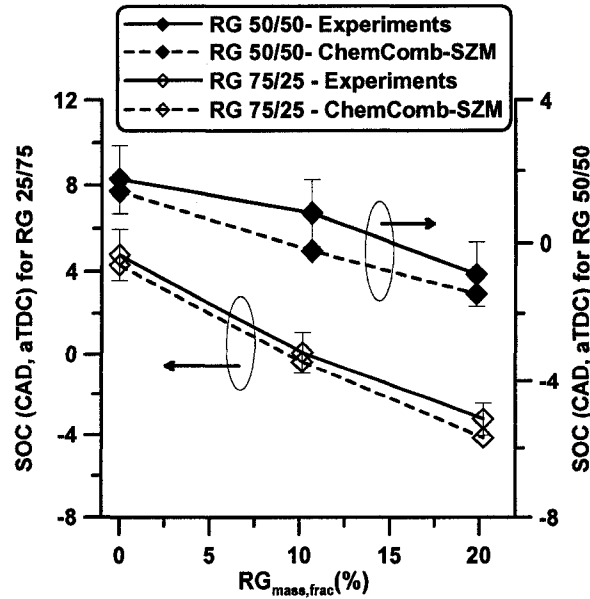


Figure 6.33: Comparison of combustion timing for two cases of RG 50/50 and RG 75/25, experimental results and modeling results for constant IMEP cases indicated in Figure 6.22, error bars indicate $\pm 2\sigma_{n-1}$

by 20% increased γ by 0.005 unit, while the same amount of RG blend fraction increase, changed γ for RG 50/50 case by 0.003 unit. An Otto air-cycle calculation shows that increase in γ by 0.005 unit, would increase the Otto-cycle after-compression temperature at CR=19.5 by more than 10K. Figure 6.33 shows that both RG 75/25 and RG 50/50 had similar effect on natural gas HCCI combustion timing. Both H_2 and CO have similar heat capacities and migrating from RG 75/25 to RG 50/50 does not change the total heat capacity of the mixture considerably. Hence, the effect of RG composition on natural gas HCCI combustion timing is related to chemistry. Figure 6.34 shows that change in the ratio of specific heats were similar for two cases of RG 75/25 and RG 50/50. Kongsereparp and Checkel (2007) [166] discussed the thermal effect of RG on HCCI combustion of natural gas using a precise ChemComb-MZM modeling.

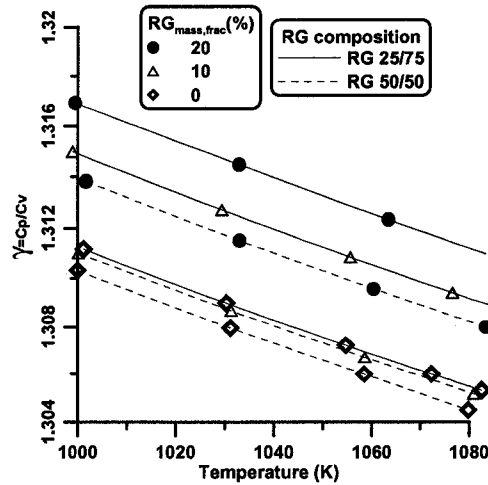


Figure 6.34: Effect of RG blend fraction on ratio of specific heats for two cases of RG 50/50 and RG 75/25, experimental results versus modeling results for constant IMEP cases indicated by circles in Figure 6.22

6.5 Summary

Effect of RG on natural gas HCCI combustion was studied experimentally using a CFR variable compression ratio engine, and numerically using an in-house made chemical kinetic model. In the experiments, the CFR engine was operated at two different modes of naturally aspirated and supercharged with relatively low intake boost pressure.

RG blending expanded the operating region of natural gas HCCI combustion toward the lean limit of operation. Using RG, the operation of the engine was possible in far leaner mixture comparing with the condition of pure natural gas fueling. It was found that RG in this case behaved as an octane number reducer and increased the autoignition property of natural gas. On the lean operation boundary, RG enhanced the autoignition by advancing combustion timing at identical initial conditions compared to pure natural gas that expanded the lean boundary of the operating region. An expansion of λ band by 0.73 unit was observed at RG blend fraction of 60% for naturally aspirated natural gas HCCI combustion.

Natural gas HCCI combustion is intense and exhibits a very high maximum pressure, high maximum rate of pressure rise and most of the operating points are accompanied with several knocking cycles. Blending RG with natural gas at constant λ and EGR, increased combustion intensity. 10% RG blending in the naturally aspirated mode, increased P_{\max} by 1.1 bar and $(dP/d\theta)_{\max}$ by 1.3 bar. The same amount of RG blend fraction in the supercharged mode increased P_{\max} by 8.5 bar and $(dP/d\theta)_{\max}$ by 3.4 bar. However, expansion of the operating range toward the lean boundary increased the possibility of lean operation and less intense combustion.

Keeping all influential parameters, including λ and EGR constant, increasing RG blend fraction advanced combustion timing of natural gas HCCI. In the naturally aspirated mode, increasing RG blend fraction by 10% advanced combustion timing by 1.3 CAD and reduced combustion duration by 0.3 CAD. The same amount of RG blending for the supercharged mode, advanced combustion timing by 3.5 CAD and reduced combustion duration to 1 CAD. For constant combustion timing, this can be translated to a lower intake heating requirement. Natural gas HCCI combustion requires high intake temperature and high compression ratio. RG can be used to lower the intake heating requirement. While intake heating is not a practical combustion timing control method due to slow response time, adjusting RG blend fraction on a cycle-by-cycle basis is possible.

Modeling analysis confirmed the findings of experiments. ChemComb-SZM predicted an average combustion timing advancing of 4.2 CAD for supercharged natural gas HCCI combustion. Advancing combustion timing by RG blending for natural gas HCCI combustion was related to increased after-compression temperature resulted from reduced heat capacity of the mixture. Changing the RG composition from RG 75/25 to RG 50/50 reduced the effectiveness of combustion timing advancing by RG. Both modeling and experimental results showed a slightly lower effectiveness of combustion timing advancing by RG 50/50. 10% increase in RG 75/25 blend fraction advanced

combustion timing by 4.0 CAD. ChemComb-SZM predicted a value of 4.2 CAD combustion timing advancing for this case. 10% increase in RG 50/50 blend fraction advanced combustion timing by 1.3 CAD and ChemComb-SZM predicted a value of 1.5 CAD combustion timing advancing for this case.

Conclusion

An experimental study has been conducted to investigate the effect of reformer gas (RG) on Homogenous Charge Compression Ignition (HCCI) combustion of natural gas, n-Heptane, iso-Octane, and some primary reference fuels (PRFs). The study aimed at exploring the possibility of combustion timing control using RG.

7.1 HCCI Engine Laboratory Development

An HCCI combustion engine lab was developed to provide fundamental HCCI combustion data for a wide range of fuel properties. The lab was equipped with data acquisition system capable of measuring Cooperative Fuel Research (CFR) engine operating parameters and cylinder pressure trace with 0.1 CAD resolution at any speed. The HCCI combustion engine laboratory was capable of

- Binary (liquid or gaseous) fuel mixture delivery to the intake plenum.
- Adjusting pressure and temperature of both liquid and gaseous fueling system.
- Variable effective compression ratio from 9.5 to 19.5.

- Intake heating with controlled mixture temperature at any set point between 60 °C to 200 °C.
- Intake supercharging at intake pressure up to 10 psig.

7.2 HCCI Combustion Timing

HCCI combustion timing is a complex function of several initial conditions. The base line experiments alongside a factorial design test revealed that:

- The engine's compression ratio had a strong effect on HCCI combustion timing. Increasing compression ratio advanced combustion timing with a penalty in power, efficiency, and emissions.
- Intake mixture temperature ($T_{\text{intake,mix}}$) had a strong effect on HCCI combustion timing. Increasing $T_{\text{intake,mix}}$ had similar effects to increasing compression ratio.
- Engine speed indirectly affected combustion timing. Increasing engine speed retarded combustion timing significantly.
- Mixture quality (λ and EGR dilution) had the dominant effect on combustion timing. For natural gas and high octane fuels, a combination of λ and EGR controlled combustion timing. Increasing λ and/or increasing EGR for natural gas and high octane fuels retarded combustion timing, thus reducing combustion intensity indicated by P_{max} and $(dP/d\theta)_{\text{max}}$. Combustion timing retardation using λ and EGR penalized the indicated power. Both thermal and combustion efficiencies were increased. For low octane fuels and n-Heptane, combustion timing was a strong function of EGR and a weak function of λ .
- For the case of PRF fuels in the naturally aspirated mode, increase in λ by 1 unit keeping other parameters constant, retarded combustion timing by an average of 5 CAD. It also reduced P_{max} by 25 bar and

$(dP/d\theta)_{\max}$ by 15 bar/CAD. While combustion retardation was effectively possible by λ increase, it reduced indicated power. Increase in λ by 1 unit reduced IMEP by more than 2.1 bar which was a significant reduction in high internal friction low power CFR engine.

- In the supercharged mode, increasing λ by 1 unit, retarded natural gas HCCI combustion timing by 10 CAD, reduced P_{\max} by 30 bar, and reduced $(dP/d\theta)_{\max}$ by 15 bar/CAD.
- In the supercharged mode, increasing λ by 1 unit, retarded iso-Octane HCCI combustion timing by 5 CAD, reduced P_{\max} by 25 bar, and reduced $(dP/d\theta)_{\max}$ by 9.5 bar/CAD.
- In the supercharged mode, n-Heptane HCCI combustion timing was insensitive to λ . However, λ effectively changed the ratio of low temperature heat release to high temperature heat release (LTR/HTR-Ratio). Increasing λ by 1 unit, increased LTR/HTR-Ratio by 5%.
- Keeping all other influential parameters constant, the intake pressure was effective on HCCI combustion timing. Decreasing intake absolute pressure by 10 kPa, retarded HCCI combustion timing by 4 CAD.

7.3 Basic HCCI Combustion Operation

- Achieving proper HCCI combustion in the CFR engine using high octane fuels such as natural gas required high intake temperature and high compression ratio. Despite this, the operating region of naturally aspirated mode was extremely limited between knock and low load operation.
- Increasing n-Heptane fraction in PRF mixture, expanded the operating range at the same compression ratio and intake temperature.
- As the intake mixture (air, fuel, RG, EGR) temperature was kept constant during experiments, EGR thermal effects were neutralized. Be-

cause of low engine speed and well-mixed intake mixture, EGR inhomogeneity effects also were neutralized. Maximum engine power was achieved at maximum EGR.

- n-Heptane HCCI combustion was possible to achieve at relatively low intake temperature and compression ratio. The operating range was wider than that of high octane fuels and even wider in the supercharged mode. Double stage combustion was observed for HCCI combustion of n-Heptane.

7.4 Effect of RG on Low Octane Fuels HCCI Combustion

For the low octane fuel, n-Heptane (PRF0) and PRF20 were tested with two RG compositions at two operating modes: naturally aspirated and supercharged.

- In the naturally aspirated mode, RG blending expanded the operating region toward the high power side. It expanded the rich side and limited the lean side of the operating region. Increasing RG blend fraction retarded combustion timing. The retardation of combustion timing was similar for the two cases of PRF0 and PRF20.
- Increasing RG blend fraction by 10% keeping all other influential parameters constant, retarded low octane HCCI combustion timing by an average of 6 CAD. The same combustion retardation by λ would require λ increase by 1.2 unit that would result to IMEP reduction by 2.5 bar. Increasing RG blend fraction, decreased P_{\max} by 3 bar and $(dP/d\theta)_{\max}$ by 2 bar/CAD.
- Retardation of combustion timing allowed more optimized combustion timing, resulting in power and efficiency improvement with less intense combustion (lower P_{\max} and $(dP/d\theta)_{\max}$). 1%-2% indicated efficiency

gain was observed by 10% RG blending. Considering a fuel reforming efficiency of 78%, the total cycle efficiency drop caused by reforming is less than 1% for 10% RG blending which is compensated by efficiency increase by more optimized combustion timing.

- Supercharged n-Heptane HCCI combustion with RG blending was examined. Increasing RG blend fraction postponed combustion timing, improved power and efficiency, and emissions were not increased considerably. RG caused a smoother HCCI combustion by reducing P_{\max} and $(dP/d\theta)_{\max}$. Increasing RG blend fraction by 10%, retarded HCCI combustion timing by 4.4 CAD in the supercharged mode.
- Heat release analysis of n-Heptane HCCI combustion blended with RG showed that because of RG blending, low temperature heat release was decreased, negative temperature coefficient was prolonged and high temperature heat release happened later in the cycle. The ratio of low temperature heat release to high temperature heat release was also decreased. It was found that RG is an effective reaction inhibitor at the first stage of combustion. Increasing RG blend fraction by 10% reduced maximum low temperature heat release by 15%.
- For a specific case in the n-Heptane HCCI combustion in the supercharged mode, increasing RG blend fraction from 0% to 26%, increased IMEP from 2.8 bar to 3.9 bar and indicated thermal efficiency from 29% to 36%.
- Modeling analysis showed that RG decreased the key radical concentration in the first stage of combustion. Reaction rates and total concentration of important intermediate radicals such as H_2O_2 and CH_2O was decreased. Suppression of the first stage of combustion radical pool by RG caused a delay in the main combustion timing.

- RG composition variation did not change the engine operating parameters considerably. RG 75/25 was slightly more effective on combustion timing alteration than that of RG 50/50.
- RG was found an as effective combustion timing controller for low octane HCCI combustion. While the fuel autoignition resistance is low enough to be ignited at a moderate intake temperature and compression ratio, RG optimized combustion timing resulting to improved power and efficiency. It was found that at constant load RG can be used to effectively control combustion timing.

7.5 Effect of RG on High Octane Fuels HCCI Combustion

HCCI combustion of high octane fuels was tested with two fuels of iso-Octane (PRF100) and PRF80 and with two RG compositions of RG 75/25 and RG 50/50 in the naturally aspirated and supercharged modes.

- Variation of RG blend fraction in the fuel mixture did not change the engine operating parameters and combustion characteristics when PRF100 was used in the naturally aspirated mode. Combustion timing was relatively constant.
- Migrating from PRF100 to PRF80, effects were similar to those found with n-Heptane. Increasing RG blend fraction improved power and efficiency and retarded the combustion timing effectively. Increasing RG blend fraction by 10% in PRF80 HCCI combustion in the naturally aspirated mode, retarded combustion timing by 2.4 CAD.
- In the supercharged mode, however, the operating range shifted slightly toward richer mixtures. While power and efficiency remained relatively constant, combustion timing was retarded and combustion intensity was reduced with RG blending. Increasing RG blend fraction by 10% for

iso-Octane HCCI combustion in the supercharged mode, retarded combustion timing by 3.2 CAD.

7.6 Effect of RG on Natural Gas HCCI Combustion

Natural gas HCCI combustion was tested using two RG compositions and at two operating modes of naturally aspirated and supercharged.

- RG blending of natural gas HCCI combustion reduced the intake heating requirement.
- Increasing RG blend fraction in the fuel mixture considerably expanded the naturally aspirated operating region toward the rich side, pushing back the knock boundary. It also increased operating region width. While the range of λ at RG blend fraction = 0% was $\Delta\lambda = 0.13$, it was $\Delta\lambda = 0.73$ at RG blend fraction = 60%.
- Increasing RG blend fraction keeping λ and EGR constant in the naturally aspirated mode, advanced combustion timing. Advancing combustion timing at constant energy flow to the engine (λ and EGR) increased P_{\max} and $(dP/d\theta)_{\max}$, increased knock intensity, increased NO_x emissions, decreased HC emissions (due to faster combustion) and increased CO emissions (due to presence of CO in RG), and decreased indicated power and efficiency.
- In the supercharged natural gas HCCI combustion mode RG did not shift the operating region as much, however the same advancing combustion timing and increasing combustion intensity (higher P_{\max} and $(dP/d\theta)_{\max}$, shorter combustion duration) was observed.
- Increasing RG blend fraction by 10%, advanced natural gas HCCI combustion in the naturally aspirated mode by 1.3 CAD and in the super-

charged mode by 3.5 CAD.

- Advancing natural gas HCCI combustion timing is translated to lowering intake heating requirement by RG blending. For example, 10% H₂ blending can reduce intake heating requirement by 20 °C at constant combustion timing.
- RG composition variation did not have a strong effect on engine and combustion parameters. RG 75/25 was more effective on combustion timing advance than RG 50/50.
- Modeling analysis of the RG effect on HCCI combustion of natural gas, confirmed advancing of combustion timing. Alteration of combustion timing in this case was due to the change to specific heat ratio of the mixture, which affects after-compression temperature. No obvious chemistry effects were observed.

7.7 General Conclusions

Comparing all experimental results in the base-line HCCI combustion, low octane HCCI combustion, high octane HCCI combustion, and natural gas HCCI combustion concludes that effectiveness of RG on HCCI combustion timing control is strongly depended on fuel chemistry and engine operating parameters. If the engine is operated with intense initial conditions, or the operating point is near the knock boundary, chemical effects of RG are negligible. Temperature effects neutralizes RG chemical effects. It was also observed that RG effectiveness on HCCI combustion timing control is increased by increasing low temperature heat release characteristics of the fuel. Hence, migrating from PRF100 to PRF80, or moving the operating region toward less intensive initial conditions increases low temperature heat release; and hence, increases RG effectiveness on HCCI combustion timing control. For the specific case of natural gas, RG reduces intake heating requirements and expands the lean

boundary of the operating region.

7.8 Contributions

The purpose of HCCI combustion engine laboratory development was to establish a solid fundamental research facility for the growing HCCI combustion research. As the result of the current research study:

- An HCCI combustion engine laboratory was designed, developed, and successfully operated. Two simultaneous research projects were performed in the same experimental setup with minor changes.
- An experimental analysis of effects of RG on HCCI combustion of varieties of fuels, including natural gas, iso-Octane, n-Heptane and PRFs was performed. Suitable HCCI fuel for RG blending was identified.
- Supporting data for validation and tuning of a chemical kinetics HCCI combustion model was provided.

7.9 Future Work

HCCI combustion timing control with RG blending is a simple practical solution to a complex problem. In the final conclusion of the Roadmap Workshop on Nonpetroleum-based Fuels and Advanced Combustion Research hosted by Environment Canada (Ottawa, November 2007), use of partial reforming was mentioned as one of the solutions for using medium-refined fuels for advanced combustion such as HCCI. Hence, further research on effect of RG on HCCI combustion for a variety of fuels is required. While the current study showed several aspects of effects of RG on HCCI combustion timing, new questions and novel research areas were formed. Some of possible researches are:

- Using a light commercial single cylinder engine to operate at high efficiency and a wide operating region of HCCI combustion.

- Using an actual reformer to control combustion timing of low octane double-stage combustion fuels.
- Studying possibilities of EGR reforming by injecting the base fuel to the external EGR line.
- Studying the possibility of internal fuel reforming in a multi-cylinder engine equipped with variable valve timing and using the internally reformed fuel to adjust combustion timing.
- Using a high pressure common rail diesel engine, studying the possibility of injecting RG directly to control combustion timing of a multi-stage combustion.
- Studying effect of fuel chemistry such as cetane number, volatility, and aromatic content on effectiveness of RG on HCCI combustion timing control.

References

- [1] J. B. Heywood, Internal Combustion Engine Fundamentals, McGraw-Hill Inc., 1988.
- [2] R. Stone, Introduction to Internal Combustion Engines, 3rd Edition, SAE, Inc., 1999.
- [3] R. H. Thring, Homogeneous charge compression ignition (HCCI) engines, SAE Paper 892068.
- [4] P. M. Najt, D. E. Foster, Compression-ignited homogeneous charge combustion, SAE Paper 830264.
- [5] P. Duret, J. Lavy, Gasoline controlled auto-ignition (CAI) potential and prospects for the future automotive application, SAE Paper 2000-04-0390.
- [6] T. Aoyama, Y. Hattori, J. Mizuta, Y. Sato, An experimental study on premixed-charge compression ignition gasoline engine, SAE Paper 960081.
- [7] R. Hasegawa, H. Yanagihara, HCCI combustion in DI diesel engine, SAE Paper 2003-01-0745.
- [8] Y. Takeda, N. Keiichi, N. Keiichi, Emission characteristics of premixed lean diesel combustion with extremely early staged fuel injection, SAE Paper 961163.
- [9] J. Yang, T. Culp, T. Kenney, Development of a gasoline engine system using HCCI technology the concept and the test results, SAE Paper 2002-01-2832.
- [10] M. Noguchi, Y. Tanaka, T. Tanaka, Y. Takeuchi, A study on gasoline engine combustion by observation of intermediate reactive products during combustion, SAE Paper 790840.
- [11] S. Onishi, S. H. Jo, K. Shoda, P. D. Jo, S. Kato, Active thermo-atmosphere combustion (ATAC) a new combustion process for internal combustion engines, SAE Paper 790501.

- [12] Y. Ishibashi, M. Asai, Improving the exhaust emissions of two-stroke engines by applying the activated radical combustion, SAE Paper 960742.
- [13] K. Goto, A. Iijima, K. Yoshida, H. Shoji, Analysis of the characteristics of HCCI combustion and ATAC combustion using the same test engine, SAE Paper 2004-32-0097.
- [14] S. Kimura, O. Aoki, H. Ogawa, S. Muranaka, Y. Enomoto, New combustion concept for ultra-clean and high-efficiency small DI diesel engines, SAE Paper 1999-01-3681.
- [15] T. Shudo, Y. Ono, T. Takahashi, Ignition control by DME-reformed gas in HCCI combustion of DME, SAE Paper 2003-01-1824.
- [16] A. Helmantel, I. Denbratt, HCCI operation of a passenger car common-rail DI diesel engine with early injection of conventional diesel fuel, SAE Paper 2004-01-0935.
- [17] L. Brooke, General motors puts first HCCI prototype on the road, *Automotive Engineering* (2007) 24–26.
- [18] N. Iida, Combustion analysis of methanol-fueled active thermo-atmosphere combustion (ATAC) engine using a spectroscopic observation, SAE Paper 940684.
- [19] R. Gentili, S. Frigo, L. Tognotti, P. Habert, J. Lavy, Experimental study on ATAC (active thermo-atmosphere combustion) in a two-stroke gasoline engine, SAE Paper 970363.
- [20] G. Kontarakis, N. Collings, T. Ma, Demonstration of HCCI using a single-cylinder, four-stroke SI engine with modified valve timing, SAE Paper 2000-01-2870.
- [21] D. Law, D. Kemp, J. Allen, G. Kirkpatrick, T. Copland, Controlled combustion in an ic-engine with a fully variable valve train, SAE Paper 2000-01-0251.
- [22] M. Y. Au, J. W. Girard, R. Dibble, D. Flowers, S. M. Aceves, J. Martinez-Frias, R. Smith, C. Seibel, U. Maas, 1.9-liter four-cylinder HCCI engine operation with exhaust gas recirculation, SAE Paper 2001-01-1894.
- [23] P. Amnus, F. Mauss, M. Kraft, A. Vressner, B. Johansson, NO_x and N₂O formation in HCCI engines, SAE Paper 2005-01-0126.
- [24] M. Lejeune, D. Lortet, J. Benajes, Jose-Manuel, Potential of premixed combustion with flash late injection on a heavy-duty diesel engine, SAE Paper 2004-01-1906.
- [25] K. Okude, K. Mori, S. Shiino, T. Moriya, Premixed compression ignition (PCI) combustion for simultaneous reduction of NO_x and soot in diesel engine, SAE Paper 2004-01-1907.

- [26] P. F. Flynn, R. P. Durrett, G. L. Hunter, A. O. z. Loye, O. C. Akinyemi, J. E. Dec, C. K. Westbrook, Diesel combustion: An integrated view combining laser diagnostics, chemical kinetics, and empirical validation, SAE Paper 1999-01-0509.
- [27] M. Christensen, B. Johansson, Supercharged homogeneous charge compression ignition (HCCI) with exhaust gas recirculation and pilot fuel, SAE Paper 2000-01-1835.
- [28] J.-O. Olsson, P. Tunestl, G. Haraldsson, B. Johansson, A turbocharged dual-fuel HCCI engine, SAE Paper 2001-01-1896.
- [29] A. W. Gray, T. W. Ryan, Homogeneous charge compression ignition (HCCI) of diesel fuel, SAE Paper 971676.
- [30] H. Zhao, Z. Peng, J. Williams, N. Ladommatos, Understanding the effects of recycled burnt gases on the controlled autoignition (CAI) combustion in four-stroke gasoline engines, SAE Paper 2001-01-3607.
- [31] R. H. Stanglmaier, C. E. Roberts, Homogeneous charge compression ignition (HCCI): Benefits, compromises, and future engine applications, SAE Paper 1999-01-3682.
- [32] H. Ogawa, N. Miyamoto, N. Kaneko, H. Ando, Combustion control and operating range expansion in an HCCI engine with selective use of fuels with different low temperature, SAE Paper 2003-01-1827.
- [33] L. Koopmans, I. Denbratt, A four stroke camless engine, operated in homogeneous charge compression ignition mode with commercial gasoline, SAE Paper 2001-01-3610.
- [34] D. Jun, N. Iida, A study of high combustion efficiency and low co emission in a natural gas HCCI engine, SAE Paper 2004-01-1974.
- [35] R. H. Stanglmaier, T. W. Ryan, J. S. Souder, HCCI operation of a dual-fuel natural gas engine for improved fuel efficiency and ultra-low NOx emissions at low-to-moderate engine loads, SAE Paper 2001-01-1897.
- [36] A. Oakley, H. Zhao, N. Ladommatos, T. Ma, Experimental studies on controlled auto-ignition (CAI) combustion of gasoline in a 4-stroke engine, SAE Paper 2001-01-1030.
- [37] J. A. Eng, A study of hydrocarbon emissions from a homogenous charge spark ignition engine, Phd thesis, Princeton University (1998).
- [38] W. Yang, The chemistry controlling postcombustion hydrocarbon oxidation and homogeneous charge compression ignition, Phd thesis, Drexel University (2002).
- [39] A. Hultqvist, M. Christensen, B. Johansson, The application of ceramic and catalytic coatings to reduce the unburned hydrocarbon emissions from a homogeneous charge, SAE Paper 2000-01-1833.

- [40] T. Urushihara, K. Hiraya, A. Kakuhou, T. Itoh, Expansion of HCCI operating region by the combination of direct fuel injection, negative valve overlap and internal fuel reformation, SAE Paper 2003-01-0749.
- [41] T. Aroonsrisopon, P. Werner, J. O. Waldman, V. Sohm, D. E. Foster, T. Morikawa, M. Iida, Expanding the HCCI operation with the charge stratification, SAE Paper 2004-01-1756.
- [42] N. Milovanovic, R. Chen, A review of experimental and simulation studies on controlled auto-ignition combustion, SAE Paper 2001-01-1890.
- [43] G. Coma, P. Gastaldi, HCCI: a combustion for the future?, *International Journal of Vehicle Design* 41 (2006) 18–31.
- [44] B. Johansson, Homogeneous charge compression ignition: the future of ic engines?, *International Journal of Vehicle Design* 44 (1/2) (2007) 1–19.
- [45] D. Flowers, S. M. Aceves, J. Martinez-Frias, J. R. Smith, M. Au, J. Girard, R. Dibble, Operation of a four-cylinder 1.9 L propane-fueled homogeneous charge compression ignition engine: Basic operating, SAE Paper 2001-01-1895.
- [46] G. Haraldsson, P. Tunestl, B. Johansson, J. Hyvnen, HCCI combustion phasing in a multi cylinder engine using variable compression ratio, SAE Paper 2002-01-2858.
- [47] J. Hyvnen, G. Haraldsson, B. Johansson, Operating range in a multi-cylinder HCCI engine using variable compression ratio, SAE Paper 2003-01-1829.
- [48] M. Christensen, B. Johansson, P. Amnus, F. Mauss, Supercharged homogeneous charge compression ignition, SAE Paper 980787.
- [49] L. Koopmans, E. Strmberg, I. Denbratt, The influence of PRF and commercial fuels with high octane number on the auto-ignition timing of an engine operated in HCCI combustion mode with negative valve overlap, SAE Paper 2004-01-1967.
- [50] P. Strandh, J. Bengtsson, R. Johansson, P. Tunestl, B. Johansson, Cycle-to-cycle control of a dual-fuel HCCI engine, SAE Paper 2004-01-0941.
- [51] M. Yao, Z. Zheng, B. Zhang, Z. Chen, The effect of PRF fuel octane number on HCCI operation, SAE Paper 2004-01-2992.
- [52] M. M. Schechter, M. B. Levin, Camless engine, SAE Paper 960581.
- [53] R. Chladny, C. Koch, A. Lynch, Modeling automotive gas-exchange solenoid valve actuators, Magnetics, *IEEE Transactions on* 41 (3) (2005) 1155–1162.
- [54] D. Law, D. Kemp, J. Allen, G. Kirkpatrick, T. Copland, Controlled combustion in an IC-engine with a fully variable valve train, SAE Paper 2001-01-0251.

- [55] N. Milovanovic, R. Chen, J. Turner, Influence of the variable valve timing strategy on the control of a homogeneous charge compression (HCCI) engine, SAE Paper 2004-01-1899.
- [56] P. Strandh, J. Bengtsson, R. Johansson, P. Tunestal, B. Johansson, Variable valve actuation for timing control of a homogeneous charge compression ignition engine, SAE Paper 2005-01-0147.
- [57] J. A. Topinka, M. D. Gerty, J. B. Heywood, J. C. Keck, Knock behavior of a lean-burn, H₂ and CO-enhanced, SI gasoline engine concept, SAE Paper 2004-01-0975.
- [58] S. Peucheret, M. L. Wyszynski, R. S. Lehrle, S. Golunski, H. Xuc, Use of catalytic reforming to aid natural gas HCCI combustion in engines: experimental and modelling results of open-loop fuel reforming, International Journal of Hydrogen Energy 30 (2005) 1583–1594.
- [59] Y. Jamal, M. L. Wyszynski, On-board generation of hydrogen-rich gaseous fuels a review, International Journal of Hydrogen Energy 19 (7) (1994) 557–572.
- [60] A. L. Dicks, Hydrogen generation from natural gas for the fuel cell systems of tomorrow, Journal of Power Sources 61 (1996) 113–124.
- [61] A. Docter, A. Lamm, Gasoline fuel cell systems, Journal of Power Sources 84 (1999) 194–200.
- [62] F. Joensen, J. R. Rostrup-Nielsen, Conversion of hydrocarbons and alcohols for fuel cells, Journal of Power Sources 105 (2) (2002) 195–201.
- [63] J. M. Ogden, Review of small stationary reformers for hydrogen production, Tech. Rep. IEA/H₂/TR-02/002, Princeton University (2001).
- [64] A. Naidja, C. R. Krishna, T. Butcher, D. Mahajan, Cool flame partial oxidation and its role in combustion and reforming of fuels for fuel cell systems, Progress in Energy and Combustion Science 29 (2003) 155–191.
- [65] B. E. Milton, J. C. Keck, Laminar burning velocity in stoichiometric hydrogen and hydrogen-hydrocarbon gas mixtures, Combustion and Flame 58 (1984) 13–22.
- [66] G. Yu, C. K. Law, C. K. Wu, Laminar flame speeds of hydrocarbon + air mixtures with hydrogen addition, Combustion and Flame 63 (1986) 339–347.
- [67] M. J. Rauckis, W. J. McLean, The effect of hydrogen addition on ignition delays and flame propagation in spark ignition engines, Combustion Science and Technology 19 (1979) 207–216.
- [68] B. Nagalingam, F. Duebel, K. Schmillen, Performance study using natural gas, hydrogen-supplemented natural gas and hydrogen in AVL research engine, International Journal of Hydrogen Energy 8 (9) (1983) 715–720.

- [69] G. A. Karim, I. Wierzbka, Y. Al-Alousi, Methane-hydrogen mixture as fuel, *International Journal of Hydrogen Energy* 21 (7) (1996) 625–631.
- [70] S. O. B. Shrestha, G. A. Karim, Hydrogen as an additive to methane for spark ignition engine applications, *International Journal of Hydrogen Energy* 24 (1999) 466–475.
- [71] J. B. Heywood, F. R. Vilchis, Comparison of flame development in a spark-ignition engine fueled with propane and hydrogen, *Combustion Science and Technology* 38 (1984) 313–324.
- [72] Allenby, W. C. Chang, A. Megaritis, M. L. Wyszyski, Hydrogen enrichment: a way to maintain combustion stability in a natural gas fuelled engine with exhaust gas recirculation, the potential of fuel reforming, *Proceedings of the I MECH E Part D Journal of Automobile Engineering* 215 (2001) 405–418.
- [73] A. A. Quader, J. E. Kirwan, M. J. Grieve, Engine performance and emissions near the dilute limit with hydrogen enrichment using an on-board reforming strategy, *SAE Paper* 2004-01-1356.
- [74] E. J. Tully, J. B. Heywood, Lean-burn characteristics of a gasoline engine enriched with hydrogen from a plasmatron fuel reformer, *SAE Paper* 2003-01-0630.
- [75] T. Allgeier, M. Klenk, T. Landefeld, E. Conte, K. Boulouchos, J. Czerwinski, Advanced emission and fuel economy concept using combined injection of gasoline and hydrogen in SI engines, *SAE Paper* 2004-01-1270.
- [76] W. G. Lovell, Knocking characteristics of hydrocarbons, *Industrial and Engineering Chemistry* (1948) 2388–2438.
- [77] D. M. Newitt, The oxidation of hydrocarbons at high pressure, *Proceedings of the Symposium on Combustion* 1-2 (1948) 157–168.
- [78] W. J. Levedahl, F. L. Howard, Two-stage autoignition of some hydrocarbons for studying ignition delay, *Industrial and Engineering Chemistry* 43 (12) (1951) 2805–2814.
- [79] J. R. Thomas, H. W. Crandall, Preflame combustion of hydrocarbons. spectroscopic studies of reaction intermediates, *Industrial and Engineering Chemistry* 43 (12) (1951) 2761–2764.
- [80] C. Walcutt, J. M. Mason, E. B. Rifkin, Effect of preflame oxidation reactions on engine knock, *Industrial and Engineering Chemistry* 46 (5) (1954) 1029–1034.
- [81] W. J. Levedahl, Multistage autoignition of engine fuels, *Symposium (International) on Combustion* 5 (1) (1955) 372–385.

- [82] Y. K. Wong, G. A. Karim, A kinetic examination of the effects of recycled exhaust gases on the autoignition of homogeneous n-heptane-air mixtures in engines, SAE Paper 2000-01-2037.
- [83] A. J. Pahnke, P. M. Cohen, B. M. Sturgis, Pre-flame oxidation of hydrocarbons in a motored engine, *Industrial and Engineering Chemistry* 46 (5) (1954) 1024–1029.
- [84] A. D. Walsh, The knock ratings of fuels, *Symposium (International) on Combustion* 9 (1) (1963) 1046–1055.
- [85] A. S. C. Ma, N. P. W. Moore, Auto-ignition and knock characteristics of benzene-n-heptane-air mixtures, *Combustion and Flame* 10 (3) (1966) 245–258.
- [86] W. S. Affleck, A. Fish, Two-stage ignition under engine conditions parallels that at low pressures, *Symposium (International) on Combustion* 11 (1) (1967) 1003–1013.
- [87] A. Fish, I. A. Read, W. S. Affleck, W. W. Haskell, The controlling role of cool flames in two-stage ignition, *Combustion and Flame* 13 (1) (1969) 39–49.
- [88] J. R. Smith, R. M. Green, C. K. Westbrook, W. J. Pitz, An experimental and modeling study of engine knock, *Symposium (International) on Combustion* 20 (1) (1985) 91–100.
- [89] C. K. Westbrook, Chemical kinetics of hydrocarbon ignition in practical combustion systems, *Symposium (International) on Combustion* 28 (2) (2000) 1563–1577.
- [90] W. R. Leppard, A comparison of olefin and paraffin autoignition chemistries—a motored-engine study, SAE Paper 892081.
- [91] W. R. Leppard, The chemical origin of fuel octane sensitivity, SAE Paper 902137.
- [92] W. R. Leppard, The autoignition chemistries of primary reference fuels, olefin/paraffin binary mixtures, and non-linear octane blending, SAE Paper 922325.
- [93] G. A. Karim, M. O. Khan, N. P. W. Moore, Gross chemical kinetics from motored piston engines, SAE Paper 700060.
- [94] M. P. Halstead, C. P. Qmnn, Inhibition of autoignition at high pressure, *Combustion and Flame* 20 (2) (1973) 223–230.
- [95] S. Refael, E. Sher, Autoignition of hydrogen-enriched n-butane-air mixture: A theoretical study, *Symposium (International) on Combustion* 23 (1) (1991) 1789–1796.

- [96] R. Minetti, M. Carlier, M. Ribaucour, E. Therssen, L. R. Sochet, Comparison of oxidation and autoignition of the two primary reference fuels by rapid compression, Symposium (International) on Combustion 26 (1) (1996) 747–753.
- [97] S. W. Benson, The kinetics and thermochemistry of chemical oxidation with application to combustion and flames, Progress in Energy and Combustion Science 7 (2) (1981) 125–134.
- [98] C. K. Westbrook, F. L. Dryerb, Chemical kinetic modeling of hydrocarbon combustion, Progress in Energy and Combustion Science 10 (1) (1984) 1–57.
- [99] C. K. Westbrook, W. J. Pitz, Detailed kinetic modeling of autoignition chemistry, SAE Paper 872107.
- [100] C. K. Westbrook, W. J. Pitz, W. R. Leppard, The autoignition chemistry of paraffinic fuels and pro-knock and anti-knock additives: a detailed chemical kinetic study, SAE Paper 912314.
- [101] C. K. Westbrook, Chemical kinetics of hydrocarbon ignition in practical combustion systems, Proceedings of the Combustion Institute 28 (2000) 1563–1577.
- [102] R. A. Cox, J. A. Cole, Chemical aspects of the autoignition of hydrocarbon—air mixtures, Combustion and Flame 60 (2) (1985) 109–123.
- [103] H. Hu, J. Keck, Autoignition of adiabatically compressed combustible gas mixtures, SAE Paper 872110.
- [104] H. J. Curran, P. Gaffuri, W. J. Pitz, C. K. Westbrook, A comprehensive modeling study of n-heptane oxidation, Combustion and Flame 114 (1-2) (1998) 149–177.
- [105] T. Shudo, Y. Ono, HCCI combustion of hydrogen, carbon monoxide and dimethyl ether, SAE Paper 2002-01-0112.
- [106] T. Shudo, Y. Ono, T. Takahashi, Influence of hydrogen and carbon monoxide on HCCI combustion of dimethyl ether, SAE Paper 2002-01-2828.
- [107] T. Shudo, T. Takahashi, Influence of reformed gas composition on HCCI combustion of onboard methanol-reformed gases, SAE Paper 2004-01-1908.
- [108] T. Shudo, An HCCI combustion engine system using on-board reformed gases of methanol with waste heat recovery: ignition control by hydrogen, International Journal of Vehicle Design 41 (2006) 206–225.
- [109] T. Shudo, S. Kitahara, H. Ogawa, Influence of carbon dioxide on combustion in an HCCI engine with the ignition-control by hydrogen, SAE Paper 2006-01-3248.

- [110] S. Peucheret, M. L. Wyszynski, Exhaust gas reforming of methane to aid natural gas HCCI combustion: Experimental results of open loop hydrogen production and basic thermodynamic analysis, in: 7th Biennial Conference on Engineering Systems Design and Analysis, Manchester, UK, 2004, pp. 453–460.
- [111] D. Yap, A. Megaritis, S. Peucheret, M. L. Wyszynski, H. Xu, Effect of hydrogen addition on natural gas HCCI combustion, SAE Paper 2004-01-1972.
- [112] A. Tsolakis, A. Megaritis, Partially premixed charge compression ignition engine with on-board H₂ production by exhaust gas fuel reforming of diesel and biodiesel, *International Journal of Hydrogen Energy* 30 (2005) 731–745.
- [113] D. Yap, S. M. Peucheret, A. Megaritis, M. L. Wyszynski, H. Xu, Natural gas HCCI engine operation with exhaust gas fuel reforming, *International Journal of Hydrogen Energy* 31 (2006) 587–595.
- [114] J. A. Eng, W. R. Leppard, T. M. Sloane, The effect of POx on the autoignition chemistry of n- heptane and isooctane in an HCCI engine, SAE Paper 2002-01-2861.
- [115] M. J. Atkins, Experimental examination of the effects of fuel octane and diluent on HCCI combustion, M.sc. thesis, University of Alberta (2004).
- [116] D. M. Arthur, Using hydrogen to extend EGR limit of SI engines, M.sc., University of Alberta (2005).
- [117] D. R. Lancaster, R. B. Krieger, J. H. Lienesch, Measurement and analysis of engine pressure data, SAE Paper 750026.
- [118] C. A. Amann, Cylinder-pressure measurement and its use in engine research, SAE Paper 852067.
- [119] T. K. Hayes, L. D. Savage, S. C. Sorenson, Cylinder pressure data acquisition and heat release analysis on a personal computer, SAE Paper 860029.
- [120] A. L. Randolph, Methods of processing cylinder-pressure transducer signals to maximize data accuracy, SAE Paper 900170.
- [121] K. S. Kim, S. S. Kim, Measurement of dynamic TDC in SI engines using microwave sensor, proximity probe and pressure transducers, SAE Paper 891823.
- [122] M. F. J. Brunt, G. G. Lucas, The effect of crank angle resolution on cylinder pressure analysis, SAE Paper 910041.
- [123] M. F. J. Brunt, A. L. Emtage, Evaluation of IMEP routines and analysis errors, SAE Paper 960609.
- [124] M. F. J. Brunt, C. R. Pond, Evaluation of techniques for absolute cylinder pressure correction, SAE Paper 970036.

- [125] D. Lynch, W. J. Smith, Comparison of AFR calculation methods using gas analysis and mass flow measurement, SAE Paper 971013.
- [126] N. Cavina, F. Ponti, Air fuel ratio estimation using in-cylinder pressure frequency analysis, Transaction of the ASME 125 (2003) 812–819.
- [127] C. J. Mueller, The quantification of mixture stoichiometry when fuel molecules contain oxidizer elements or oxidizer molecules contain fuel elements, SAE Paper 2005-01-3705.
- [128] D. H. Cuttler, N. S. Girgis, Photography of combustion during knocking cycles in disc and compact chambers, SAE Paper 880195.
- [129] G. Konig, C. G. W. Sheppard, End gas autoignition and knock in a spark ignition engine 902135.
- [130] P. V. Puzinauskas, Examination of methods used to characterize engine knock, SAE Paper 920808.
- [131] G. Benson, E. A. Fletcher, T. E. Murphy, H. C. Scherrer, Knock (detonation) control by engine combustion chamber shape, SAE Paper 830509.
- [132] M. Haghgoie, Effect of fuel octane number and inlet air temperature on knock characteristics of a single cylinder engine, SAE Paper 902134.
- [133] M. D. Checkel, J. D. Dale, Computerized knock detection from engine pressure records, SAE Paper 860028.
- [134] M. D. Checkel, J. D. Dale, Testing a third derivative knock indicator on a production engine, SAE Paper 861216.
- [135] M. D. Checkel, J. D. Dale, Pressure trace knock measurement in a current SI production engine, SAE Paper 890243.
- [136] H. Ando, J. Takemura, E. Koujina, A knock anticipating strategy based on the real time combustion mode analysis, SAE Paper 890882.
- [137] S. Michael, K. Shigahara, D. N. Assanis, Correlation between knock intensity and heat transfer under light and heavy knocking conditions in a spark ignition engine, SAE Paper 960495.
- [138] T. Katranik, F. Trenc, S. R. Oprenik, A new criterion to determine the start of combustion in diesel engines, ASME Journal of gas turbine and power 128 (2006) 928–933.
- [139] G. M. Rassweiler, L. Withrow, Motion pictures of engine flames correlated with pressure cards, SAE Transactions 42 (5) (1938) 185–204.
- [140] G. Woschni, Universally applicable equation for the instantaneous heat transfer coefficient in the internal combustion engine, SAE Paper 670931.
- [141] J. Chang, O. Gralp, Z. Filipi, D. Assanis, T.-W. Kuo, P. Najt, R. Rask, New heat transfer correlation for an HCCI engine derived from measurements of instantaneous surface heat flux, SAE Paper 2004-01-2996.

- [142] P. I. Good, Resampling methods A practical guide to data analysis, 3rd Edition, Birkhauser, 2005.
- [143] J. Hyvnen, G. Haraldsson, B. Johansson, Supercharging HCCI to extend the operating range in a multi-cylinder VCR-HCCI engine, SAE Paper 2003-01-3214.
- [144] A. Bhave, M. Kraft, F. Mauss, A. Oakley, H. Zhao, Evaluating the EGR-AFR operating range of a HCCI engine, SAE Paper 2005-01-0161.
- [145] H. Kuzuyama, M. Machida, K. Akihama, K. Inagaki, M. Ueda, A study on natural gas fueled homogeneous charge compression ignition engine expanding the operating range and combustion mode switching, SAE Paper 2007-01-0176.
- [146] H. Ogawa, K. Azuma, N. Miyamoto, Combustion control and operating range expansion in an homogeneous charge compression ignition engine with suppression of low-temperature oxidation by methanol: influence of compression ratio and octane number of main fuel., International Journal of Engine Research 8 (1) (2007) 139–145.
- [147] H. Xu, M. L. Wyszynski, A. Megaritis, D. Yap, T. Wilson, J. Qiao, S. Richardson, S. Golunski, S. Peucheret, Research on expansion of operating windows of controlled homogeneous auto-ignition engines., International Journal of Engine Research 8 (1) (2007) 29–40.
- [148] J.-O. Olsson, P. Tunestl, J. Ulfvik, B. Johansson, The effect of cooled EGR on emissions and performance of a turbocharged HCCI engine, SAE Paper 2003-01-0743.
- [149] H. Zhao, Z. Peng, N. Ladommatos, Understanding of controlled autoignition combustion in a four-stroke gasoline engine, Proc Instn Mech Engrs 215 (D) (2001) 1297–1310.
- [150] S. S. Morimoto, Y. Kawabata, T. Sakurai, T. Amano, Operating characteristics of a natural gas-fired homogeneous charge compression ignition engine (performance improvement using EGR), SAE paper 2001-01-1034.
- [151] K. Hiraya, K. Hasegawa, T. Urushihara, A. Iiyama, T. Itoh, A study on gasoline-fueled compression ignition engine a trial of operation region expansion, SAE Paper 2002-01-0416.
- [152] H. Zhao, J. Li, T. Ma, N. Ladommatos, Performance and analysis of a 4-stroke multi-cylinder gasoline engine with CAI combustion, SAE Paper 2002-01-0420.
- [153] Z. Peng, H. Zhao, N. Ladommatos, Effects of air/fuel ratios and EGR rates on HCCI combustion of n-heptane, a diesel type fuel, SAE Paper 2003-01-0747.
- [154] R. Tominaga, S. Morimoto, Y. Kawabata, S. Matsuo, T. Amano, Effects of heterogeneous EGR on the natural gas-fueled HCCI engine using experiments, CFD and detailed kinetics, SAE Paper 2004-01-0945.

- [155] J. Li, H. Zhao, N. Ladommatos, T. Ma, Research and development of controlled auto-ignition (CAI) combustion in a 4-stroke multi-cylinder gasoline engine, SAE Paper 2001-01-3608.
- [156] G. E. P. Box, J. S. Hunter, W. J. Hunter, Statistics for Experiments: Design, Innovation, and Discovery, John Wiley & Sons, Inc., 2005.
- [157] D. C. Montgomery, Design and Analysis of Experiments, John Wiley & Sons, Inc., 1996.
- [158] M. J. Anderson, P. J. Whitcomb, DOE simplified: practical tools for effective experimentation, Productivity Press, New York, 2000.
- [159] V. Hosseini, M. D. Checkel, Effect of reformer gas on HCCI combustion-part II: Low octane fuels, SAE Paper 2007-01-0206.
- [160] V. Hosseini, M. D. Checkel, Alternative mode combustion study: HCCI fueled with heptane and spark ignition fueled with reformer gas, in: ASME Internal Combustion Engine Division 2005 Fall Technical Conference, ASME, Ottawa, Canada, 2005.
- [161] I. Thomas W Ryan, S. S. Lestz, The laminar burning velocity of iso-octane and n-heptane, methanol, methane, and propane at elevated temperature and pressures in the presence of diluent, SAE Paper 800103.
- [162] J. Warnatz, Hydrocarbon oxidation high-temperature chemistry, Pure and Applied Chemistry 72 (11) (2000) 2101–2110.
- [163] P. Kongsereparp, B. Kashani, M. D. Checkel, A stand-alone multi-zone model for combustion in HCCI engines, in: Fall Technical Conference of the ASME Internal Combustion Engine Division, Ottawa, Canada, 2005.
- [164] P. Kongsereparp, M. D. Checkel, Investigating the effects of reformed fuel blending in a natural gas- and n-heptane-HCCI engine using a multi-zone model. submitted to sae world congress 2007, SAE Paper 2007-01-0205.
- [165] P. Kongsereparp, M. D. Checkel, Novel method of setting initial conditions for multi-zone HCCI combustion modeling, SAE Paper 2007-01-0674.
- [166] P. Kongsereparp, M. D. Checkel, Investigating the effects of reformed fuel blending in a methane- or n-heptane-HCCI engine using a multi-zone model, SAE Paper 2007-01-0205.
- [167] V. Golovichev, Semi-reduced n-heptane autoignition mechanisms, Vol. 1, Chalmers Institute of Technology, Sweden, <http://www.tfd.chalmers.se/valeri/MECH.html>, (last visited in February 2007).
- [168] G. Subramanian, A. P. Da Cruz, R. Bounaceur, L. Vervisch, Chemical impact of CO and H₂ addition on the auto-ignition delay of homogenous n-heptane/air mixtures, Combustion Science and Technology 179 (9) (2007) 1937 – 1962.

- [169] T. Shudo, H. Yamada, Hydrogen as an ignition-controlling agent for HCCI combustion engine by suppressing the low-temperature oxidation, *International Journal of Hydrogen Energy* 32 (14) (2007) 3066–3072.
- [170] V. Hosseini, M. D. Checkel, Effect of reformer gas on HCCI combustion-part I: High octane fuels, SAE Paper 2007-01-0208.
- [171] M. Christensen, B. Johansson, P. Einewall, Homogeneous charge compression ignition (HCCI) using isooctane, ethanol and natural gas a comparison with spark-ignition operation, SAE Paper 972874.
- [172] G. Gnanam, A. Sobiesiak, G. Reader, C. Zhang, An HCCI engine fuelled with iso-octane and ethanol, SAE Paper 2006-01-3246.
- [173] K. Swan, M. Shahbakhti, C. R. Koch, Predicting start of combustion using a modified knock integral method for an HCCI engine, SAE Paper 2006-01-1086.
- [174] H. J. Curran, P. Gaffuri, W. J. Pitz, C. K. Westbrook, A comprehensive modeling study of iso-octane oxidation, *Combustion and Flame* 129 (3) (2002) 253–280.
- [175] V. Hosseini, M. D. Checkel, Using reformer gas to enhance HCCI combustion of CNG in a CFR engine, SAE Paper 2006-01-3247.
- [176] V. Hosseini, M. D. Checkel, Reformer gas enrichment of natural gas homogeneous charge compression ignition (HCCI) combustion, in: *Combustion Institute/ Canadian Section, Spring meeting, Waterloo, 2006*.
- [177] J.-O. Olsson, P. Tunestl, B. Johansson, S. Fiveland, R. Agama, M. Willi, D. Assanis, Compression ratio influence on maximum load of a natural gas fueled HCCI engine, SAE Paper 2002-01-0111.
- [178] G. P. Smith, D. M. Golden, M. Frenklach, N. W. Moriarty, B. Eiteneer, M. Goldenberg, C. Bowman, R. Hanson, S. Song, W. Gardiner, V. V. Lissianski, Gri-mech 3.0 data, http://www.me.berkeley.edu/gri_mech/, Nov 2006.
- [179] C. L. Yaws, *Chemical Properties Handbook*, McGraw-Hill Inc., 1999.
- [180] L. D. Thede, *Practical analog and digital filter design*, Artech House, Incorporated, 2005.
- [181] M. Iida, T. Aroonsrisopon, M. Hayashi, D. Foster, J. Martin, The effect of intake air temperature, compression ratio and coolant temperature on the start of heat release in an HCCI (homogeneous charge compression ignition) engine, SAE Paper 2001-01-1880.

Appendix A

Chemical and Physical Properties

A.1 Natural Gas

Natural gas was taken from Edmonton's domestic natural gas supply from Atco pipeline that comes from Edmonton Ethane Extraction plant. Natural gas was compressed to two banks of high pressure tanks. The high pressure composite stiffened stainless steel tank that was connected to CFR engine was regularly refueled using the banks of high pressure gas. The composition of natural gas was determined by Atco using a gas chromatograph. As described by Arthur [116] the properties of natural gas is indicated in Table A.1. These properties of natural gas was used for all experimental calculations such as λ , RG blend fraction, and efficiencies. It also was used as the input for ChemComb-SZM.

Table A.1: Domestic natural gas properties

Property	Value
Normalized CH ₄ dry molar fraction	95.39%
Normalized C ₂ H ₆ dry molar fraction	1.90%
Normalized N ₂ dry molar fraction	1.93%
Normalized CO ₂ dry molar fraction	0.78%
Molar mass [g/mol]	16.76
Density at STP [kg/m ³]	0.748
H/C ratio	3.92
LHV [kJ/kg]	44,818

A.2 n-Heptane

n-Heptane properties for the purpose of experimental calculations was obtained from electronic version of Chemical Properties Handbook ([179]). In [179] the density of liquids is presented as a function of temperature and critical temperature as:

$$\rho = AB\left(\frac{1-T}{T_c}\right)^n \quad (\text{A.1})$$

where ρ is the density of liquid, T is temperature, T_c is critical temperature and A and B are correlation coefficients. Table A.2 shows the coefficients of Equation A.1 for n-Heptane and other properties of n-Heptane that was used in the course of this study.

Table A.2: n-Heptane properties

Property	Value
Molecular Formula	C ₇ H ₁₆
Substance name	Normal heptane
CAS registry number	142-82-5
A	0.23237
B	0.26020
n	0.27910
T _c [K]	540.26
T _{min} [K]	182.57
T _{max} [K]	540.26
Density @ 25 °C [g/cm ³]	0.682
Enthalpy of combustion @ 77 °F [kJ/kg]	44558.1

A.3 iso-Octane

iso-Octane properties for the purpose of experimental calculations was obtained from electronic version of Chemical Properties Handbook ([179]). The same density equation (Equation A.1) was used for iso-Octane. Table A.3 shows the coefficients of Equation A.1 for iso-Octane and other properties of iso-Octane that was used in the course of this study.

Table A.3: iso-Octane properties

Property	Value
Molecular Formula	C_8H_{18}
Substance name	2,2,4-trimethylpentane
CAS registry number	540-84-1
A	0.24563
B	0.27373
n	0.28460
T_c [K]	543.96
T_{min} [K]	165.78
T_{max} [K]	543.96
Density @ 25 °C [g/cm ³]	0.690
Enthalpy of combustion @ 77 °F [kJ/kg]	44342.6

A.4 PRFs

Primary reference fuels are mixed on volume basis. For the purpose of calculation of primary reference fuels properties, based on operating temperature, the mass fraction of each of n-Heptane and iso-Octane in the PRF mixture was calculated. Using mass fraction, all subsequent properties of PRF mixture was calculated.

A.5 RG

Reformer gas properties was calculated using the individual properties of H_2 and CO obtained from Heywood [1]. Table A.4 shows the properties of H_2 and CO used in this study for the purpose of experimental calculations.

Table A.4: H_2 and CO properties from [1]

Property	H_2	CO
Molecular weight (kg/kmol)	2.015	28.01
LHV (MJ/kg)	120.0	10.1

Measurement and Control Devices Specifications

Several control and measurement devices were used in this study. Most of the equipments were standard general application devices. For example T, K, and J type thermocouples were used to measure various temperatures, and Valydine diaphragm type differential pressure transducers were used to measure the intake and exhaust pressures.

Some specific devices were used to measure the highly sensitive parameters in this study. Among them, flow rates of air and fuel, and cylinder pressure are described here.

B.1 Air mass flow meter

A TSI hot wire sensor as described by Arthur [116] was used for the purpose of air mass flow meter measurement. The air mass flow rate is a highly sensitive parameter that directly affects the air/fuel ratio calculation and is critical for simulation purposes. The flow meter had a linear analog output and intake pressure variation through supercharging did not change the calibration curve. Table B.1 shows the specifications of air mass flow meter.

Table B.1: Hot wire TSI air mass flow meter specifications

Parameter	Value/spec
TSI model	4235-01-01
Gas	Air
Flow Range [standard L/min]	20 to 1000
output (linear, mA)	4-20
Gas Temperature [°C]	-40 to +60
Pressure range [psig]	up to 150
Response time	less than 25 ms
Supply voltage [VDC]	12-15

B.2 Gaseous fuel mass flow meter

Three Omega gaseous flammable substance mass flow meters were used in this study for the purpose of measurement of mass flow rates of natural gas, high flow reformer gas, and low flow reformer gas. All three mass flow meters were operated by the principle of heated tube.

Natural gas mass flow meter had the same operating range of high RG mass flow meter of 0-50 standard L/min. The low RG flow meter had a narrower operating range of 0-5 standard L/min. Table B.2 shows the common specifications of Omega mass flow meter used in this study.

Table B.2: Omega gaseous flammable mass flow meter specifications

Parameter	value/spec
Omega model	FMA21XX
Gas	natural gas and RG
Power supply [VAC]	115 with AC adaptor
Analog output [VDC]	0-5
Maximum gas pressure [psig]	500 for stainless steel
Response time [s]	1-2
Operating temperature [°C]	0-50

B.3 Liquid fuel volume flow meter

Two positive displacement piston type Max Machinery liquid volume flow meters were used for the purpose of this study for high and low volume flow

Table B.3: General specifications of Max Machinery volume flow meters

Parameter	value/spec
Temperature rating (body or fluid) [°C]	-48 to 150
Transmitter temperature rating [°C]	-20 to 65
Maximum case pressure [psi]	1000
Supply voltage -model 213 [VDC]	4.5 to 30
Supply voltage -model 272 [VDC]	± 15
Supply current [mA]	15 maximum
Displacement [cm ³ /rev]	0.887

rates. Each flow meter was equipped with a separate transmitter. The flow meter model 213-310 was equipped with a pulse output transmitter model 284-512 and was used for the low range of flow rates. This flow meter was producing a pulse output signal that was suitable for low flow rates avoiding output fluctuation of flow meter crankshaft as the result of reciprocating movement of pistons. Flow meter model 213-311 was the same as 213-310 but transmitter was different. The transmitter model 272-565 for flow meter 213-311 produced an analog output of 0-10 VDC. Table B.3 shows the general specifications of Max Machinery volume flow meters.

B.4 Cylinder pressure

The cylinder pressure was measured using a Kistler 6043A water cooled piezo-electric pressure transducer with a Kistler 507 charge amplifier. Table B.4 shows the general specifications of the Kistler pressure transducer.

Table B.4: Specifications of Kistler pressure transducer

Parameter	value/spec
Range [bar]	0-250
Operating temperature range [°C]	-50 to +350
Sensitivity [pC/bar]	-20
Load-change drift [bar/s]	< ±0.5

Appendix **C**

Calibration Curves

Several devices were calibrated on a daily basis and the calibration values were altered during the course of study. Arthur [116] described the calibration procedure for the California Analytical Instrument exhaust gas analyzer in details. The same calibration method was used to calibrate the exhaust gas analyzers with the available known gas mixtures provided by Praxair.

Intake and exhaust pressure sensors also calibrated several times using a pressure calibrator. The calibration procedure is rather general to be discussed here. In the following sections, the calibration curves for the specific and important parameters is presented.

C.1 Cylinder pressure sensor calibration

The pressure transducer was calibrated using a dead weight pressure calibration unit capable of calibrating pressure transducers up to 2000 psi. Table B.4 shows the general specs of the pressure transducer. The calibration was performed twice for two cases of natural aspiration operation and supercharged operation, as in supercharged mode maximum cylinder pressure was higher.

Figure C.1 shows the calibration curve for the low pressure range (natural aspiration mode). The linear regression of the data points resulted to:

$$P = 125.50 \times V - 0.49 \tag{C.1}$$

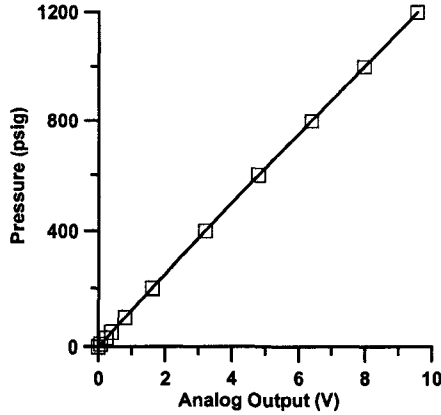


Figure C.1: Kistler 6043A60 pressure transducer calibration (with Kistler 507 charge amplifier, sensitivity= 2.04, range multiplier=200,full scale =3.476 V, date: December 12, 2004

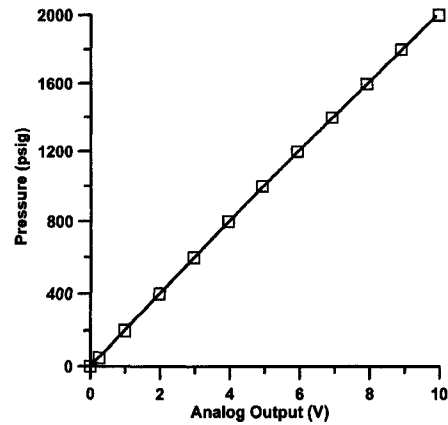


Figure C.2: Kistler 6043A60 Pressure transducer calibration (with Kistler 507 charge amplifier) sensitivity= 10.00, range multiplier=200, date: March 29, 2007

with coefficient of determination of $R^2 = 0.999998$. In Equation C.1, P is cylinder pressure in psig and V is charge amplifier analog output in Volts.

For the case of supercharged operation the pressure transducer was calibrated again covering the whole range of maximum pressure. Figure C.2 shows the calibration curve for this case.

Using the least square method, the calibration equation for the case of supercharged operation is indicated in Equation C.2.

$$P = 201.46 \times V + 2.34 \quad (C.2)$$

with coefficient of determination of $R^2 = 0.999951$. P is in psig and V is in Volts.

C.2 Liquid fuel flow meter calibration

Two Max Machinery positive displacement flow meters were used for the purpose of this study which one of them produced analog output and the other one square pulse. Table B.3 shows the general specs of the flow meters. Max

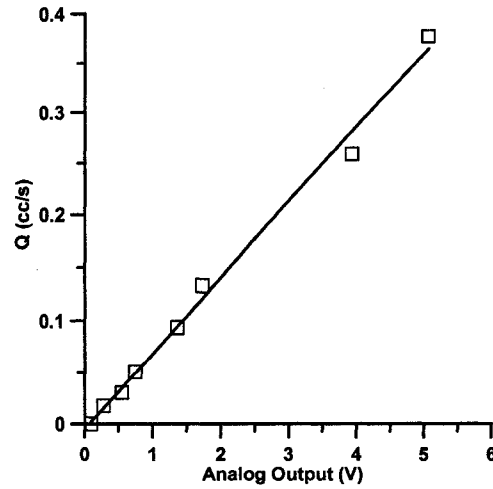


Figure C.3: Max Machinery flow meter 213-311 and transducer 272-566 (number 14 in Figure 2.5) calibration curve, maximum sensitivity range, Date: January 15, 2007

Machinery model 213-311 with transducer model 272-565 had an analog output (number 14 in Figure 2.5). Using the liquid fueling system (Figure 2.5) and a drain valve before the injector, the flow meter was calibrated at several steady state flow conditions at the same operational temperature and pressure of experiments. Figure C.3 shows the calibration curve.

Equation C.3 shows the result of least square linear regression.

$$Q = 0.0727 \times V - 0.0048 \quad (C.3)$$

in which Q is the volume flow rate in cm^3/s and V is analog output in volts. The coefficient of determination $R^2 = 0.992986$.

Max Machinery flow meter 213-310 and transducer 284-512 were calibrated in the factory and according to the calibration sheet, an average of 110.84 pulses per cm^3 of liquid fuel volume was counted in data acquisition system

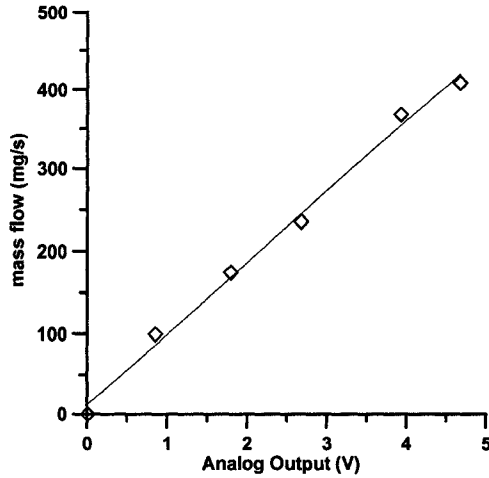


Figure C.4: Omega natural gas flow meter FMA-A2117 flow meter (0-50 SLPM range) calibration, Date: October 6, 2005

C.3 Gaseous fuel flow meter calibration

Three Omega gaseous fuel flow meters were used for the purpose of this study. Table B.2 shows the general specifications of these flow meters.

C.3.1 Natural gas flow meter

Using a digital scale that was connected to data acquisition system through a serial port, and operating the engine at steady state conditions, several calibration points were collected for natural gas flow meter. Figure C.4 shows the calibration results. Equation C.4 shows the result of least square linear regression.

$$m = 86.94 \times V + 11.72 \quad (\text{C.4})$$

in which m is the mass flow rate in mg/s and V is analog output in volts. The coefficient of determination $R^2 = 0.993698$.

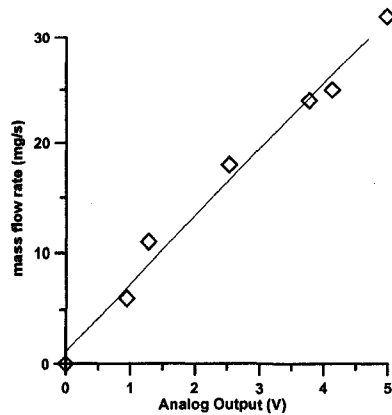


Figure C.5: Omega RG 25/75 flow meter (0-5 SLPM range) calibration, Date: March 22, 2007

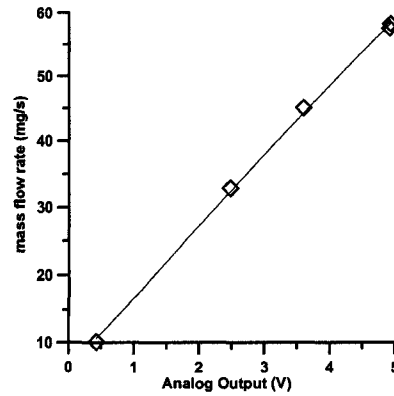


Figure C.6: Omega RG 50/50 flow meter (0-5 SLPM range) calibration, Date: May 25, 2007

C.3.2 RG low mass flow

The same method of natural gas flow meter was used for low flow RG mass flow meter calibration. Figure C.5 shows the calibration results for the case of RG 25/75 composition.

Equation C.5 shows the result of least square linear regression.

$$m = 6.12 \times V + 1.14 \quad (\text{C.5})$$

in which m is the mass flow rate in mg/s and V is analog output in volts. The coefficient of determination $R^2 = 0.987806$.

For the case of RG 50/50, the same method was used and Figure C.6 shows the calibration curve. Equation C.6 shows the result of least square linear regression.

$$m = 10.61 \times V + 6.05 \quad (\text{C.6})$$

in which m is the mass flow rate in mg/s and V is analog output in volts. The coefficient of determination $R^2 = 0.998945$.

C.3.3 RG high mass flow

The same method of natural gas flow meter was used for low flow RG mass flow meter calibration. Figure C.7 shows the calibration results.

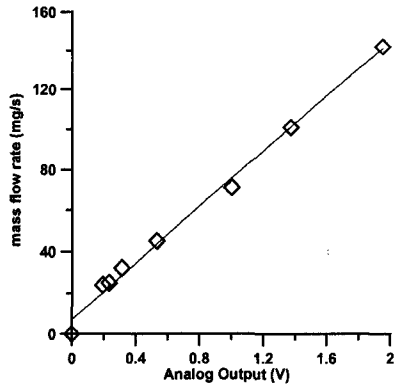


Figure C.7: Omega RG 25/75 flow meter FMA-A2117 flow meter (0-50 SLPM range) calibration, Date: March 22, 2007

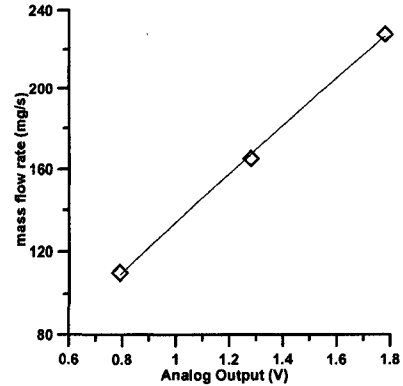


Figure C.8: Omega RG 50/50 flow meter FMA-A2117 flow meter (0-50 SLPM range) calibration, Date: May 25, 2007

Equation C.7 shows the result of least square linear regression.

$$m = 68.68 \times V + 7.09 \quad (\text{C.7})$$

in which m is the mass flow rate in mg/s and V is analog output in volts. The coefficient of determination $R^2 = 0.996$.

Figure C.8 shows the calibration results for high RG mass flow meter operated with RG 50/50 composition.

Equation C.8 shows the result of least square linear regression.

$$m = 119.01 \times V + 14.97 \quad (\text{C.8})$$

in which m is the mass flow rate in mg/s and V is analog output in volts. The coefficient of determination $R^2 = 0.999133$.

Appendix D

Pressure Trace Signal Analysis

The engine pressure signal was collected using a Kistler pressure transducer in combination with Kistler charge amplifier. The pressure signal was gathered in raw voltage signal and was converted to appropriate unit later on using off-line calculations.

The pressure signal was timed using an index signal from a BEI optical Encoder. The index signal which was happening once in every revolution was used as a trigger signal to start the pressure signal acquisition. The location of this trigger signal was carefully determined on the crank angle position and with respect to TDC. While the signal was being acquired based on the rate of pressure rise the proper cycle (compression or exhaust) was determined and the signal was adjusted accordingly.

The original pressure trace was gathered mostly for 100 consecutive cycles with 0.1 CAD resolution. Hence, for each cycle 7200 samples was gathered. At the speed of 800 RPM where most of the experiments in this study were conducted, the sampling rate was 48 kHz.

Several previous studies have described pressure signal pegging, filtering, and analysis such as Lancaster et al (1975) [117], Amann (1985) [118], Checkel and Dale (1986) [133], Hayes et al (1986) [119], Kim and Kim (1989) [121], Randolph (1990) [120], Brunt and Lucas (1991) [122], Brunt and Pond (1997) [124]. For the purpose of pegging first the un-timed pressure signal in Volts

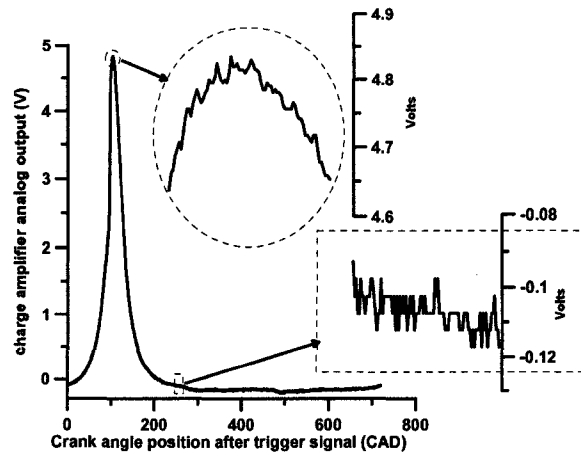


Figure D.1: A sample of a raw voltage output of a pressure trace magnified in two locations of around top dead center and late in expansion stroke, note that the cycle exhibited some knocking oscillation

was converted to a timed signal starting at -180 CAD,aTDC and ended to +180 CAD,aTDC. The pressure signal data during exhaust and intake cycles were discarded. Figure D.1 shows a sample of raw pressure trace voltage that is magnified in two location to show the knock oscillations and general noise. Then the calibration value of pressure transducer was used to convert the raw voltage signal to a known unit in this case bar. For the purpose of pegging pressure signal to a known pressure value, the intake pressure at and around intake valve close was used. The whole pressure signal was shifted such that the pressure signal during the late stage of intake valve opening was equal to the intake pressure. Figure D.2-a and -b shows a sample of an original pressure trace compared with filtered pressure trace around top dead center. Note that for the knocking cycle in Figure D.2-b, a slight misalignment happened around TDC.

Because of high sampling rate, electronic and electromagnetic created noises, data acquisition and engine actual created noises, and vibration of the pressure wave inside the cylinder, the pressure trace is always accompanied by various amount of noise. This noise is more sever in spark ignition mode when

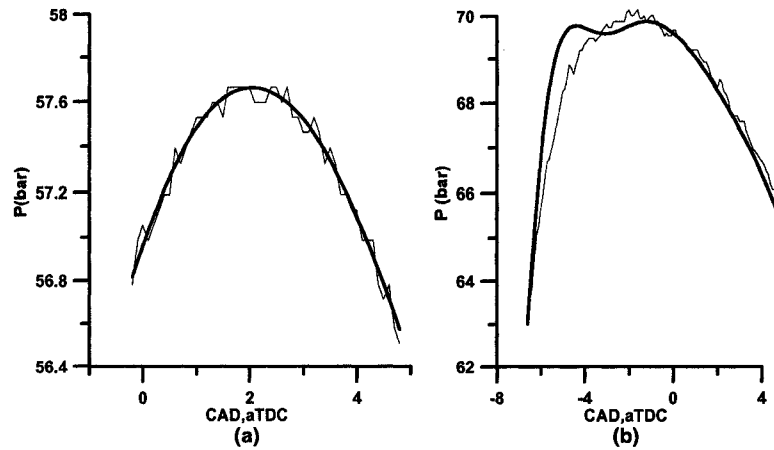


Figure D.2: A comparison of noisy signal with filtered signal for (a) a non-knocking cycle and (b) knocking cycle

the spark discharge happens. For the further analysis of pressure trace, it is required to have a smooth noise-free pressure signal. Any differentiation of a noise pressure trace signal magnifies the noise level to a near to 1.0 signal to noise ratio.

Several techniques are available for pressure trace filtration. It is very important to filter the pressure signal such that the shape of the pressure signal is preserved, the timing of pressure signal remains constant, and all real oscillation of pressure trace remains intact. The range of methods that a pressure signal covers from a simple averaging over consecutive cycles, multi-point, least-square curve fitting, and using digital filtering techniques. In this study the pressure signal was filtered using a digital filter.

The practical guide to design a digital filter by Thede (2005) [180] was used to choose and implement the proper digital filter. The Butterworth approximation function was used as the conversion function. As stated in [180], Butterworth function is often called maximally flat response function because no other approximation has smoother transition to the passband to the stopband. Based on the sampling frequency of 48kHz at 800 RPM, the cut off frequency was chosen at 1000 Hz and the order of filter was chosen at 4 using

a trial and error procedure. At cut off frequency $f_c=1000$ Hz, all knock oscillation signals were filtered as in this engine the knock oscillation was reported around 5.7 to 5.8 kHz. The knock analysis was performed separately on the raw pressure signal as discussed in Appendix F.

Although Butterworth 4th order digital filter was an appropriate choice, some consideration on pressure trace filtering was required. As the signal was filtered, the start and end of pressure trace was distorted by the pressure signal. Avoiding that, one hundred dummy data was added to the start and end of pressure signal before filtering and after completion of filtering process they were taken out. Also, a forward filtration of signal was shifted the original signal on a time scale. A backward filtration of signal would solve this problem but changes the shape of pressure signal.

Assume that the original pegged calibrated signal is P_1 . The filter was applied once on P_1 forward. The result is P_2 that is filtered but slightly was shifted. Then the filter was applied on P_2 backward to obtain P_3 . Now this signal is not shifted but the shape is slightly changed because of double filtration. The timing difference between P_{max} in P_2 and P_3 was calculated. Then P_2 timing was shifted to the amount of time difference between P_2 and P_3 to obtain P_4 . Now P_4 is only once filtered from P_1 and timing also is corrected. The following Matlab program was written for low pass and band pass filtration of pressure trace signal.

D.1 Matlab Program for low pass and band pass filter

D.1.1 Main Program

```
% Reading the list of raw pressure signal files from the excel file
[excel_2D_array excel_column_titles]=xlsread('file_list.xls');
[end_data bb]=size(excel_2D_array); file_ID=excel_2D_array(:,2);
% position of TDC relative to Encoder trigger signal
```

```

TDC_def=104.1; TDC=input([' Top Dead Center Position (default =
',num2str(TDC_def),' )-----> ']); if
length(TDC)==0;TDC=TDC_def;end; disp('') disp('')
% Calibration value for pressure transducer
pcal_def=201.46; pcal=input([' Pressure Cal.Value for
P(psi)=cal*V(default cal=',num2str(pcal_def),' ) ----->
']);
if length(pcal)==0; pcal=pcal_def;end; disp('') disp('')
% calculating compression start point and expansion end point
comp_start=(TDC*10)-1800; if comp_start<0;
%compression stroke starts
comp_start=7200+comp_start;end; exp_end=TDC*10+1800;
%expansion stroke ends
if exp_end>7200; exp_end=exp_end-7200;end;
%engine speed
NS_def=700; NS=input(['Engine Speed (RPM),(default = '
,num2str(NS_def),' ) ----> ']); if isempty(NS)==1; NS=NS_def;
end;
% Cut off frequency for low pass filter
LP_fc_def=1000; % default cut-off frequency =1000
LP_fc=input(['Enter Cut-Off Frequency for Butterworth Digital
Filter, Default= ',num2str(LP_fc_def),' Hz']); if
isempty(LP_fc)==1;LP_fc=LP_fc_def;end; disp(''); disp('');
LP_order_def=4; LP_order=input(['Enter order of Butterworth Low Pass
Digital Filter, Default= ',num2str(LP_order_def)]); if
isempty(LP_order)==1;LP_order=LP_order_def;end;
LP_fs=NS*3600/60; %sampling rate(Hz)
LP_wn=2*LP_fc/LP_fs; [LP_b LP_a]=butter(LP_order,LP_wn);
% Cut off frequency for band pass signal (knock analysis)
BP_fc1_def=5000; % default cut-off frequency =1000
BP_fc1=input(['Enter start pass Frequency for Butterworth Band Pass

```

```

Digital Filter,   Default= ',num2str(BP_fc1_def),' Hz']); if
isempty(BP_fc1)==1;BP_fc1=BP_fc1_def;end; disp(''); disp('');
BP_fc2_def=6000; % default cut-off frequency =1000
BP_fc2=input(['Enter end pass Frequency for Butterworth Band Pass
Digital Filter,   Default= ',num2str(BP_fc2_def),' Hz']); if
isempty(BP_fc2)==1;BP_fc2=BP_fc2_def;end; disp(''); disp('');
BP_order_def=4; BP_order=input(['Enter order of Butterworth Band
Pass Digital Filter,   Default= ',num2str(BP_order_def)']); if
isempty(BP_order)==1;BP_order=BP_order_def;end;
BP_fs=NS*3600/60; %sampling rate(Hz)
BP_wn1=2*BP_fc1/BP_fs; BP_wn2=2*BP_fc2/BP_fs; BP_wn=[BP_wn1 BP_wn2];
[BP_b BP_a]=butter(BP_order,BP_wn); point_number=file_ID; stopnow=0;
count=1; while stopnow==0 string_temp=num2str(file_ID(count));
string_temp(length(string_temp)+1:length(string_temp)+6)='-P.xls';
pressure_data=xlsread(string_temp); [row col]=size(pressure_data);
outcolumn=0;
disp(['Pegging and Referencing for File
',num2str(count),' of ', num2str(end_data), ' .... Point # ',
num2str(point_number(count)),' in progress...']); for column=1:col;
% reading one column of pressure data file in volt
p1=pressure_data(:,column);
if p1(1800)~= 0
% converting voltage to pressure(psi)
p2=pcal*p1;
%converting from psi to bar
p3=p2*6.894757e3/1e5; if comp_start==0; comp_start=1; exp_end=3600;
end; if comp_start<7100
%taking 10 degree average of non-referenced pressure
p3_intake_mean=mean(p3(comp_start:comp_start+100)); end; if
comp_start>7100 p3_intake_mean=(1/2)*(mean(p3(comp_start:7200))+

```

```

mean(p3(1:100-7200+comp_start))); end; peg=excel_2D_array(count,3);
% pegging all pressure values,
delta_p=peg/100-p3_intake_mean; p4=p3+delta_p; if
comp_start<exp_end; p5=p4(comp_start:exp_end-1); end; if
comp_start>exp_end; p5=[p4(comp_start:7200);p4(1:exp_end-1)]; end;
%p_raw is non-filtered, properly timed, pegged pressure in bar
p_raw=p5; outcolumn=outcolumn+1; p_raw_file(:,outcolumn)=p_raw;
clear p1 p2 p3 p4 p_raw end; end;
save_name1=[num2str(point_number(count)),'-P-raw.xls'];
xlswrite(save_name1,p_raw_file,'sheet1','A1'); disp(['Low Pass
Filtering for File ',num2str(count),' of ', num2str(end_data), '
.... Point # ', num2str(point_number(count)),' in progress...']);
p_LP_filtered_file=LP_butter_filter(p_raw_file,LP_b,LP_a,outcolumn);
save_name2=[num2str(point_number(count)),'-P-filtered.xls'];
xlswrite(save_name2,p_LP_filtered_file,'sheet1','A1'); disp(['Band
Pass Filtering for File ',num2str(count),' of ', num2str(end_data),
' .... Point # ', num2str(point_number(count)),' in
progress...']);
p_BP_filtered_file=BP_butter_filter(p_raw_file,BP_b,BP_a,outcolumn);
save_name3=[num2str(point_number(count)),'-P-Band-Pass.xls'];
xlswrite(save_name3,p_BP_filtered_file,'sheet1','A1');
disp(['Calculating pressure parameters for File ',num2str(count),'
of ', num2str(end_data), ' .... Point # ',
num2str(point_number(count)),' in progress...']);
press_para_file=pressure_parameter
(p_LP_filtered_file,p_raw_file,p_BP_filtered_file,outcolumn);
title_={'max filtered press[bar]' 'max filtered press loc[CAD,aTDC]'
'max raw press[bar]' 'max raw press loc[CAD,aTDC]' ... '(max
filtered press rate [bar/CAD]' 'max filtered press rate loc
[CAD,aTDC]' 'max raw press rate [bar/CAD]' 'max raw press rate loc

```

```

[CAD,aTDC]'. . . 'knock =
max(p_filtered-p_raw)-average(p_filtered-p_raw)(bar)'. . . 'RMS of
Band Pass [bar^2]'}; clear p_LP_filtered_file clear
p_BP_filtered_file clear p_raw_file
save_name3=[num2str(point_number(count)),'-P-Parameters.xls'];
xlswrite(save_name3,title_,'sheet1','A1');
xlswrite(save_name3,press_para_file,'sheet1','A2');
clearpress_para_file; count=count+1; if count> end_data stopnow=1;
end; end; disp('END'); toc;

```

D.1.2 Low pass filter Matlab function

```

function p_LP_filtered_file =
LP_butter_filter(p_raw_file,LP_b,LP_a,outcolumn)
p_LP_filtered_file=zeros(3600,outcolumn); for column=1:outcolumn
p_raw=p_raw_file(:,column);
% making dummy points for start and end overshoots
dum_vec1=mean(p_raw(1:100)).*ones(100,1);
dum_vec2=mean(p_raw(3500:3600)).*ones(100,1);
p1=[dum_vec1;p_raw;dum_vec2]; p2=filter(LP_b,LP_a,p1);
% filtering for the first time
p3=zeros(3800,1);
% inverting filtered signal
for i=1:3800;p3(i)=p2(3801-i);end;
p4=filter(LP_b,LP_a,p3);
% filtering inverted-filtered signal
p5=zeros(3800,1);
% inverting filtered-inverted-filtered signal
for i=1:3800;p5(i)=p4(3801-i);end; [maxp2 indexp2]=max(p2); [maxp5
indexp5]=max(p5);
%calculating phase between original signal and filtered signal

```

```

delta_index=indexp2-indexp5;
p6=zeros(3800,1); for i=1:3800; if delta_index<0 i1=i-delta_index;
else i1=i+delta_index; end; if i1>3800; i1=i1-3800; end;
% shifting original-filtered signal with the amount of phase
p6(i)=p2(i1); end;
% excluding dummy points from data
p7=p6(101:3700);
p_LP_filtered=p7;
p_LP_filtered_file(:,column)=p_LP_filtered;
clear p_raw p1 p2 p3 p4 p5 p6 p7p p_LP_filtered
end;

```

D.1.3 Band pass filter Matlab function

```

function [p_BP_filtered_file, RMS_BP_vector] =
BP_butter_filter(p_raw_file,BP_b,BP_a,outcolumn)
p_BP_filtered_file=zeros(3600,outcolumn);
RMS_BP_vector=zeros(outcolumn,1); for column=1:outcolumn
p_raw=p_raw_file(:,column);
% Band Pass filtering
BP_p=filter(BP_b,BP_a,p_raw); [pmax pmaxloc]=max(p_raw);
first=pmaxloc-100;if first<1;first=1;end;
mean_around_pmax=mean(BP_p(first:pmaxloc+100));
BP_knock_portion=BP_p(first:pmaxloc+100);
n=length(BP_knock_portion); RMS_BP=norm(BP_knock_portion)/sqrt(n);
p_BP_filtered_file(:,column)=BP_p; RMS_BP_vector(column,1)=RMS_BP;
clear BP_p p_raw RMS_BP end;

```

Motoring Curves and CR Estimation

The cylinder head in the CFR engine used in the current study is a special-made cylinder head with six access holes around the combustion chamber. The head is categorized as an octane-head. Removing the bearing plate also changed the engine configuration from its original setup and hence the compression ratio in this study is different from the standard CFR compression ratio in other studies.

During the experiments, from each compression ratio setup and on each day of experiment two motoring pressure traces were collected and saved as the reference for the pressure trace. For motoring pressure trace measurement, intake temperature, manifold absolute pressure, and motoring speed were recorded. As all operating points were saved in Excel files with consecutive number names, each set of data points with the same compression ratio had numbers between cold and hot motoring pressure trace file names. For example, for supercharged HCCI case test on April 19, 2007, the cold motoring pressure trace file was 1340-P-filtered.xls, the hot motoring pressure trace file was 1433-P-filtered.xls, and all data points between 1341-P-filtered.xls to 1432-P-filtered.xls had the same compression ratio.

The gap between the piston crown and top of combustion chamber was measured and used for geometrical compression ratio calculation. For example, when the gap was 0.1880 inch, the engine stroke was constant at 4.5 inch,

Table E.1: Geometrical and effective compression ratio with indication of motoring P_{\max}

Point #	GAP (inch)	GCR	P_{Intake} (kPa)	T (°C)	Speed (RPM)	P_{\max} (bar)	ECR
1216	0.1880	24.9	92.05	232.8	476	47.5	18.8
1215	0.1880	24.9	91.41	152.7	723	42.8	18.0
1327	0.1895	24.7	86.85	21.7	465	46.21	18.8
1326	0.1895	24.7	91.4	143.2	719	43.1	18.1
1340	0.3540	13.7	91.47	23.9	557	25.4	11.8
1433	0.3540	13.7	92.6	113	761	24.3	11.6
1434	0.3520	13.7	91	30	560	24.3	11.6
1512	0.3540	13.7	91.74	23.2	541	25.9	11.9
1572	0.3540	13.7	93.86	121.5	766	25.09	11.7
1686	0.1800	26.0	92.62	146	723	45.04	18.6
1687	0.3500	13.8	92.7	25	540	25.88	11.8
1714	0.4680	10.6	92.7	113.7	773	18.11	9.3
1715	0.2680	17.7	91.7	25	540	33.1	14.4

hence, the geometrical compression ratio became $GCR = \frac{4.5+0.1880}{0.1880} = 24.9$. Running ChemComb-SZM with the experimental initial conditions and a try-and-error procedure, when the P_{\max} obtained by model matched the experimental P_{\max} , the CR of model was named effective CR (ECR) and used in all experimental results of the current study. Considering that ChemComb-SZM is an approximation, single zone model that does not count for blow-by, the ECR would be different from CR reported by other researchers that use CFR engine. Table E.1 shows the summary of experimental and modeling results for several cases.

In Table E.1 Point # is the unique number of motoring pressure trace Excel file, GAP is the distance between piston crown and top pf combustion chamber, GCR is geometrical compression ratio, P_{Intake} is manifold absolute pressure during motoring test, $T_{\text{intake,mix}}$ is intake mixture temperature (in this case just air) entering cylinder during motoring test, speed is motoring speed, and P_{\max} is the experimental pressure trace that was matched with modeling pressure trace to obtain effective compression ratio (ECR). Equation 2.2 in Chapter 2 was calculated using Table E.1 data.

Table E.2: A comparison of experimental P_{\max} for CFR engine motoring under identical initial conditions at University of Alberta (UofA- current study) and Alberta Research Council (ARC- standard CFR) research facilities

Gap (inch)	P_{\max} in UofA (psi)	P_{\max} in ARC (psi)	SCR	ECR
0.5000	201	233	10.00	7.83
0.4500	239	260	11.00	8.71
0.4000	270	297	12.25	9.58
0.3500	306	340	13.86	10.25
0.300	358	394	16.00	11.44
0.250	422	466	19.00	12.92

In order to compare the ECR used in this study with common normal CFR engine compression ratio, a series of tests were conducted in Alberta Research Council where they operate CFR engine to rate the octane and cetane number of fuels in the standard procedure of CFR engine operation according to ASTM 2699 and ASTM 2700 standards. For the same gap, the maximum pressure was measured in both CFR engines in University of Alberta engine research facility (the current study) and Alberta Research Council (standard CFR). Table E.2 compares the P_{\max} obtained during motoring tests with identical initial conditions in the custom-made University of Alberta CFR engine (current study) and standard Alberta Research Council CFR engine.

In Table E.2 gap is the distance between piston crown to top of combustion chamber, SCR is standard compression ratio obtained from ASTM manual, and ECR is effective compression ratio calculated by regression correlation of data in Table E.1 using ChemComb-SZM.

Knock Characterization Parameters

Normally even when the knock is not expected there is good chance of knocking cycles between non-knocking cycles. Even some times in an operating point both knocking cycle and misfiring cycle are observed. This comes from variation of air/fuel ratio and randomness characteristics especially in conventional SI and CI combustion. Usually in order to define that a point is or is not acceptable in the engine operating map knock detection criterion is set on a specified parameter. Then in a range of consecutive cycles, number of cycles that are exceeding knock threshold are counted and if the ratio of knocking cycles to non-knocking cycles (this is usually called knock occurrence frequency (KOF)) exceeds a certain fraction for example 10%, the operating point is counted as a knocking point. However in this study the objective is not getting a practical engine map but exploring the combustion characteristics at certain condition. Hence non of the points were rejected as an unpractical point due to excessive knocking vibration of the engine. Instead the boundaries of the operating region were defined and for each operating point a knock quantity was assigned that comes from averaging knocking strength of individual cycles with a certain confidence interval. The following description applies to knock quantification in an isolated cycle. In the following section knock quantification parameters that were examined and used for the purpose of knock quantification are presented:

F.1 Filtered and Un-filtered Pressure Signal Difference (ΔP_P)

Haghgooie (1990) [132] acquired cylinder pressure data at high sampling rate during knocking portion of cycle and averaged it over one crank angle degree (CAD) increment. Then a cubic spline was used to smooth the fluctuated pressure. ΔP_P was defined as the difference between fluctuated pressure and smoothed spline. Knocking point was defined as ΔP_P exceeded five times of average value of pressure over the increment.

Here ΔP_P was defined in a similar way. Assume that the pressure signal is properly pegged and timed. Such a pressure trace was named P_{raw} . Then a 4th order Butterworth digital filter with cut-off frequency of 1000 Hz was used to filter measurement noise and knocking fluctuation from P_{raw} . Butterworth approximating function is often called the maximally flat response because no other approximation has smoother transition through the pass band to the stop band. Proper phase-shifting technique was applied to compensate for phase lag of filtering procedure. Sampling rate was based on the engine speed as in-cylinder pressure was sampled at the rate of 0.1 CAD reading resolution. For example at 700 RPM, sampling rate was 42000 Hz. Then a portion of cycle from 10 CAD before $P_{max,loc}$ time to 10 CAD after $P_{max,loc}$ was considered. Filtered pressure signal was named P_{filt} . Then ΔP_P was defined as follow for considered portion of pressure trace:

$$\Delta P = Max(|P_{raw} - P_{filt}|) - Mean(|P_{raw} - P_{filt}|) \quad (F.1)$$

ΔP_P was examined for several engine cycles and operating points. Figure F.1 shows ΔP_P definition and compares it for two knocking and non-knocking cycles. Figure F.1-a-1 and Figure F.1-a-2 are related to a knocking operating point. Figure F.1-b-1 and Figure F.1-b-2 are related to a non-knocking operating point. Note the difference between Y-axis scales in Figure F.1-a-2 and Figure F.1-b-2. Non-knocking cycle indicated much lower ΔP_P in comparison with knocking cycle.

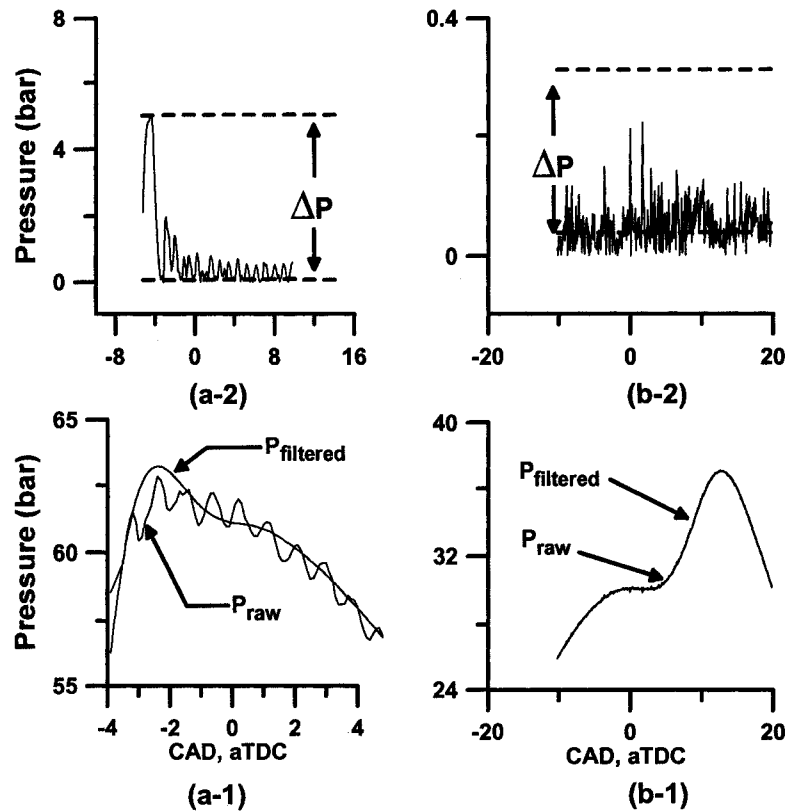


Figure F.1: ΔP_P definition and indication in two various operating points in an HCCI engine at CR=14.4 , N=700 RPM, fueled with PRF80 and EGR=40%. (a) knocking cycle, $\lambda=1.27$, $\Delta P_P = 4.94$ bar (b) non-knocking cycle $\lambda=1.64$, $\Delta P_P = 0.27$ bar

F.2 Root Mean Square of Band Pass Filtered Pressure Trace (RMS_P)

In this method a Butterworth 4th order band pass filter was used to separate knock frequency oscillation. First and second frequencies are chosen as 5000 and 6000 Hz around known knock frequency of the engine used in experiments. It has been found in previous studies on the same engine that knock frequency is about 5.7 kHz [133, 134, 135]. Then RMS of band passed signal is calculated in the same interval as ΔP_P . Figure F.2 compares RMS of the same cycles of Figure F.1. Note the difference of x-axes for $P_{max,time}$ in Figure F.2-a and

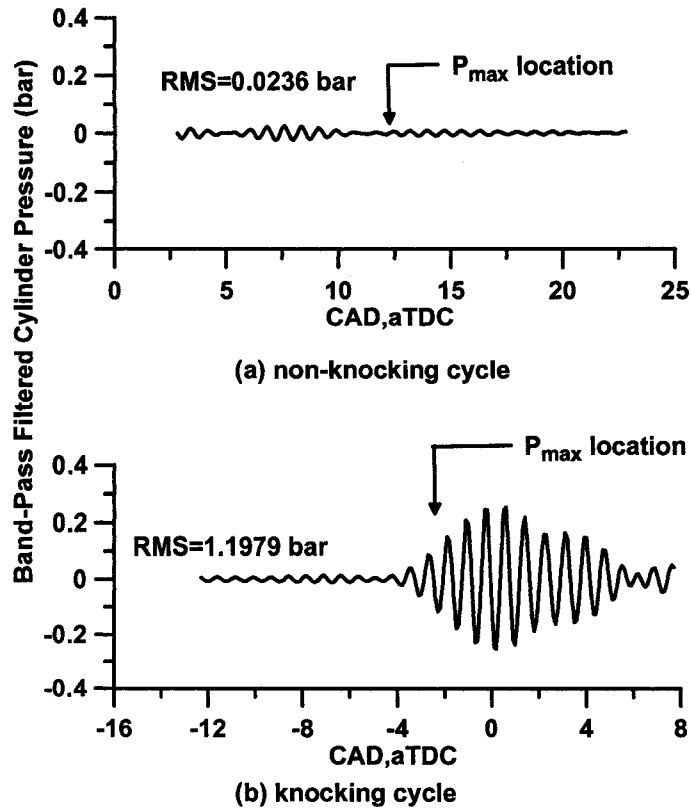


Figure F.2: RMS definition and indication in two various operating points in an HCCI engine at CR=14.4 , N=700 RPM, fueled with PRF80 and EGR=40%. (a) $\lambda=1.64$, RMS=0.0236 bar (b) $\lambda=1.27$, RMS=1.1979 bar

Figure F.2-b.

F.3 Vibration Analysis of Cylinder Structure

The voltage output of the accelerometer were used directly to quantify the cylinder structure vibration. Two parameters were extracted from the sensor output. The signal RMS ($RMS_{Acc.}$) and peak-to-peak ($Pk_{Acc.}$) in the vicinity of -10 CAD before TDC to 50 CAD after TDC were calculated as indicators of cylinder vibration.

F.4 Evaluation of Knock Indicators

In-cylinder maximum pressure rate or maximum first derivative of cylinder pressure with respect to crank angle rotation $(dP/d\theta)_{\max}$ was considered as the base line for defining knock for the HCCI engine. As discussed before $(dP/d\theta)_{\max}$ is a defining parameter for knock and noise level. Taking $(dP/d\theta)_{\max}$ as a base parameter, we considered a value of $(dP/d\theta)_{\max}$ as knock limit boundary. Usually a value of 10 bar/CAD is considered as the knock boundary (e.g. Iida et al (2001) [181]). Figure F.3 shows the relation of P_{\max} and $(dP/d\theta)_{\max}$ at various CR and RON.

P_{\max} was linearly dependent to $(dP/d\theta)_{\max}$ when CR is constant. Figure F.3 also indicates that RON did not have any effect on P_{\max} at any constant CR. Even several of indicted operating points in Figure F.3 were fueled with a mixture of PRF and RG while P_{\max} appeared in the same category of constant CR points. For conducted tests as valve events and throttle position (wide

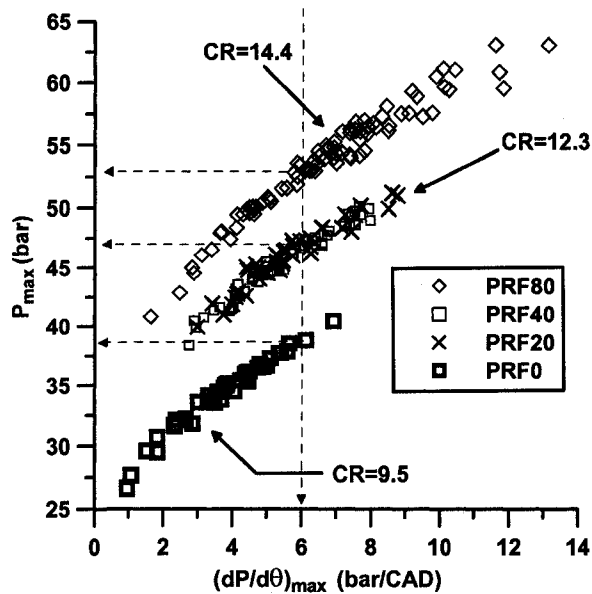


Figure F.3: Maximum cylinder pressure (P_{\max}) versus maximum cylinder pressure rate $(dP/d\theta)_{\max}$ at CR=9.5, 12.3, and 14.4, also various RON=0, 20, 40, and 80. HCCI combustion in CFR engine, N=700 RPM, various λ and EGR.

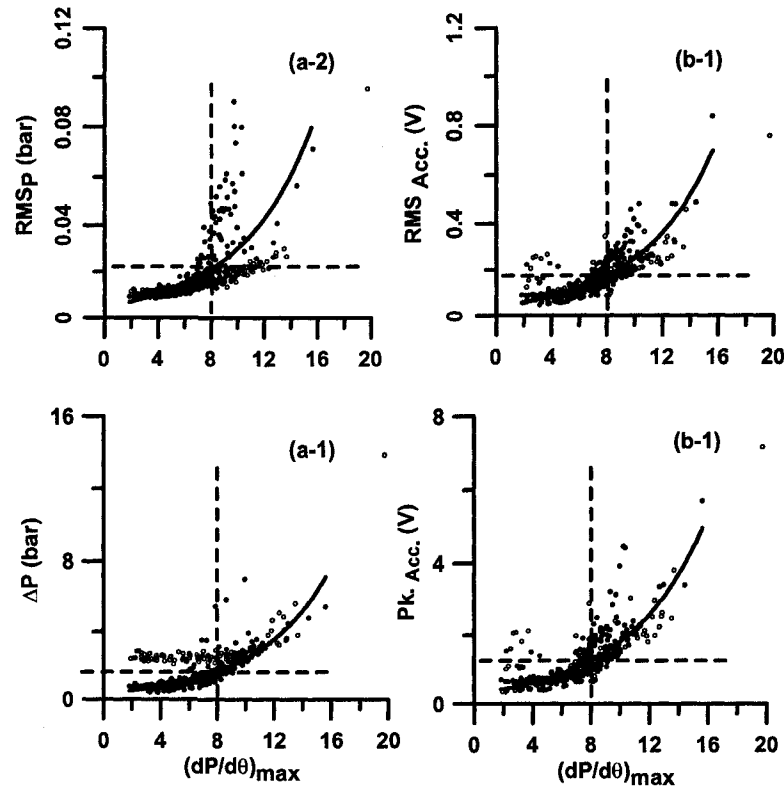


Figure F.4: A comparison of knock measuring parameters using a nonlinear least square fit and marking $(dP/d\theta)_{\max} = 8$ bar/CAD

open) were constant, it can be assumed that effective CR was also constant when keeping a constant geometrical CR. In a variable valve timing engine effective CR is changing on a cycle-by-cycle basis; hence, P_{\max} will not behave linearly with $(dP/d\theta)_{\max}$. As an example, consider a limit of $(dP/d\theta)_{\max} = 6$ bar/CAD for knock boundary. Then at various compression ratios of 9.5, 12.3, and 14.4 various P_{\max} was obtained for knock boundary as indicated in Figure F.3 with dash lines.

Figure F.4 shows the relation of ΔP_P , RMS_P , $Pk_{Acc.}$, and $RMS_{Acc.}$ with $(dP/d\theta)_{\max}$.

All parameters coincide on certain exponential lines for various CR, RON, λ , EGR and RG mass fractions except for the case of natural gas on ΔP_P . Several observations can be made from Figure F.4. For all knock detection

parameters, the value remains under certain level when rate of pressure rise is low. Then after a certain value the parameter value increases exponentially. The exponential functions shown in the Figure F.4 shows the effect clearly. There are some scatter in data both in high $(dP/d\theta)_{\max}$ and low $(dP/d\theta)_{\max}$. For high $(dP/d\theta)_{\max}$ case severe knocking causes graduate increase of knock from one cycle to the next one because of disturbing thermal heat transfer boundary layer and more existence of hot spots inside the combustion chamber. For low $(dP/d\theta)_{\max}$ case, usually these operating points are associated with high cyclic variation that $COV_{IMEP} > 10\%$ and for such operating points the engine operation in HCCI mode fluctuates between misfiring/partial burning in one cycle to knock in the next cycle because of returning extreme amount of unburned fuel from misfiring cycle through EGR to the next cycle that causes a temporary rich mixture, high rate of pressure rise and knock. Non-compatible behavior of natural gas cases in Figure F.4-1-a is also because of this phenomenon. Natural gas supercharged cases were accompanied by high cyclic variation that for several cases the engine was fluctuation between misfiring and knocking cycles. Note that all four parameters indicated in Figure F.4 are averaged over 100 cycles.

Appendix **G**

Error and Uncertainty Analysis

As mentioned in Chapter 2, the parameters in this study were divided into three groups of primary, secondary and cyclic variation related parameters. The uncertainty and error analysis were performed differently for each group.

G.1 Primary variables error analysis

The primary group of parameters include fuel flow rate, RG flow rate, air flow rate, all measured temperatures, intake and exhaust pressures, and exhaust gas species concentrations. Internal error analysis was used for this group of parameters. Performing repeated measurement, each primary parameters α was measured at least $n=20$ times in a steady state engine operation. For example Figure G.1 shows a sample box plot of four independent primary variables.

For the variable α the error was calculated as $\varepsilon_{\alpha} = 2 * \sigma_{n-1}$ where σ_{n-1} is the standard deviation for a sample size n and ε_{α} is calculated with 95% confidence limit. For example, for the cases of Figure G.1, $\varepsilon_{m_{RG}} = 0.22$ mg/s, $\varepsilon_{m_{Air}} = 0.02$ g/s, $\varepsilon_{P_{intake}} = 0.03$ kPa, and $\varepsilon_{HC} = 11$ ppm.

Internal error analysis results were compared with the error calculation based on the calibration curve for those parameters that use a calibration value. For example, Figure C.4 shows the calibration curve for natural gas mass flow

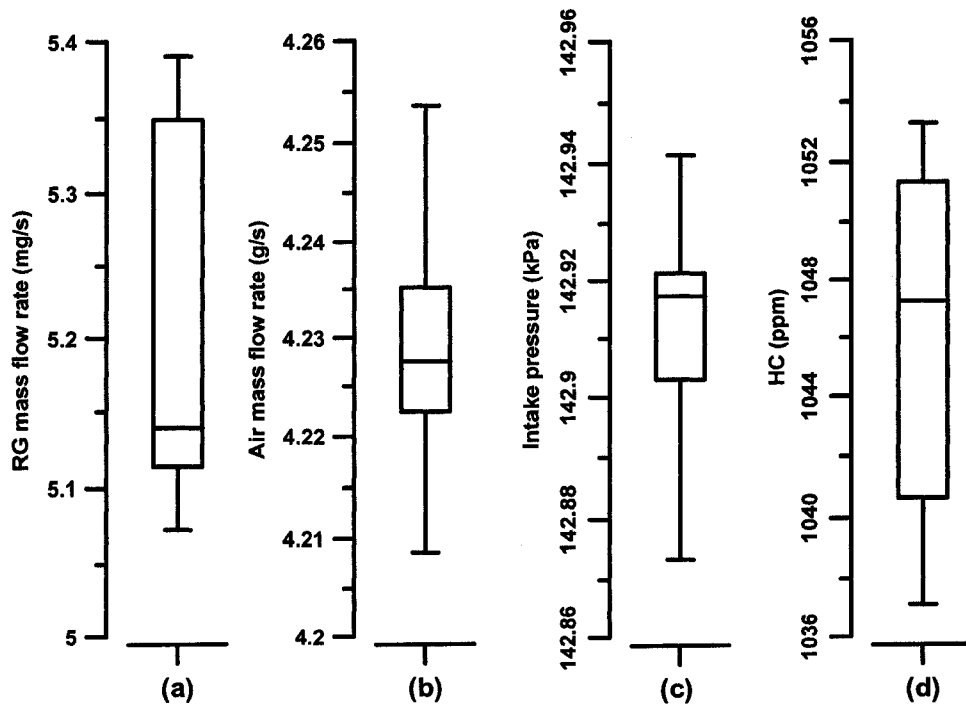


Figure G.1: A Box plot sample for four primary variables of (a) RG mass flow rate, (b) intake air mass flow rate , (c) intake absolute pressure, and (d) HC concentration in the exhaust, HCCI combustion of n-Heptane in the supercharged mode at 800 RPM

meter. Based on the linear regression fit indicated in Figure C.4, coefficient of determination $R^2=0.993698$. Statistical analysis of the linear regression fit in Figure C.4 shows that residual mean square, $\bar{\sigma}^2 = 192.512$, and $\bar{\sigma} = 13.8748$. Considering a resolution of 0.01 V for analog output measurement, calculated $\bar{\sigma} = 13.8748$ is translated to 0.13 mg/s for the uncertainty of natural gas mass flow rate. Then the error calculated from calibration curve was compared to individual internal error calculated for natural gas mass flow using repeated measurement technique. The largest value was considered as the error for the primary parameter.

G.2 Secondary variables error analysis

The secondary variables are those variables that were directly calculated from primary variables such as λ , RG blend fraction, efficiencies, and indicated specific emissions. External error analysis was used for the secondary variable error analysis.

For example, to calculate error for λ in the case of n-Heptane base fuel with RG 25/75 enrichment, the equivalence ratio ϕ is calculated using Valence method by:

$$\phi = \frac{44\dot{n}_{\text{n-Heptane}} + 2.5\dot{n}_{\text{RG}}}{0.5\dot{n}_{\text{RG}} + 4\dot{n}_{\text{Air}}} \quad (\text{G.1})$$

where \dot{n} is the molar flow rate of each component calculated by having the mass flow rates and molecular weights. Assume: $\alpha = \dot{n}_{\text{n-Heptane}}$, $\gamma = \dot{n}_{\text{RG}}$, $\zeta = \dot{n}_{\text{Air}}$, and $\beta = 0.5\gamma + 4\zeta$. In addition, assume:

$$\alpha_1 = \frac{44}{\beta} \quad (\text{G.2})$$

$$\alpha_2 = \frac{2.5\beta - 0.5(44\alpha + 2.5\gamma)}{\beta^2} \quad (\text{G.3})$$

$$\alpha_3 = -4\frac{44\alpha + 2.5\gamma}{\beta^2} \quad (\text{G.4})$$

Then, the error of equivalence ratio becomes:

$$\varepsilon_\phi = \sqrt{\alpha_1\varepsilon_\alpha^2 + \alpha_2\varepsilon_\gamma^2 + \alpha_3\varepsilon_\zeta^2} \quad (\text{G.5})$$

Having

$$\lambda = \frac{1}{\phi} \quad (\text{G.6})$$

then λ error becomes:

$$\varepsilon_\lambda = \sqrt{\frac{\varepsilon_\phi^2}{\phi^2}} \quad (\text{G.7})$$

The same technique applied to other secondary variables to estimate the uncertainty.

G.3 Cyclic variation related variables error analysis

In several cases in the current study, the indicated parameters were averaged over 100 consecutive cycles. Parameters such as IMEP, SOC, CD, P_{\max} , $(dP/d\theta)_{\max}$, and NTC are some of them. Cyclic variation in HCCI combustion is less than that of conventional combustion, but compared to absolute error calculated from internal and external error analysis is significant. Averaging over 100 consecutive cycles, the cyclic error associated with each parameter (α) was calculated by $\varepsilon_{\alpha} = 2 * \sigma_{n-1}$ where $n=100$ in this case. These values of cyclic variations were indicated as error bars in the associated plots.

Additional Experimental Results

H.1 Baseline Experiments- Emission Results

A monotone increase of isCO and isHC in exhaust is one of the reasons for thermal efficiency decrease by increasing λ . Figure H.1 and Figure H.2 show the HC and CO emissions of HCCI combustion using PRFs. HCCI combustion disadvantage of high HC and CO emissions is clear in Figures H.1 and H.2.

In both cases, HC and CO increased by increasing λ . Some dependency of both HC and CO emissions to EGR also was observed. At any constant EGR line, increasing λ shifted the operating region toward low load boundary. Increasing air/fuel ratio replaces the fuel molecules by biatomic and triatomic molecules of air resulting to decrease the heat capacity of the mixture and higher after compression temperature. On the other hand, leaner air/fuel ratio deviates the combustion temperature to lower values. Lower combustion and expansion temperature resulted to less oxidation of CO and HC and higher exhaust emissions. Although there is an obvious trend of HC and CO emission reduction when going to higher EGR rates, looking carefully to HC and CO plots reveals that in constant λ cases at various EGR rates (which is rare because of limited operating range) higher EGR rates indicate much higher HC and CO emission. In fact, general trend of lower HC and CO emis-

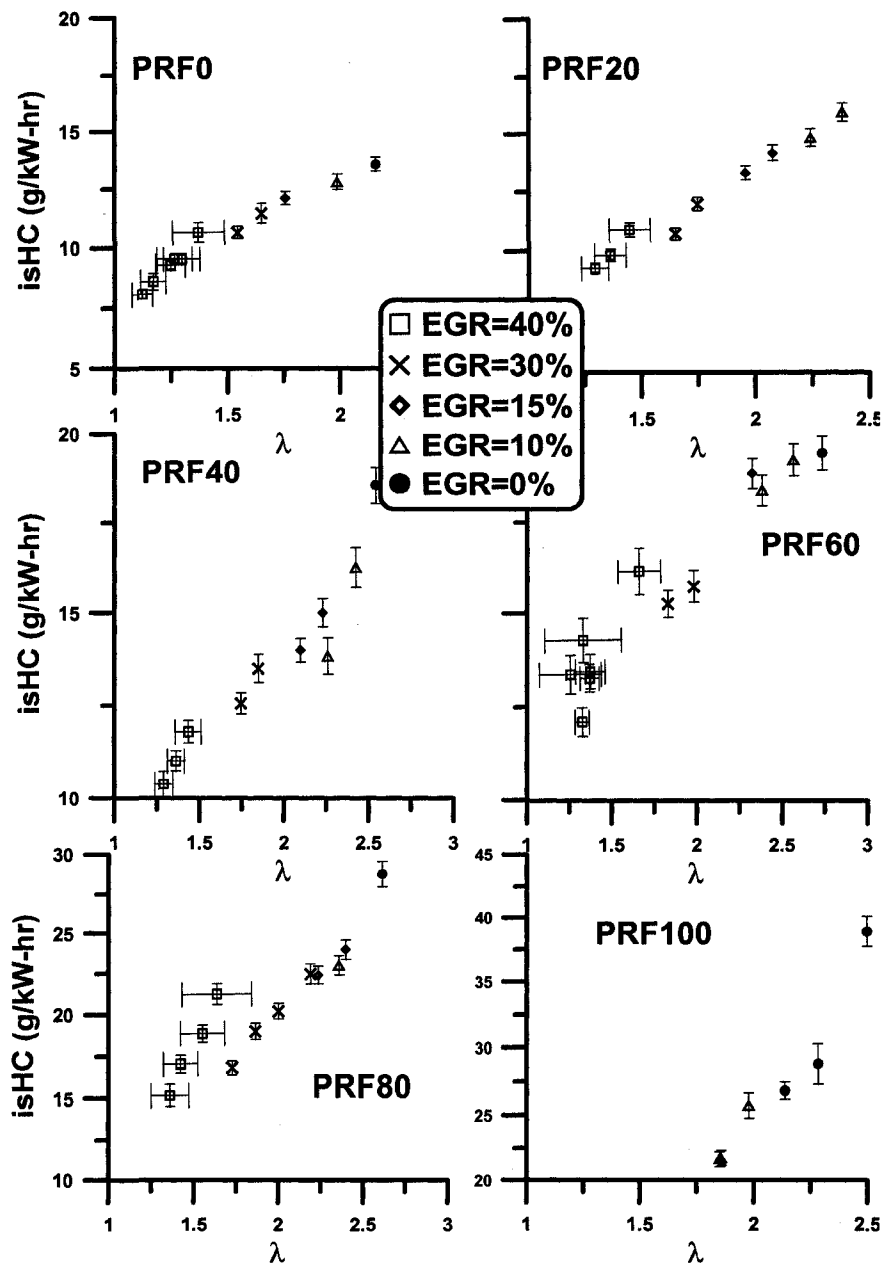


Figure H.1: Effect of λ and EGR on indicated specific HC emissions, initial conditions indicated in Table 3.1

sions at higher EGR rates is just because of the mixture quality that is near to stoichiometric at higher EGR fractions. EGR itself increased HC and CO

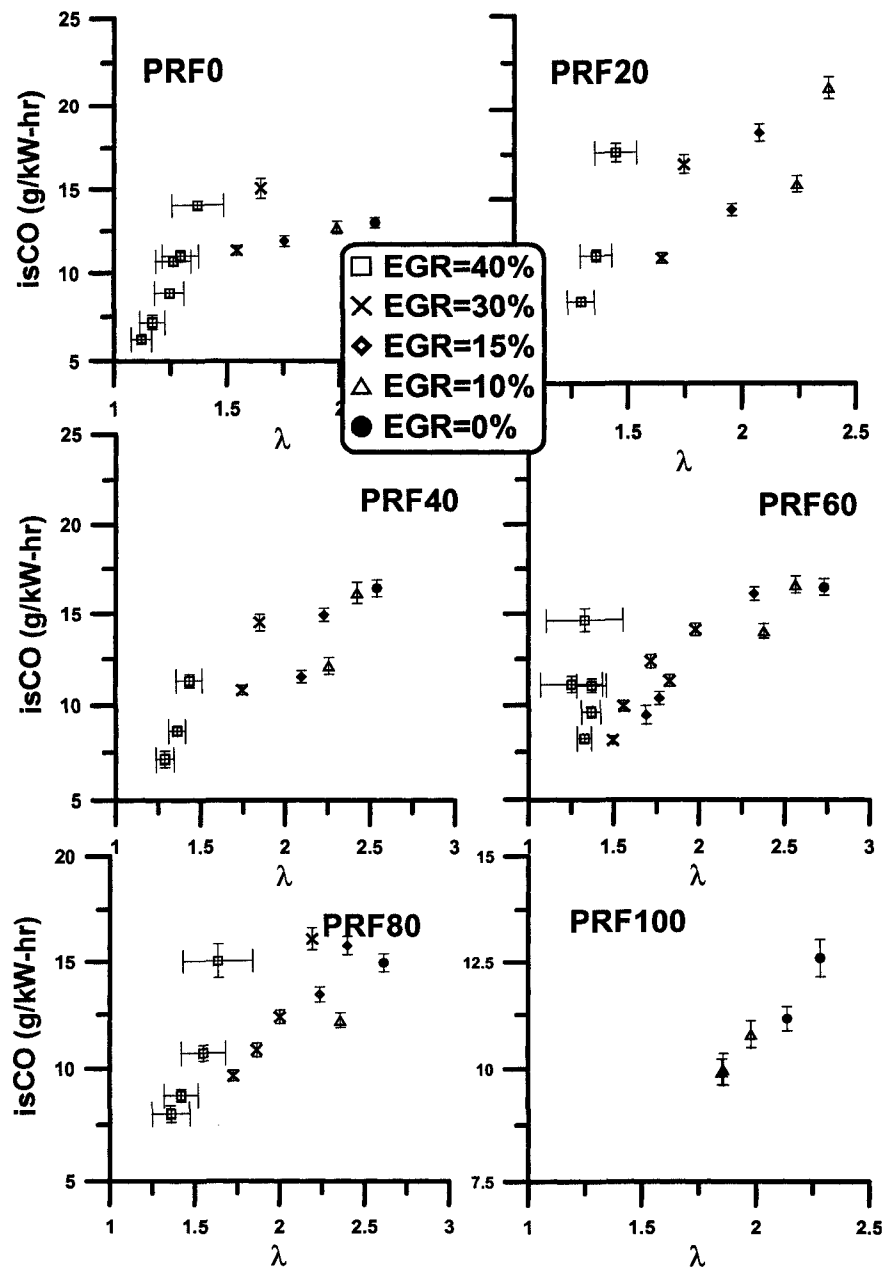


Figure H.2: Effect of λ and EGR on indicated specific CO emissions, initial conditions indicated in Table 3.1

emissions as it was expected from previous HCCI studies. The same trend also is observed in conventional combustion modes.

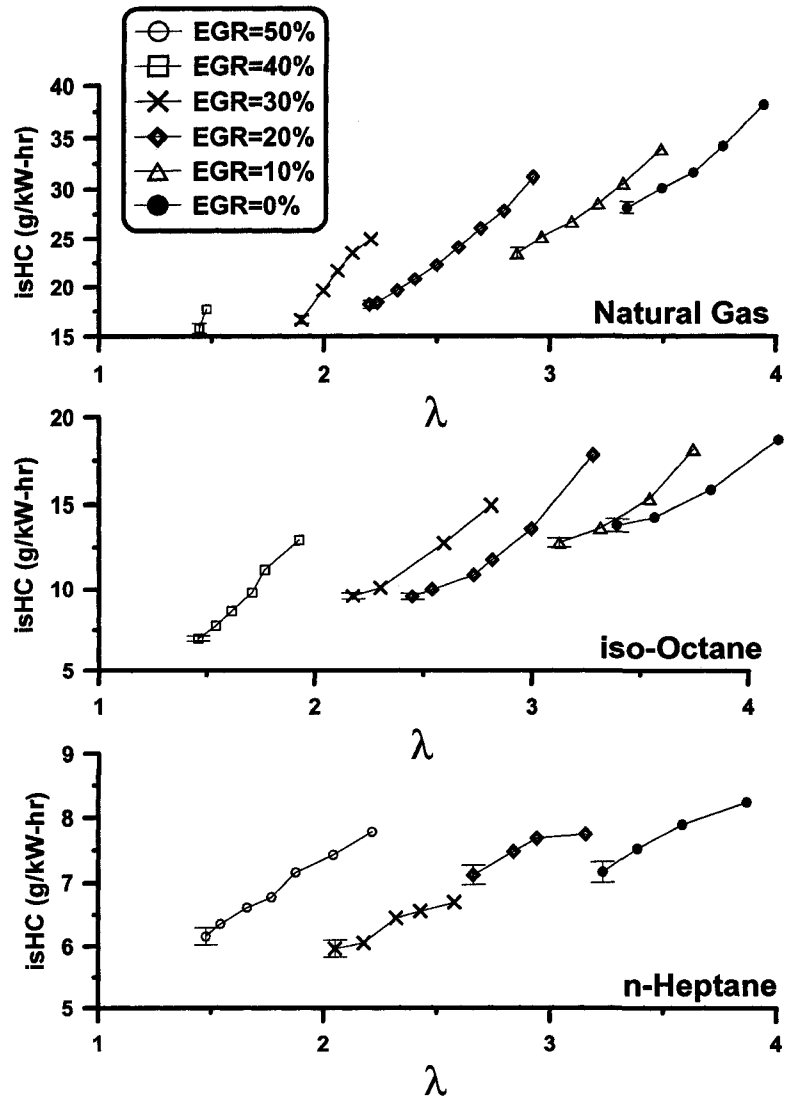


Figure H.3: Effect of λ and EGR on indicated specific HC, Supercharged HCCI combustion of natural gas, n-Heptane and iso-Octane, initial conditions indicated in Table 3.2

The same general trends were observed for both HC and CO emissions for HCCI combustion supercharged cases. For supercharged HCCI natural gas case, HC and CO emissions were extremely high as the operating region was selected toward the lean side and partial burning boundary to avoid excessive

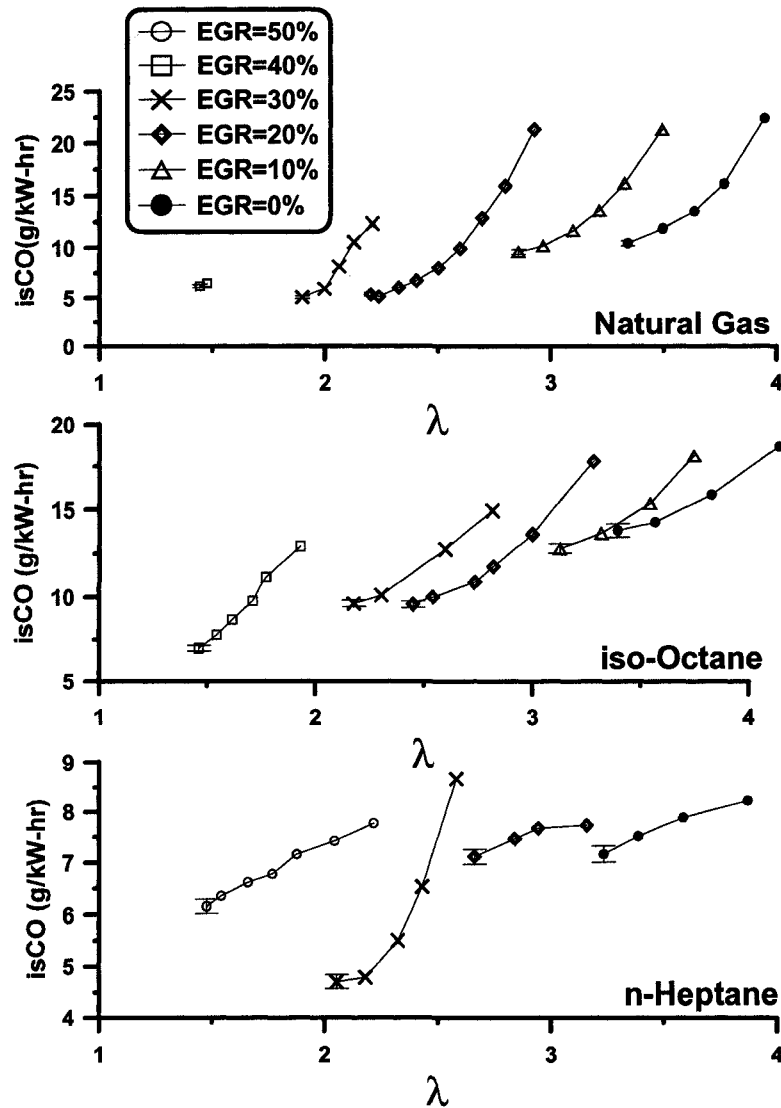


Figure H.4: Effect of λ and EGR on indicated specific CO, Supercharged HCCI combustion of natural gas, n-Heptane and iso-Octane, initial conditions indicated in Table 3.2

knock and high P_{max} . Hence overall HC and CO emission were produced with natural gas were high in comparison with normal HCCI combustion. Always increasing λ and/or EGR increased isHC and isCO emissions considerably. Approaching misfiring/partial burning boundary increased the emissions con-

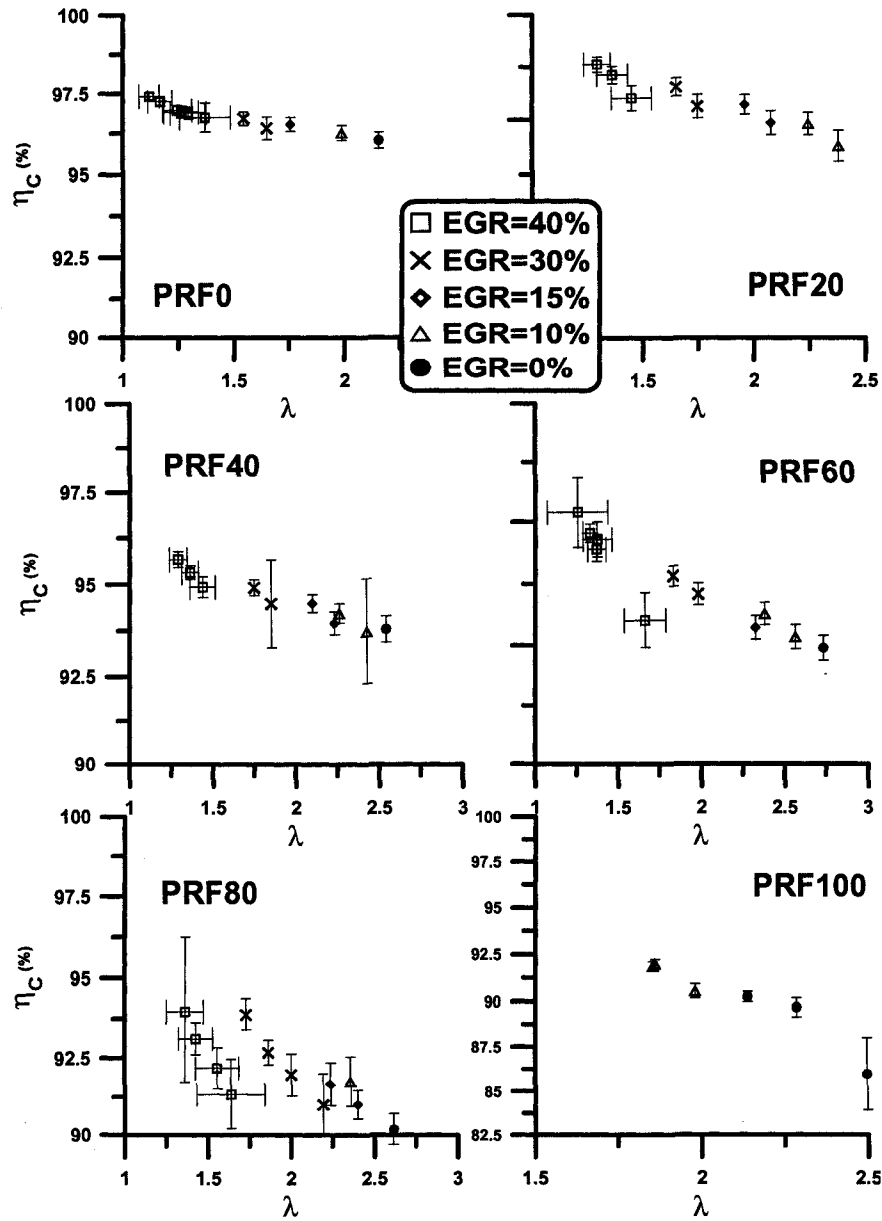


Figure H.5: Effect of λ and EGR on combustion efficiency emissions, initial conditions indicated in Table 3.1

siderably.

Increasing HC and CO emission by shifting the operating region toward leaner mixture causes a penalty in combustion efficiency that was calculated using

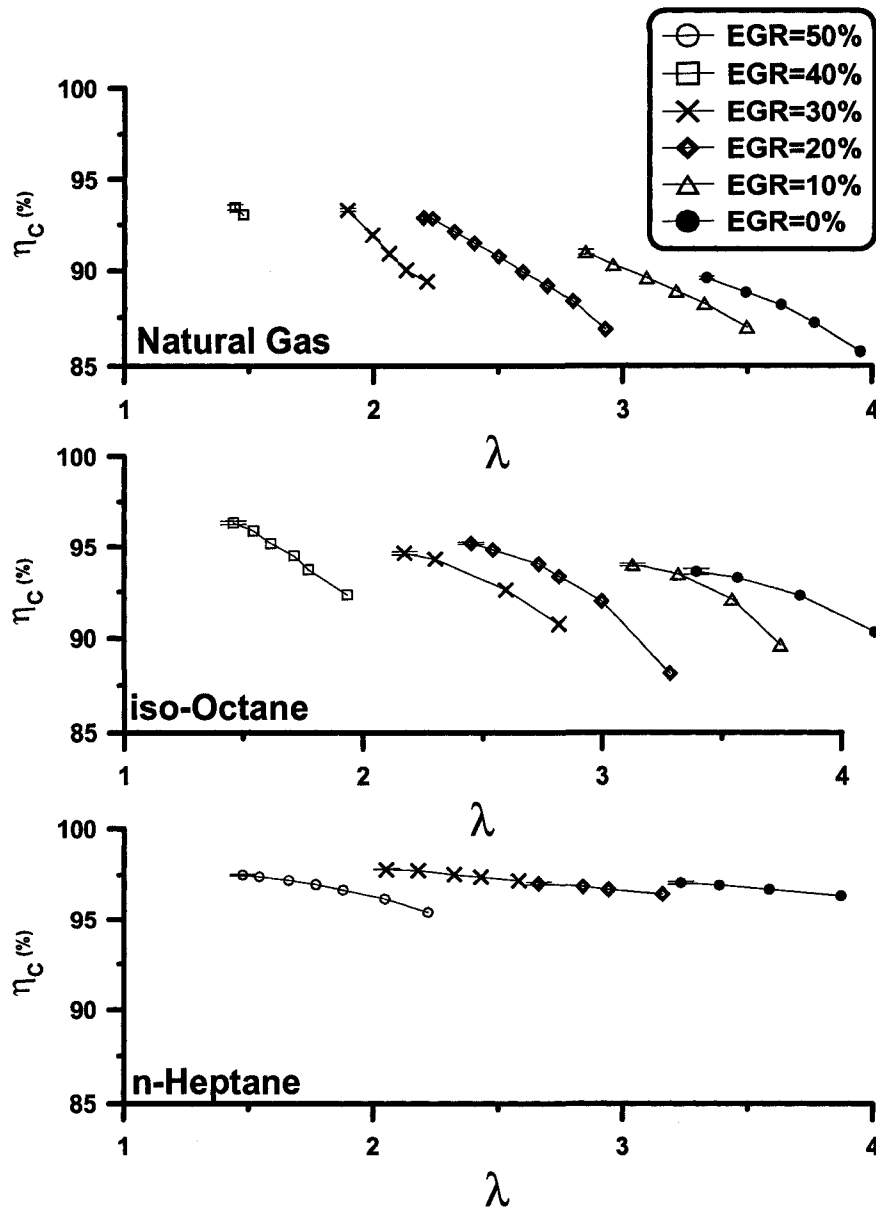


Figure H.6: Effect of λ and EGR on combustion efficiency, Supercharged HCCI combustion of natural gas, n-Heptane and iso-Octane, initial conditions indicated in Table 3.2

Equation 2.12 and is indicated in Figure 3.17 and Figure H.6 for both PRFs and supercharged cases. Combustion efficiency trends were closely followed

HC and CO emission trends. Highest combustion efficiency was achieved at lower λ values.

As it has been discussed earlier from [30, 149] this effect is the strongest among the other possible EGR effects and hence by increasing $T_{\text{intake,mix}}$ and CR the thermal effect of EGR was minimized or vanished.

H.2 Baseline Experiments- Effect of λ and EGR on Knock

Combustion knock intensity was affected by λ and EGR as indicated in Figure H.7. Knock intensity parameters definition was defined in Appendix F. The high cyclic uncertainty of the mean knock intensity for ΔP_P is because of the nature of the phenomenon. Most of the time in 100 consecutive cycles pressure traces, there are several knocking cycles that their occurrences are increased by increasing knock intensity. Hence is some operating points the combination of knocking cycles and non-knocking cycles produces a high cyclic variation uncertainty that is shown in Figure H.7. For the operating points near to the knock boundary, ΔP_P cyclic variation was higher because of switching between knock and misfiring from cycle to cycle at high EGR rates. Details of cyclic error calculation can be found in Appendix G. At any constant EGR rate the knock intensity cyclic variation is maximum at the richest λ value as it laid on knocking region of the operating window.

Knock intensity increased with decreasing EGR and/or λ for most cases. However, EGR effect was observed to be more effective on reducing knock intensity than that of λ .

The same observation was made for supercharged cases. In these cases instead of ΔP_P calculated from pressure trace, raw voltage output of an accelerometer was used to quantify the knock as described in Appendix F. The error bar shows the cyclic variation uncertainty of the mean peak-to-peak voltage. Knock intensity was decreased by increasing λ and/or EGR with dominant

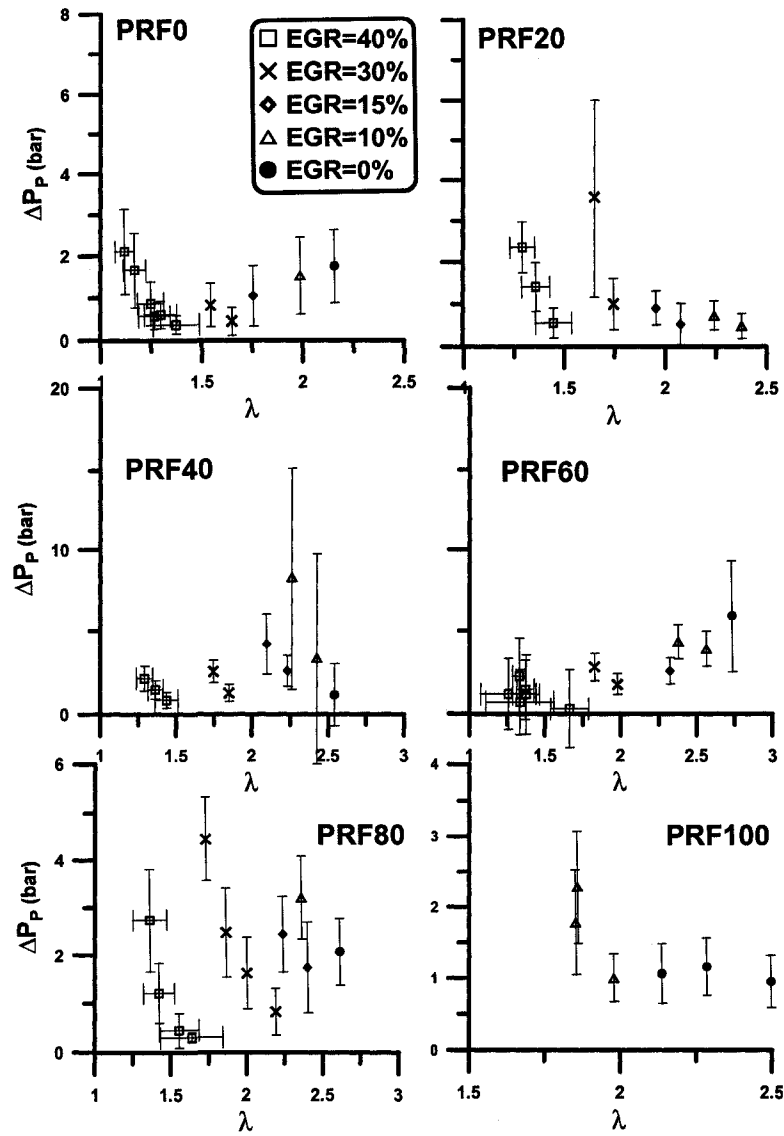


Figure H.7: Effect of λ and EGR on knock intensity (ΔP_P), Experimental matrix indicated in Table 3.1

effect belonging to λ .

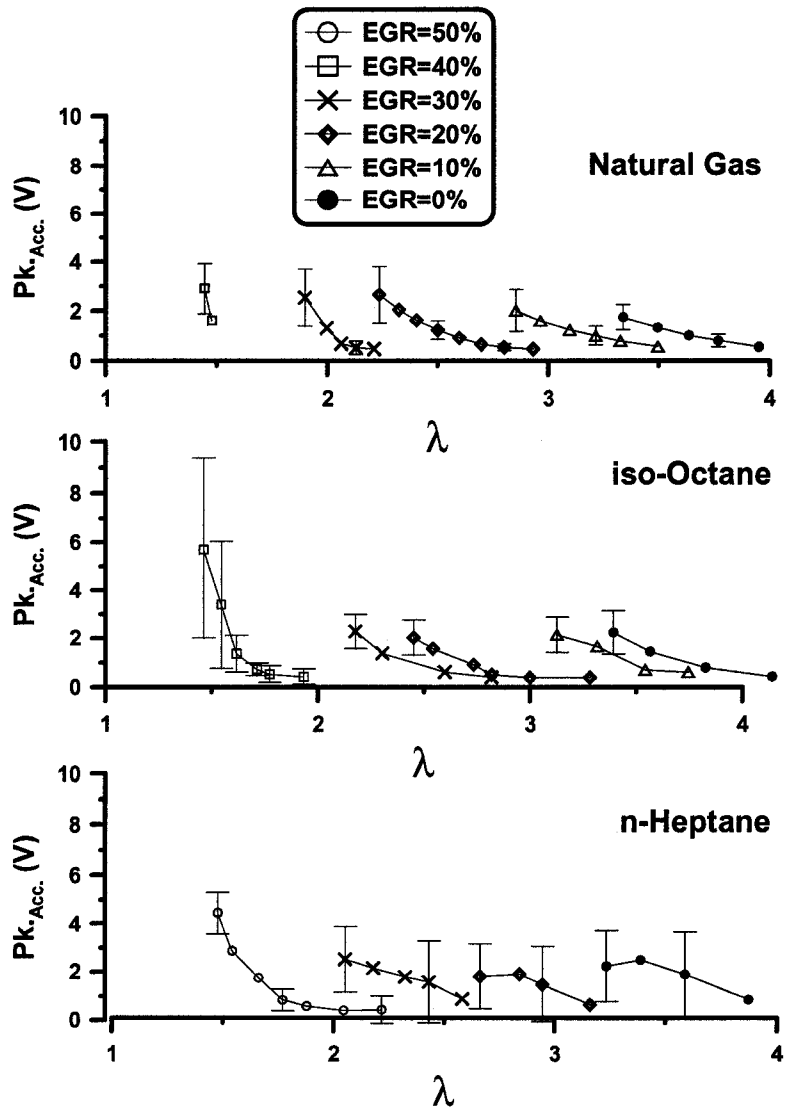


Figure H.8: Effect of λ and EGR on knock intensity measured by peak-to-peak voltage output of accelerometer ($Pk_{Acc.}$), Supercharged HCCI combustion of natural gas, n-Heptane and iso-Octane, initial conditions indicated in Table 3.2